

**HYBRID FRP-CONCRETE BRIDGE
DECK SYSTEMS
Project No.: C-02-07**

**FINAL REPORT I:
DEVELOPMENT AND SYSTEM PERFORMANCE
VALIDATION**

Amjad J. Aref, Ph. D.

Professor

Department of Civil, Structural and Environmental Engineering

University at Buffalo-State University of New York

Buffalo, NY, 14260

and

Wael I. Alnahhal

Research Assistant

Department of Civil, Structural and Environmental Engineering

University at Buffalo-State University of New York

Buffalo, NY, 14260

October 2009

DISCLAIMER

This report was funded in part through grant(s) from the Federal Highway Administration, United States Department of Transportation, under the State Planning and Research Program, Section 505 of Title 23, U.S. Code. The contents of this report do not necessarily reflect the official views or policy of the United States Department of Transportation, the Federal Highway Administration or the New York State Department of Transportation. This report does not constitute a standard, specification, regulation, product endorsement, or an endorsement of manufacturers.

| | | | |
|------------------------------------------------------------------------------------------------------------------------------------------------------------------------------------------------------------------------------------------------------------------------------------------------------------------------------------------------------------------------------------------------------------------|----------------------------------------------------------------------|--------------------------------------------------------------|-----------|
| 1. Report No. C-02-07 | 2. Government Accession No. | 3. Recipient's Catalog No. | |
| 4. Title and Subtitle HYBRID FRP-CONCRETE BRIDGE DECK SYSTEM REPORT I: DEVELOPMENT AND SYSTEM PERFORMANCE VALIDATION | | 5. Report Date October 2009 | |
| 7. Author(s) Amjad J. Aref and Wael I. Alnahhal | | 6. Performing Organization Code: | |
| 9. Performing Organization Name and Address State University of New York at Buffalo 212 Ketter Hall – Buffalo – NY - 14260 | | 8. Performing Organization Report No. | |
| 12. Sponsoring Agency Name and Address NYS Department of Transportation 50 Wolf Road Albany, New York 12232 | | 10. Work Unit No. (TRAIS) | |
| | | 11. Contract or Grant No. | |
| | | 13. Type of Report and Period Covered Final Report | |
| | | 14. Sponsoring Agency Code | |
| 15. Supplementary Notes Project funded in part with funds from the Federal Highway administration | | | |
| 16. Abstract In this study, the concept of the hybrid FRP-concrete structural systems was applied to both bridge superstructure and deck systems. Results from the both experimental and computational analysis for both the hybrid bridge superstructure and deck systems confirmed that the hybrid FRP-concrete bridge systems have an excellent performance from structural engineering point of view. | | | |
| 17. Key Words FRP Composites, Hybrid Design, Bridge Deck, Concrete, Bridge Superstructure | | 18. Distribution Statement No restrictions | |
| 19. Security Classification (of this report) Unclassified | 20. Security Classification (of this page) Unclassified | 21. No of Pages 238 | 22. Price |

TABLE OF CONTENTS

| | Page |
|---------------------------------------------------------------------------|-----------|
| EXECUTIVE SUMMARY | 1 |
| ACKNOWLEDGEMENT..... | 4 |
| CHAPTER 1 INTRODUCTION..... | 5 |
| 1.1 GENERAL | 5 |
| 1.2 RESEARCH OBJECTIVES..... | 6 |
| 1.3 REPORT ORGANIZATION | 7 |
| CHAPTER 2 BACKGROUND AND LITERATURE REVIEW | 9 |
| 2.1 STATUS OF UNITED STATES BRIDGES..... | 9 |
| 2.2 COMPOSITES FOR BRIDGE APPLICATIONS | 10 |
| 2.3 HYBRID FRP-CONCRETE STRUCTURAL SYSTEM..... | 12 |
| CHAPTER 3 THE PROPOSED HYBRID FRP-CONCRETE BRIDGE SYSTEMS..... | 25 |
| 3.1 HYBRID FRP-CONCRETE BRIDGE CONFIGURATIONS | 25 |
| 3.2 LOADS..... | 27 |
| 3.2.1 <i>Dead Loads</i> | 27 |
| 3.2.2 <i>Live Loads</i> | 27 |
| 3.3 DESIGN CRITERIA..... | 28 |
| 3.3.1 <i>Deflection Criteria</i> | 28 |
| 3.3.2 <i>Strength Criteria</i> | 29 |
| 3.4 LINEAR FINITE ELEMENT ANALYSIS | 29 |
| 3.4.1 <i>Material Properties and Modeling</i> | 29 |
| 3.4.2 <i>Boundary Conditions</i> | 30 |
| 3.4.3 <i>An Analysis of Discretization Error</i> | 30 |
| 3.4.4 <i>Linear Static Finite Element Analysis</i> | 30 |
| 3.4.4.1 <i>Deflection Criteria</i> | 30 |

| | |
|-------------------------------------------------------------------------------------------|-----------|
| 3.4.4.2 Service I Limit | 31 |
| 3.4.4.3 Strength Check..... | 32 |
| 3.4.4.4 Flexural Loading Test..... | 33 |
| 3.5 SUMMARY | 33 |
| CHAPTER 4 PRELIMINARY OPTIMIZATION OF HYBRID FRP-CONCRETE BRIDGE SYSTEMS | 46 |
| 4.1 STRUCTURAL OPTIMIZATION | 46 |
| 4.2 FRP STRUCTURAL OPTIMIZATION | 47 |
| 4.3 OPTIMALITY CRITERIA FORMULATION..... | 48 |
| 4.4 OPTIMIZATION PROCEDURE FOR HYBRID FRP-CONCRETE BRIDGE SYSTEMS..... | 49 |
| 4.5 NUMERICAL RESULTS | 51 |
| 4.5.1 Optimization of the Proposed Hybrid FRP- Concrete Superstructure..... | 51 |
| 4.5.2 Optimization of the Proposed Hybrid FRP- Concrete Deck on Steel Girder.. | 52 |
| CHAPTER 5 EXPERIMENTAL STUDY OF HYBRID BRIDGE SUPERSTRUCTURE..... | 57 |
| 5.1 MATERIALS..... | 57 |
| 5.1.1 Fiber Reinforced Polymers | 57 |
| 5.1.1.1 Composite Manufacturing | 58 |
| 5.1.1.2 Mechanical Properties of GFRP Laminate | 59 |
| 5.1.2 Concrete..... | 59 |
| 5.1.2.1 Tensile strength of concrete..... | 60 |
| 5.2 TEST SPECIMEN..... | 60 |
| 5.2.1 Superstructure Model Configuration..... | 60 |
| 5.2.2 Scaling Factors | 61 |
| 5.3 EXPERIMENTAL SET-UP..... | 62 |
| 5.4 EXPERIMENTAL PROTOCOL | 62 |
| 5.4.1 Non Destructive Test..... | 63 |
| 5.4.1.1 Positive Flexural Test (FRP-only Specimen)..... | 63 |
| 5.4.1.2 Positive Flexural Test (Hybrid FRP-Concrete Specimen)..... | 63 |
| 5.4.1.3 Negative Flexural Test..... | 64 |
| 5.4.2 Destructive Tests..... | 64 |

| | |
|----------------------------------------------------------------------------|------------|
| 5.4.2.1 Positive Flexural Test | 64 |
| 5.4.2.2 Shear Test | 65 |
| 5.5 TEST RESULTS..... | 65 |
| 5.5.1 <i>Non Destructive Tests</i> | 65 |
| 5.5.1.1 Positive Moment Flexural Load (FRP-Only Specimen)..... | 65 |
| 5.5.1.2 Positive Moment Flexural Load (Hybrid FRP Concrete Specimen) | 67 |
| 5.5.1.3 Off-Axis Positive Flexural Load..... | 68 |
| 5.5.1.4 Negative Flexural Load..... | 69 |
| 5.5.2 <i>Destructive Tests</i> | 70 |
| 5.5.2.1 Positive Flexural Load | 70 |
| 5.5.2.2 Shear Load | 72 |
| 5.6 SUMMARY | 73 |
| | |
| CHAPTER 6 EXPERIMENTAL STUDY OF HYBRID BRIDGE DECK ON | |
| STEEL GIRDERS | 126 |
| 6.1 BRIDGE CONFIGURATIONS | 126 |
| 6.2 JOINING TECHNIQUE FOR THE HYBRID DECK SYSTEM..... | 128 |
| 6.2.1 <i>Panel-Panel Connections</i> | 129 |
| 6.2.2 <i>Connection of Hybrid deck on Steel Girders</i> | 130 |
| 6.2.2.1 Shear Studs Connections..... | 131 |
| 6.2.2.2 Clamped Connections | 132 |
| 6.2.2.3 Bolted Connections..... | 133 |
| 6.2.2.4 Adhesive Connections | 133 |
| 6.2.2.5 Summary | 134 |
| 6.3 SERVICE LOAD EFFECTIVE FLANGE WIDTH..... | 135 |
| 6.3.1 <i>Transformed Section Calculations</i> | 137 |
| 6.4 INSTRUMENTATION | 137 |
| 6.5 EXPERIMENTAL SET-UP | 138 |
| 6.6 EXPERIMENTAL PROTOCOL | 139 |
| 6.7 TEST RESULTS..... | 139 |
| 6.7.1 <i>Service Load Case 1</i> | 140 |
| 6.7.2 <i>Service Load Case 2</i> | 141 |
| 6.7.3 <i>Service Load Case 3</i> | 142 |

| | |
|---------------------------------------------------------------------|------------|
| 6.7.4 Service Load Case 4..... | 143 |
| 6.7.5 Service Load Case 5..... | 143 |
| 6.7.6 Service Load Case 6..... | 144 |
| 6.7.7 Service Load Case 7..... | 145 |
| 6.8 SUMMARY | 146 |
| CHAPTER 7 FINITE ELEMENT ANALYSIS | 205 |
| 7.1 BRIDGE SUPERSTRUCTURE..... | 205 |
| 7.1.1 Geometric and Boundary Condition Modeling..... | 205 |
| 7.1.2 Material Modeling | 206 |
| 7.1.3 Static Stress Analysis | 206 |
| 7.1.3.1 Prototype Bridge Superstructure..... | 206 |
| 7.1.4 Verification with Experimental Results | 207 |
| 7.2 BRIDGE DECK ON STEEL GIRDERS | 208 |
| 7.2.1 Geometric and Boundary Condition Modeling..... | 208 |
| 7.2.2 Material Modeling | 209 |
| 7.2.3 Verifications with Experimental Results..... | 209 |
| 7.3 SUMMARY | 209 |
| CHAPTER 8 SUMMARY, CONCLUSIONS AND RECOMMENDATIONS ... | 224 |
| 8.1 SUMMARY | 224 |
| 8.2 THE PROPOSED HYBRID BRIDGE | 224 |
| 8.2.1 Design Optimization | 225 |
| 8.2.2 Experimental Studies | 226 |
| 8.2.2.1 Bridge Superstructure | 226 |
| 8.2.2.2 Hybrid FRP-Concrete Deck..... | 226 |
| 8.2.3 Finite Element Analysis | 227 |
| 8.3 CONCLUSIONS | 228 |
| 8.4 RECOMMENDATIONS FOR FUTURE INVESTIGATIONS/ IMPLEMENTATION | 228 |
| REFERENCES | 231 |
| APPENDIX A CLASSICAL LAMINATE THEORY | A-1 |

| | |
|---------------------------------------------------------------------------|-------------|
| APPENDIX B SERVICE LOAD EFFECTIVE FLANGE WIDTH | |
| CALCULATIONS | B-1 |
| APPENDIX C NONLINEAR BEHAVIOR AND FAILURE PREDICTION OF | |
| HYBRID FRP BRIDGE SYSTEMS | C-1 |
| C.1 CONSTITUTIVE MODELS FOR FRP COMPOSITES | C-1 |
| <i>C.1.1 Continuum damage models for FRP Composites</i> | <i>C-2</i> |
| C.1.1.1 ABAQUS Damage Model for FRP Composites | C-3 |
| C.1.1.2 Linde’s Damage Model for FRP Composites | C-9 |
| <i>C.1.2 Plasticity-Based Constitutive Model for FRP Composites</i> | <i>C-12</i> |
| C.1.2.1 Model Description | C-12 |
| C.2 CONCRETE MATERIAL MODEL..... | C-17 |
| C.3 STEEL MATERIAL MODEL..... | C-18 |
| C.4 ANALYSIS DESCRIPTION..... | C-18 |
| <i>C.4.1 Bridge Superstructure</i> | <i>C-18</i> |
| <i>C.4.2 Bridge Deck on Steel Girders</i> | <i>C-19</i> |
| C.5 RESULTS AND DISCUSSION..... | C-19 |
| <i>C.5.1 Bridge Superstructure</i> | <i>C-19</i> |
| <i>C.5.2 Bridge Deck on Steel Girders</i> | <i>C-20</i> |
| C.6 SUMMARY | C-20 |
| C.7 REFERENCES..... | C-21 |

LIST OF FIGURES

| | Page |
|---------------------------------------------------------------------------------------------------------------------------|-------------|
| Figure 2.1 Percentage of Deficient Bridges in U. S. (NBI, 2003) | 19 |
| Figure 2.2 Bridges by Type of Superstructure Material (NBI, 2002)..... | 19 |
| Figure 2.3 Year of Construction for U. S. Bridges. (NBI, 2003)..... | 20 |
| Figure 2.4 Hybrid FRP-Concrete Deck Proposed by Hillman and Murray (1990)..... | 20 |
| Figure 2.5 Hybrid FRP-Concrete Bridge Deck Studied by Bakeri and Sunder (1991)... | 21 |
| Figure 2.6 Sections of Hybrid FRP-Concrete specimens analyzed by Saiidi et al. (1994) | 21 |
| Figure 2.7 Cross-Section of Hybrid FRP-Concrete Beam Studied by Deskovic et al. (1995)..... | 22 |
| Figure 2.8 Beam Cross-Section Types Considered by Hall and Mottram (1998)..... | 22 |
| Figure 2.9 Cross-Sections of the Hybrid Beams Used by Ribeiro et al. (2001) | 22 |
| Figure 2.10 Cross-Section of Hybrid Beam Tested by Erp et al. (2002)..... | 23 |
| Figure 2.11 Cross-Section of Different Types of GFRP Tubes Filled With Concrete Tested by Fam And Rizkalla (2002)..... | 23 |
| Figure 2.12 Cross-Section of Two Hybrid Beam Types Analyzed by Hullat et al. (2003) | 24 |
| Figure 2.13 Cross-Section of Hybrid Bridge Superstructure Tested by Kitane et al. (2004)..... | 24 |
| Figure 3.1 Cross Section of Systems I of the Hybrid FRP-Concrete Superstructure (dimension in mm)..... | 37 |
| Figure 3.2 Systems II of the Hybrid FRP-Concrete Superstructure (dimension in <i>m</i>) | 38 |
| Figure 3.3 Effects of Concrete Thickness on Different Items (: current design)..... | 39 |
| Figure 3.4 HL-93 Vehicle Loading Configuration | 40 |
| Figure 3.5 Finite Element Models for Systems I and II..... | 41 |
| Figure 3.6 Vertical Displacement at Mid-Span vs. Total Number of Model Elements... | 42 |
| Figure 3.7 Vertical Displacement Contours for the Service I Limit for Bridge System II | 43 |

| | |
|------------------------------------------------------------------------------------------------------------------------|----|
| Figure 3.8 Deformed Shapes at Different Load Levels for System I | 44 |
| Figure 3.9 Deformed Shapes at Different Load Levels for System II | 45 |
| Figure 4.1 Flow Chart for Optimization Procedure | 54 |
| Figure 4.2 Steel Bridge with a Hybrid FRP-Concrete Bridge Deck (dimension in m) ... | 55 |
| Figure 4.3 Effects of Number of Cells on Hybrid Deck Stiffness and Strength..... | 56 |
| Figure 5.1 Tensile Test Fixture | 79 |
| Figure 5.2 Engineering Stress-Strain Curves from Tensile Tests..... | 80 |
| Figure 5.3 Compressive Stress-Strain Curves of Concrete..... | 81 |
| Figure 5.4 Cross Section of the Hybrid FRP-Concrete Superstructure Model (units in mm)..... | 82 |
| Figure 5.5 Individual Trapezoidal Box Section before Assembly..... | 83 |
| Figure 5.6 Assembly of Three Trapezoidal Box Sections by the Vacuum Bag Process. 83 | |
| Figure 5.7 Layer of Glass Fiber Wetted With Vinyl Ester Resin Placed Between Box Sections as Bonding Material | 84 |
| Figure 5.8 Shear Keys (dimension in mm) | 84 |
| Figure 5.9 Test Configuration for Quasi-Static Positive Moment Flexural Test (dimensions in m) | 85 |
| Figure 5.10 Test Set Up for Quasi-Static Positive Moment Flexural Test | 86 |
| Figure 5.11 Spreader Beam..... | 86 |
| Figure 5.12 Instrumentation for the Positive Moment Flexural Test (Dimensions in mm) | 87 |
| Figure 5.13 Load Configuration | 88 |
| Figure 5.14 Layout of the LEDs on the Top Surface for the Positive Moment Flexural Test (dimensions in mm) | 89 |
| Figure 5.15 Layout of the LEDs on the Top Surface for the Negative Moment Flexural Test (dimensions in mm) | 89 |
| Figure 5.16 Test Configuration for Quasi-Static Negative Moment Flexural Test (dimensions in m) | 90 |
| Figure 5.17 Test Configuration for Quasi-Static Negative Moment Flexural Test (dimensions in m) (cont.)..... | 91 |

| | |
|----------------------------------------------------------------------------------------------------------------------------------------|-----|
| Figure 5.18 Instrumentation for the Negative Moment Flexural Test (dimensions in mm) | 92 |
| Figure 5.19 Displacement Protocol of the Destructive Flexural Test | 93 |
| Figure 5.20 Test Configuration for Quasi-Static Shear Test (dimensions in m) | 94 |
| Figure 5.21 Instrumentation for the Shear Test (dimensions in mm) | 95 |
| Figure 5.22 Displacement of the Elastomeric Bearing Pad Measured at Section A | 96 |
| Figure 5.23 Forces vs. Displacement at the Bottom Surface (FRP-Only Specimen in Positive Moment Flexure) | 97 |
| Figure 5.24 Forces vs. Displacement at the Top Surface (FRP-Only Specimen in Positive Flexure) | 98 |
| Figure 5.25 Deformed Shapes at Different Load Levels for FRP-only Specimen in Positive Flexure | 99 |
| Figure 5.26 Deformed Shapes at Different Load Levels for Hybrid Specimen in Flexure (Top Surface) | 100 |
| Figure 5.27 Deformed Shapes at Different Load Levels for Hybrid Specimen in Flexure (Top Surface) | 101 |
| Figure 5.28 Deformed Shapes at Different Load Levels for FRP-only Specimen in Positive Flexure | 102 |
| Figure 5.29 Comparison of Deformed Shapes at $0.5 \times$ Tandem Load between FRP-only and Hybrid Specimens in Positive Moment Flexure | 103 |
| Figure 5.30 Strain Variations on the Exterior Web at Section E (Hybrid Specimen in Positive Flexure) | 104 |
| Figure 5.31 Strain Variations on the Exterior Web at Section H (Hybrid Specimen in Positive Flexure) | 104 |
| Figure 5.32 Longitudinal Strain Variations along the Centerline at Top Surface (Hybrid Specimen in Positive Flexure) | 104 |
| Figure 5.33 Longitudinal Strain Variations along the Centerline at Bottom Surface, Hybrid Specimen in Positive Flexure | 105 |
| Figure 5.34 Longitudinal Strain Variations along Section E, Hybrid Specimen in Positive Flexure | 105 |

| | |
|---------------------------------------------------------------------------------------------------------------------------|-----|
| Figure 5.35 Transverse Strain Variations along Section E, Hybrid Specimen in Positive Flexure | 105 |
| Figure 5.36 Deformed Shapes at Different Load Levels for the Hybrid Specimen, Off-Axis Flexure..... | 106 |
| Figure 5.37 Strain Variations on the Exterior Web at Section E, Off-Axis Flexure | 107 |
| Figure 5.38 Strain Variations on the Exterior Web at Section H, Off-Axis Flexure..... | 107 |
| Figure 5.39 Longitudinal Strain Variations along the Centerline at Top Surface, Off-Axis Flexure | 107 |
| Figure 5.40 Longitudinal Strain Variations along the Centerline at Bottom Surface, Off-Axis Flexure..... | 108 |
| Figure 5.41 Longitudinal Strain Variations along Section E, Off-Axis Flexure | 108 |
| Figure 5.42 Longitudinal Strain Variations along Section E, Off-Axis Flexure | 108 |
| Figure 5.43 Forces vs. Displacement at the Bottom Surface (Negative Flexure)..... | 109 |
| Figure 5.44 Forces vs. Displacement at the Top Surface (Negative Moment Flexure). | 110 |
| Figure 5.45 Forces versus Displacement Relations for the Hybrid Specimen under Negative Flexure Test..... | 111 |
| Figure 5.46 Deformed Shapes at Different Load Levels for Hybrid Specimen in Negative Flexure | 112 |
| Figure 5.47 Longitudinal Strain Variations along the Centerline at Top Surface (Hybrid Specimen in Negative Flexure)..... | 113 |
| Figure 5.48 Longitudinal Strain Variations along Section E (Hybrid Specimen in Negative Flexure)..... | 113 |
| Figure 5.49 Forces vs. Displacement at the Bottom Surface (Destructive Flexure)..... | 114 |
| Figure 5.50 Forces vs. Displacement at the Top Surface (Destructive Flexure)..... | 115 |
| Figure 5.51 Different Failure Modes of Superstructure Specimen at Destructive Test | 117 |
| Figure 5.52 Deformed Shapes at Different Load Levels in Destructive Flexure at Top Surface | 118 |
| Figure 5.53 Deformed Shapes at Different Load Levels in Destructive Flexure at Top Surface (cont.)..... | 119 |
| Figure 5.54 Strain Variations on the Exterior Web at Section E (Destructive Flexure) | 120 |
| Figure 5.55 Strain Variations on the Exterior Web at Section H (Destructive Flexure) | 120 |

| | |
|--------------------------------------------------------------------------------------------------------------------|-----|
| Figure 5.56 Longitudinal Strain Variations along the Centerline at Top Surface (Destructive Flexure) | 120 |
| Figure 5.57 Longitudinal Strain Variations along the Centerline at Bottom Surface (Destructive Flexure) | 121 |
| Figure 5.58 Longitudinal Strain Variations along Section E (Destructive Flexure)..... | 121 |
| Figure 5.59 Deformed Shapes at Different Load Levels for Hybrid Specimen in Shear | 122 |
| Figure 5.60 Failure Modes under the Shear Loading | 124 |
| Figure 5.61 Shear Strain Variations on the Exterior Web at Section M (Destructive Shear) | 125 |
| Figure 5.62 Longitudinal Strain Variations along the Centerline at Bottom Surface (Destructive Shear) | 125 |
| Figure 6.1 3/4 Scale Model of Steel Bridge with a Hybrid FRP-Concrete Bridge Deck (units in mm)..... | 149 |
| Figure 6.2 Cross Section of the 3/4 Scale Model of a Hybrid FRP-Concrete Bridge Deck Panels (units in mm) | 150 |
| Figure 6.3 Manufacturing Steps for the Hybrid Deck | 151 |
| Figure 6.4 Shear Keys (units in mm)..... | 152 |
| Figure 6.5 Elevation of the Three Steel Girders Model (units in m)..... | 152 |
| Figure 6.6 Details of Girders Supports | 153 |
| Figure 6.7 Adhesively Bonded and Bolted Joints (Zetterberg, 2001) | 154 |
| Figure 6.8 Superdeck TM Shear Stud Connection..... | 154 |
| Figure 6.9 Schematic of Three Different Connections (Moon et al., 2002) | 156 |
| Figure 6.10 Proposed Connection for FRP Decks to Steel Girders (Righman et al., 2004) | 157 |
| Figure 6.11 KSCI Clamp Connection | 157 |
| Figure 6.12 Details of Bolted Connection | 157 |
| Figure 6.13 Schematic of Proposed Deck-to-Girder Connection (Park et al., 2004) | 158 |
| Figure 6.14 Schematic of Proposed Deck-to-Girder Connection (Kim et al., 2005)..... | 159 |
| Figure 6.15 Shear Studs Details for the Proposed Hybrid Deck..... | 159 |
| Figure 6.16 Shear Stud Configuration (units in mm) | 160 |

| | |
|------------------------------------------------------------------------------------------------------------|-----|
| Figure 6.17 Idealized Cross Section of the Transformed Section of the Bridge | 161 |
| Figure 6.18 Strain Gages Locations for Deck Top Surface and Steel Girders (dimensions in m)..... | 162 |
| Figure 6.19 Strain Gages Locations for Bottom Surface and Webs of the Hybrid Deck (dimensions in m) | 163 |
| Figure 6.20 Potentiometer Locations for Bottom Surface and Webs of the Hybrid Deck (dimensions in m) | 164 |
| Figure 6.21 Layout of LEDs Locations for the Service Test Cases 1 to 5 (dimensions in m) | 165 |
| Figure 6.22 Layout of LEDs Locations for the Service Test Cases 6 and 7 (dimensions in m) | 166 |
| Figure 6.23 Test Configuration for Service Test (dimensions in m) | 167 |
| Figure 6.24 Photographs of Steps in Specimen Setup | 169 |
| Figure 6.25 Seven Service Load Cases..... | 170 |
| Figure 6.26 Test Set-Up for Service Load-Case 1 | 171 |
| Figure 6.27 Deformed Shapes of the Deck at Different Load Levels under Load Case No.1..... | 172 |
| Figure 6.28 Deformed Shapes at Different Load Levels under Load Case No. 1 | 174 |
| Figure 6.29 Strain Profile at Different Sections under Load Case No. 1..... | 174 |
| Figure 6.30 Strain Profile at Different Sections of the Deck under Load Case No. 1 ... | 175 |
| Figure 6.31 Deformed Shapes of the Deck at Different Load Levels under Load Case No. 2..... | 176 |
| Figure 6.32 Deformed Shapes at Different Load Levels under Load Case No. 2 | 177 |
| Figure 6.33 Strain Profile through Different Sections under Load Case No. 2..... | 178 |
| Figure 6.34 Strain Profile through Different Sections of the Deck under Load Case No. 2 | 179 |
| Figure 6.35 Test Set-Up for Service Load-Case 3 | 180 |
| Figure 6.36 Deformed Shapes of the Deck at Different Load Levels under Load Case No. 3..... | 181 |
| Figure 6.37 Deformed Shapes at Different Load Levels under Load Case No. 3 | 182 |
| Figure 6.38 Strain Profile through Different Sections under Load Case No. 3 | 183 |

| | |
|--------------------------------------------------------------------------------------------------|-----|
| Figure 6.39 Strain Profile through Different Sections of the Deck under Load Case No. 3 | 184 |
| Figure 6.40 Test Set-Up for Service Load-Case 4..... | 185 |
| Figure 6.41 Deformed Shapes of the Deck at Different Load Levels under Load Case No. 4..... | 186 |
| Figure 6.42 Deformed Shapes at Different Load Levels under Load Case No. 4 | 187 |
| Figure 6.43 Strain Profile through Different Sections under Load Case No. 4..... | 188 |
| Figure 6.44 Strain Profile through Different Sections of the Deck under Load Case No. 4 | 189 |
| Figure 6.45 Test Set-Up for Service Load-Case 5..... | 190 |
| Figure 6.46 Deformed Shapes of the Deck at Different Load Levels under Load Case No. 5..... | 191 |
| Figure 6.47 Deformed Shapes at Different Load Levels under Load Case No. 5 | 192 |
| Figure 6.48 Strain Profile through Different Sections under Load Case No. 5..... | 193 |
| Figure 6.49 Strain Profile through Different Sections of the Deck under Load Case No. 5 | 194 |
| Figure 6.50 Test Set-Up for Service Load-Case 6..... | 195 |
| Figure 6.51 Deformed Shapes of the Deck at Different Load Levels under Load Case No. 6..... | 196 |
| Figure 6.52 Deformed Shapes at Different Load Levels under Load Case No. 6 | 197 |
| Figure 6.53 Strain Profile through Different Sections under Load Case No. 6..... | 198 |
| Figure 6.54 Strain Profile through Different Sections of the Deck under Load Case No. 6 | 199 |
| Figure 6.55 Test Set-Up for Service Load-Case 7..... | 200 |
| Figure 6.56 Deformed Shapes of the Deck at Different Load Levels under Load Case No. 7..... | 201 |
| Figure 6.57 Deformed Shapes at Different Load Levels under Load Case No. 7 | 202 |
| Figure 6.58 Strain Profile through Different Sections under Load Case No. 7..... | 203 |
| Figure 6.59 Strain Profile through Different Sections of the Deck under Load Case No. 7 | 204 |
| Figure 7.1 Finite Element Model of the Prototype Bridge Superstructure | 211 |

| | |
|---------------------------------------------------------------------------------------------------|------|
| Figure 7.2 Vertical Displacement Contour for the Deflection Check | 212 |
| Figure 7.3 Tsai-Hill Failure Index for the Strength I Limit at the Top Surface | 212 |
| Figure 7.4 Deformed Shapes at Sections I and H | 213 |
| Figure 7.5 Deformed Shapes at Sections G and F | 214 |
| Figure 7.6 Deformed Shapes at the Bottom and Top Surfaces..... | 215 |
| Figure 7.7 Force-Displacement Response | 216 |
| Figure 7.8 Strain Variation on the Exterior Web at Section E..... | 217 |
| Figure 7.9 Longitudinal Strain Variation in Section E | 217 |
| Figure 7.10 Finite Element Model of the Prototype Bridge Deck..... | 218 |
| Figure 7.11 Deformed Shapes under Load Case No. 1..... | 219 |
| Figure 7.12 Deformed Shapes under Load Case No. 2..... | 220 |
| Figure 7.13 Deformed Shapes under Load Case No. 3..... | 221 |
| Figure 7.14 Strain Profiles through Section C under Load Case No. 2..... | 222 |
| Figure 7.15 Strain Profiles through the Steel Girder at Section H under Load Case No. 2. | 223 |
| Figure A.1 Laminated Plate Geometry | A-4 |
| Figure A.2 Force and Moment Resultants | A-6 |
| Figure B.1 Cross Section of the Transformed Section of the Bridge | B-10 |
| Figure C.1 Coordinate System of FRP composites | C-24 |
| Figure C.2 Equivalent Stress versus Equivalent Displacement..... | C-24 |
| Figure C.3 Damage variable as a function of equivalent displacement..... | C-25 |
| Figure C.4 Linear Damage Evaluation | C-25 |
| Figure C.5 Puppo-Evensen Yield Surface | C-26 |
| Figure C.6 Response of concrete to uniaxial loading in tension and compression..... | C-27 |
| Figure C.7 Force-Displacement Responses at Top Surface..... | C-28 |
| Figure C.8 Force-Displacement Responses at Bottom Surface..... | C-29 |
| Figure C.9 Force-Displacement Responses at K-12 (Inelastic FEA) | C-30 |
| Figure C.10 Force-Displacement Responses at location under the loading point | C-30 |

LIST OF TABLES

| | Page |
|--------------------------------------------------------------------------------------------------------------------------------------------|-------------|
| Table 3-1 Thickness and Stacking Sequence of Different Layers of Systems I and II | 34 |
| Table 3-2 Distance from the support at $y=0$ to the Rear Axle | 34 |
| Table 3-3 Mechanical Properties of GFRP | 35 |
| Table 3-4 Mechanical Properties of Concrete | 35 |
| Table 3-5 Comparison of Total Weight of Systems I and II..... | 36 |
| Table 3-6 Comparison of Selected FEA Results of System I and II | 36 |
| Table 4-1 Thickness and Stacking Sequence of the Optimized Superstructure | 53 |
| Table 4-2 Thickness and Stacking Sequence of the Optimized Deck | 53 |
| Table 5-1 Typical Properties of DERAKANE 411 at Room Temperature (Dow Plastics, 1999) | 74 |
| Table 5-2 Tensile Properties of GFRP | 74 |
| Table 5-3 Summary of GFRP Mechanical Properties (An Cor Industrial Plastics, Inc) .. | 75 |
| Table 5-4 Thickness and Stacking Sequence of the Superstructure Model..... | 75 |
| Table 5-5 Weight Proportions of the Ingredients | 76 |
| Table 5-6 Mechanical Properties of Concrete | 76 |
| Table 5-7 Direct Tensile Strength (Units in MPa)..... | 77 |
| Table 5-8 Similitude Scaling Factors..... | 77 |
| Table 5-9 Measured Maximum Strains at Selected Locations in Destructive Flexure.... | 78 |
| Table 6-1 Thickness and Stacking Sequence of the Hybrid Deck Model | 147 |
| Table 6-2 Effective Flange Width (b_{eff}), and Effective Flange Width Ratio (b_{eff}/b) for Interior and Exterior Girders..... | 147 |
| Table 7-1 Analytical and Experimental Results | 210 |

EXECUTIVE SUMMARY

It is a major challenge to build bridge systems that have long-term durability and low maintenance requirements. A solution to this challenge may be to use new materials or to implement new structural systems. Fiber reinforced polymer (FRP) composites have continued to play an important role in solving some of persistent problems in infrastructure applications because of its high specific strength, light weight, and durability.

Structural engineers always have valued the combination of materials into a hybrid structural system that takes advantage of the properties inherent in each of its constituents. In this study, the concept of the hybrid FRP-concrete structural systems is applied to both bridge superstructure and deck systems. The hybrid FRP-concrete bridge superstructure and deck systems are intended to have durable, structurally sound, and cost effective hybrid system that will take full advantage of the inherent properties of both FRP materials and concrete. The hybrid-FRP deck system can be installed in new construction, or can be attached to existing deck substructure after removing deteriorated concrete deck.

In this report, two hybrid FRP-concrete bridge systems were investigated. The first system consists of trapezoidal cell units forming either a bridge superstructure or a bridge deck unit. The second one is formed by arch cells. The two systems rely on using cellular components to form the core of the deck system, and an outer shell to wrap around those cells to form the integral unit of the bridge. Both systems were investigated analytically by using finite element (FE) analysis. From the rigorous FE studies, it was concluded that first system is more efficient than the second. Therefore, the first hybrid FRP-concrete system had been used to investigate the feasibility of the FRP-concrete structural systems in the rest of the study. The proposed system consists of trapezoidal FRP cell units surrounded by an FRP outer shell forming a bridge system. A thin layer of concrete is placed in the compression zone. Concrete is confined by GFRP laminates which provide protection from environmental exposure. Moreover, the concrete layers reduce the local

deformation of the top surface of the bridge under concentrated loads. Webs of the box section were designed at an incline to reduce shear force between sections.

For the experimental phase of the study, a prototype bridge superstructure was designed as a simply-supported single span one-lane bridge with a span length of 18.3 m. Geometrical parameters of the proposed bridge system were determined by detailed finite element analyses. FEA was used to verify the structural behavior of this hybrid bridge superstructure prior to embarking on manufacturing and testing. Performance of this hybrid bridge superstructure was examined both experimentally and computationally. A test specimen, fabricated as a one-fourth scale model of the prototype bridge, was subjected to a series of loading tests: nondestructive tests (flexure, off-axis flexure, and negative flexure), and destructive tests (flexure and shear).

Also, as a trail case for FRP-concrete bridge deck supported on steel girders, a prototype bridge system was designed as a simply supported steel bridge with a hybrid FRP-concrete deck. Details for connecting the hybrid decks with steel girders were investigated both experimentally and computationally. A test specimen, fabricated as a 3/4 scale model of the prototype bridge, was evaluated by series of service flexural loading tests under different loading conditions. Also, the composite action between the hybrid deck and steel girders was analyzed and tested. Moreover, the effective flange width in the hybrid FRP-concrete deck acting compositely with the steel girders was evaluated at service conditions.

Results from the both experimental and computational analysis for both the hybrid bridge superstructure and deck systems confirmed that the hybrid FRP-concrete bridge systems have an excellent performance from structural engineering point of view. The experimental results showed robust performance where cracking in the exterior GFRP laminates, interface failure, and slippage between GFRP and concrete under AASHTO design loads for the hybrid bridge superstructure were not exhibited. Also, both test specimens easily satisfied the AASHTO live load deflection limit. In addition, the shear connections at girder-deck interface of the deck specimen on steel girders demonstrated an excellent performance under service load. It was observed that the hybrid deck and the steel girders are interacting in a partially composite way at large load; as evinced by the discontinuity in strain at the hybrid deck-to-steel interface. Effective width calculations of

the hybrid deck showed that the effective flange width for hybrid decks are less than AASHTO prescribed effective width for concrete decks. Results from finite element analysis and experiments compared well in term of both global and local behaviors.

ACKNOWLEDGEMENT

The work in this report was conducted in collaboration with New York State Department of Transportation (NYSDOT). The authors would like to thank Dr. Sreenivas Alampalli for his guidance and support throughout this project. In particular, we greatly appreciate the careful review of the report and suggestions he provided.

CHAPTER 1

INTRODUCTION

1.1 GENERAL

The United States (U. S.) has one of the largest highway networks in the world. The efficiency and safety of this network plays an essential role in the continued economic health of the country. The total number of bridges in the U. S. as of 2003 is 615,718 (National Bridge Inventory (NBI), 2003), and nearly 26.3 percent of these bridges are either structurally deficient or functionally obsolete. There is however a major challenge to reduce or eliminate deficient structures. It is well known that bridges deteriorate with age. Deterioration rate studies suggest that concrete bridge structures deteriorate slowly during the first few decades of their design life (typically 50 years), followed by a rapid decline during the last decade. Since 68.9 percent of the 615,718 bridges in the U. S. were built more than 25 years ago, and mainly of concrete, U. S. bridges will require increasing future maintenance, major rehabilitation, or in some cases replacement to maintain the integrity of the U. S. highway system. Compounding this issue is the dramatic increase in both the weight and number of heavy commercial vehicles, which impose an exponential increase in damage to the infrastructure.

Since the late 1980's, there has been steady and substantial progress in restoring and maintaining the transportation system. The cost to continue this work will be high as major pieces of the State's overall system will require reconstruction over the next 25 years. The cost of maintaining deteriorated bridges is very high. The U.S. Department of Transportation (DOT) estimated that the average annual cost to maintain bridge condition for the 20 year period from 2001-2020 would be \$7.3 billion, and that the average annual cost to improve bridge conditions would be \$ 9.4 billion. Tight budgets put pressure on transportation agencies to find new construction materials that make bridges less expensive to build, maintain, and replace. Longer design life structures, using the latest materials and design technologies, are needed so that the U. S. can maintain a functional

transportation network, provide longer service life, and improve the safety of the highway network. Among new structural materials, fiber reinforced polymers (FRP) composites have continued to play an important role in solving some of persistent problems in infrastructure applications due to their superior material properties such as high specific stiffness, high specific strength, high corrosion resistance, light weight, and durability. Based on these advantages and a wide variety of practical applications, the composites industry has grown approximately 460% over the past 30 years, from 360,000 tons in 1970 to 1.68 million tons in 2000 (Busel, 2000). As FRP composites are accepted in new markets, the composite industry is projected to continue to grow. Due to these advantages, the FRP composites could be part of the solution to the national bridge problem. Composites can be used for the construction of an entire bridge structure, as a decking material to be supported by concrete or steel girders, or to rehabilitate existing bridges.

In spite of all these advantages, FRP composites have higher initial costs than conventional materials used in infrastructure application. To overcome this obstacle and to make the best use of materials, combinations of FRP and conventional materials have recently been investigated by a number of researchers. The advantages of the hybrid structural systems include the cost effectiveness and the ability to optimize the cross section based on material properties of each component. According to Mirmiran (2001), the most effective use of FRP composites is in the form of hybrid construction with concrete, where FRP acts as a load carrying constituent and a protective measure for concrete.

1.2 RESEARCH OBJECTIVES

The primary objective of this study is to apply a hybrid FRP-concrete structural system to both bridge superstructure and deck systems and verify the viability of the proposed system experimentally and computationally. The following points summarize the objectives of this study:

1. Investigate the most appropriate hybrid structural system for bridge system that combines FRP and concrete.

2. Develop a preliminary optimization for the proposed hybrid FRP-concrete bridge system.
3. Develop a design procedure for both the hybrid bridge superstructure and the hybrid deck on steel girders according to AASHTO design loads.
4. Perform experimental studies of the proposed hybrid bridge deck and superstructure to verify the system performance.
5. Evaluate the effective flange width in the hybrid FRP-concrete deck acting compositely with underlying steel girders at service conditions.
6. Develop a detailed finite element analysis of both the hybrid bridge superstructure and the hybrid deck on steel girders to verify the experimental test results.

1.3 REPORT ORGANIZATION

This report contains eight chapters followed by appendices. Chapter Two documents the current condition of U.S. bridges, the literature survey describing research dealing with hybrid FRP-concrete structural systems specially bridge deck systems and the various innovative applications of hybrid FRP-concrete systems developed to date. Chapter Three describes the investigation of two different hybrid FRP-concrete bridge systems to decide the most appropriate hybrid structural system for bridge systems. A preliminary optimization for the proposed hybrid FRP-concrete bridge system is presented in Chapter Four. Chapter Five provides a detailed description of one-fourth scale model of a simply-supported single span one-lane bridge superstructure with a span length of 18.3 m. The outcomes of the experimental investigation of the scale model are also provided in Chapter Five.

A detailed description of a 3/4 scale model of a simply supported steel bridge with a hybrid FRP-concrete deck is provided in Chapter Six. In addition, the outcome of the experimental investigation of the 3/4 scale model is provided. Chapter Seven describes the detailed finite element models of both the hybrid bridge superstructure and the hybrid deck on steel girders used to verify the experimental test results. In the last Chapter, the conclusions of this study and recommendations for future work are summarized. References are listed immediately following Chapter Eight. Appendix A follows the reference section and describes the classical laminate theory, and other information

pertaining to FRP materials. Appendix B provides detailed calculations for measurement of the effective flange width of the proposed hybrid deck. Nonlinear and failure material models to be incorporated in the finite element analyses to examine the inelastic behavior and failure prediction of both the hybrid bridge deck and superstructure are developed in Appendix C.

CHAPTER 2

BACKGROUND AND LITERATURE REVIEW

It is a major challenge to build bridge systems that have long-term durability and low maintenance requirements. A solution to this challenge may be to use new materials or to implement new structural systems. According to a study by Brailsford et al. (1995), bridge decks are ranked the No. 1 bridge maintenance item by State Department of Transportation (DOT) agencies. Recently, researchers proposed novel hybrid fiber reinforced polymer (FRP)-concrete deck systems through analytical and experimental procedures. The hybrid deck systems will produce durable, structurally sound, and cost effective hybrid systems that will take full advantages of both FRP materials and concrete. In this chapter, the current condition of U.S. bridges is discussed. Also, this chapter reviews the literature dealing with hybrid FRP-concrete structural systems, and various innovative applications of hybrid FRP-concrete systems developed to date.

2.1 STATUS OF UNITED STATES BRIDGES

The United States has one of the largest highway networks in the world. The efficiency and safety of this network plays essential role for the continued economic health of the country. Among the infrastructure systems, the total number of highway bridges in the U.S. as of 2003 is 615,718 (*National Bridge Inventory (NBI), 2003*). States, local agencies, authorities, and the Federal Highways Administration (FHWA) conduct inspections of their bridges and culverts on public roads. NBI is the official repository for information collected through the inspection programs, reflecting the condition of the Nation's bridges. The most common indicator used to describe bridge condition is the number of deficient bridges. Figure 2.1 shows the percentage of deficient bridges in the United States during the last ten years. According to the 2003 status of the Nation Highways, Bridges and Transit: Condition and Performance, there are two types of deficient bridges: structurally deficient and functionally obsolete. Bridges are considered

structurally deficient if they are restricted to light vehicles, require immediate rehabilitation to remain open, or are closed. Bridges are considered functionally obsolete if they have deck geometry, load carrying capacity, clearance, or approach roadway alignment that no longer meet the criteria for the system of which the bridge is a part. However, the Federal Highway Administration's FY 2002 Performance Plan used a new indicator that is the percentage of deck area on deficient bridges. There are 90 million square meters out of 317 million square meters of deck area on deficient bridges.

Due to the increase in the federal bridge investment, the level of bridge deficiency has improved from 31% in 1996 to 29.6% in 2002. Although, the level of investments increased 25% percent between 1997 and 2000, the level of deficiency only decreased by 2%. This shows how difficult it is to significantly reduce the number of deficient bridges. The U.S. Department of Transportation (DOT) estimated that the average annual cost just to maintain bridge condition for the 20 years period from 2001-2020 would be \$7.3 billion, and that the average annual cost to improve bridge conditions would be \$ 9.4 billion.

Materials used for the nation's bridge superstructures are concrete, steel, prestressed concrete and timber. Figure 2.2 shows the percentage of bridges by type of superstructure material.

It is well known that bridges deteriorate with age. Because there is a large volume of bridges that were built in the 1960's (the interstate era), several of these bridges will require increasing future maintenance, major rehabilitation, or in some cases replacement to maintain the integrity of the Nation's highway system. The number of bridges verses year of construction is shown in Figure 2.3. Structures with longer design life, using the latest material and design technologies, are needed so that the nation can maintain a functional transportation network, provide longer service life, and improve the safety of the highway network.

2.2 COMPOSITES FOR BRIDGE APPLICATIONS

The present state of the nation's bridges shows that at least 29% of the bridges are structurally deficient or functionally obsolete. Of all deficient elements in a bridge superstructure, the bridge deck required the most maintenance (Brailsford, 1995). The

U.S. Department of Transportation (DOT) estimated that the average annual cost just to maintain bridge condition for the 20-years period of 2001-2020 would be \$7.3 billion, and that the average annual maintaining of bridges has motivated engineers to investigate new materials or to implement new structural systems.

Recently, attention has been focused on FRP as alternative bridge materials. The superior durability of composites has potential to reduce the maintenance cost and lengthen the service life of bridges. Advantages of FRP composites for civil infrastructure/construction applications include (Karbhari and Zhao, 2000; Bakis et al., 2002):

- Durability (highly resistance to corrosion and fatigue).
- High stiffness-to-weight ratio.
- High strength-to-weight ratio
- High strength.
- Light weight.
- Rapid installation, substantially reducing construction time and labor costs.
- Lower or competitive life-cycle cost.
- High quality manufacturing processes under controlled environment.
- Ease to transport and handling.
- Produce and system design can be optimized for specific loads.
- Reliability of pre-engineered systems.
- Enhanced Fatigue life.
- Controllable thermal properties.
- Directional strength.
- Chemical resistance.
- No cracking.

According to the Market Development Alliance of the FRP composite industry (2002), FRP composite materials were applied in the early 1940's in the defense industry, particularly for use in aerospace and naval application. During the late 1970's and early 1980's, FRP composites have emerged as part of the civil infrastructure. There has been an increasing effort in the area of composite reinforcement for concrete bridges. The world's first highway bridge deck using composite tendons was built in Germany in 1986. The current application is to use FRP composites for the entire deck or as a part of

the actual superstructure system itself. The first U.S. all-composite vehicular bridge deck was built in 1996 in Russell, Kansas. Today, there are hundreds of finished and on-going bridge projects using FRP composite materials all over the world (Tang and Podolny, 1998).

With emerging application of FRP in the infrastructures, there exist several challenges. The following list includes challenges that need to be addressed prior to widespread implementation of FRP materials in bridge applications:

- The lack of a comprehensive database of lifetime durability related to some FRP composites that are used in civil infrastructures.
- The lack of a generally accepted design and analysis codes for FRP bridge decks.
- The relatively low absolute stiffness of FRP composites usually causes difficulties in fully utilizing their strength, and often stiffness has controlled design rather than strength.
- High initial material cost compared with conventional methods. Expected improvement in manufacturing, transporting and installation as well as life cycle differences might not make FRP cost competitive with conventional RC. Unless significant improvements also occur in the cost of constituent materials, FRP technology will be limited to just parts of bridge construction such bridge decks or bridge repair (Nystrom et al., 2003).

2.3 HYBRID FRP-CONCRETE STRUCTURAL SYSTEM

Due to the high initial material cost of FRP composites compared with conventional materials, some researchers have recently investigated cost-effective hybrid structures composed by FRP composites and concrete. The use of FRP composites in combination with a traditional material, such as concrete, allows the engineers to take advantage of the excellent properties inherent in each of its constituents, and allows the optimum use of both materials.

Hillman and Murray (1990) proposed the innovative idea of a hybrid FRP-concrete structural system for flexural members, which led to the concept of hybrid beam (HB). The proposed system was constructed using FRP deck with concrete fill. The proposed deck was manufactured using the pultrusion process. The pultruded deck consists of a

series of deep inverted T-beams, shown in Figure 2.4. Intermediate flanges connect the beams. Most of the concrete was located above the neutral axis of the composite section. The weight reduction between 50% and 60% has reported when compared with a common slab system.

Bakeri and Sunder (1991) presented an innovative structural concept for hybrid FRP-concrete bridge deck systems. The proposed deck system was a simply curved membrane of FRP filled with concrete, shown in Figure 2.5. The idea was to use the FRP in tension and the concrete in compression. A finite element analysis was performed to evaluate the mechanical performance of the proposed deck system. A hybrid FRP-concrete system was found to be promising particularly from the viewpoint of cost. For this hybrid bridge deck system has achieved a deflection less than $S/800$, where S represents the stringer spacing upon loading to service load condition.

Saiidi et al. (1994) presented an experimental and analytical study of hybrid beams that consist of graphite/epoxy (G/E) sections and reinforced concrete slabs, shown in Figure 2.6. An epoxy resin was used to provide the bond between graphite sections and concrete. They concluded that the use of epoxy resin to bond concrete to G/E sections was found to be only partially effective.

Deskovic et al. (1995a) investigated the short-term behavior of hybrid FRP-concrete beams. A concrete layer substitutes the glass fiber reinforced polymers (GFRP) compressive flange of traditional pultruded box sections; thus, reducing the materials cost and increasing the stiffness. A very thin layer of carbon fiber-reinforced plastic (CFRP) was placed on the tension flange. The proposed hybrid FRP-concrete cross-sections for simply supported beams in both building and bridge applications are shown in Figure 2.7. Three large-scale beams were fabricated and tested in flexure to experimentally verify the strength, stiffness, and ductility characteristics of the hybrid FRP-concrete members. The experimental results as well as finite-element analyses confirmed that the ideal bond between GFRP-concrete interfaces should be provided by the combination of adhesives and mechanical connectors.

Deskovic et al. (1995b) also investigated the long-term behavior of the proposed hybrid FRP-concrete beam experimentally and analytically. They concluded that the proposed beam possesses good response characteristics when long-term loading was considered.

Samaan et al. (1998) presented a simple model to predict the complete bilinear stress-strain response of FRP-confined concrete in both axial and lateral directions. The model was based on correlation between the expansion rate of concrete and the hoop stiffness of the restraining member. By comparing the analytical predictions of the model with the experimental results for a total of thirty specimens, good correlation has obtained in both the axial and lateral directions.

Hall and Mottram (1998) tested twelve hybrid FRP-concrete beams to failure in four-point bending. Figure 2.8 shows cross section of the proposed beam. The FRP reinforcement used was two T-up-stands and a continuous base. To see the importance of the bonding between a FRP panel and concrete, an epoxy mortar was applied at the interface of one-half of the twelve specimens, and no treatment was done for the remaining half. Experimental results showed that adhesively bonded specimens had better composite action than specimens with no treatment at the interface. A generalized analytical model for flexural behavior based on the assumption of conventional reinforced concrete in flexure, the stress-strain relations of the reinforcement and concrete, and an iterative analysis procedure was proposed.

Seible et al. (1998) investigated a 2×10 m two span bridge with light weight concrete filled circular CFRP composite tubes. Their preliminary estimates indicate that two different bridge systems (the concrete filled CFRP beams with RC deck and concrete filled CFRP beam with pultruded modular E-glass deck) are 20 % and 100 % more expensive, respectively, when compared to a conventional RC slab bridge. Their study showed that the design was stiffness driven, and also significant strength reserve remains in the carbon shell.

Mirmiran et al. (1999a) conducted acoustic emission (AE) monitoring of over 40 hybrid FRP-concrete specimens with different lengths, cross sections, jacket types, and jacket thickness. The experimental results showed that a correlation exists between the AE activity and the extent of damage within the specimen. Also, unbonded specimens emit more AE signals mainly due to the friction between the concrete and FRP tube.

Mirmiran et al. (1999b) presented a study on the beam-column behavior of a structural member made of concrete-filled FRP tubes (CFFTs). Beam-column behavior of concrete-filled FRP tubes was investigated by testing five specimens at various combinations of

axial and transverse loads. They concluded that the Euler-Bernoulli theory was applicable for CFFTs, provided that composite action between the tube and the concrete core was fully developed. They also reported that failure of CFFTs was ductile and with much warning. Furthermore, toughness, and ductility measures for CFFT beam-column specimens were quite comparable to those of their equivalent conventional RC sections. Davol et al. (2001) characterized the response of a hybrid composite concrete system under flexural loading. The circular FRP shells are filled with concrete that was used to carry compressive loads and to stabilize the shell against buckling on the compression side as well as to aid in the joining of adjacent members. Although concrete is highly nonlinear and nonhomogeneous, the approach taken here assumes a linear elastic response used incrementally to include the nonlinear effects. Compression behavior was discussed with emphasis on understanding the dilatation behavior of the concrete core. The proposed models predict the longitudinal, hoop, and shear strain in the FRP shell. Two large-scale circular FRP shells tested in four points bending to validate the analytical models.

Riberio et al. (2001) studied the flexural behavior of hybrid FRP-concrete beams. The proposed beams were composed of a U shape pultrusion profile, shown in Figure 2.9, which will work in tension and a polymer concrete filling that will work mainly in compression. Four different hybrid beams were designed and tested in four-point bending. Two of them had all the section full of polymer concrete and the other two with only a layer of concrete located in the upper part of the profile. Flexural specific rigidity and synergetic effect were used as indication for the flexural performance of the proposed beams. Flexural specific rigidity is a ratio between the flexural rigidity and the specific weight, while synergetic effect is a ratio of the ultimate load of the assembly to the sum of the ultimate loads of its two elements. The results showed two different failure modes; 1) due to bond failure between concrete and the GFRP profile, immediately followed by explosive rupture of concrete, and 2) due to tensile failure of the lower surface of GFRP profile at the midspan. All type I beams had the first failure mode. Also II and IV beams have the same mode but concrete did not break, and rupture was more ductile. Type III beams showed the second failure mode and showed the highest synergetic effect (refer to Figure 2.9 for layout of the different beam types).

Yang et al. (2002) presented an analytical and numerical study on interfacial stress of axisymmetric FRP-concrete hybrid columns. They assumed that the interface between the concrete and the FRP plate was assumed perfectly bonded and it was assumed that both the concrete and the FRP were elastic. Theoretical and numerical results confirmed that there exists a high stress concentration at the end of hybrid column. The maximum shear stress at the end of hybrid column was the main cause for interfacial debonding between concrete and FRP plates. They also concluded that the distribution and maximum interfacial shear stress are influenced by the modulus ratio of concrete and FRP, and thickness of FRP.

Van Erp et al. (2002) proposed hybrid FRP-concrete beams for bridge applications. The weight of the hybrid beam was about one-third that of the corresponding concrete beam. The proposed structural type was the box section shown in Figure 2.10. A layer of concrete was placed on top of GFRP box in the compressive zone of the section. Composite action between the concrete and the FRP plate was achieved through the use of a high quality epoxy adhesives. Unlike Deskovic's proposed beam (1995a), an additional FRP top flange has been designed to carry significant compressive loads. As a result, concrete crushing was a warning of failure in this design instead of CFRP failure, and the cross section reduces to an FRP box section after crushing of concrete. Two bridges having span length of 6 m and 10 m were constructed in order to investigate the dynamic/fatigue behavior of the proposed beam. By combining two sets of seven 10 m span beams together by using a high quality epoxy adhesive, two sections with a width of approximately 2.5 m were created. A full-scale bridge (10 m span, 5m width) was installed in Toowoomba, Australia in January 2002. It was installed in less than 30 minutes, and extensive field-testing on its short-and long-term behaviors has been underway. Test on individual bridge beams showed that the failure behavior of the proposed beam was very predictable, and it has excellent fatigue behavior.

Fam and Rizkalla (2002) investigated the flexural behavior of concrete-filled fiber-reinforced polymer circular tubes. A total of 20 beams were tested in bending using four-point loading. Nine different types of GFRP tubes and one steel tube were used to fabricate the tested beams. The different configurations that were considered include: totally filled tubes, concrete filled tubes with a central hole, and tube in tube (both

concentric and eccentric) with concrete filling in between, shown in Figure 2.11. They concluded that: (1) concrete fill prevents local buckling and also contributes to the inertia of the section, which ultimately increases the flexural strength and stiffness of the member; (2) the higher the stiffness of the hollow FRP tube, the lower the gain in flexural strength and stiffness of the member; (3) the load-deflection behavior of concrete-filled GFRP tubes was almost linear; (4) although concrete-filled pultruded GFRP tubes show higher stiffness than concrete-filled filament-wound tubes of the same thickness, they fail prematurely by horizontal shear due to the lack of fibers in the hoop direction; (5) concrete-filled FRP tubes with thicker walls or a higher percentage of fibers in the axial direction tend to fail in compression; (6) a higher flexural strength-to-weight ratio was achieved by providing a central hole in the core. Also flexural strength and stiffness increase if the inner tube was eccentric toward the tension side; (7) a shear transfer mechanism should be used in flexural members to avoid slip between concrete core and FRP tube.

Hulatt et al. (2003) investigated failure mechanisms associated with hybrid FRP-concrete beams. Long-term effects of fatigue and creep were also investigated. The beams had a T-cross-section and had two designs, shown in Figure 2.12, one to fail by buckling of the webs and the other by a shear bond failure between the concrete and composite interface. Both types of beams were analyzed theoretically using a simplified transformed method of analysis. Also, a linear FE analysis was carried out on both beams types to compare the results obtained theoretically and experimentally. Some conclusions were: (1) the critical post buckling failure of the first beam type occurred after an initial web buckling took place under a low load. However, the catastrophic failure of the beam occurred in the maximum shear region of the beam at a load of five times that of the first buckle with a compressive failure of the concrete; (2) the adhesive bond was adequate for both types of beams and the bond between the permanent shuttering and concrete was intact after failure; (3) the long-term testing of the hybrid beams showed that FRP materials have an appreciable resistance to sustained and fatigue loads.

Kitane et al. (2004) proposed a basic concept of a hybrid FRP-concrete bridge superstructure. The proposed structural type was a trapezoidal box sections, shown in Figure 2.13. A thin layer of concrete was placed in the compressive zone of the section,

and was surrounded with GFRP. The concrete thickness was chosen to be less than 10% of the bridge depth. Design procedures for hybrid FRP-concrete bridge superstructure and a conceptual design were proposed. A series of a quasi-static loading tests and a fatigue-loading test were performed on a one-fifth-scale model of the 18.3 m hybrid bridge superstructure. A detailed finite element analysis was performed along with simple methods of analysis for the hybrid bridge. Results from this research showed that the hybrid FRP-concrete bridge superstructure was highly feasible from a structural engineering point of view.

Uddin et al. (2006) proposed an innovative carbon fiber reinforced polymer (CFRP)-autoclaved aerated concrete (AAC) panels. The proposed panels were based on the concept of a sandwich construction with strong and stiff CFRP composite skins bonded to an inner AAC panel. An experimental protocol based on a four point bending test was used to characterize the stiffness, ductility, and strength of the hybrid CFRP-AAC sandwich panels. Results from this research showed that there was a considerable increase in the load capacity and ductility of the CFRP-AAC panels compared to plain AAC panels. In addition, most of the CFRP-AAC panels (specially the shear reinforced) remained intact even after the ultimate load had been reached with no visible damage.

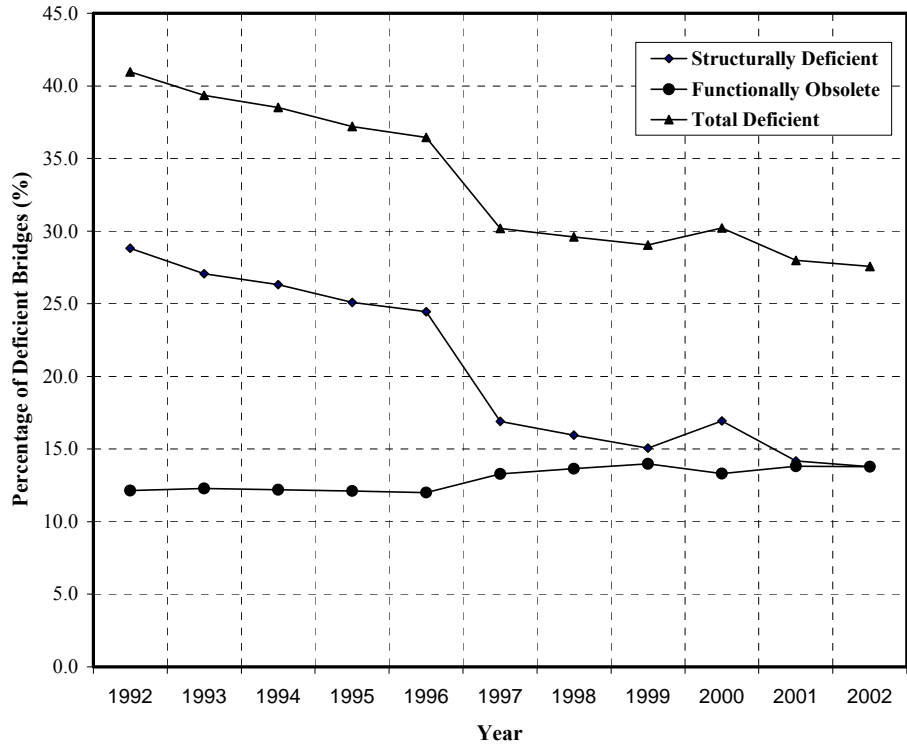


Figure 2.1 Percentage of Deficient Bridges in U. S. (NBI, 2003)

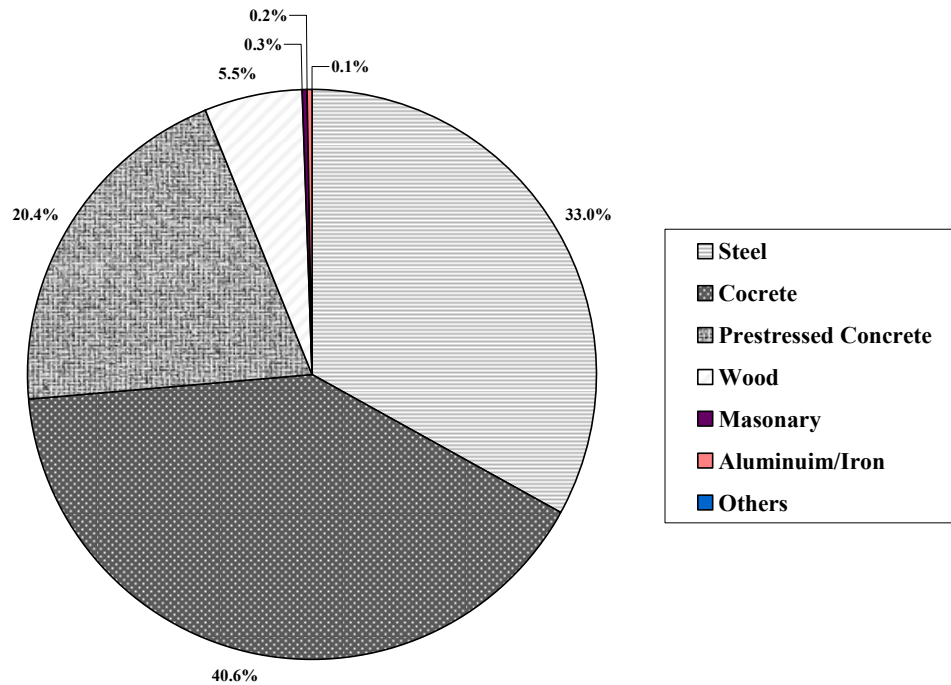


Figure 2.2 Bridges by Type of Superstructure Material (NBI, 2002)

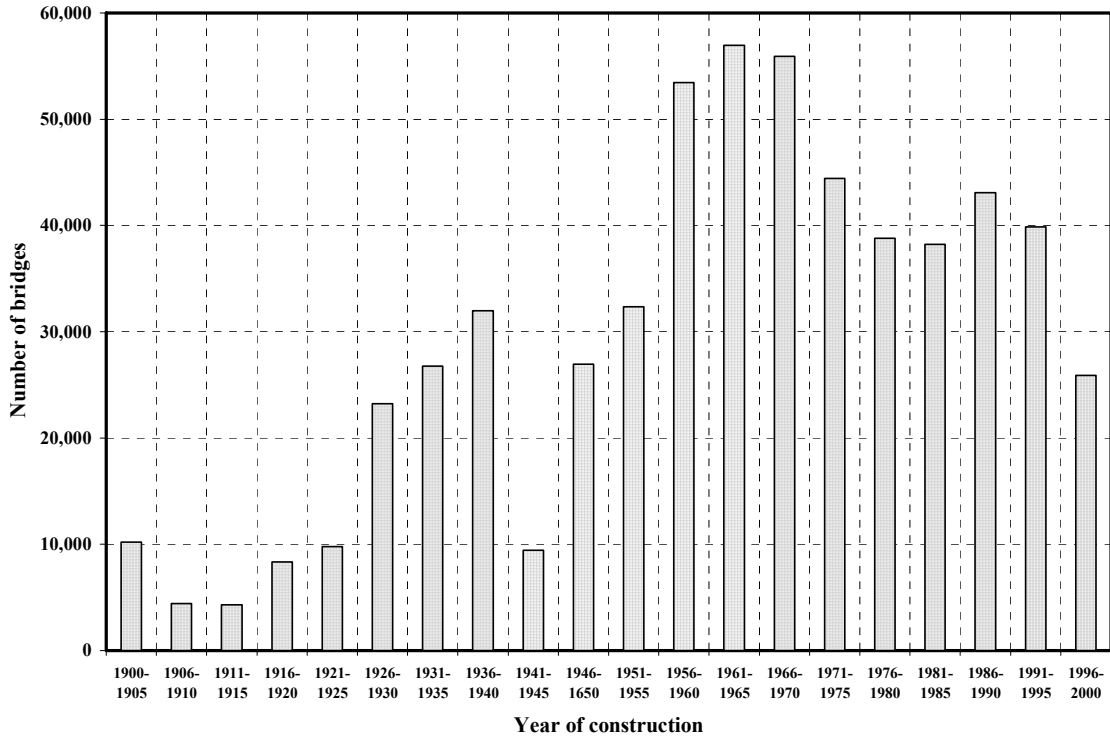


Figure 2.3 Year of Construction for U. S. Bridges. (NBI, 2003)

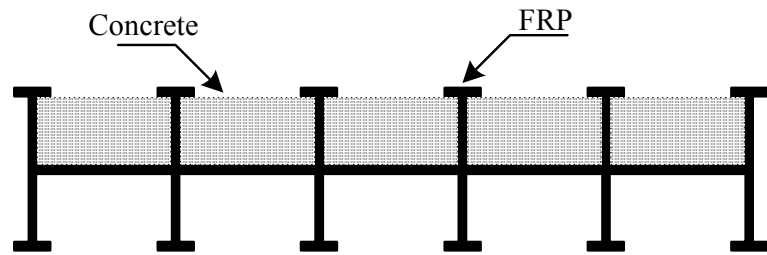


Figure 2.4 Hybrid FRP-Concrete Deck Proposed by Hillman and Murray (1990)

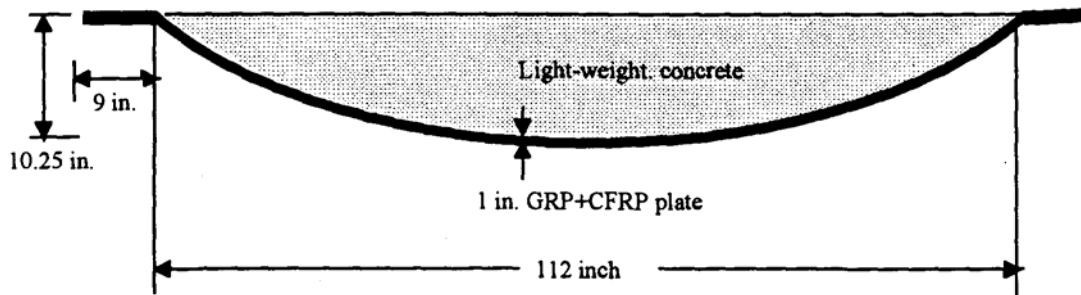


Figure 2.5 Hybrid FRP-Concrete Bridge Deck Studied by Bakeri and Sunder (1991)

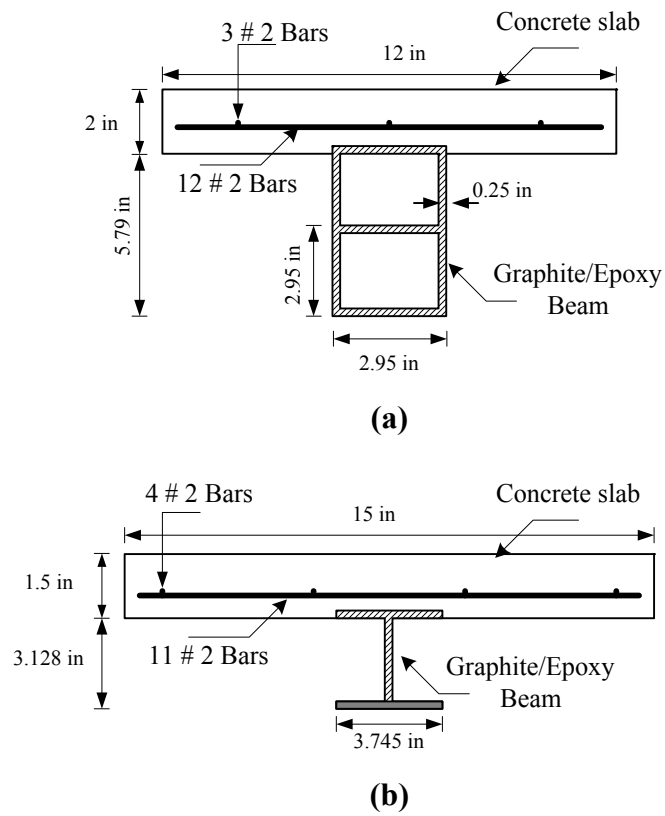


Figure 2.6 Sections of Hybrid FRP-Concrete specimens analyzed by Saiidi et al. (1994)

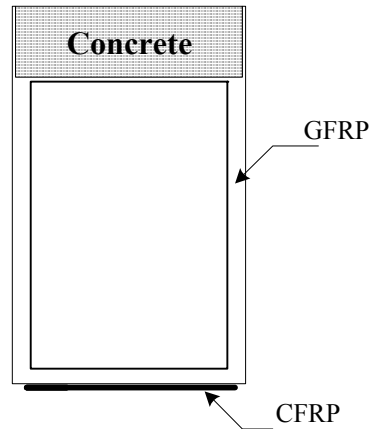


Figure 2.7 Cross-Section of Hybrid FRP-Concrete Beam Studied by Deskovic et al. (1995)

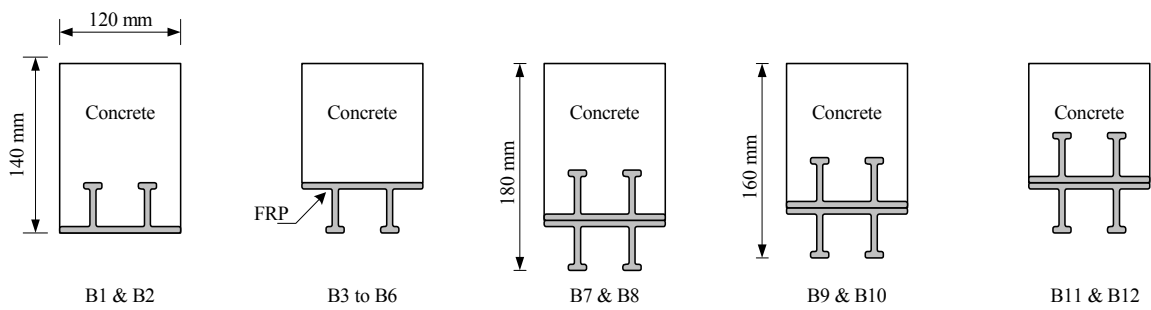


Figure 2.8 Beam Cross-Section Types Considered by Hall and Mottram (1998)

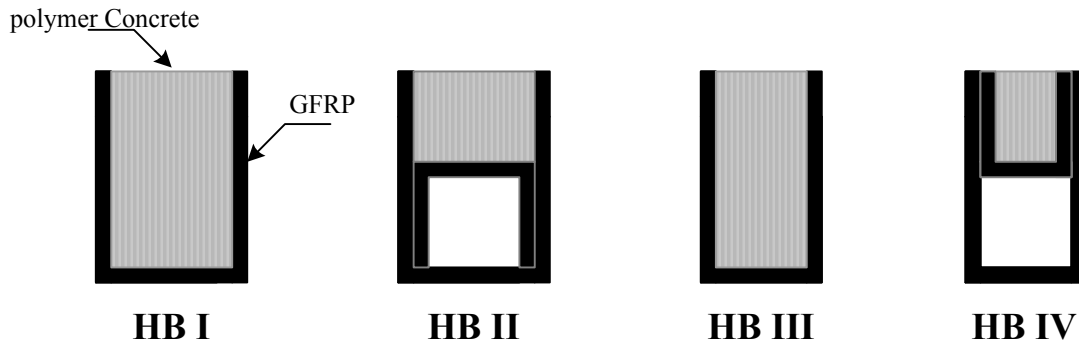
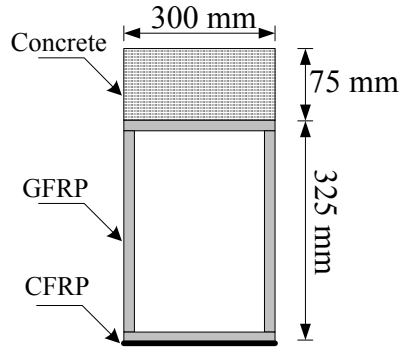
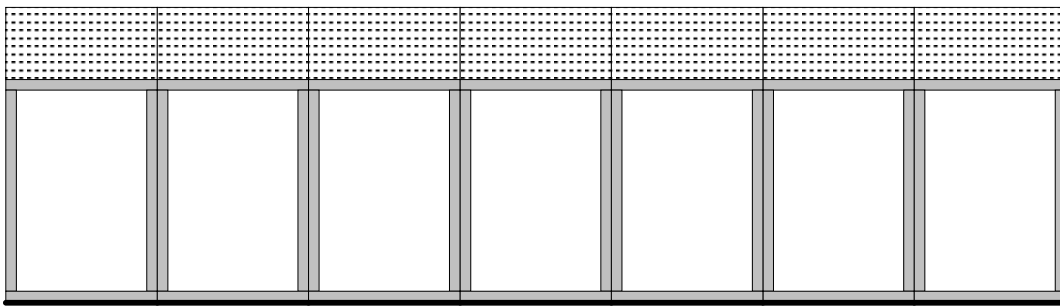


Figure 2.9 Cross-Sections of the Hybrid Beams Used by Ribeiro et al. (2001)



(a) Cross Section of Individual Beam



(b) Cross Section of 2.5 m width Bridge Section

Figure 2.10 Cross-Section of Hybrid Beam Tested by Erp et al. (2002)

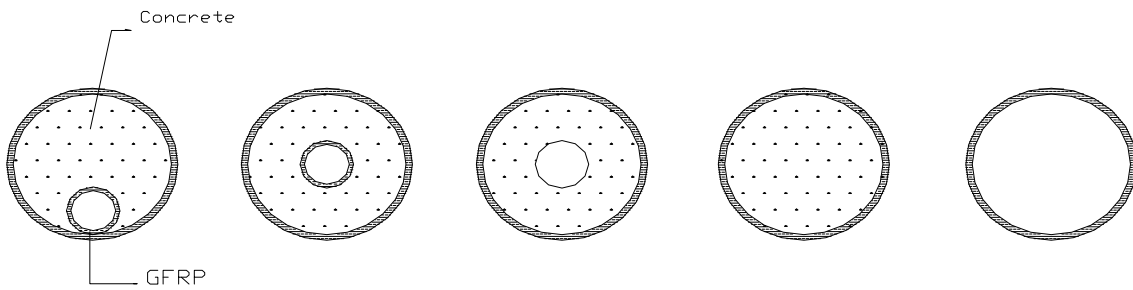


Figure 2.11 Cross-Section of Different Types of GFRP Tubes Filled With Concrete Tested by Fam And Rizkalla (2002)

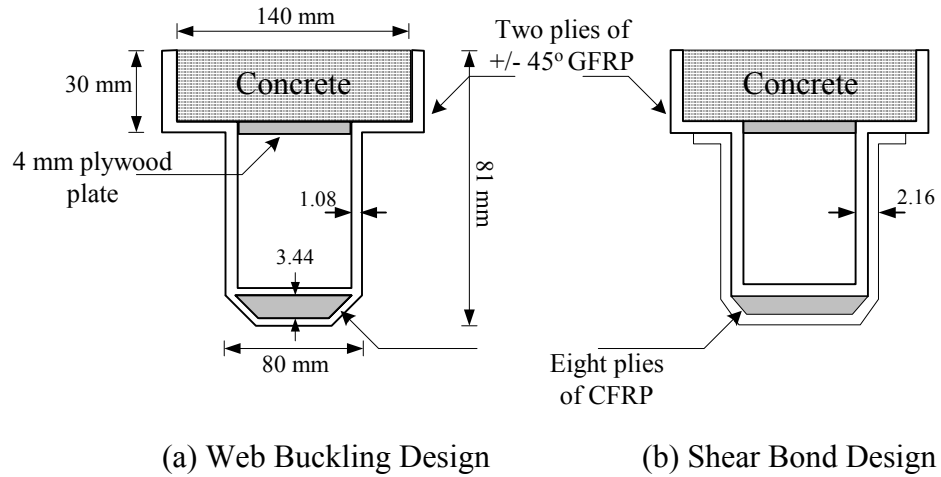


Figure 2.12 Cross-Section of Two Hybrid Beam Types Analyzed by Hullat et al. (2003)

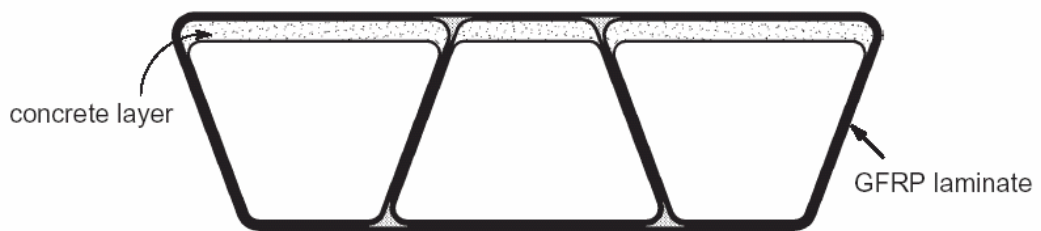


Figure 2.13 Cross-Section of Hybrid Bridge Superstructure Tested by Kitane et al. (2004)

THE PROPOSED HYBRID FRP-CONCRETE BRIDGE SYSTEMS

3.1 HYBRID FRP-CONCRETE BRIDGE CONFIGURATIONS

In this chapter, two hybrid FRP-concrete bridge systems were investigated numerically by using finite element (FE) analysis. Both systems were investigated to select the most efficient one that will subsequently be used to investigate the feasibility of the FRP-concrete structural systems in the remainder of the study. The first system (system I) consists of trapezoidal cell units forming either a bridge superstructure or a bridge deck unit. The second one (system II) is formed by arch cells. The two systems rely on using cellular components to form the core of the deck system, and an outer shell to wrap around those cells to form the integral unit of the bridge. To evaluate the two systems, a bridge superstructure was designed as a simply-supported single span one-lane bridge with a width of 4.267 m (15 ft). The bridge has a length of 18.288 m (60 ft). System I is comprised of trapezoidal cross-sections surrounded by an outer shell as shown in Figure 3.1. According to Ashby (1991), thin walled box sections are the most efficient structural forms for beams. A thin layer of concrete is placed in the compression zone of section. Concrete was confined by glass fiber reinforced polymers (GFRP) laminates that protect it from the environmental exposure. Moreover, the concrete layers reduce the local deformation of the top surface of the bridge under concentrated loads that represent truck wheel loads. Trapezoidal box sections with an inclination angle helps to reduce shear force at the interface of two box sections. According to Kitane (2004), the inclination of $3/8$ has the smallest deformation at the riding surface. Thus, inclination of $3/8$ was chosen for the proposed bridge system. The thickness of the concrete layer is a key design parameter to optimize the hybrid structural system. According to Kitane

(2004), concrete can be used efficiently to increase the flexural rigidity until the concrete thickness equals about 10% of the bridge depth. Therefore, the thickness was chosen as 99 mm, which is 8.5% of the total depth of the bridge. The inner tube having a two-ply laminate with the fiber orientations of $0^\circ [0^\circ_2]$ was first constructed with a laminate construction, and the outer tube is constructed over the inner tube laminate with a laminate construction $[0^\circ (45^\circ)_2]$. The outer-most laminate stacking sequence is $[0^\circ_4]$. This proposed bridge system has several inherent advantages over all-composite bridge which can be summarized as follows:

- GFRP is corrosion-resistant and the concrete is not exposed to the environment: the system will require less maintenance than conventional bridges.
- Concrete is designed to be always in compression in the longitudinal direction. The fact that concrete is not used in the tension side leads to significant weight reduction when compared to a concrete-filled FRP tube design.
- It has been reported that the local deformation under a loading point may become large for all-composite bridge decks (Bakeri and Sunder, 1990; Aref, 1997). A layer of concrete can reduce this local deformation of the top flange.

System II is formed by two components: arch cells and rectangular with semi-circular cells. Each arch cell is formed by two semicircular laminates, and in between the concrete is placed. Moreover, the rectangular with semi-circular cell is formed by two rectangular with semi-circle laminates, and in between the concrete will be placed as shown in

Figure 3.2. This design has several inherent advantages:

- The circular shape used in this system avoids stress concentrations that are present at the corners of I and box sections.
- The proposed design develops shell action in the transverse direction that is extremely important to ensure adequate transverse rigidity.

An optimization of the concrete layer thickness for System II was not taken into account in this stage. Instead, the effects of concrete thickness on various properties were examined as shown in Figure 3.3. These properties are: (a) total weight; (b) flexural rigidity; and (c) specific flexural rigidity. The specific flexural rigidity is defined as flexural rigidity divided by weight per unit length. These properties are normalized with respect to those obtained for the case of FRP-only system. It is clear that as the concrete

thickness increases, both the weight and the flexural rigidity increases. But the rate of concrete increase is higher than the rate of flexural rigidity increase. Therefore, the specific flexural rigidity decreases as the concrete thickness increases. It can be observed also that the rate of the increase in flexural rigidity is decreased when concrete thickness equal to about 9.75% of the bridge depth. Thus, the thickness was chosen as 960 mm, which is 9.75 % of the total depth of the bridge. The inner tube having fiber orientations of $[0^{\circ}_3]$ is first constructed with a laminate construction, and the outer tube is constructed over the inner tube laminate with a laminate construction $[0^{\circ}_2]$. The outer-most laminate stacking sequence is $[45^{\circ}_2]$. The cover laminate stacking sequence is $[0^{\circ}_4]$. By using a 45° laminae in the outer tube laminate, the shear stiffness is increased. Table 3-1 shows the stacking sequence and thickness of different layers of both bridge systems (I and II).

3.2 LOADS

The AASHTO LRFD (1998) specifications were used to design the proposed structural systems. Only dead and live load were considered in this study.

3.2.1 Dead Loads

The dead loads acting on the bridge are modeled either as the dead load of structural and non-structural elements, which is denoted as DC, or dead load of wearing surfaces and utilities, which are denoted as DW. The wearing surface load is 0.305 kN/m^2 .

3.2.2 Live Loads

The vehicular live load is designated as HL-93 and is comprised of a combination of the design tandem or design truck along with the design lane load. The design tandem is also a truck with a pair of (110 kN/m) axles spaced 1.2 m apart. The design lane load is a uniform load with a magnitude of 9.3 kN/m applied over a 3 m wide strip. The design truck load is three axles with loads of 145 kN, 145 kN, and 35 kN. The spacing between the 145 kN axles varies from 4.3 m to 9 m. Load configuration of these loads are shown in Figure 3.4. The distance from the one support to the rear axle of a vehicle, which is denoted as d , is chosen to produce the maximum effect for deflection or moment. Table

3-2 shows the distance, d , to produce either the maximum deflection or the maximum moment.

3.3 DESIGN CRITERIA

Two design criteria are considered in designing the hybrid FRP-concrete superstructure bridge. First, we consider the stiffness criterion that includes a limit on maximum vertical displacement. The second criterion is strength, which includes first ply failure of the structure, buckling, and shear failure.

3.3.1 Deflection Criteria

It is recommended in AASHTO LRFD Bridge Design Specifications (1998) that the maximum deflection under live loads needs to be smaller than $L/800$ (L : span length). For the live load deflection calculation, the deflection should be taken as the larger of

- $(1+IM) \times$ design truck alone
- 25% of $(1+IM) \times$ design truck load and lane load.

where IM is dynamic load allowance and has a value of 0.33 in this case. The load case for $(1+IM) \times$ truck load was used in this study to check the serviceability condition because it produced a larger displacement than the other case. The span (L) of the hybrid bridge is 18.288 m . The maximum deflection under $(1+IM) \times$ truck load has to be smaller than 22.9 mm ($L/800$).

The load combination of the service I limit is specified as (AASHTO, 1998).

$$DC + DW + LL \tag{3.1}$$

where, in this study,

$$LL = LANE + (1+IM) \times TRUCK$$

DC: Dead load of components and attachments

DW: Dead load of wearing surfaces and utilities

LL: Live load effect

LANE: Design lane load

TRUCK: Design Truck

IM: Dynamic allowance factor

This service limit state refers to the load combination relating to the normal operation use of the bridge. It also relates to deflection control of the bridge design and crack control of concrete.

3.3.2 Strength Criteria

The load combination for the strength I limit is specified as (AASHTO, 1998).

$$1.25D_c + 1.5DW + 1.75LL \quad (3.2)$$

All the force effects due to this condition are required to be under strengths of different failure modes such as flexure, shear, and buckling. No part of the GFRP should experience any ply failure.

3.4 LINEAR FINITE ELEMENT ANALYSIS

For a detailed finite element analysis (FEA) of the hybrid FRP-concrete bridge superstructure, MSC PATRAN (1999) was used to generate of the geometry and the finite element mesh. The finite element calculations were performed using ABAQUS (Hibbit, Karlsson & Sorensen, Inc., 2002).

3.4.1 Material Properties and Modeling

The FRP laminates are constructed using E-glass in the form of a woven fabric because of relative cost saving when compared to other forms of fibers. Vinyl ester resin is chosen as the matrix because of its high durability, and extremely high corrosion resistance. The mechanical properties of the GFRP composite material were provided for the finite element analysis by An-Cor Industrial Plastics, Inc. Table 3-3 depicts the material properties of GFRP that are utilized in the finite element models. Normal weight concrete is used in this study. The mechanical properties of concrete used in this study are presented in Table 3-4. The linear FEA can predict the behavior of the hybrid bridge with enough accuracy if the strain induced in the materials is within the strain range where the elastic moduli of the materials were computed. Both concrete and GFRP behave nonlinearly in a higher strain range. However material nonlinearity of these materials will not be considered in the FEA in this stage. Further study of nonlinearity of these materials beyond the elastic range is undertaken in subsequent chapters. A typical

linear model for both GFRP laminates and concrete is used in this study. GFRP laminates were modeled by a four-node shell element (S4R5), while concrete was modeled by a general 3D solid element (C3D8). Figure 3.5 shows the finite element model for both bridge Systems I and II.

3.4.2 Boundary Conditions

Boundary conditions were imposed on two lines of nodes of the bottom surface. Nodes at $y = 0$ and $z = 0$ were restrained in the y and z directions, and nodes at $y = L$ and $z = 0$ were restrained in the z direction. In addition, nodes at $x = 0$, $z = 0$, and $y = 0$ and L were restrained in the x direction.

3.4.3 An Analysis of Discretization Error

To obtain a FEA solution and a measure of the error in that solution, a series of analyses with increasing levels of refinement were performed for both systems. Convergence of the finite element solution is obtained for both systems (I and II), and the refined meshes are then used in the linear static analyses. Dead load was applied to both systems (I and II). Figure 3.6 shows that the discretization error in both systems (I and II) converges to zero, which is a good indication of the accuracy of their finite element mesh.

3.4.4 Linear Static Finite Element Analysis

3.4.4.1 Deflection Criteria

To check whether the maximum deflection under $(1+IM) \times$ truck load is smaller than $L/800$ (22.9 mm), the load equivalent to $(1+IM) \times$ truck load was applied to both systems (I and II). The maximum vertical displacement was 12.9 mm ($0.563 \times L/800$) for bridge system I, and was 13.8 mm ($0.603 \times L/800$) for bridge system II. Both systems have much smaller deflection than the deflection limit of 22.9 mm. With further design refinements, one can reduce the weight and consequently bring the maximum deflection closer to $(L/800)$.

3.4.4.2 Service I Limit

The load combination for the service I limit described in Eq. 3.1 was applied to both bridge systems (I and II). The maximum vertical displacement was 25.2 mm ($1.1 \times L/800$) for bridge system I. and was 29.3 mm ($1.279 \times L/800$) for system II. Moreover, System II has local deformation under truck load especially at the middle-top surface of the bridge superstructure as shown in Figure 3.7. The maximum local vertical displacement at this area reaches 36.6 mm. Filling materials at area between two arches and the top-middle surface is recommended to overcome the local deflection.

The Tsai-Hill criterion appears to be much more applicable to failure prediction for E-glass/Epoxy composite material than maximum stress or maximum strain failure criteria (Jones 1990). Hence, the Tsai-Hill failure criterion was used as a measure of failure of the FRP laminates in this study. The Tsai-Hill failure equation is shown in Eq. 3.3

$$\left(\frac{\sigma_1}{X_1}\right)^2 - \frac{\sigma_1\sigma_2}{X_1X_2} + \left(\frac{\sigma_2}{X_2}\right)^2 + \left(\frac{\sigma_6}{X_6}\right)^2 = 1 \quad (3.3)$$

where

X_1 : Strength in the principal 1 direction

σ_1 : Stress in the principal 1 direction

X_2 : Strength in the principal 2 direction

σ_2 : Stress in the principal 2 direction

X_6 : Shear strength

σ_6 : Shear stress

It can be observed from the service I limit analysis that the maximum Tsai-Hill failure index for GFRP laminates in both bridge systems is well below 1.0. The maximum Tsai-Hill index for GFRP laminates in System I is 0.0316, and it is 0.0529 for System II. Also, we observed that the stress concentration is induced at edge corners of bridge System I, and the maximum Tsai-Hill index for GFRP laminates at these corners is 0.157. There are no stress concentrations in bridge System II. Stress concentration can be avoided at edge corners of System I by adding a vertical diaphragm at the edge near the support. The safety factor when considering the first ply failure can be obtained as

$$R = \sqrt{\frac{1}{I_{TH}}} \quad (3.4)$$

where

I_{TH} : The maximum Tsai-Hill index in the entire structure.

The compressive stresses of concrete elements are all smaller than its compressive strength limit ($0.8 \times f'_c$), in both bridge systems (I and II). The maximum compressive stress of concrete elements of System I is 5.79 MPa ($0.235 \times f'_c$), which is located at the top of the concrete layer right under the tire area of the second axle. The maximum compressive stress in the concrete elements of System II is 8.23 MPa ($0.334 \times f'_c$), which is located at the top surface of the arch unit cell at the mid-span of bridge superstructure. The maximum tensile stresses of concrete in bridge system I is 2.65 MPa ($0.847 \times f'_r$) which is located at the bottom of the concrete layer right under the tire area of the second axle; the maximum tensile stresses in the System II is 8.23 MPa ($2.63 \times f'_r$) which exceeds the tensile strength of concrete located at the bottom surface of the arch unit cell at the mid-span of the bridge superstructure. When the tensile stress exceeds the tensile strength, cracks will form.

The maximum transverse shear stress at the interface between two trapezoidal box sections in System I is 1.4 MPa which is much smaller than shear strength of commercially available resins that range from 10.35 to 34.5 MPa (Aref, 1997).

3.4.4.3 Strength Check

The load combination for the strength I limit described in Eq. 3.2 was applied to both bridge systems. The maximum vertical displacement was 39.9 mm ($1.74 \times L/800$) for bridge system I and was 44.8 mm ($1.956 \times L/800$) for System II. System II also has local deformation under truck load especially near the middle-top surface of the bridge superstructure. The maximum local vertical displacement at this area reaches 56.0 mm.

The maximum Tsai-Hill failure index for GFRP laminates in both bridge systems is well below 1.0. The maximum Tsai-Hill index for GFRP laminates in System I is 0.0491 and 0.075 for System II at the bottom surface of the bridge superstructure where the two-cell subassemblies are connected. Also, we observed that the maximum Tsai-Hill index for

GFRP laminates reaches at these corners about 0.245 due to stress concentration. The maximum transverse shear stress at interface between two trapezoidal box sections in system I is 2.2 MPa which is much smaller than shear strength of commercially available resin. The compressive stress in the concrete elements is smaller than the compressive strength limit ($0.8 \times f'_c$): 9.38 MPa ($0.38 \times f'_c$) in System I located at the top of the concrete layer under the tire area of the second axle and 12.9 MPa. ($0.52 \times f'_c$) in System II located at the top surface of the arch unit cell at the mid-span of bridge superstructure.

3.4.4.4 Flexural Loading Test

Both bridge systems were analyzed to examine their flexural behavior. The flexural loading configuration simulates the tandem load specified in the AASHTO LRFD Bridge Design Specifications (1998). Figure 3.8 and Figure 3.9 shows the deformed shapes of the bottom and top surfaces of Systems I and II, under different load levels. It is apparent from these figures that System I is stiffer than system II.

3.5 SUMMARY

Table 3-5 enables a comparison of weight between both hybrid FRP-concrete systems. System I is lighter than System II, and stronger and stiffer than System II. Table 3-6 enables a comparison of results from the deflection check analysis, the service I limit analysis as well as the strength I limit analysis between bridge system I and system II. From these results, it can be concluded that System I is more efficient than System II and System I has used to investigate the feasibility of the FRP-concrete structural systems in the remainder of the study.

Table 3-1 Thickness and Stacking Sequence of Different Layers of Systems I and II

| | System I | | System II | |
|---------------------------------|-----------------------------|----------------|-------------------|----------------|
| | Stacking Sequence | Thickness (mm) | Stacking Sequence | Thickness (mm) |
| Inner Tube Laminate | $[0^{\circ}_2]$ | 13 | $[0^{\circ}_3]$ | 21 |
| Outer Tube Laminate | $[0^{\circ}(45^{\circ})_2]$ | 22.3 | $[0^{\circ}_2]$ | 14 |
| Outer-Most Tube Laminate | $[0^{\circ}_4]$ | 29.7 | $[45^{\circ}_2]$ | 14 |
| Cover Tube Laminate | ----- | ----- | $[0^{\circ}_4]$ | 28 |

Table 3-2 Distance from the support at $y=0$ to the Rear Axle

| | | Truck | | Tandem | |
|---------------------------|-------------------------|-------|----------|--------|----------|
| | | (m) | (× Span) | (m) | (× Span) |
| Maximum Moment | Location of Rear Axle | 5.57 | 0.305 | 8.24 | 0.451 |
| | Location of Max. Moment | 9.87 | 0.540 | 9.44 | 0.516 |
| Maximum Deflection | Location of Rear Axle | 6.36 | 0.348 | 8.54 | 0.467 |
| | Location of Max. Moment | 9.12 | 0.4999 | 9.14 | 0.500 |

Table 3-3 Mechanical Properties of GFRP

| Mechanical Property | Fill | Warp |
|-------------------------------------|-------------|-------------|
| Young's Modulus (GPa) | 18.6 | 18.6 |
| Poisson's Ratio | 0.1348 | 0.1348 |
| Ultimate Compressive Strength (MPa) | -241 | -241 |
| Ultimate Tensile Strength (MPa) | 288 | 288 |
| Ultimate Shear Strength (MPa) | 56.1 | 56.1 |

Table 3-4 Mechanical Properties of Concrete

| Mechanical Property | Value |
|------------------------------------|--------------|
| Young's Modulus (GPa) | 24.822 |
| Poisson's Ratio | 0.18 |
| Compressive Strength, f'_c (MPa) | 24.65 |

Table 3-5 Comparison of Total Weight of Systems I and II

| | Weight (Tons) | | |
|------------------|---------------|----------|-------|
| | GFRP | Concrete | Total |
| System I | 27.77 | 18.01 | 45.82 |
| System II | 27.77 | 23.59 | 51.36 |

Table 3-6 Comparison of Selected FEA Results of System I and II

| | | System I | System II |
|-------------------------|------------------------------|----------|-----------|
| Deflection Check | Max. Deflection (L/800) | 0.563 | 0.603 |
| | Max. Deflection (L/800) | 1.1 | 1.279 |
| Service I Limit | Max. Tsai Hill Failure Index | 0.0316 | 0.0529 |
| | Safety Factor | 5.63 | 4.35 |
| Strength I Limit | Max. Deflection (L/800) | 1.74 | 1.956 |
| | Max. Tsai Hill Failure Index | 0.0491 | 0.0653 |
| | Safety Factor | 4.51 | 3.91 |

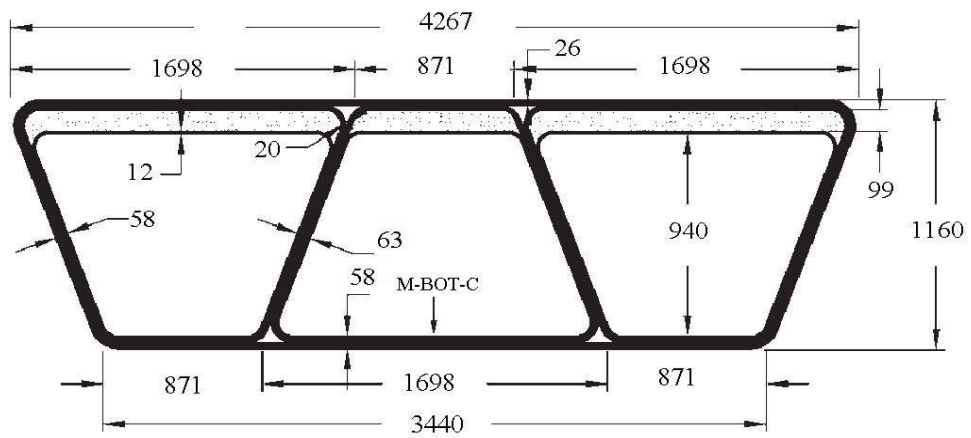
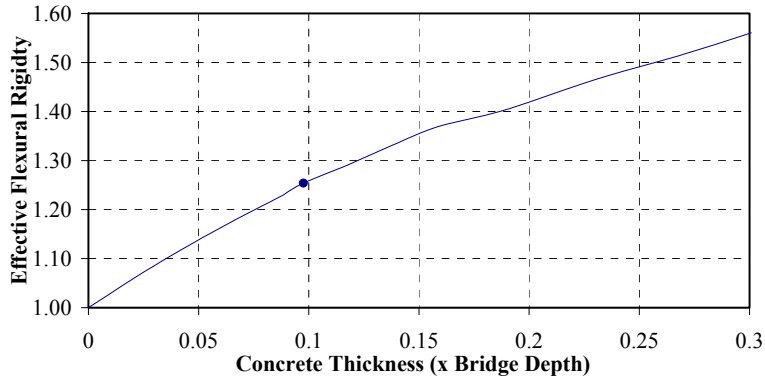
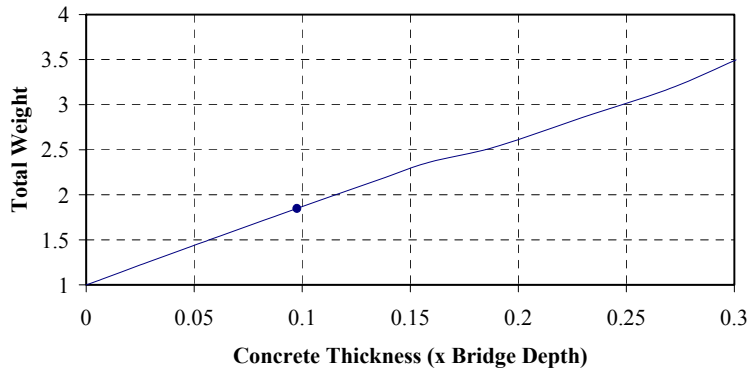


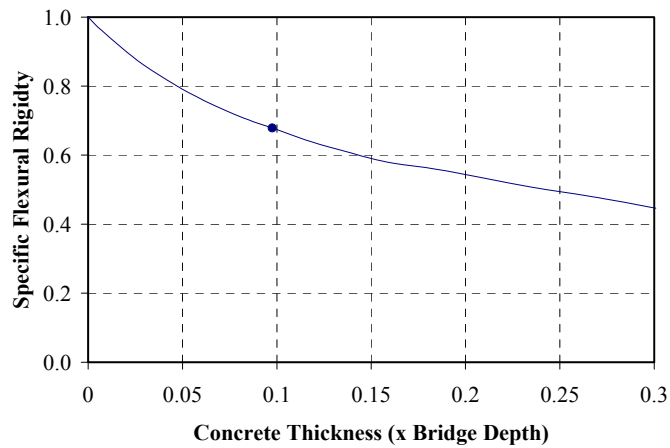
Figure 3.1 Cross Section of Systems I of the Hybrid FRP-Concrete Superstructure
(dimension in mm)



(a) Effective Flexural Rigidity

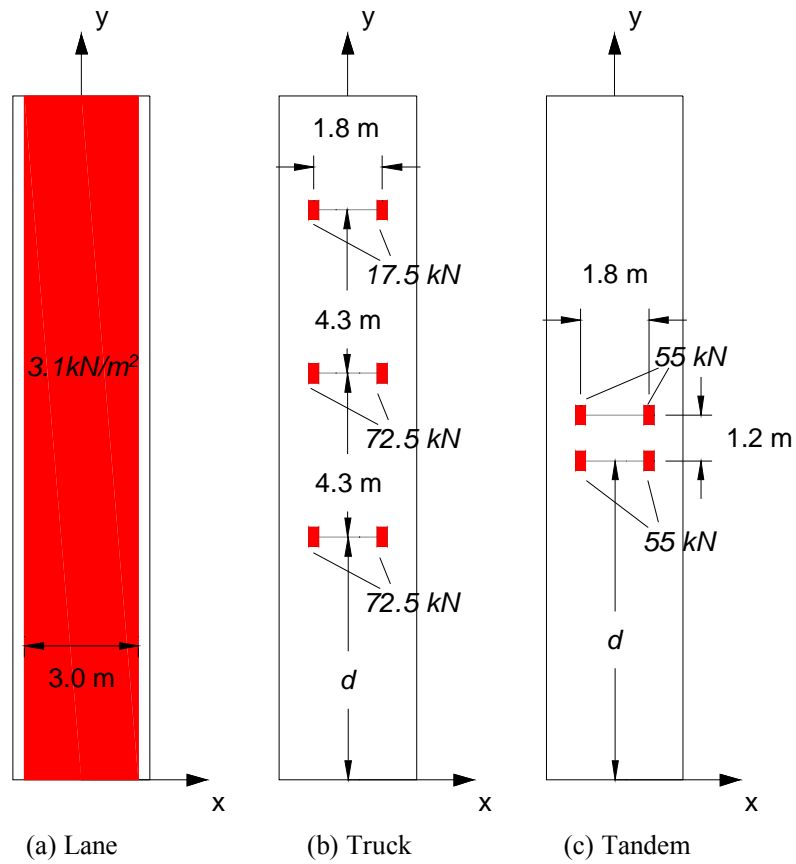


(b) Total Weight

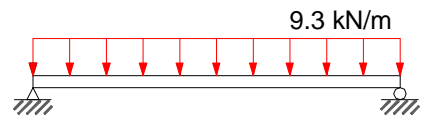


(c) Specific Flexural Rigidity

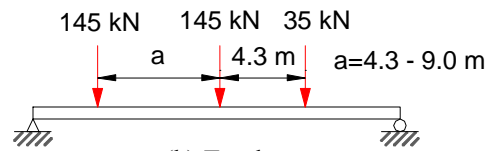
Figure 3.3 Effects of Concrete Thickness on Different Items (●: current design)



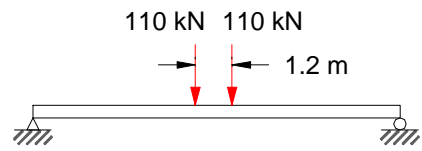
(i) Top View



(a) Lane



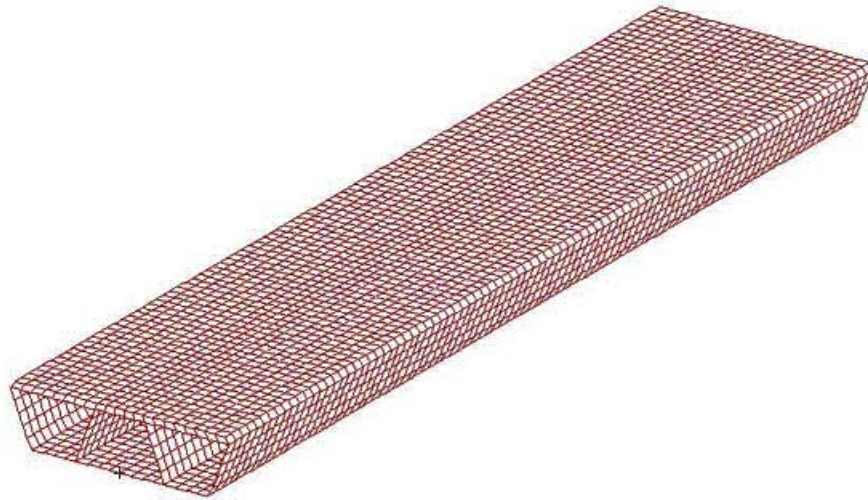
(b) Truck



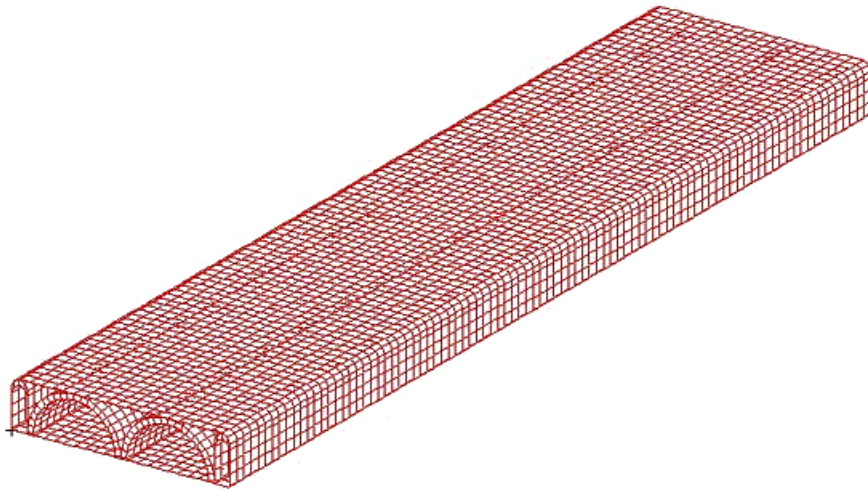
(c) Tandem

(ii) Elevation

Figure 3.4 HL-93 Vehicle Loading Configuration

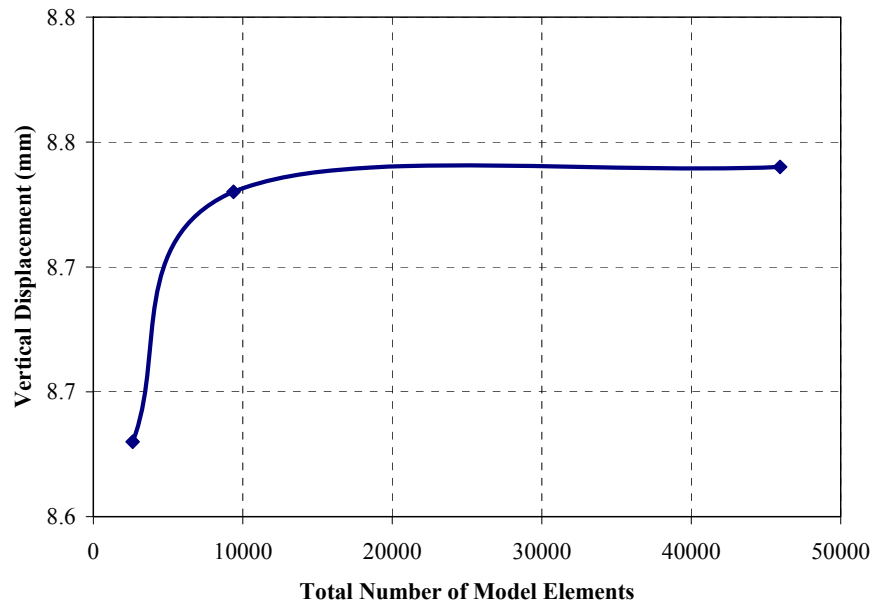


(a) System I

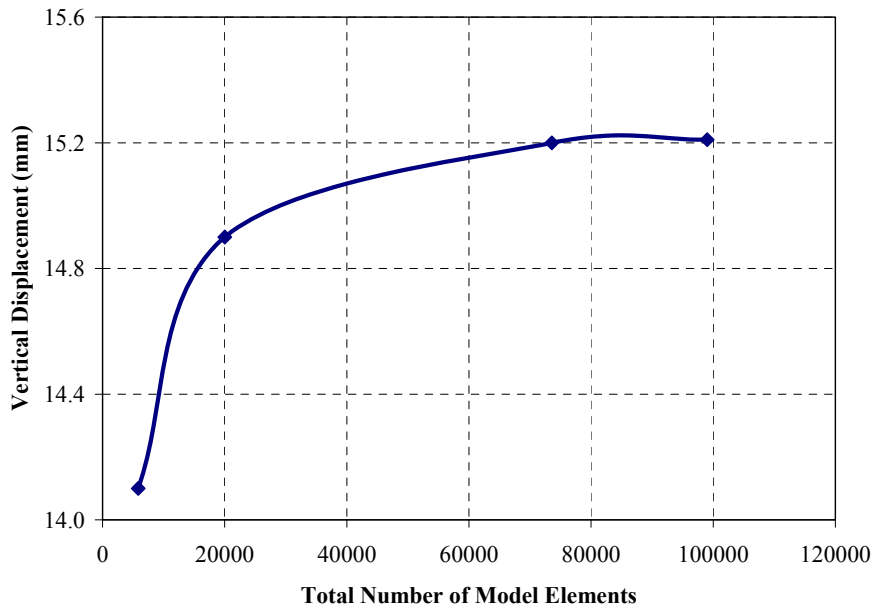


(b) System II

Figure 3.5 Finite Element Models for Systems I and II



(a) System I



(b) System II

Figure 3.6 Vertical Displacement at Mid-Span vs. Total Number of Model Elements

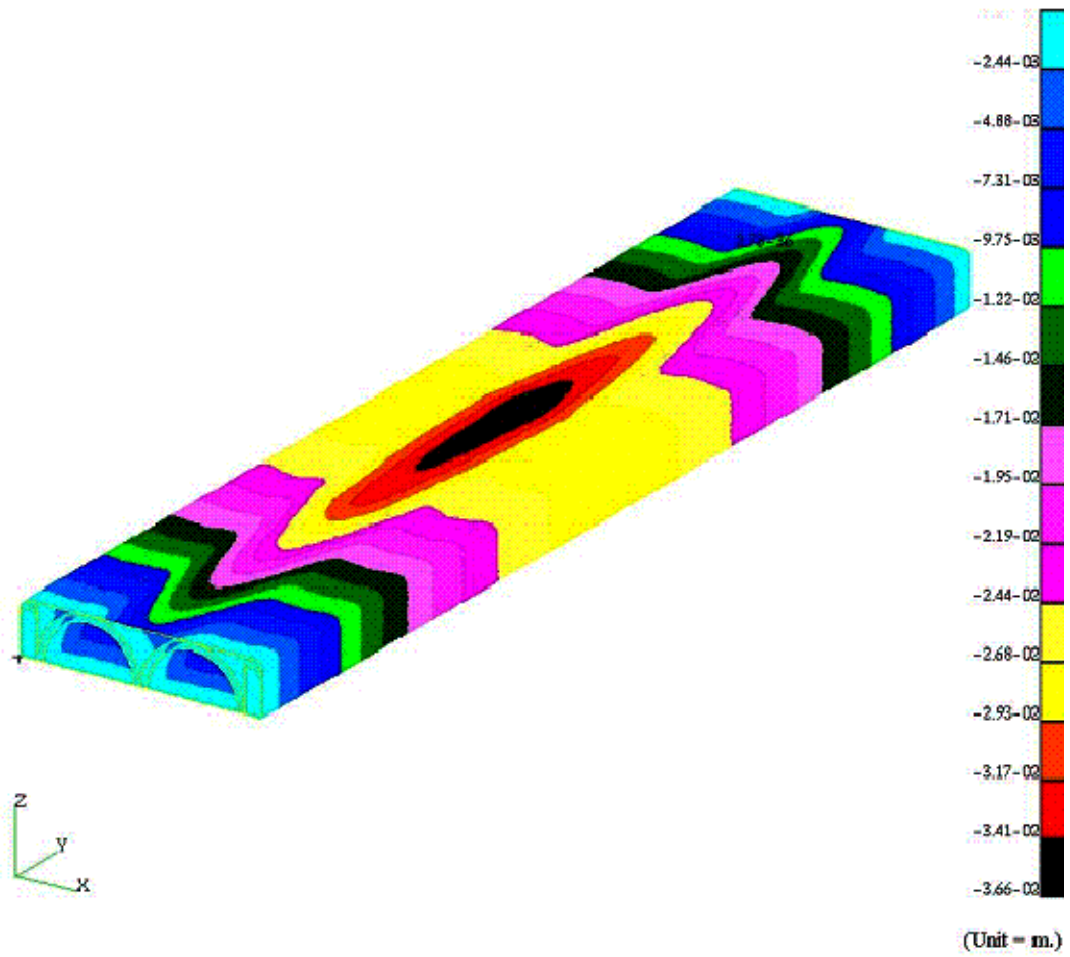
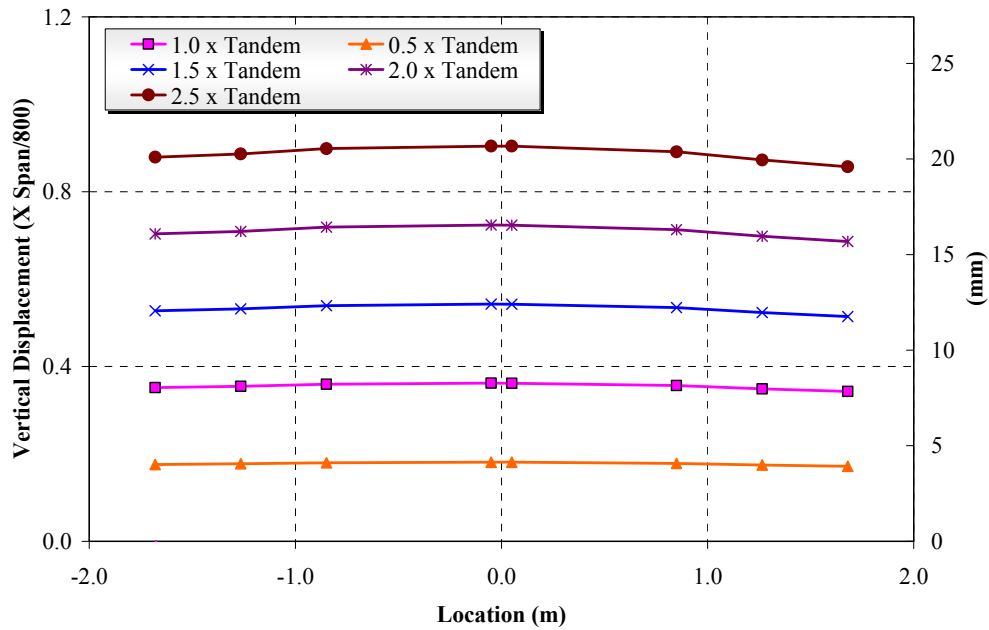
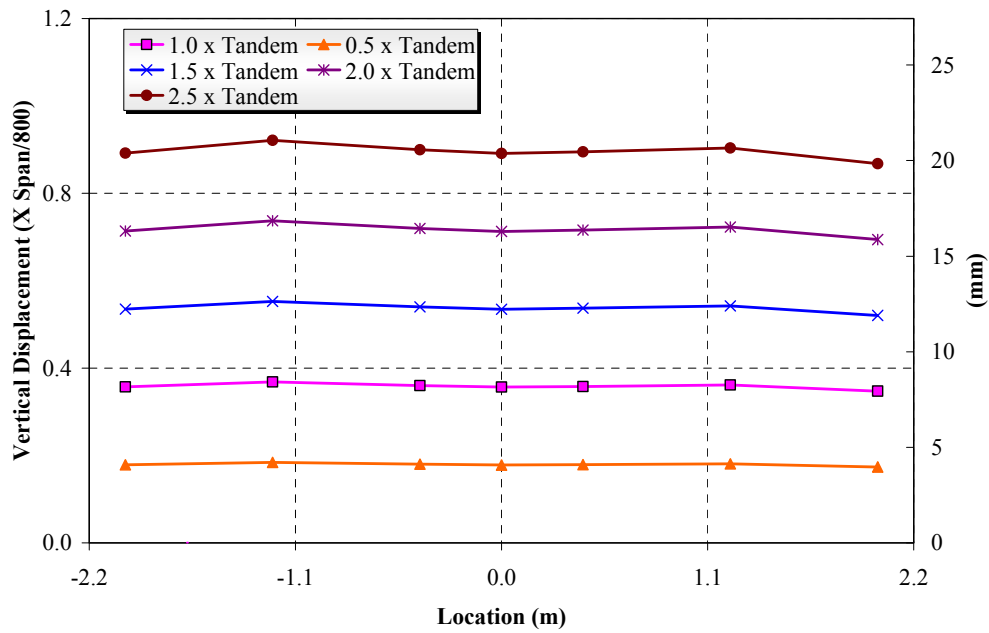


Figure 3.7 Vertical Displacement Contours for the Service I Limit for Bridge System II

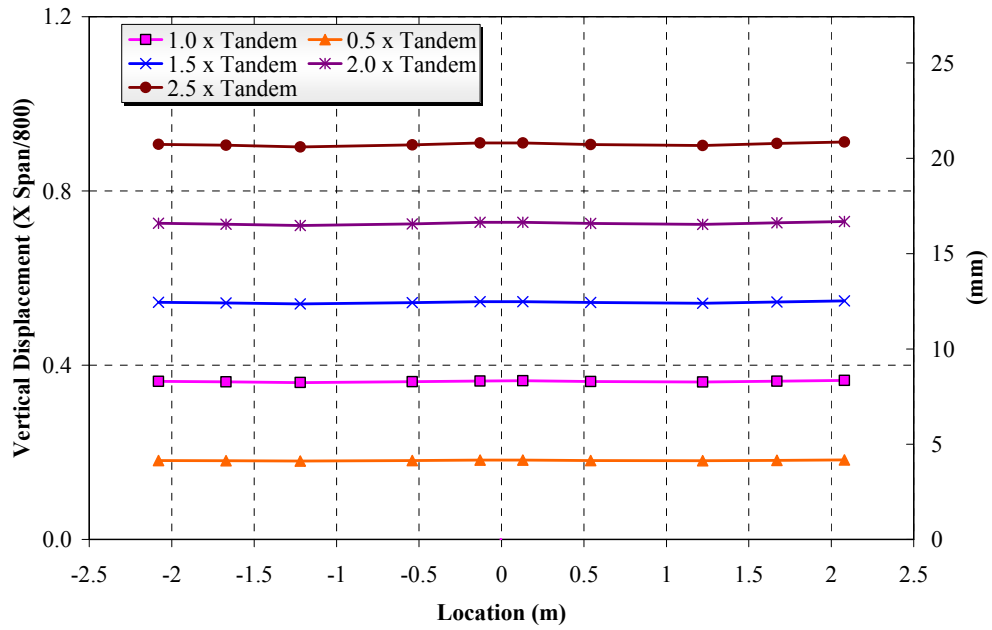


(a) Bottom Surface

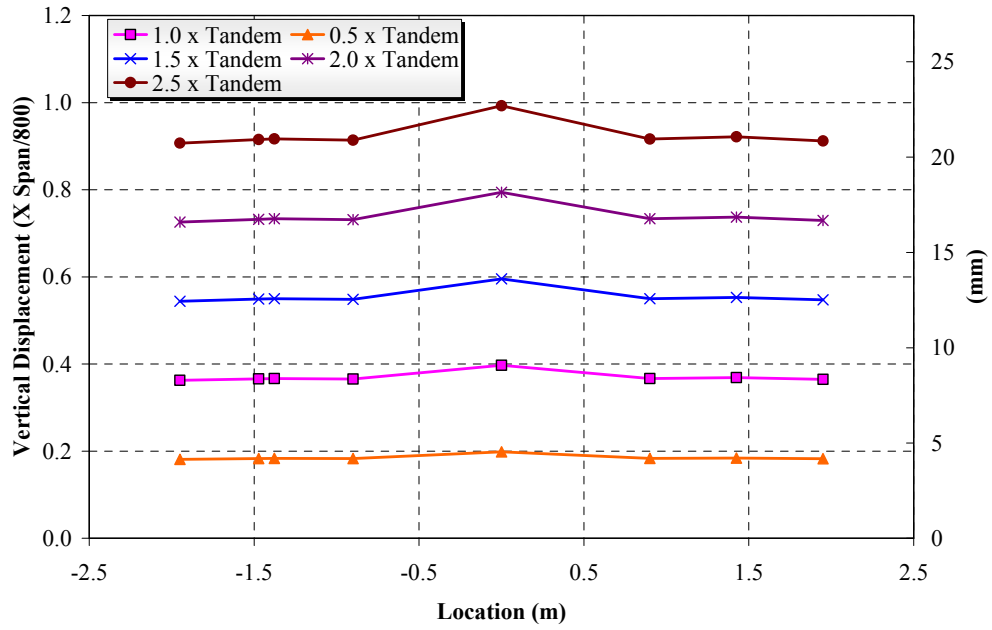


(b) Top Surface

Figure 3.8 Deformed Shapes at Different Load Levels for System I



(a) Bottom Surface



(b) Top Surface

Figure 3.9 Deformed Shapes at Different Load Levels for System II

PRELIMINARY OPTIMIZATION OF HYBRID FRP- CONCRETE BRIDGE SYSTEMS

4.1 STRUCTURAL OPTIMIZATION

Optimization can be defined as the process of finding the conditions that give the maximum or minimum value of a function. It is the act of obtaining the best result under given circumstances. In general, the optimization problem has an objective function, which measures the goodness of the design. The maximization of the goodness is generally performed within some limits that constrain the choice of design. Such limits are called constraints. Finally, the optimization problem has design variables, which are the parameters that change during the design process. Design variables can be continuous or discrete.

Optimization methods can be generally classified in two categories, deterministic and probabilistic. Mathematical programming methods are most prevailing of the first category. Evolutionary algorithms are widely used class of probabilistic methods and in particular evolutionary programming, genetic algorithms and genetic programming. Deterministic methods can be subdivided into two categories, classical solutions of constrained and unconstrained systems, and numerical search techniques. The classical tools are used for finding the maxima and minima of a function. In general, the numerical techniques start with an initial design and proceed in small steps intended to improve the value of the objective function.

Structural optimization has been a topic of interest for over 100 years. As far back as 1890, Maxwell (1890) established some theorems related to rational design of structures, which were further generalized by Michell (1904). Schmit (1960) applied non-linear programming to structural design. Another approach based on optimality criteria were

introduced in the late 1960's. Venkayya (1971) proposed an optimality criterion whereby the minimum-weight of structure is the one in which the strain energy density is constant throughout the structure.

This optimality criterion is applied in this study to develop a preliminary optimization algorithm for both proposed hybrid FRP-concrete bridge deck and superstructure systems. In the following subsection, we will present a brief literature review of current research in FRP structural optimization.

4.2 FRP STRUCTURAL OPTIMIZATION

Optimization of composite structures has gained a lot attention in recent years to reduce the cost and weight of such structures. Ply orientation, ply thickness, stacking sequence, and geometrical variables were usually used as design variables. Several researchers investigated the optimum structural design of FRP structural systems. Fukunaga and Vanerplaats (1991) performed optimum minimum weight design of laminated composite panels under strength and displacement constraints. They used linear approximation for the stress components and displacement components and displacement components; transformed design variables with respect to the layer angles were also introduced to reduce the nonlinearity between the strength constraints and the layer angles. He et al. (2003) investigated an approach using genetic algorithms to minimize the weight of structural components by simultaneously changing the cross sectional shape and ply orientation of the FRP laminates.

Many researchers have applied optimization techniques to the design of composite structures based on mathematical programming methods or optimality criteria methods. Fukunaga (1991) optimized the structural strength by tailoring the layer orientation angle and layer thickness. Aref (1999) investigated an approach using the optimality criteria method combined with the Ritz solution of the transformed plate to minimize the weight of FRP deck system by changing the layer thickness. Other researchers extended their studies to multi-objective optimization. For example, Adali et al. (1996) used the objective weighting method for the pre-buckling, buckling, and post-buckling optimization of laminated plates. Spallino et al (2002) developed a multi-objective optimal design methodology based on evolution strategies and game theory approach.

4.3 OPTIMALITY CRITERIA FORMULATION

Optimality criteria presented in this section was based on derivation by Venkayya (1989) and Khot (1981). The optimization problem takes the general form:

$$\text{Minimize: } f(x) = f(x_1, x_2, \dots, x_n) \quad (4.1)$$

$$\text{Subjected to the constraints: } g_j(x) \geq 0, \quad j = 1, \dots, n_m \quad (4.2)$$

$$h_k = 0, \quad k = 1, \dots, n_l \quad (4.3)$$

where $f(x)$ is the objective function of n variables, g_j are inequality constraints, n_m is the number of inequality constraint; h_k are the equality constraints, and n_l is the number of equality constraints.

The Kuhn-Tucker conditions (Venkayya, 1989; Khot, 1981) state the necessary conditions for a local minimum x^* of the constrained problem using Lagrange multipliers $\lambda_1^*, \dots, \lambda_{n_m}^*$, that is:

$$g_j(x^*) \geq 0, \quad j = 1, \dots, n_m \quad (4.4)$$

$$\lambda_j^* g_j(x^*) \geq 0, \quad j = 1, \dots, n_m \quad (4.5)$$

$$\lambda_j^* \geq 0, \quad j = 1, \dots, n_m \quad (4.6)$$

$$\frac{\partial f}{\partial x_i} - \sum_{j=1}^{n_m} \lambda_j^* \frac{\partial g_j}{\partial x_i} = 0, \quad i = 1, \dots, n \quad (4.7)$$

The necessary condition for a local minimum of the optimization problem with a single constraint can be reformulated as

$$\frac{\partial f}{\partial x_i} - \lambda_j \frac{\partial g_j}{\partial x_i} = 0, \quad i = 1, \dots, n \quad (4.8)$$

Now Eq. 4.8 above can be written as

$$\lambda = \frac{\partial f}{\partial x_i} / \frac{\partial g}{\partial x_i}, \quad i = 1, \dots, n \quad (4.9)$$

In the case of a nonlinear objective function or nonlinear constraints with respect to the design variables, an approximate value of the Lagrange multiplier can be obtained from

$$\lambda = \left[\frac{1}{g_o} \sum_{i=1}^n x_i \frac{\partial g}{\partial x_i} e_i^{1/\eta} \right]^\eta \quad (4.10)$$

and

$$g_o = g + \sum_{i=1}^n x_i \frac{\partial g_j}{\partial x_i} \quad (4.11)$$

where η is a resizing parameter that controls the step size, and e_i is the ratio of the sensitivity derivatives of the constraints and the objective function and can be written as

$$e_i = \frac{\partial g}{\partial x_i} / \frac{\partial f}{\partial x_i}, \quad i = 1, \dots, n \quad (4.12)$$

This was based on imposing a condition on the constraint to be critical at the resized design (Haftka et al. 1990).

When the objective function or constraint is nonlinear with respect to the design variables, a resizing scheme was required to change the size of the design variables until the objective function has converged. The resizing techniques adopted in this study can be written as

$$x_i^{new} = x_i^{old} (\lambda e_i)^{1/\eta}, \quad i = 1, \dots, n \quad (4.13)$$

The resizing steps were repeated until the objective function has converged.

4.4 OPTIMIZATION PROCEDURE FOR HYBRID FRP-CONCRETE BRIDGE SYSTEMS

One of the most important reasons for optimizing FRP composites is to reduce the structural weight. It was assumed herein that the cost is directly related to the weight of the bridge. Therefore, the weight of the hybrid bridge system was used in this study as the objective function with a modification to account for the difference in cost between concrete and GFRP. The weight of concrete was ignored in this study.

The design variables of a hybrid-FRP bridge system include: bridge geometry, number of cells, ply orientation, stacking sequence, ply thickness, and concrete thickness. The design variables were limited in this study to the thickness of the plies in the inner, outer, and most outer tube laminates of the proposed bridge system; the other design variables have pre-assigned values.

Design of a bridge system must be subjected to both stiffness and strength constraints based on the AASHTO specifications (1998). However, since the design of FRP bridge systems is stiffness-driven, a single constraint on the maximum vertical deflection was imposed. The deflection limitation suggested by AASHTO LRFD is

$$\delta_{req.} = \frac{L}{800} \quad (4.14)$$

where L is the span of the bridge.

We can explicitly differentiate both the objective function (weight of FRP-only bridge) and the constraint (the maximum deflection) with respect to the design variables. The constraint in this study can be written as

$$g(t_i) = 1 - \frac{w_{max}}{\delta_{req.}} \quad (4.15)$$

where w_{max} is the maximum vertical displacement.

Beam analysis was presented in this study as the simple methods of evaluation of deflection of the bridge for a given set of design variables. In the process of modeling a bridge as a beam or a plate, cross sectional properties must be determined. Since the hybrid bridge systems shown here were designed only for a simply-supported condition, thus, the following discussions were limited to a simply-supported bridge, and the classical lamination theory (see Appendix A) is the basis of discussion in this section.

It was assumed in the beam analysis that the cross section in the xz plane will not deform. The x , y , and z directions were referred to as longitudinal, transverse, and vertical directions, respectively. The bridge was modeled as a beam with span length, L , effective flexural rigidity, EI_{eff} . Therefore, the evaluation of EI_{eff} is the main task of modeling the bridge superstructure as a beam. Equation calculates the effective bending rigidity.

$$EI_{eff} = \int_{A_y} \bar{E}_y \bar{z}^2 dA \quad (4.16)$$

where $\bar{z} = z - z_{NA}$

The location of neutral axis z_{NA} can be obtained by the following equation.

$$z_{NA} = \frac{\int_{A_y} \bar{E}_y z dA}{\int_{A_y} \bar{E}_y dA} \quad (4.17)$$

The effective engineering properties of a laminate were obtained based on the classical laminate theory (see Appendix A).

The basic optimality criteria algorithm was implemented in a computer program to perform the optimization of the proposed hybrid systems. The flow chart in Figure 4.1 summarizes the main steps presented in this section.

4.5 NUMERICAL RESULTS

The preliminary optimization procedure presented in the previous section was employed to optimize two different proposed FRP bridge systems; the hybrid FRP-concrete bridge superstructure, and the hybrid FRP-concrete bridge deck on steel girder. Just the weight of the FRP composites was used as the objective function. The change in weight over the weight of the previous step was used to check for convergence for a specific tolerance. The tolerance used in this study is 0.0001. The rate of convergence depends on the parameter η . The value of η used in this study is 2.

4.5.1 Optimization of the Proposed Hybrid FRP- Concrete Superstructure

The proposed hybrid bridge superstructure was designed as a simply-supported single span one-lane bridge with a width of 4.267 m (15 ft). The bridge has a length of 18.288 m (60 ft). Following the AASHTO LRFD specifications, the bridge was subjected to design truck load when checking the serviceability limit of the bridge. The location of design truck load was arranged to obtain the maximum deflection as illustrated in Table 3-2. The impact load (IM) was applied to the truck design load and was taken as 33 % of design truck load in our case. The design variables were limited to the thickness of the plies in the inner, outer, and most outer tube laminates.

Table 4-1 shows the thickness and stacking sequence of the optimized hybrid superstructure. The optimization scheme reduced the weight of the superstructure by 35 % from the initial design presented in Chapter 3.

4.5.2 Optimization of the Proposed Hybrid FRP- Concrete Deck on Steel Girder

The proposed bridge is a simply supported steel bridge with a hybrid FRP-concrete deck. The bridge has a length of 6.5 m and a width of 4.06 m. The hybrid bridge deck has a depth of 0.2 m. As seen in Figure 4.2, the hybrid FRP decks were connected to a typical steel bridge. The bridge consists of three W-beam girders (W14 ×74). Each of the three girders was spaced at 1.22 m and there was a deck overhang of 0.304 m at the exterior girders. Shear studs were used to connect the concrete deck to the steel girders thus forming composite structure.

The number of cells of the hybrid deck was not optimized. Instead, the effects of the number of cells on the various properties were examined as shown in Figure 4.3. It is clear that as number of cells increases, both the stiffness and strength increases. The difference between the stiffness and strength of the decks with 21 and 27 cells is small. The number of cells was chosen as 21 cells.

Similar to the optimization of the hybrid superstructure, the proposed hybrid deck was optimized using the optimization procedure outlined in Section 4.4. Table 4-2 shows the thickness and stacking sequence of the optimized hybrid superstructure.

Table 4-1 Thickness and Stacking Sequence of the Optimized Superstructure

| | Stacking Sequence | Thickness (mm) |
|----------------------------------|-----------------------------|-----------------------|
| Inner Tube Laminate | $[0^{\circ}_2]$ | 10.67 |
| Outer Tube Laminate | $[0^{\circ}(45^{\circ})_2]$ | 9.14 |
| Outer- Most Tube Laminate | $[0^{\circ}_4]$ | 16.76 |

Table 4-2 Thickness and Stacking Sequence of the Optimized Deck

| | Stacking Sequence | Thickness (mm) |
|----------------------------------|--------------------------|-----------------------|
| Inner Tube Laminate | $[0^{\circ}_4]$ | 1.524 |
| Outer Tube Laminate | $[0^{\circ}_3]$ | 1.143 |
| Outer- Most Tube Laminate | $[0^{\circ}_5]$ | 1.905 |

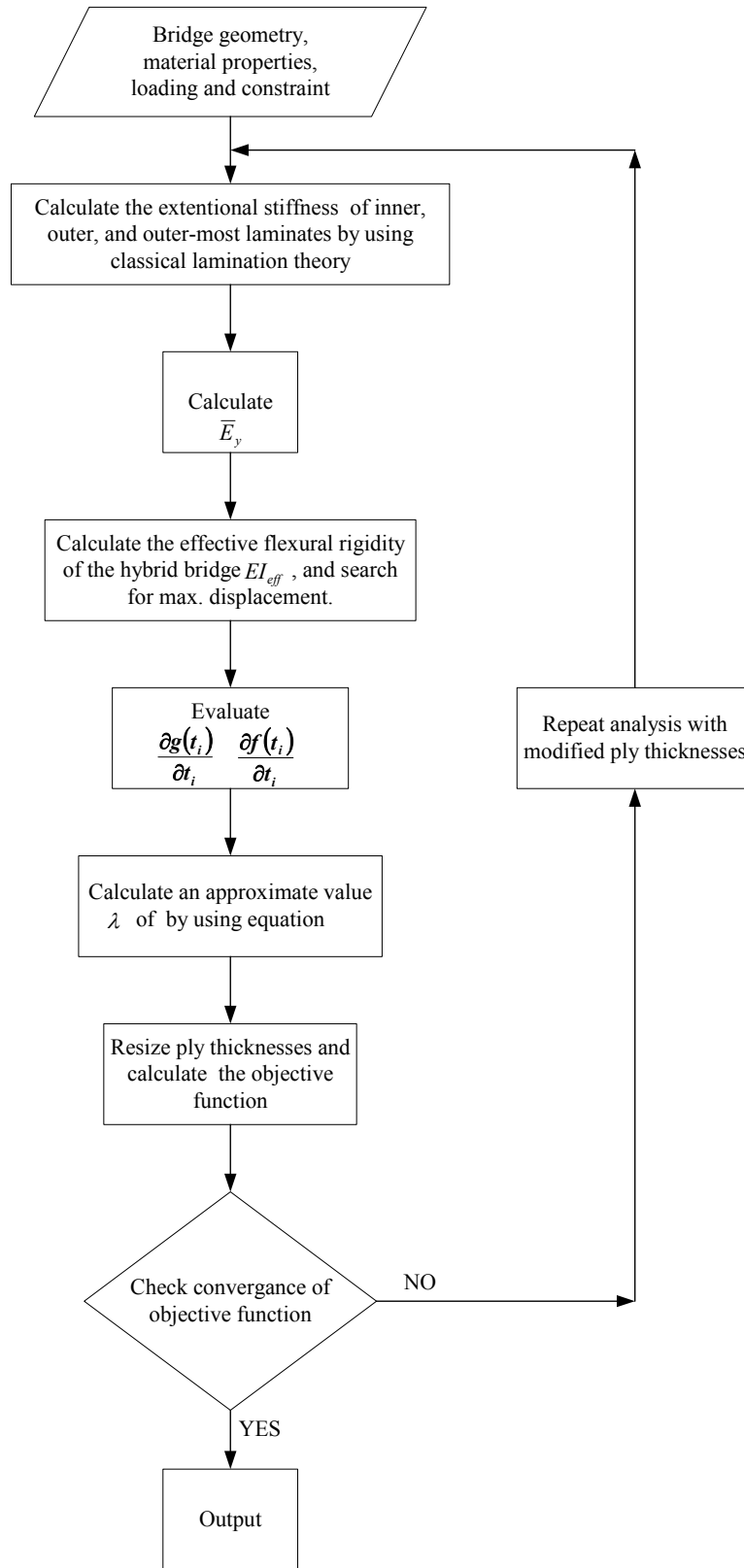
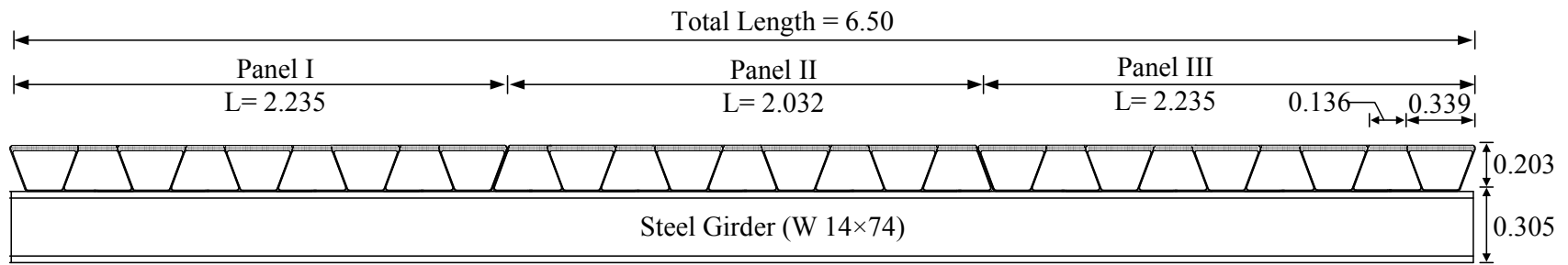
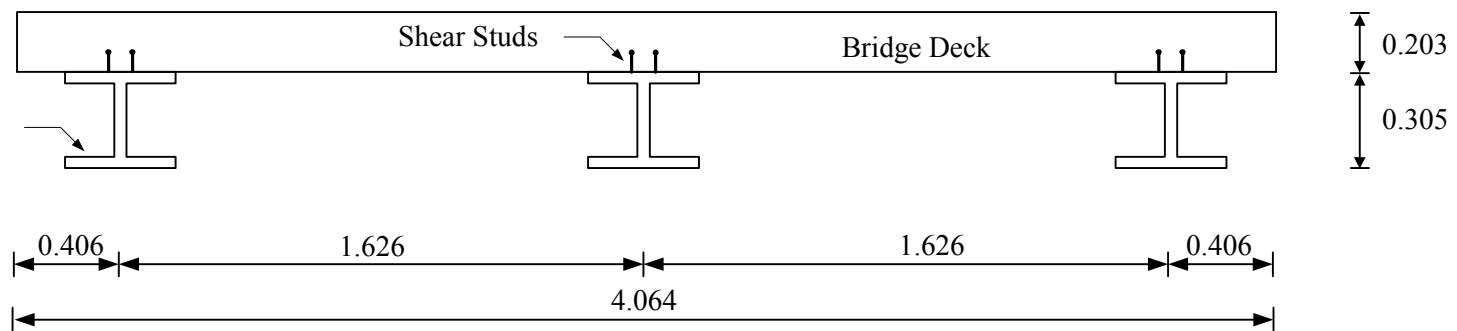


Figure 4.1 Flow Chart for Optimization Procedure



(a) Elevation



(b) Side View

Figure 4.2 Steel Bridge with a Hybrid FRP-Concrete Bridge Deck (dimension in m)

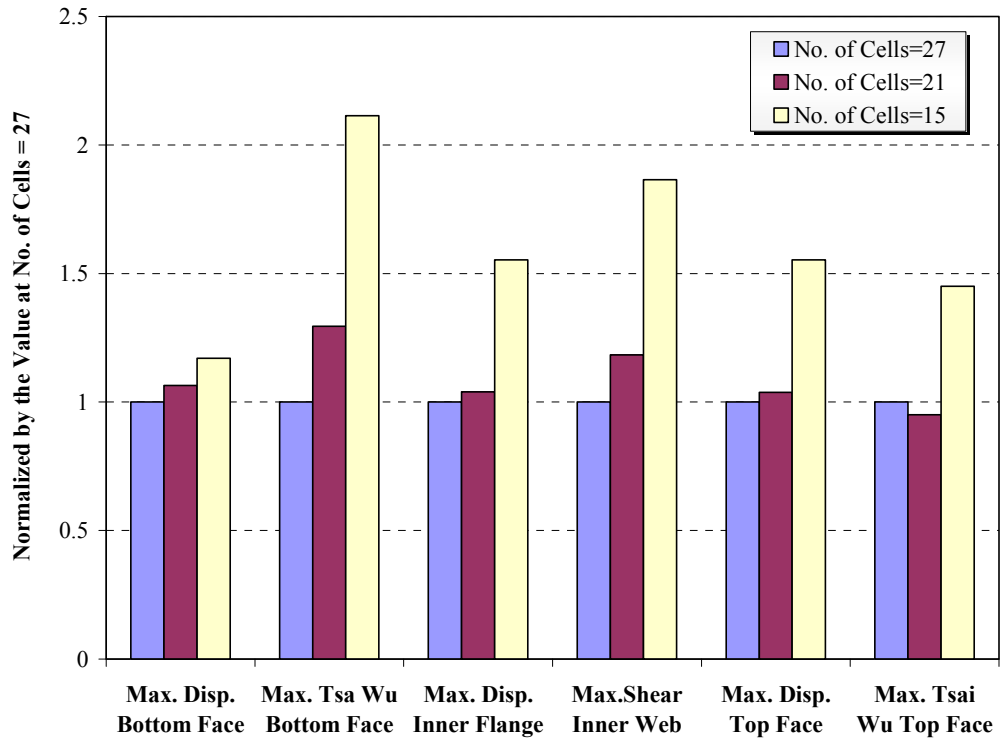


Figure 4.3 Effects of Number of Cells on Hybrid Deck Stiffness and Strength

EXPERIMENTAL STUDY OF HYBRID BRIDGE SUPERSTRUCTURE

In this chapter, the experimental performance of the hybrid bridge superstructure is examined experimentally. The experimental characterization specifications and testing design for the hybrid bridge superstructure is provided. Then, testing results obtained from a series of non-destructive and destructive tests are presented and discussed.

5.1 MATERIALS

5.1.1 Fiber Reinforced Polymers

FRPs consist of two components: fibers and matrix. The fibers possess high strength and modulus and are the main source of load resistance in any composite material. The matrix is the medium in which the fibers were embedded, protecting them from harsh environmental conditions. The predominant fiber types used in composite applications are glass, carbon and organic, while the main resin used is a thermoset matrix. Examples of thermoset matrices include polyesters, vinyl esters, epoxies, and phenolics. Although any of these materials can be used to create composite materials, the study described herein only deals with glass fibers (particularly E-glass fibers) combined with vinyl ester resins. These materials will be discussed in more detail in the following paragraphs.

Fiber glass, in particular, E-glass in the form of a woven fabric was chosen as the reinforcement of FRP because of its low cost even though carbon fiber offers higher strength and stiffness. The style of woven fabric is “Style 7781” in the industry. The weave pattern of this fabric is 8H satin construction, which offers higher strength than other weave styles such as plain and twill weaves. The fabric weighs 0.295 kg/m² and has 213 and 224 yarns per meter in the fill and warp directions, respectively. The

thickness of the fabric is 0.226 mm. The breaking strengths of the fill and warp directions are 40.5 and 42.4 kN/m, respectively.

Vinyl ester resin was chosen as the matrix. The advantage of vinyl ester resins is that it combines the positive aspects of epoxy and polyester. Vinyl ester has the good chemical resistance and the high tensile strength of epoxy resin, as well as the low viscosity and fast cure of polyester resin without the high shrinkage. As electrical and thermal insulation properties are excellent, in addition to its high impact resistance and low permeability to water. Although vinyl ester has only moderate adhesive strength to fibers, it has very good compatibility with glass fiber. When compared to other resins, vinyl ester falls between polyester and epoxy on price, most physical properties, and handling qualities. However, it exceeds both polyester and epoxy in corrosion resistance, temperature resistance, and elongation.

DERAKANE 411, which is one of vinyl ester resins produced by Dow Plastics (1999), was used in this study. DERAKANE vinyl ester resin is a premium-quality thermosetting product that can be used to fabricate a wide range of corrosion-resistant FRP materials by all conventional fabricating techniques such as contact molding, pultrusion, matched die molding, hand lay-up, and filament winding. Typical room temperature properties of the DERAKANE 411 resin are shown in Table 5-1.

5.1.1.1 Composite Manufacturing

Several techniques are available to produce composite components. These include hand lay-up, pultrusion, and filament winding. The hand lay-up method was used in this study. The hand lay-up method of composite production is the oldest method available. Though it does reliably produce the required components, the process can be very slow and labor intensive. The method involves applying successive layers of resin and fiber fabric onto a mold, which dictates the final shape of the component. After each resin-fiber layer is applied, a roller is used to press the resin into the fabric. The roller is not always successful, so voids and resin rich areas are common in components produced by this method.

5.1.1.2 Mechanical Properties of GFRP Laminate

To determine mechanical properties of a laminate made of E-glass woven fabric and vinyl ester, tensile tests were performed using an MTS universal testing machine (see Figure 5.1). The tests were performed under displacement control and the rate of loading was 0.0847 mm/sec. The sampling rate was 1.0 Hz. Tensile tests were performed according to ASTM D3039-76. Three coupons were prepared and tested for both fill, and warp directions. Table 5-2 shows the obtained tensile properties of a lamina. Figure 5.2 shows the measured stress-strain curves for the fill and warp directions. A tensile modulus of elasticity was determined by the chord modulus method. The results for each direction were very consistent. The fill direction has a higher chord modulus of elasticity and ultimate strength than the warp direction by 2% and 13.8%, respectively.

Compressive, and shear tests were performed on the GFRP by the manufacture (An-Cor Industrial Plastics, Inc.) A summary of the GFRP properties is presented in Table 5-3. Since GFRP laminates for the test coupons were fabricated by a hand lay-up process, the obtained fiber volume fraction was not high, which led to relatively low values for modulus of elasticity when compared to the typical values.

5.1.2 Concrete

As cavities that concrete was poured into in the experimental bridge model were small, coarse aggregates were not used in the concrete mix for the experimental bridge model. The maximum aggregate size was 4.75 mm. Type I Portland cement was used in the mix. Super plasticizer, ADVA Flow (Grace Construction Products, 2002a), and shrinkage reducer, Eclipse (Grace Construction Products, 2002b), were added to the mix. The weight proportions of the ingredients in the mix are shown in Table 5-5.

In this study, three cylindrical specimens (101.6 mm in diameter and 203.2 mm in length) were prepared according to ASTM C192/C192M-98. The specimens were moist cured until an age of 28 days after the mixing of concrete. The compressive test of cylindrical specimens was performed after 28 days according to ASTM C39-96. The measured strengths and Young's moduli are shown in Table 5-6; the obtained stress-strain curves are shown in Figure 5.3.

The chord modulus of concrete (ASTM C469) is often used to calculate modulus of elasticity of concrete because it yields a reliable property. The chord modulus is calculated by

$$E_c = \frac{\sigma_2 - \sigma_1}{\varepsilon_2 - 0.00005} \quad (5.1)$$

where

σ_2 : stress corresponding to 40 % of the ultimate load

σ_1 : stress corresponding to the longitudinal strain ε_1 of 0.00005

ε_2 : longitudinal strain corresponding to the stress σ_2

As shown in Table 5-6 the average chord modulus is about 30.5 GPa, which is higher than the modulus of elasticity (24,800 MPa) of normal weight concrete whose compressive strength is 27.5 MPa.

5.1.2.1 Tensile strength of concrete

Cracks in concrete members may be caused by direct tension, flexure, and combination of shear and flexure. The behavior of members often changes abruptly when tensile cracks form. Accordingly, it is important to know the tensile strength of concrete. There are several ways to measure the tensile strength of concrete, none is entirely satisfactory. Direct tensile test, modulus of rupture test, and the split cylinder test can be used to measure the tensile strength of concrete. Direct tensile test was used in this study. It has been made using 6 dumbbell-shaped specimens held in special grips. The measured tensile strengths are shown in Table 5-7.

5.2 TEST SPECIMEN

5.2.1 Superstructure Model Configuration

The test specimen is a one-fourth scale model of the 18.288 m hybrid FRP-concrete bridge superstructure. The specimen (FRP part only) was fabricated at An-Cor Industrial Plastics, Inc. in N. Tonawanda, NY. The proposed hybrid FRP-concrete model is a simply supported, single span with a width of 1.067 m, and a depth of 0.275m. The bridge model has a length 4.572 m. The model is comprised of trapezoidal cross-sections

surrounded by an outer shell, as shown in Figure 5.4. Each trapezoidal section consists of two layers of laminates: the inner tube laminate and the outer tube laminate. Each trapezoidal box section was fabricated individually by the hand lay-up process (see Figure 5.5). Three trapezoidal sections were these assembled together by using vacuum bag process as shown in Figure 5.6. By covering the three trapezoidal sections with bagging film and applying a vacuum inside the bag, a better quality product results. A layer of glass fiber chopped strand mat wetted with vinyl ester resin was applied between box sections as a bonding material (see Figure 5.7). The three trapezoidal sections were wrapped with the outer-most laminate. Table 5-4 summarizes the thickness and stacking sequence of the different layers of superstructure model. After measuring the actual thickness of the specimen using an ultrasonic thickness measurement device, it was found that the thickness of the inner flange of the east side of the specimen was less than the required thickness by 20 %.

To achieve good composite action between GFRP laminates and concrete, shear keys, as shown in Figure 5.8, were staggered at the interface of GFRP laminates and concrete. Each shear key has a length of 0.275 m for the side trapezoidal section and 0.145 m for the middle trapezoidal section in the transverse direction. They were installed on the top surface of the inner tube laminate and on the bottom surface of the outer tube laminate with an interval of 0.762 m. These shear keys are also made of GFRP composites.

5.2.2 Scaling Factors

A scaling factor, λ , is a ratio of a prototype property of to that of the laboratory specimen model. A length scale factor of 4.0 was chosen. Since the same materials were to be used for the prototype and the specimen, the scaling factors for material properties (e.g., Young's moduli, density, and so on) should be 1.0. With these conditions, other scaling factors are calculated according to the similitude law as shown in Table 5-8. Since the experiment will be performed in the same gravity field, the scaling factor for gravity must be 1.0, which leads to a contradiction between a scaling factor of force and that of gravity force. Eq. 5.2 calculates the provided scaling factor of gravity force.

$$\lambda_{GravityForce} = \lambda_{Mass} \times \lambda_g = n^3 \quad (5.2)$$

Therefore, the gravity force will be five times smaller for the specimen than what it should be and will not be represented accurately in this study. This difference can be adjusted by placing an additional weight of four times the total weight on the specimen. However, since the behavior under live loads is the primarily of our interest, no adjustment for this difference was made in this study.

5.3 EXPERIMENTAL SET-UP

Figure 5.9 shows the supports setup for quasi-static positive moment flexural test. The test specimen was supported by steel girders at its two ends. The support length is 0.305 m for both sides. Elastomeric bearing pads were placed on the steel girders to allow rotation at supports and to protect the bottom surface of the specimen from damage. Loads were applied vertically to the top surface of the test specimen by compression stack beam from the actuators attached to the strong floor. In the transverse direction, the actuators were stabilized by a steel box as shown in Figure 5.10. The load configuration simulates the tandem load specified in the AASHTO LRFD Bridge Design Specifications (1998). The design tandem load is defined as a live load that has two axles of 110 kN. One axle is 1.2 m away from the other. Each axle has two tires that are 1.8 m apart center-to center. Each tire area is 0.510 m wide and 250 m long. For the one-fourth scale model, this design tandem load becomes two axles of 6.875 kN, 0.30 m apart. Two tires of each axle are 0.45 m apart and each tire area is 0.1275 m wide and 0.625 m long. To simulate the tire areas, four GFRP plates with the same area as the scaled tire area were attached to the bottom face of the spreader beams (see Figure 5.11).

5.4 EXPERIMENTAL PROTOCOL

The main objective of the experimental protocol is to determine the structural behavior of the hybrid bridge superstructure subjected to a series of non-destructive and destructive tests. The testing protocol was organized into two phases. The first phase involved a series of non-destructive tests to obtain the structural characteristics in the elastic range under different loading conditions. The second phase involved destructive tests to investigate the capacity of the specimen.

5.4.1 Non Destructive Test

5.4.1.1 Positive Flexural Test (FRP-only Specimen)

Before concrete was poured into the cavities of the FRP-only specimen, the specimen was tested in flexure to examine its flexural behavior without concrete. The test was performed under displacement control. The maximum displacement applied was $L/800$, where L is the span length. The specimen was instrumented with potentiometer and strain gages at various locations to measure displacement and strain, respectively. Figure 5.12 shows the instrumentation layout for positive flexural test.

5.4.1.2 Positive Flexural Test (Hybrid FRP-Concrete Specimen)

After completion of the positive moment flexural loading test on the FRP-only specimen, concrete was cast into the cavities. The specimen was stood on end, and the concrete was poured from the top. Because the inner flange at the east side of the specimen was thinner than the target thickness, buckling of that inner flange was noticed under the pressure of the wet concrete. Subsequently, wood formwork was placed in the other two inner cells along the span of the specimen to prevent buckling of the inner flange. The inner flange of these two cells did not experience any buckling. The average thickness of the concrete layer in the east side of the specimen due to the inner flange buckling increased by 37 mm.

Since the GFRP laminates were translucent, light could pass through them. However, light cannot pass through concrete. By detecting the lights that passed through the top flange of the specimen, it was checked that the cavities were filled with concrete completely. The hybrid specimen was then, tested by the positive flexural and off-axis flexural loadings. An eccentricity of 100 mm was used to test the off-axis flexural behavior of the specimen. Figure 5.13 (a) and (b) show the loading configurations for the positive flexural and off-axis flexural loadings. These tests were also performed under displacement control. Figure 5.12 shows the instrumentation layout for these tests. Both displacement and strain were measured. Unidirectional, 2-directional rosette, and 3-directional rosette strain gages were used for strain measurements. Linear Variable Displacement Transducers (LVDTs) and portable coordinate measurement machine (Krypton) were used for displacement measurements. Krypton (KRY) is K600 Portable

Coordinate Tracking and Measurement System manufactured by Krypton Industrial Metrology capable of measuring 6 degree-of-freedom using a minimum of 3 light emitting diodes (LED) on a rigid body or 3 degree-of-freedom for a single LED at a maximum sample rate equal to 3000 divided the number of LEDs. The layout of the LEDs on the top surface of the specimen is shown in Figure 5.14

5.4.1.3 Negative Flexural Test

There is no published information that specifically relates to an experimental investigation of the negative moment region of hybrid FRP-concrete bridge superstructures. The test specimen was tested under negative flexural loadings to examine its resistance to negative moments. The loading configuration is shown in Figure 5.13 (c). The test specimen was supported by steel girder at its center. The support length was 0.305 m. Elastomeric bearing pads were placed on steel girders to allow rotation at supports and to protect the bottom surface of the specimen from damage. The north end of the specimen was tied between two beams as shown in Figure 5.17(b). Dewidag bars were used to connect the tie-down beam to the strong floor.

Figure 5.17 shows the supports setup for quasi-static negative moment flexural test. Loads were applied vertically to the top south-end surface of the test specimen by compression stack beam from the actuators attached to the strong floor. The specimen was instrumented with potentiometer and strain gages at various locations to measure displacements and strains, respectively. Figure 5.18 shows the instrumentation layout for negative moment flexural test. LVDTs and the KRY system were used for displacement measurements. The layout of LEDs on the top surface of the specimen is shown in Figure 5.15.

5.4.2 Destructive Tests

5.4.2.1 Positive Flexural Test

After the completion of the non-destructive tests, the specimen was tested in flexure to failure to examine its strength and failure modes. The loading configuration is shown in Figure 5.13 (a). This test was performed under displacement control and was divided into three stages: stage I, stage II, and stage III. The displacement steps are

shown in Figure 5.19. In all stages, displacement history was applied; three cycles were applied for each displacement. The displacement was increased until the specimen failed. The instrumentation layout is what shown in Figure 5.12

5.4.2.2 Shear Test

The purpose of the shear test was to investigate the bridge behavior under shear loading. An undamaged portion of the specimen from the flexural test was used for the shear test. The span length of the portion used in this test was 2311 mm. The south tire patch was 305 mm away from the south support line. This 305 mm-long section between the support and the tire patches was subjected to the maximum shear force. The shear load configuration is shown in Figure 5.20(d). The test was performed under displacement control. The displacement was applied monotonically until the load reached 311 kN, which was the capacity of the load cell. The instrumentation layout for this test is shown in Figure 5.21. Although there was no way to guarantee that the portion of the specimen sustained no damage, it was judged undamaged because load effects that the portion had experienced were not large enough and visual inspection did not find any damage. The bond between the concrete and GFRP in this portion was assumed to be in good condition.

5.5 TEST RESULTS

5.5.1 Non Destructive Tests

5.5.1.1 Positive Moment Flexural Load (FRP-Only Specimen)

No sound of cracking of GFRP was heard during the flexural loading on the FRP-only specimen. Visual inspection after the test revealed no cracking in the exterior GFRP laminates. When the load is applied to the test specimen, the elastomeric bearing pads deform. Therefore, the measured displacement is equal to the deflection of the test specimen plus the deformation of the bearing pad. To obtain actual deflection of the bridge model, the vertical deformation of the bearing pads should be subtracted from displacement measured on the specimen. As an example of what Figure 5.22 shows the

measured force-displacement response of the elastomeric pad during the flexural test of the hybrid specimen.

Figure 5.23 and Figure 5.24 show the force-displacement relationships obtained at the bottom surface at different locations of the specimen, and the top surface at section F, respectively (refer to Figure 5.12 for measurement locations). The force-displacement responses from E-BOT-W, and F-TOP-W presented in Figure 5.23 and Figure 5.24 show the initial stiffness is lower than that of the higher load region. This behavior can be explained as follows. The loading system that consists of the actuator, the wall beam, the spreader beams, and the tire patches was not connected to the surface of the specimen in the test setup. In addition, the top surface of the specimen was not perfectly flat. Therefore, there might have been small gaps between the specimen and tire patches when the loading began. These gaps could cause the lower initial stiffness until the loading system gets fully engaged. The measured force-displacement responses were almost linear. The force-displacement response from F-TOP-W depicted in Figure 5.24 (a), show larger hysteresis loops than those from other locations. This is because of potentiometer used at that location was not sufficiently calibrated.

Deformed shapes of the bottom and top surfaces of the specimen are shown in Figure 5.25 (a) and (b). In these figures, the vertical axis represents the vertical downward displacement; therefore, the actual deformed shapes should be up-side-down. It can be observed in Figure 5.25(b) that the displacement was largest at the point close to the loading point. This local deformation was expected, and it is expected to disappear or become much smaller after concrete is cast into the specimen. The measured deformed shape of both the bottom and the top surfaces look uniform and the shape was symmetrical about the center point. All the plots show nearly linear relationships between force and displacement. Also, it can be observed in Figure 5.25(a) that the displacement was largest at the point E-BOT-C. This local deformation was not expected, and there was 0.5 mm of difference in the displacement at the two locations next to each other. Again, this would have been caused by calibration problems of potentiometer at this location.

5.5.1.2 Positive Moment Flexural Load (Hybrid FRP Concrete Specimen)

Visual inspection after the test revealed no evidence of cracks or delamination in the exterior GFRP laminates. Figure 5.26, Figure 5.27, and Figure 5.28 show deformed shapes of the top surface at different load levels for sections I, H, G, E, and F (refer to Figure 12 for measurement locations). All the plots show nearly linear relationships between force and displacement. The deformed shapes of the bottom surface, as shown in Figure 5.28(a) do not have as large a variation as that of the FRP-only specimen. This also confirmed that the variation seen in the FRP-only result had been caused by the insufficient calibration of the potentiometers.

To verify the advantages of use of concrete, Figure 5.29 compares the deformed shapes of the bottom and top surfaces at load level = $0.5 \times$ tandem for both the FRP-only and hybrid specimens. As can be observed in this figure, the stiffness of the hybrid specimen became much higher than that of the FRP-only specimen. The average displacement of the bottom surface was used to calculate the secant stiffness of both the hybrid and the FRP-only specimens. The stiffness of the hybrid specimen is 35 % higher than that of the FRP-only specimen, which shows the effectiveness of concrete. In addition, the local deformation under the loading point was dramatically reduced as depicted in Figure 5.29(b). This is an additional advantage of this hybrid bridge design.

According to AASHTO (1998), the maximum deflection under $(1+IM) \times$ truck load is recommended to be smaller than $L/800 = 5.76$ mm, where L is the span length. However, $(1+IM) \times$ tandem load was used for comparison since the loading configuration in the test simulates the tandem load. One can see from Figure 5.28(a) that the deformation at the midspan of the specimen measured at E-BOT-C due to $(1+IM) \times$ tandem load was 3.86 mm ($0.67 \times L/800$). It can be concluded that the hybrid specimen satisfied the AASHTO live load deflection recommendation.

Figure 5.30 and Figure 5.31 show the measured strains on the exterior web at Sections E and H. These figures show that plane sections before deformation remains plane after deformation. The location of the neutral axis obtained from the test was shifted upward due to the concrete layer in the compression zone. As shown in Figure 5.31, the strain results indicate a linear variation of strain along the exterior web at section H except for

strains obtained at HW1L (see Figure 5.12 for the location). The unexpectedly small strain at HW1L may be caused because the gauge was not bonded to the surface properly. Longitudinal strain variations along the centerline of the top and bottom surfaces are shown in Figure 5.32 and Figure 5.33. In Figure 5.32, the measured strain at the top surface looks uniform and the shape was approximately symmetrical about the center point. Figure 5.34 and Figure 5.35 show the measured longitudinal and transverse strains at Section E (midspan), respectively. Figure 5.34 shows that the longitudinal strain does not vary among the cross section; whereas Figure 5.35 shows that the transverse strain varies dramatically in the section because Section E is very close to the loading points.

5.5.1.3 Off-Axis Positive Flexural Load

The measured deformed shapes of the top and bottom surfaces at different load levels are shown in Figure 5.36. The data show that the three trapezoidal box sections acted compositely under such a loading condition: the bond between the trapezoidal sections was sufficiently strong to enable composite action. It can be clearly seen in Figure 5.36 that the three trapezoidal sections twisted as one unit. This makes the torsional rigidity of this structure high, which is another advantage of this design.

Figure 5.37 and Figure 5.38 show the measured strains on the west exterior web at Sections E, and H. The strains measured on the west web were smaller in this test than those in the flexural test (see Figure 5.30 and Figure 5.31). This is because the vertical deflection of the west web was smaller than that of the east web as can be seen in Figure 5.36.

Figure 5.39 show the longitudinal strains measured along the centerline at top surface of the deck. At the load level of $1\times$ tandem load, the obtained strains measured at location ETCL demonstrated an excellent correlation with those from the positive moment flexural test. The maximum differences are only 6 %. This confirms that the measurement system was consistent. Figure 5.41 and Figure 5.42 show the measured longitudinal and transverse strains at Section E (midspan), respectively. Figure 5.41 shows that the longitudinal strain varies along the cross section E. Strains measured on the west side were smaller than those on the east side. This is because the vertical

deflection of the west web was smaller than that of the east web as can be seen in Figure 5.36 due to the off-axis loading.

5.5.1.4 Negative Flexural Load

No sound of cracking of concrete was heard during the negative flexural loading of the hybrid specimen under service load level. Visual inspection after the test revealed no evidence of cracks or delamination in the exterior GFRP laminates. Figure 5.43 and Figure 5.44 show the force-displacement relationships obtained at the bottom surface at different locations along the specimen, and the top surface of section L, respectively (refer to Figure 5.18 for measurement locations). KRY was used for displacement measurements at the top surface at section B, C and D (refer to Figure 5.15 for measurement locations). Figure 5.45 shows the force-displacement relationships obtained at the top surface at section B, C and D. The deformed shapes of the top and bottom surfaces are shown in Figure 5.46(a) and (b). The measured deformed shape of both the bottom and the top surfaces were uniform and the shape was symmetrical about the center point. All the plots show near linear relationships between force and displacement. The specimen experienced a relatively large displacement ($1.3 \times L/800$) when it was subjected to a small force ($0.5 \times$ tandem load). In this case, a consideration to increase the bending rigidity of the specimen to satisfy the AASHTO live load deflection limit should be investigated.

Longitudinal strain variations along the centerline of the top surfaces are shown in Figure 5.47. It can be seen that the maximum negative strain that occurs at the top surface at section E is much less than the ultimate strain of GFRP composites. That show the design of the hybrid FRP-concrete bridge superstructure under negative flexural moment is also found to be stiffness- driven instead of strength-driven. Figure 5.48 show the measured longitudinal strains at Section E (midspan). It shows that the longitudinal strain varies slightly along the cross section. The minor difference in strain about the center point is due to the unsymmetrical geometry of the specimen around the center point. Since the concrete thickness of the east side of the specimen is slightly greater than that on the west side, the flexural rigidity of the west side is smaller and the location of the neutral axis is lower, which led to smaller longitudinal strain on the top surface at the west side.

5.5.2 Destructive Tests

5.5.2.1 Positive Flexural Load

Figure 5.49 and Figure 5.50 show force-displacement responses obtained at the bottom and top surfaces during the destructive flexure loading, respectively. The displacement protocol shown in Figure 5.19 was used for the test. Instead of showing the entire force-displacement histories, envelopes of the obtained responses for certain stages of loading are shown in Figure 5.49 and Figure 5.50. Upon completion of the loading stage III-cycle-1, where the applied load reached $17.1 \times \text{tandem load}$, the LVDT were removed from beneath the specimen to avoid transducer damage. As a result, the force-displacement response at the bottom surface of the specimen does not show the failure point of the specimen seen in Figure 5.49. During the loading stage III-cycle-2, there was a loud sound that came from the cracking of concrete under the loading points. This is a local failure mode. The sudden change of stiffness can be seen in Figure 5.50 at that load level. This load is 6.3 times the AASHTO requirement of $1.75(1+IM) \times \text{tandem load}$ for live loads in the strength limit I state. Since the dead load and other live loads were not considered appropriately in this test, 6.3 cannot be called the safety factor. After the concrete cracked under the loading points, the local deformation of the top surface increased. The force-displacement curves shown in Figure 5.50 from loading stage III-cycle-2 show a decrease in the stiffness of the specimen compared to loading stage I and II. This would be because of the degradation in the stiffness of concrete, and delamination of GFRP composites under the earlier loading stages. In addition, nonlinear behavior of the specimen is seen in a high strain range as shown in Figure 5.49 and Figure 5.50. That is because the hybrid bridge specimen consists of GFRP and concrete. Both GFRP and concrete used in this study were shown to behave nonlinearly in a high strain range. A global failure mode was obtained at $20.8 \times \text{tandem load}$, which is 9.0 times the $1.75(1+IM) \times \text{tandem load}$, which is 9.0 times the AASHTO requirement for live loads in the strength limit I state.

At failure, the concrete crushed in compression and the top GFRP flange and the interior GFRP flange failed in compression, followed by the failure of webs in compression as shown in Figure 5.51. The bottom GFRP flange remained intact. The failure mechanism

can be described as follows: 1) the concrete fails in compression and the GFRP flanges resist the compressive force that was originally carried by concrete, 2) the GFRP compression flanges fail in compression when the compressive stress reaches the compressive strength; the failure was sudden due to the nature of GFRP composites. Crushing of concrete, compressive failure of the GFRP top flange, buckling failure of the GFRP interior flange, and significant delamination of GFRP laminates were observed at the failure section as shown in Figure 5.51.

KRY was used for displacement measurements on the top surface at section I, H, G and F (refer to Figure 5.14 for measurement locations). Figure 5.53 shows the deformed shapes of the top surface at section I, H, G and F. Upon completion of loading stage III-cycle-1, at which the applied load reached $17.1 \times$ tandem load, the LEDs were removed from top surface of the specimen. The deformed shapes shown in Figure 5.53 are uniform and the shape was symmetrical about the center point. All the plots show near linear relationships between force and displacement up to an applied load reached $15 \times$ tandem loads.

Figure 5.54 and Figure 5.55 show the measured strains on the exterior web at Sections E and H, respectively. Again, a linear variation of longitudinal strains over the height of the specimen was observed together with a little downward shift of the neutral axis. As noted in section 5.4.1.2, the unexpectedly small strain at HW1L was likely a result of the gauge not being bonded properly to the surface (see Figure 5.12 for the location). Variations in the longitudinal strain along the centerline of the top and bottom surfaces are shown in Figure 5.56 and Figure 5.57, respectively. Figure 5.58 shows the measured longitudinal strains at Section E (midspan).

Table 5-9 shows the measured maximum strains at selected locations (see Figure 5.12 for the gauge locations). Also, a ratio of the obtained maximum strain to the averaged ultimate strain obtained from the material tests is included in the table. When the measured strain is positive, the ratio is calculated with the ultimate tensile strain. The ratio is calculated with the ultimate compressive strain when the measured strain is negative. It turned out that the ratios are very small, the maximum of being 0.18. This maximum value was obtained at EW1L. The maximum value of the compressive strain was obtained at ETCL. The ratio at ETCL was 0.130.

After the test, visual inspection showed slippage between GFRP and concrete only (see Figure 5.51) at the middle section of the specimen, which implies that good composite action of GFRP and concrete was achieved only on the outer boxes of the specimen. This would be caused by deficiency of the manufacturing of the shear keys in the middle section by the manufactures.

5.5.2.2 Shear Load

The deformed shapes of the top and bottom surfaces are shown in Figure 5.59(a) and (b). The local deformation under the GFRP loading pads became large due to cracking of concrete. When the load level reaches about $35 \times$ tandem load, the swivel shifted toward the west side of the specimen and the spreader beams contacted the top surface of the west side of the test specimen (see Figure 5.60(b)). Also, the flange of the spread beam twisted because of the eccentricity of the load toward the west side of the specimen as shown in Figure 5.60(a). The loading was stopped at this stage for safety reasons, and the spreader beam was replaced. The specimen was then loaded to failure. The shear failure of the specimen was obtained at load level about $35 \times$ tandem load. At failure, the GFRP web failed close to the support due to the shear force as shown in Figure 5.60(e). A potentiometer at P-TOP-W (see Figure 5.21 for the location) work poorly when the load level reached $30 \times$ tandem loads. The displacement measured at the bottom surface as shown in Figure 5.59(b) was much smaller than that at the top surface. The displacement at the bottom surface increased in a stable manner as the applied load increased.

Figure 5.61 shows the shear strains obtained at the exterior web at Section M (see Figure 5.21 for the location). The maximum shear strain obtained was 4529μ , which is much smaller than the strain in the nonlinear range of the shear stress-strain curve obtained from the manufacturer. The variation of longitudinal strain along the centerline of the bottom surface is shown in Figure 5.62. The maximum strain obtained at NBCL was 2785μ at NBCL.

Punching shear failure initiated at the top surface under the GFRP loading pads, followed by the shear failure of webs as shown in Figure 5.60. Failure then occurred at the interface between the bottom GFRP flange and the interior and exterior webs. However,

the bottom GFRP flange remained intact. This failure mode is considered to be favorable because it did not lead to the collapse of the entire bridge.

5.6 SUMMARY

The superstructure specimen was subjected to a series of non-destructive and destructive quasi-static loading tests. The tests results demonstrated the excellent performance of the hybrid FRP-concrete bridge superstructure. The measured force-displacement responses were nearly linear under design loads. The maximum deflection of the specimen due to $(1+IM)\times$ tandem load was 3.86 mm ($0.67\times L/800$). The specimen easily satisfied the AASHTO live load deflection limit. The destructive tests examined the capacity of the specimen. When the applied load is increased as point loads, a local failure mode appears before a global failure mode. Concrete under the tire patches cracks at the bottom due to the bending in the transverse direction, and then, GFRP laminates fail in shear or bending as the load increases. This load is 6.3 times the AASHTO requirement of $1.75(1+IM)\times$ tandem load for live loads in the strength limit I state. A global failure mode was obtained at $20.8\times$ tandem load, which is 9.0 times the $1.75(1+IM)\times$ tandem load. At failure, concrete was crushed in compression, and the top GFRP flange and the interior GFRP flange failed in compression, followed by the failure of webs in compression. The bottom GFRP flange was, however, intact. The failure mechanism can be described as follows. Concrete fails in compression first, and then GFRP flanges have to take over the compressive force that was originally carried by concrete. GFRP compression flanges fail in compression when the compressive stress reaches the compressive strength.

Table 5-1 Typical Properties of DERAKANE 411 at Room Temperature (Dow Plastics, 1999)

| Properties | |
|-------------------------------------------------|------------------------|
| Tensile modulus (GPa) | 3.379 |
| Tensile strength (MPa) | 75.84 - 82.74 |
| Elongation (%) | 5.00 - 8.00 |
| Flexural modulus (MPa) | 3.103 |
| Flexural strength (MPa) | 110.3 - 124.1 |
| Poisson's ratio | 0.30 - 0.38 |
| Specific gravity of liquid | 1.04 |
| Specific gravity of solid | 1.126 |
| Cure shrinkage (%) | 8.30 |
| Coefficient of thermal expansion (m/m/degree C) | 64.80×10^{-6} |

Table 5-2 Tensile Properties of GFRP

| Direction | Coupon | Modulus of Elasticity (GPa) | Tensile Strength (MPa) | Ultimate Strain |
|------------------|----------------|------------------------------------|-------------------------------|------------------------|
| Fill | Fill-1 | 16.38 | 339.64 | 0.0267 |
| | Fill-2 | 16.02 | 339.64 | 0.0267 |
| | Fill-3 | 16.21 | 339.50 | 0.0267 |
| | Average | 16.20 | 339.57 | 0.0267 |
| Warp | Warp-1 | 15.48 | 299.72 | 0.0262 |
| | Warp-2 | 16.19 | 285.44 | 0.0232 |
| | Warp-3 | 15.96 | 293.30 | 0.0255 |
| | Average | 15.88 | 292.82 | 0.0250 |

Table 5-3 Summary of GFRP Mechanical Properties (An Cor Industrial Plastics, Inc)

| Test Type | Dir. | Modulus of Elasticity (GPa) | Poisson's Ratio | Strength (MPa) | Ultimate Strain |
|------------------|-------------|------------------------------------|------------------------|-----------------------|------------------------|
| Comp. | Fill | 15.70 | 0.099 | -280.20 | -0.021 |
| | Wrap | 18.25 | 0.254 | -250.35 | -0.019 |
| Shear | Fill | 2.71 | N/A | 62.2 | N/A |
| | Warp | 2.45 | N/A | 59.2 | N/A |

Table 5-4 Thickness and Stacking Sequence of the Superstructure Model

| | Stacking Sequence | Thickness (mm) |
|----------------------------------|-----------------------------|-----------------------|
| Inner Tube Laminate | $[0^{\circ}_2]$ | 10.67 |
| Outer Tube Laminate | $[0^{\circ}(45^{\circ})_2]$ | 9.14 |
| Outer- Most Tube Laminate | $[0^{\circ}_4]$ | 16.76 |

Table 5-5 Weight Proportions of the Ingredients

| Ingredients | Weight Proportion |
|-------------------------|--------------------------|
| Cement | 1.000 |
| Water | 0.380 |
| Coarse Aggregate | 1.281 |
| Fine Aggregate | 1.413 |
| ADVA Flow 140 | 0.009 |
| Eclipse | 0.008 |

Table 5-6 Mechanical Properties of Concrete

| Specimen | Strength f'_c [MPa] | Chord Modulus of Elasticity [GPa] |
|-----------------|-----------------------------------------|------------------------------------------|
| Sp-1 | 57.10 | 31.43 |
| Sp-2 | 57.20 | 31.90 |
| Sp-3 | 52.60 | 28.30 |
| Average | 55.63 | 30.50 |

Table 5-7 Direct Tensile Strength (Units in MPa)

| Specimen | Tensile Strength |
|-----------------|-------------------------|
| Sp-1 | 4.53 |
| Sp-2 | 4.70 |
| Sp-3 | 3.39 |
| Sp-4 | 4.12 |
| Sp-5 | 4.10 |
| Sp-6 | 4.08 |
| Average | 4.15 |

Table 5-8 Similitude Scaling Factors

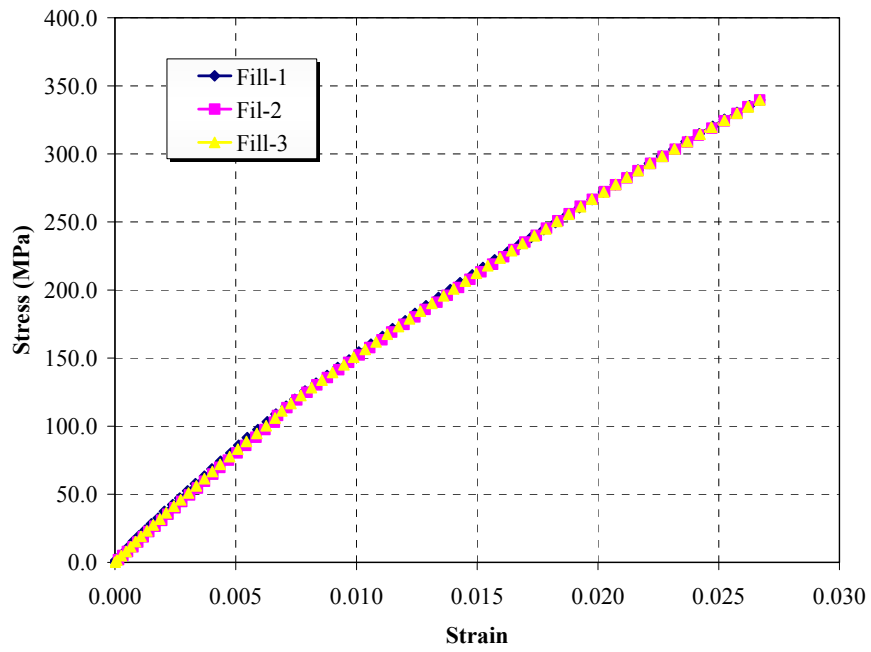
| Properties | Required Value | Provided Value |
|-------------------------------------------|-----------------------|-----------------------|
| Length λ_L | n | n |
| Volume λ_V | n^3 | n^3 |
| Force λ_F | n^2 | n^2 |
| Stress λ_σ | 1.0 | 1.0 |
| Strain λ_ϵ | 1.0 | 1.0 |
| Density λ_ρ | 1.0 | 1.0 |
| Mass λ_M | n^2 | n^3 |
| Gravitational Acc. λ_g | 1.0 | 1.0 |
| Gravitational Force λ_{gf} | n^2 | n^3 |

Table 5-9 Measured Maximum Strains at Selected Locations in Destructive Flexure

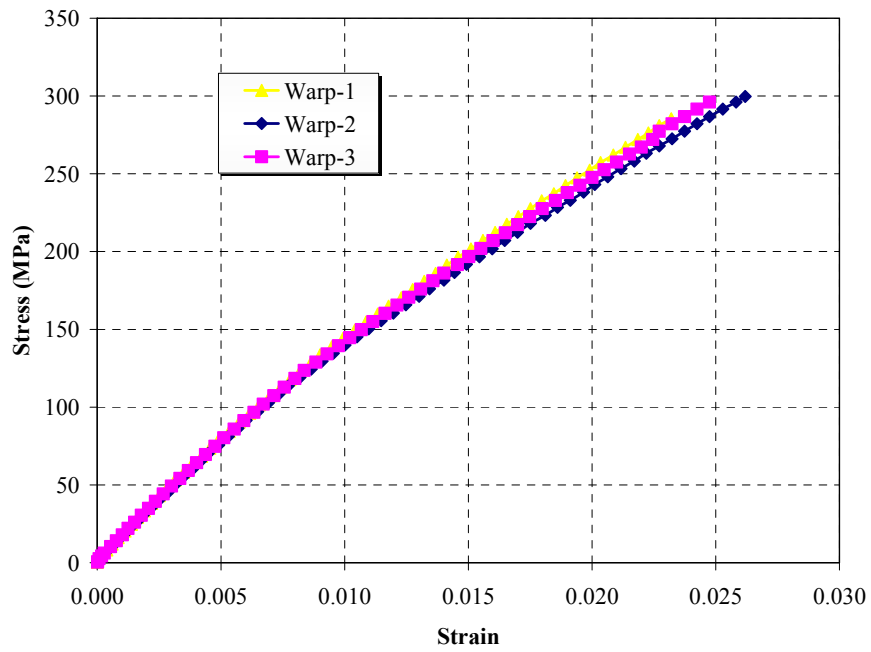
| Strain Gauge | Maximum Strain (μ) | Ratio to the Ultimate Strain |
|---------------------|------------------------------------------|-------------------------------------|
| ETWL | -1885 | 0.094 |
| EW1L | 4653 | 0.180 |
| ET5L | -2010 | 0.101 |
| HW1L | 2519 | 0.097 |
| DBCL | 4115 | 0.159 |
| ETCL | -2590 | 0.130 |
| EW5L | -932 | 0.047 |
| ITCL | -297 | 0.015 |
| CTCL | -628 | 0.031 |



Figure 5.1 Tensile Test Fixture



(a) Fill Direction



(b) Warp Direction

Figure 5.2 Engineering Stress-Strain Curves from Tensile Tests

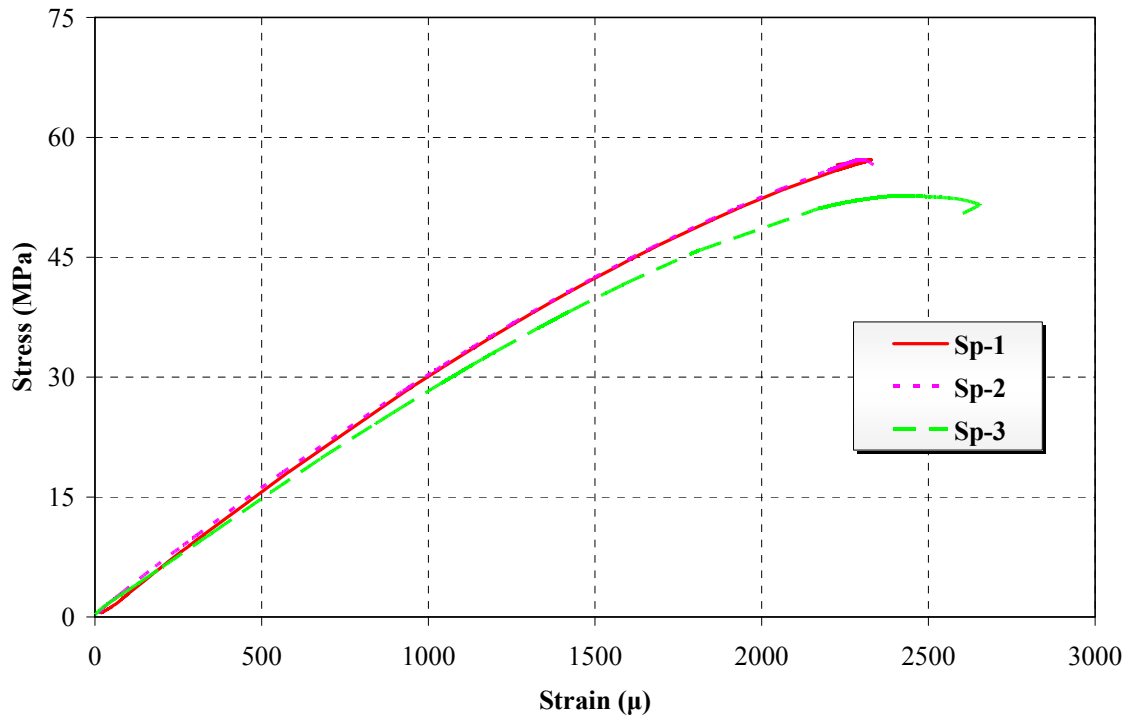
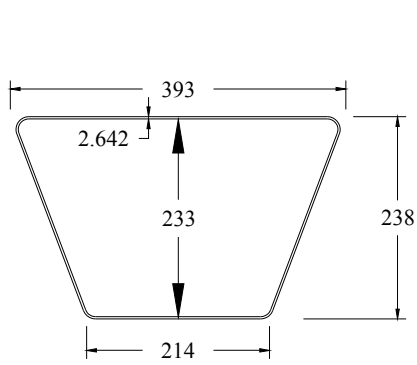
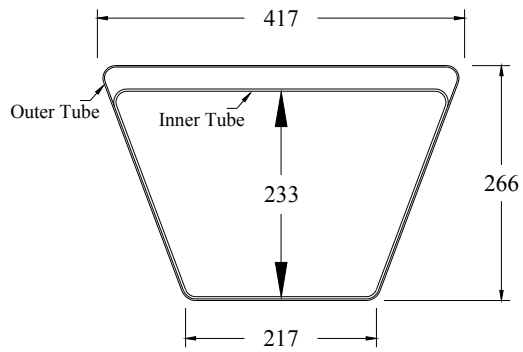


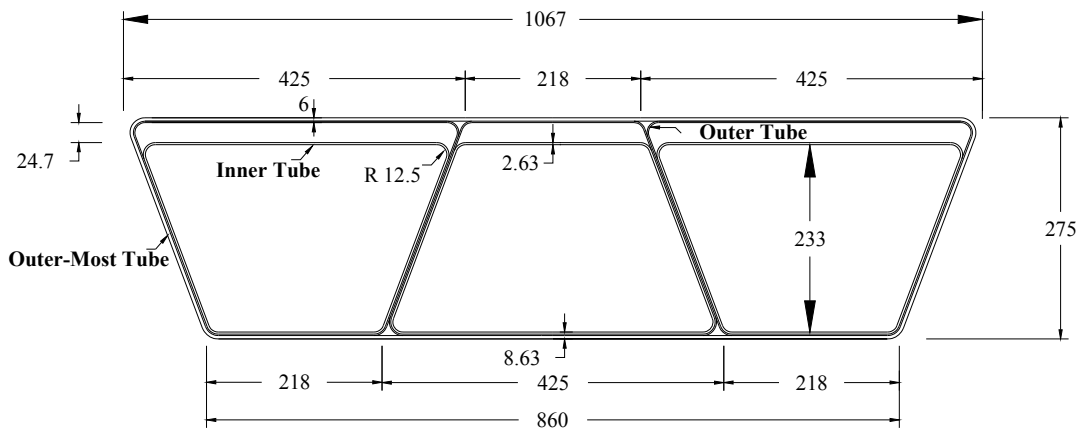
Figure 5.3 Compressive Stress-Strain Curves of Concrete



(a) Inner Tube



(b) Model Unit Cell



(c) Bridge Superstructure Model

Figure 5.4 Cross Section of the Hybrid FRP-Concrete Superstructure Model (units in mm)



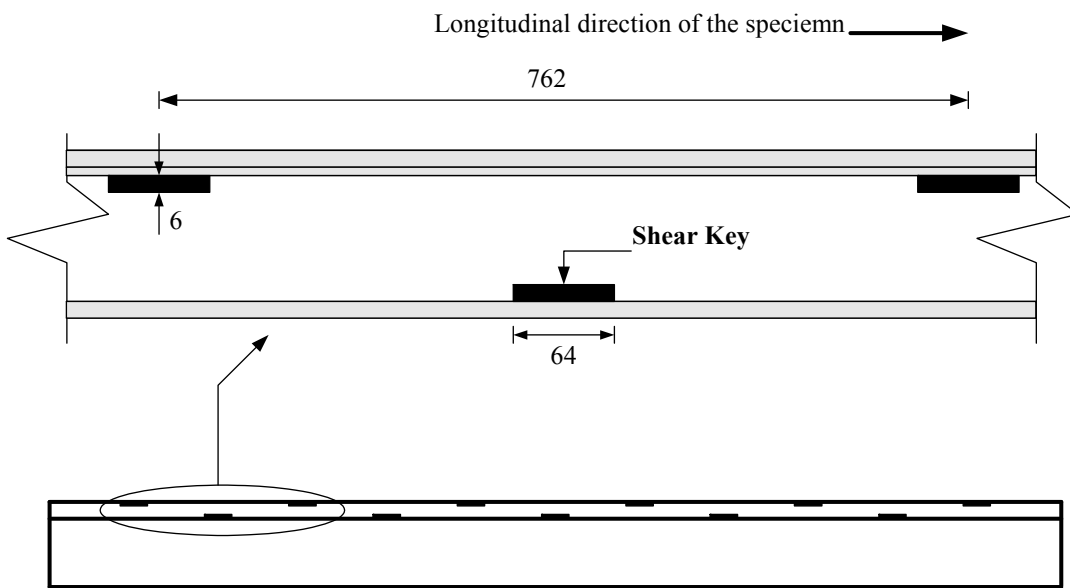
Figure 5.5 Individual Trapezoidal Box Section before Assembly



Figure 5.6 Assembly of Three Trapezoidal Box Sections by the Vacuum Bag Process

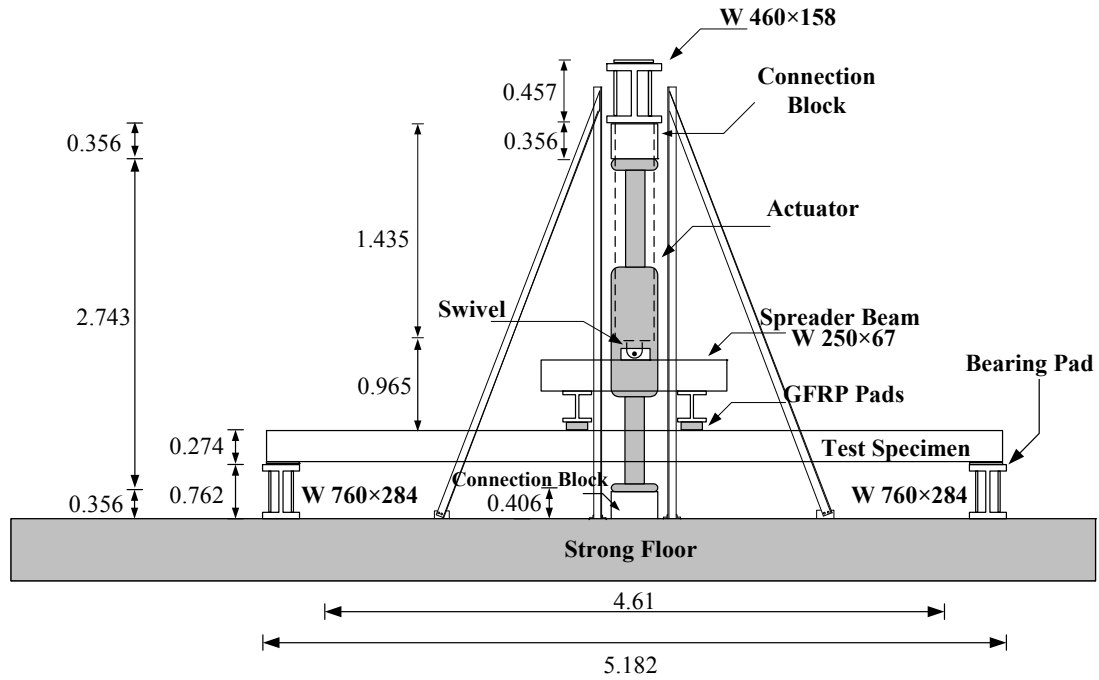


Figure 5.7 Layer of Glass Fiber Wetted With Vinyl Ester Resin Placed Between Box Sections as Bonding Material

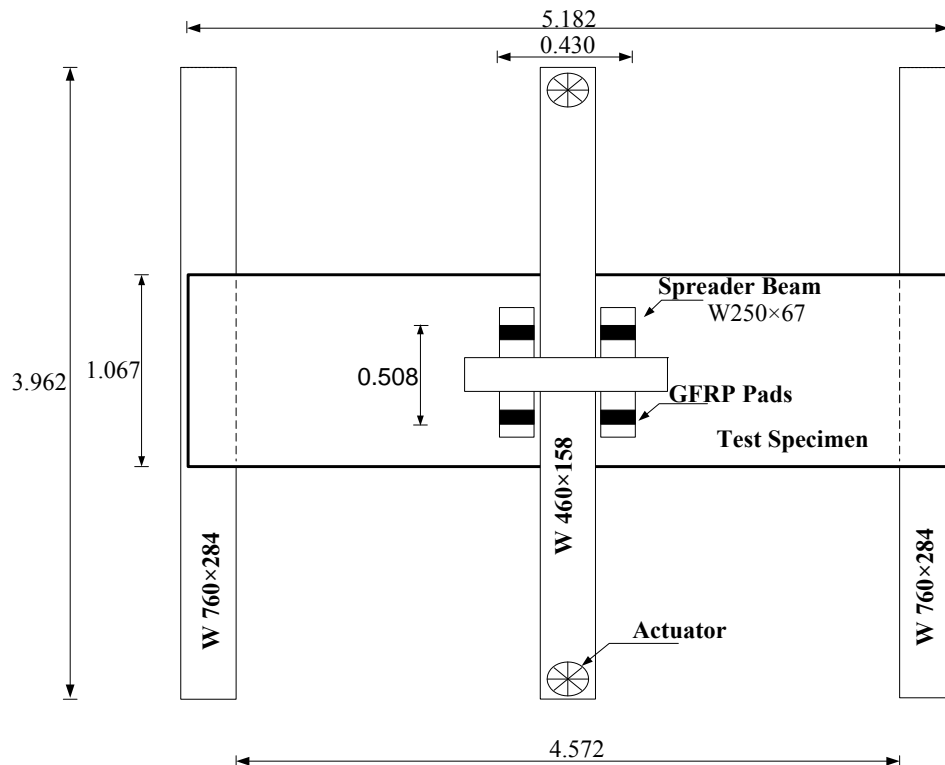


Side View of the Superstructure Specimen

Figure 5.8 Shear Keys (dimension in mm)



(a) Elevation



(b) Top View

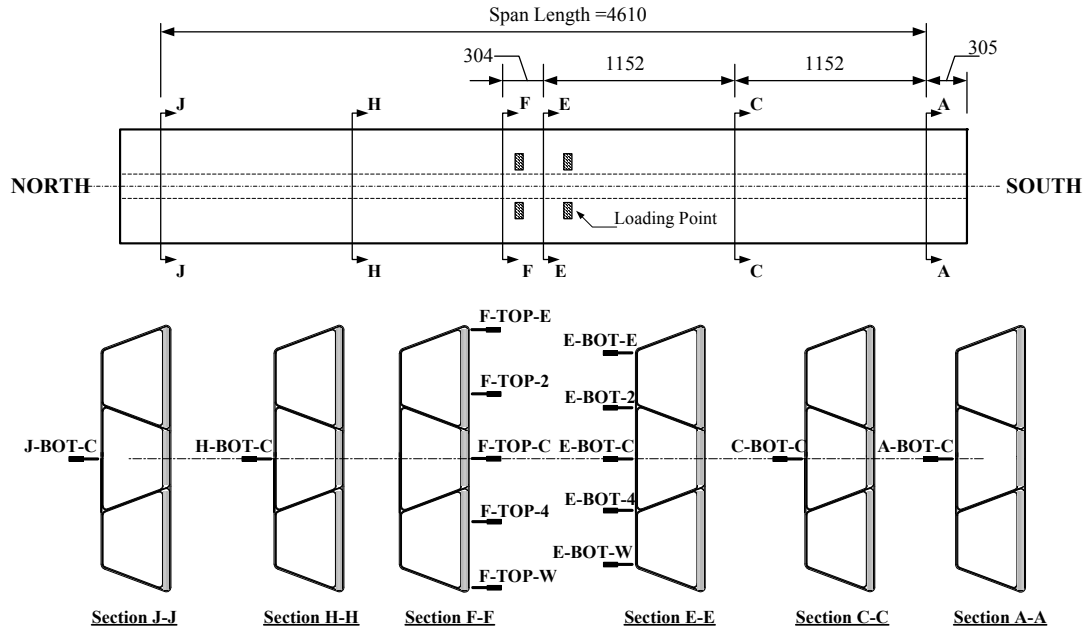
Figure 5.9 Test Configuration for Quasi-Static Positive Moment Flexural Test (dimensions in m)



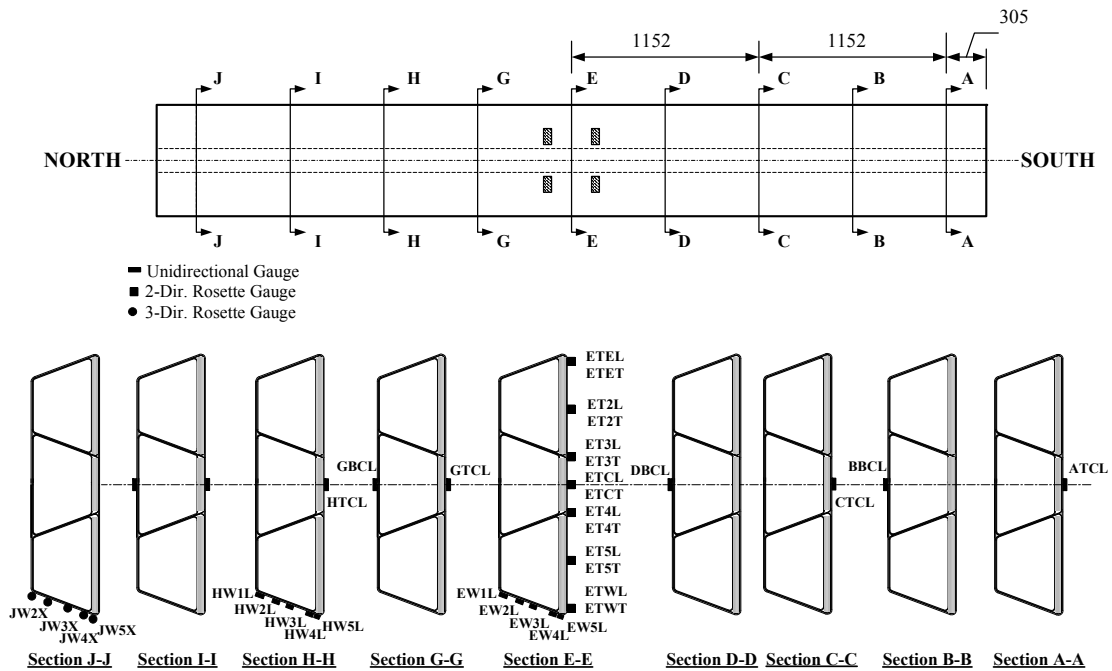
Figure 5.10 Test Set Up for Quasi-Static Positive Moment Flexural Test



Figure 5.11 Spreader Beam

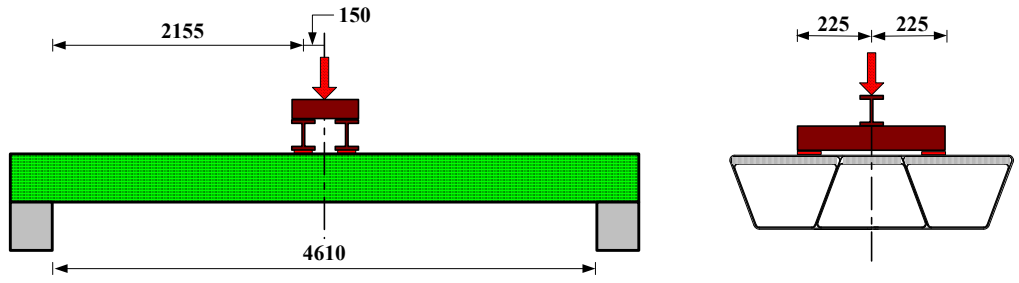


(a) Displacement Measurement



(b) Strain Measurement

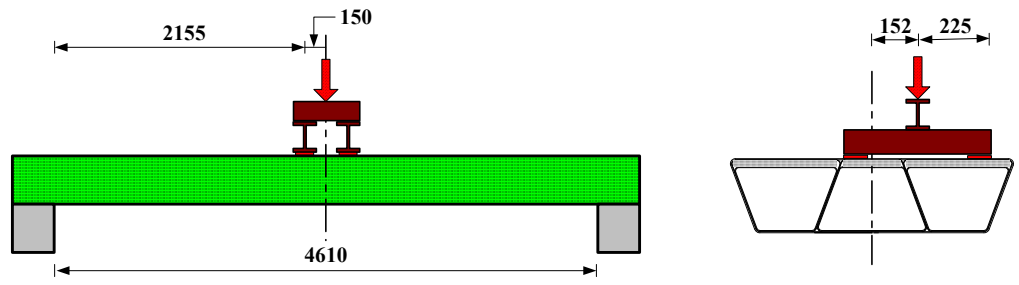
Figure 5.12 Instrumentation for the Positive Moment Flexural Test (Dimensions in mm)



(i) Elevation

(ii) Cross Section

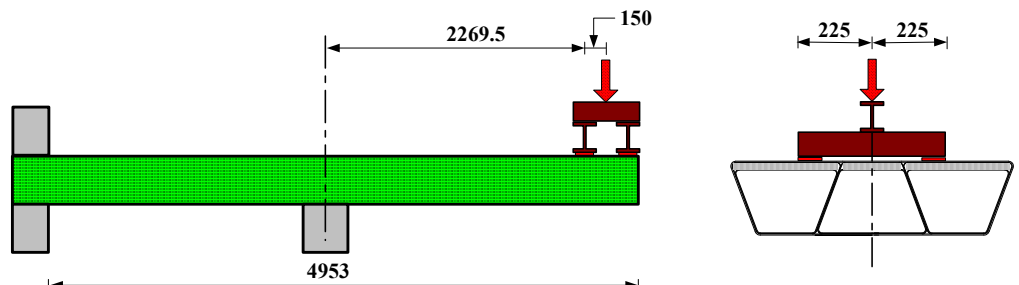
(a) Positive Flexure



(i) Elevation

(ii) Cross Section

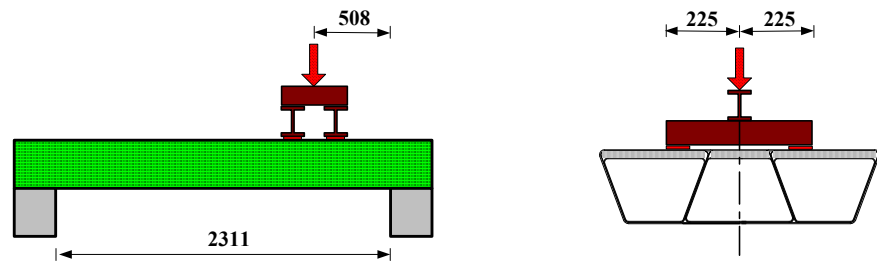
(b) Off-Axis Positive Flexure



(i) Elevation

(ii) Cross Section

(c) Negative Flexure



(i) Elevation

(ii) Cross Section

(d) Shear

Figure 5.13 Load Configuration

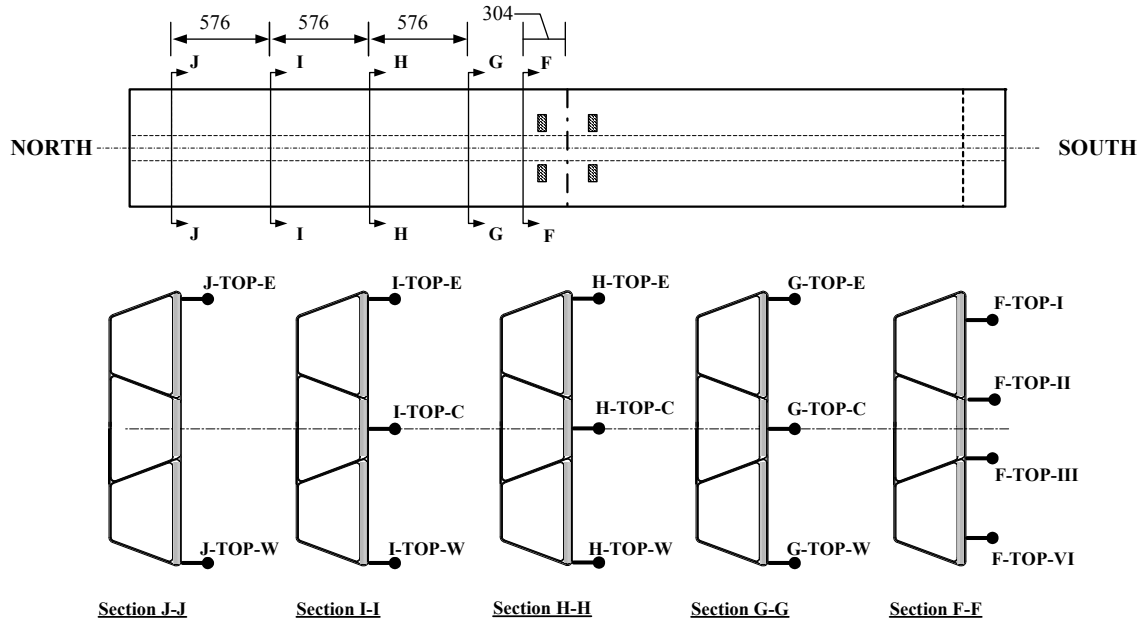


Figure 5.14 Layout of the LEDs on the Top Surface for the Positive Moment Flexural Test (dimensions in mm)

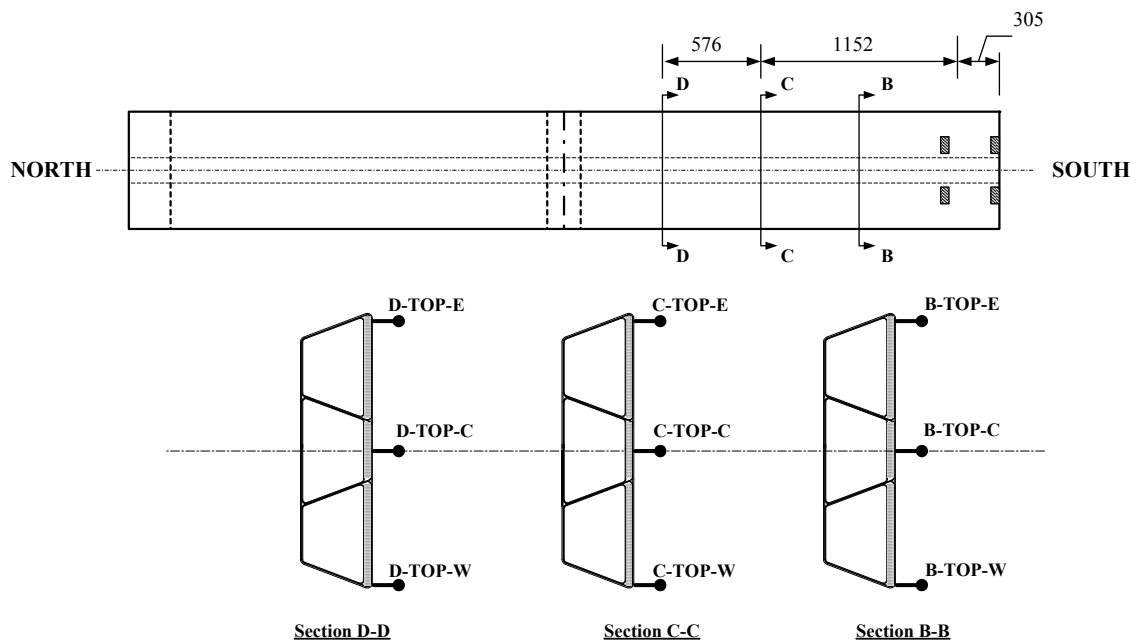
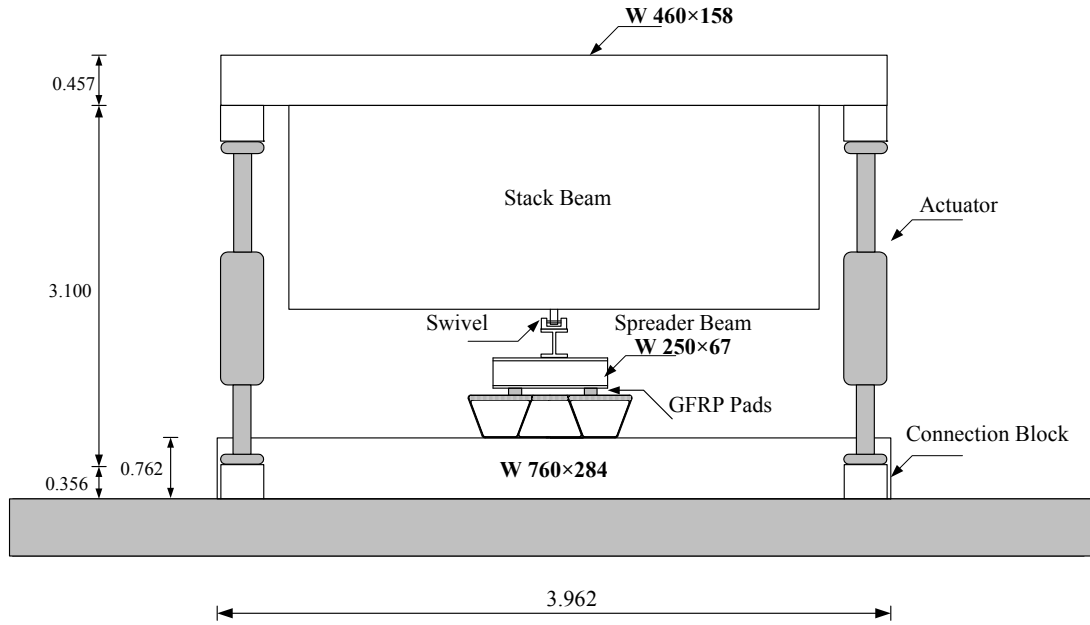
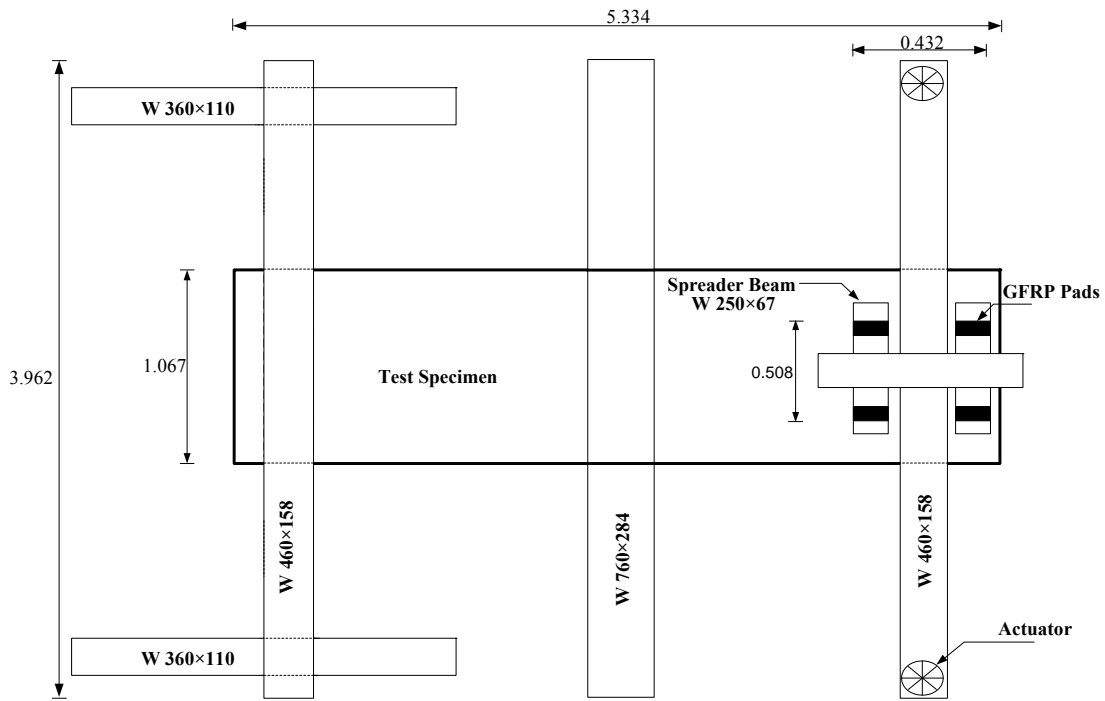


Figure 5.15 Layout of the LEDs on the Top Surface for the Negative Moment Flexural Test (dimensions in mm)

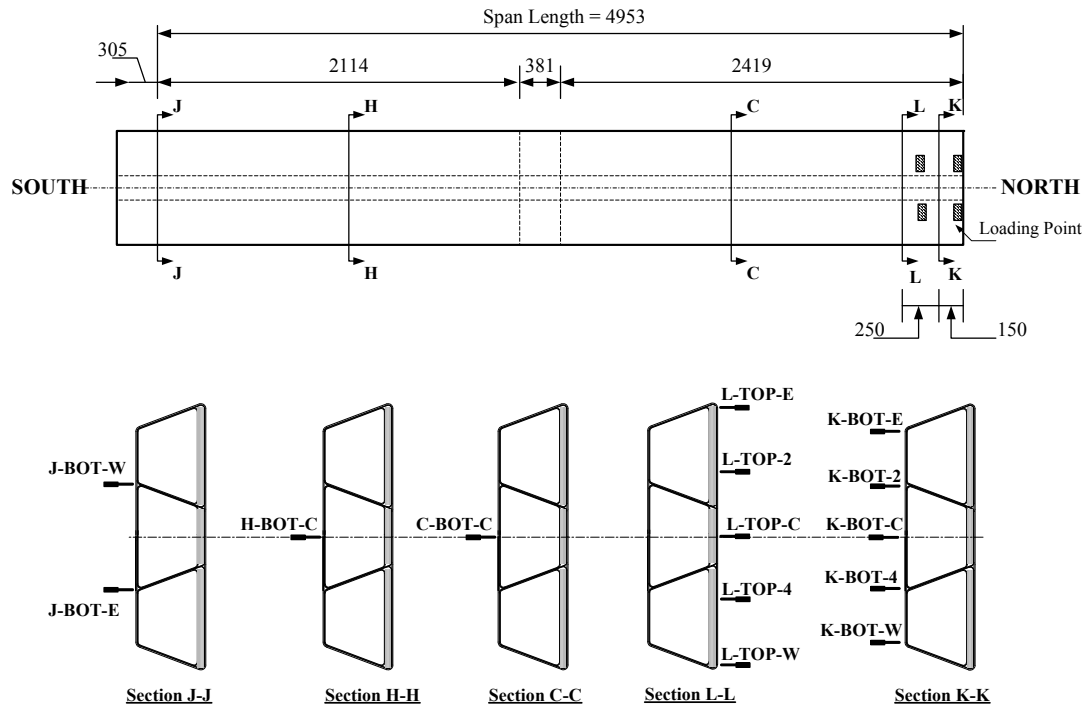


(c) Side View -South End

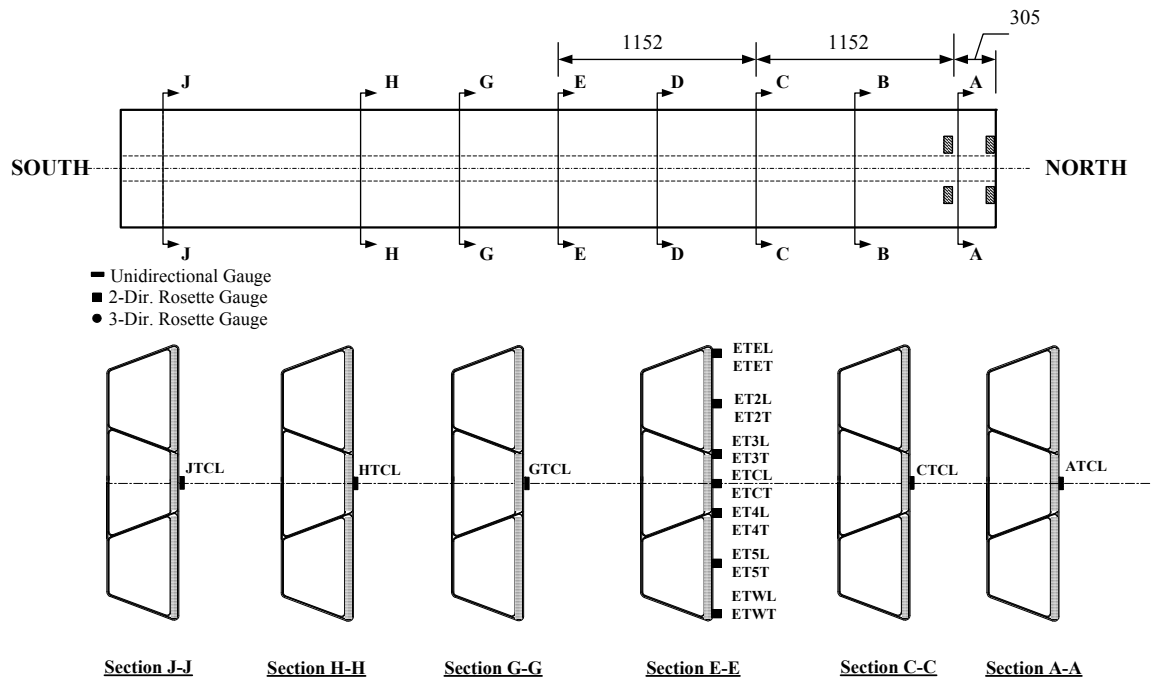


(d) Top View

Figure 5.17 Test Configuration for Quasi-Static Negative Moment Flexural Test (dimensions in m) (cont.)

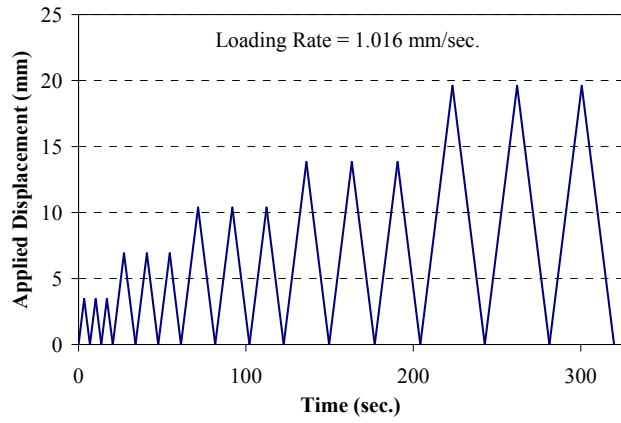


(a) Displacement Measurement

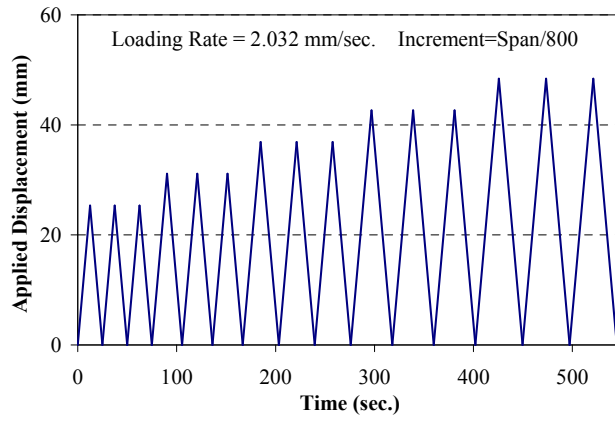


(b) Strain Measurement

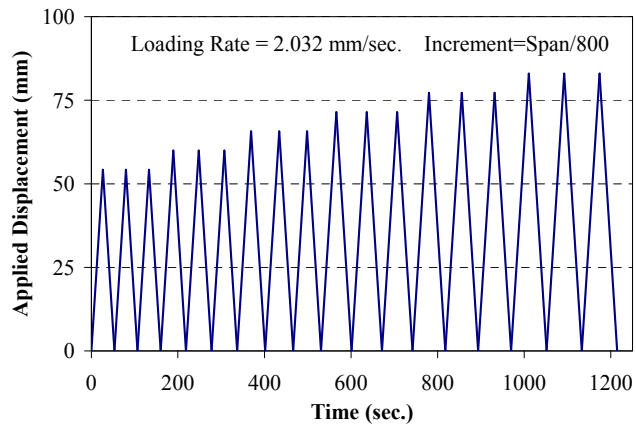
Figure 5.18 Instrumentation for the Negative Moment Flexural Test (dimensions in mm)



(a) Stage I

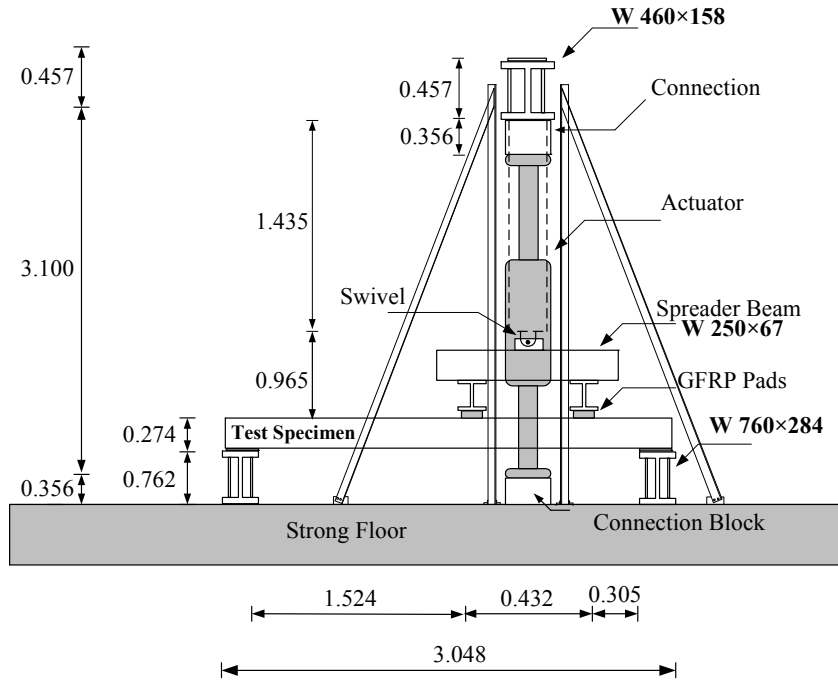


(b) Stage II

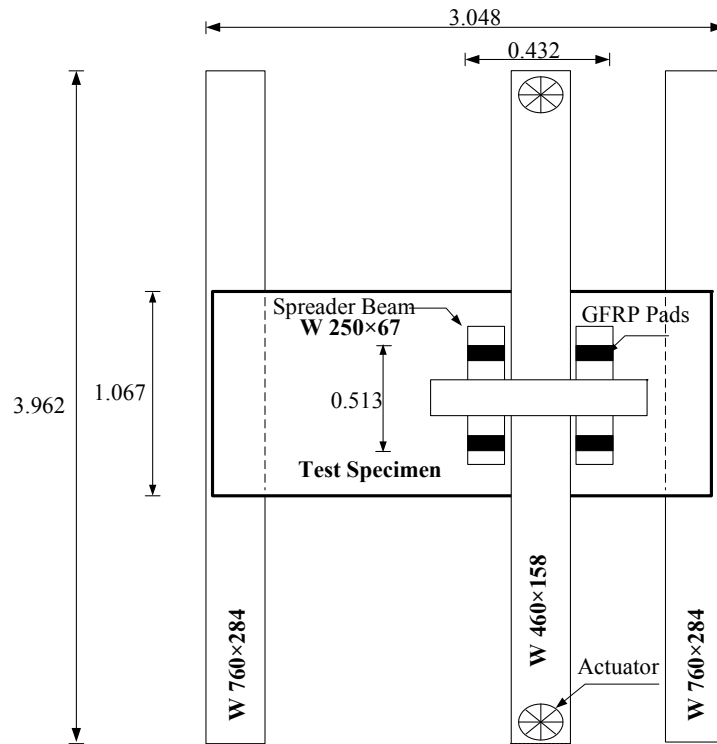


(c) Stage III

Figure 5.19 Displacement Protocol of the Destructive Flexural Test

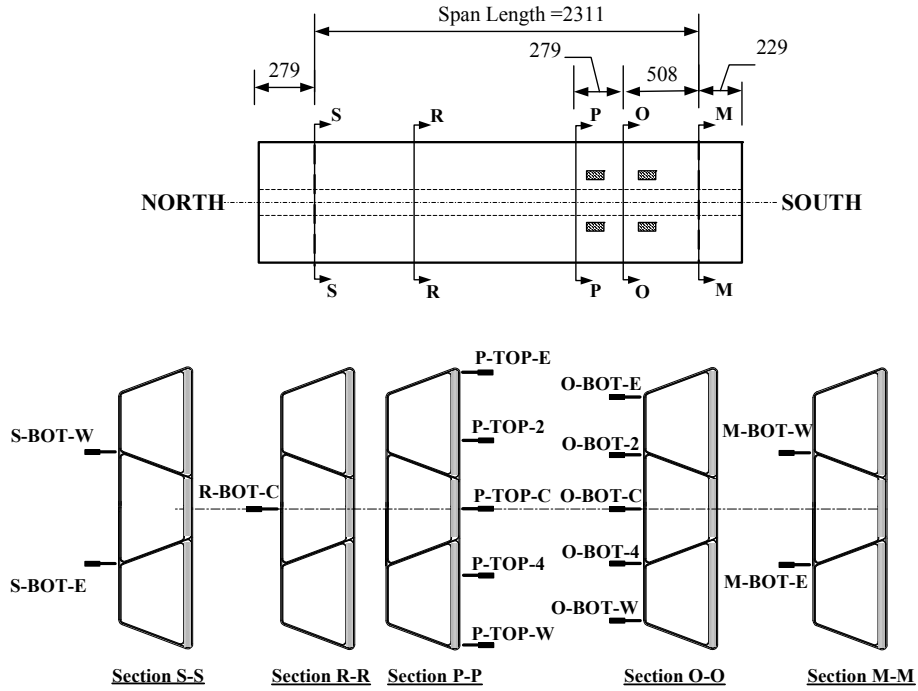


(a) Elevation

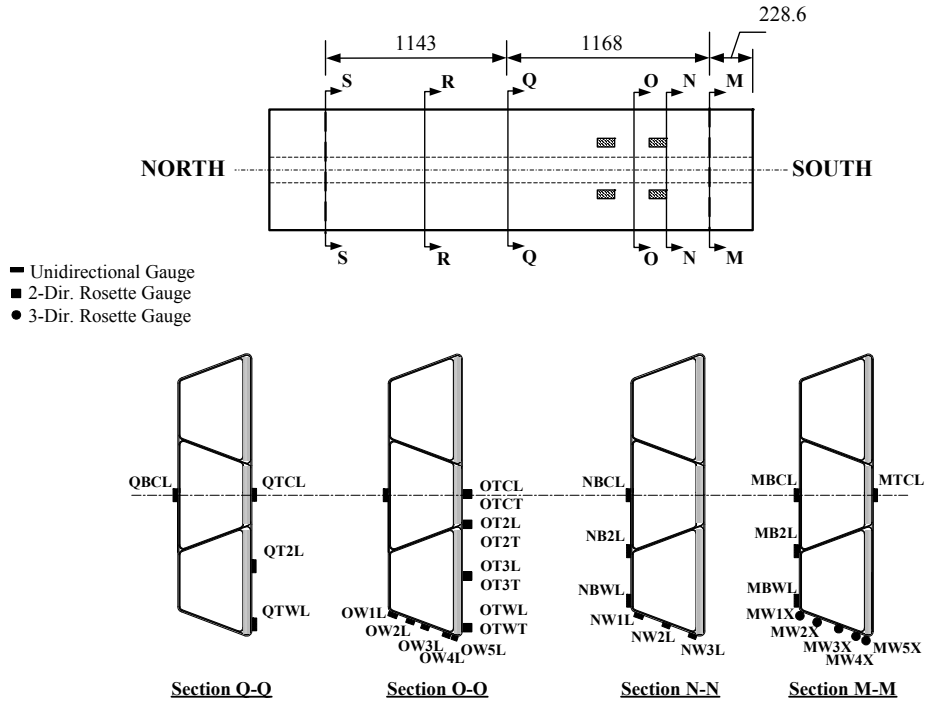


(b) Top View

Figure 5.20 Test Configuration for Quasi-Static Shear Test (dimensions in m)



(a) Displacement Measurement



(b) Strain Measurement

Figure 5.21 Instrumentation for the Shear Test (dimensions in mm)

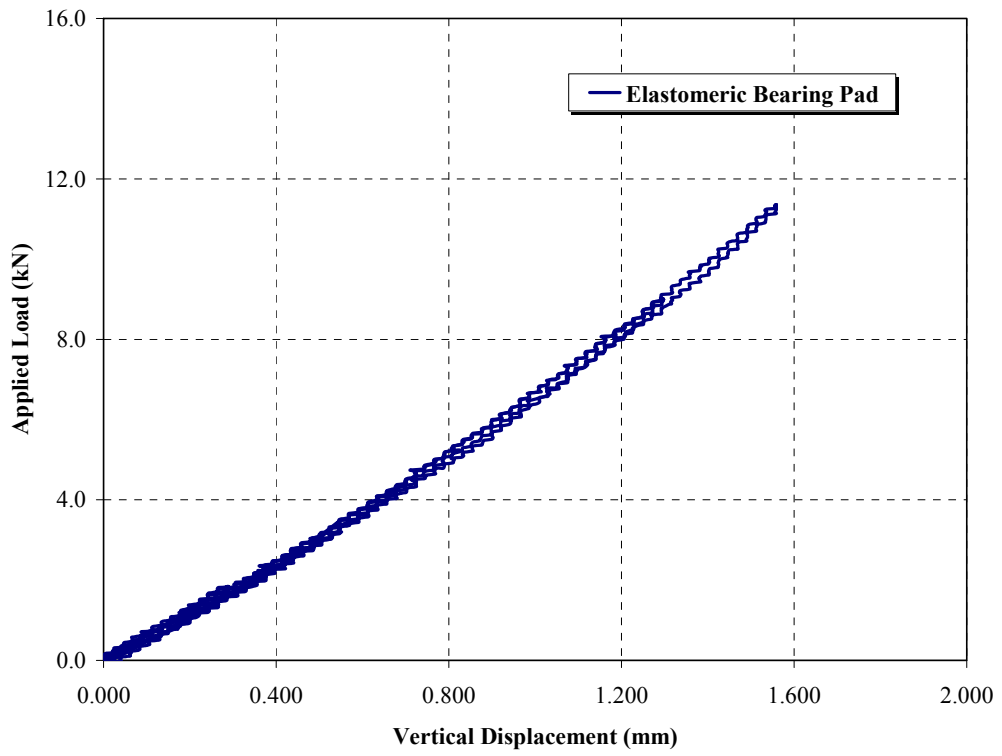
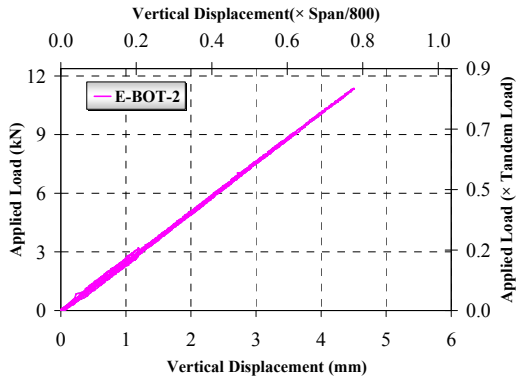
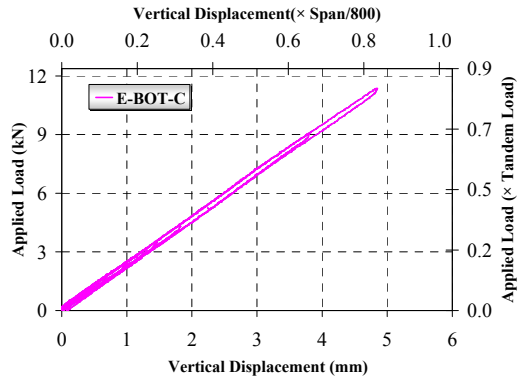


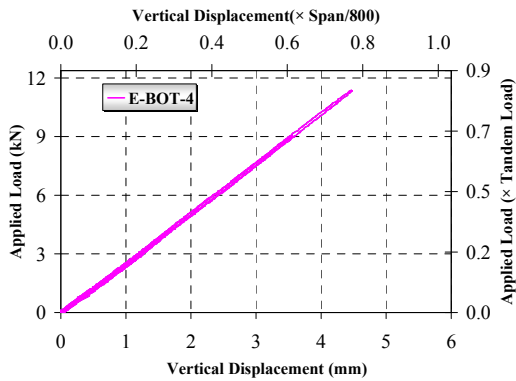
Figure 5.22 Displacement of the Elastomeric Bearing Pad Measured at Section A



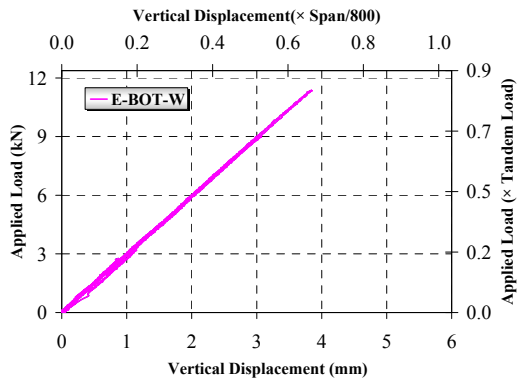
(a) E-BOT-2



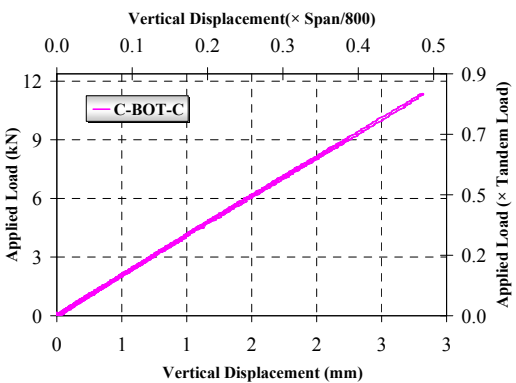
(b) E-BOT-C



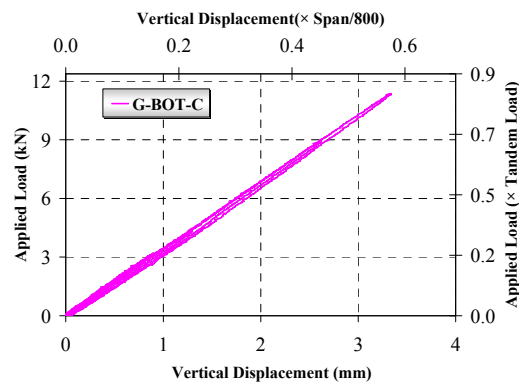
(c) E-BOT-4



(d) E-BOT-W

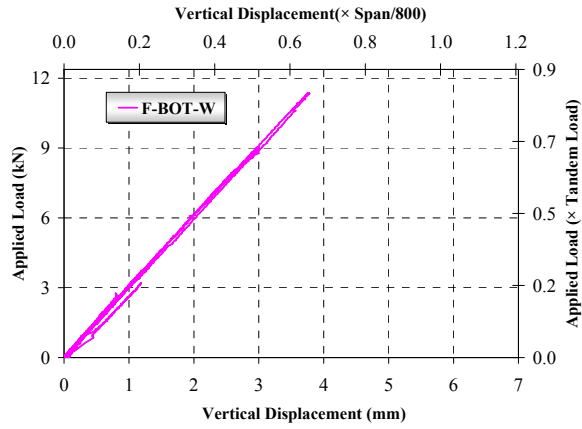


(e) C-BOT-C

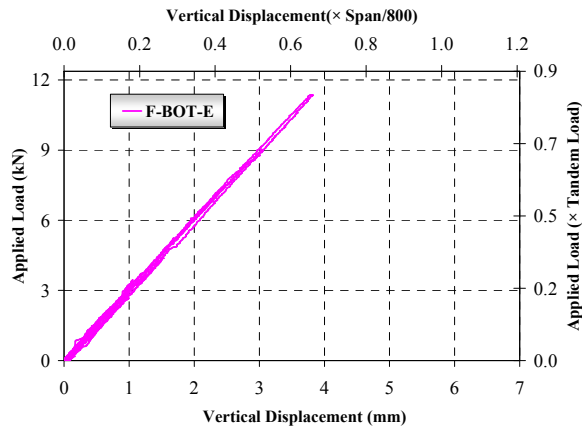


(f) G-BOT-C

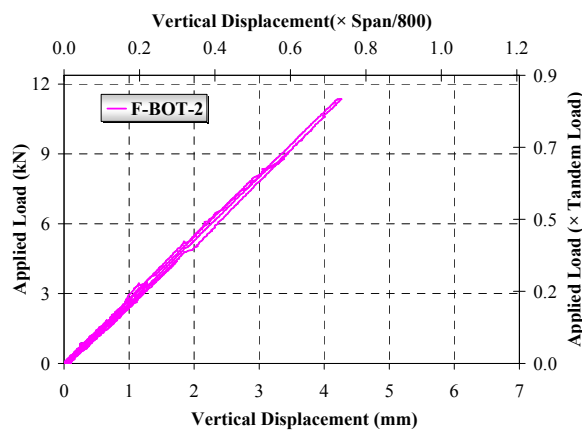
Figure 5.23 Forces vs. Displacement at the Bottom Surface (FRP-Only Specimen in Positive Moment Flexure)



(a) F-BOT-W

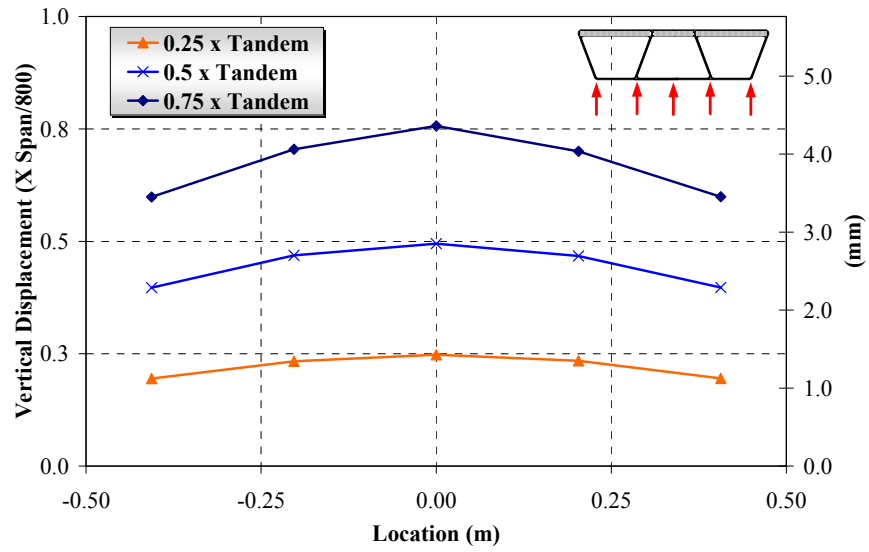


(b) F-BOT-E

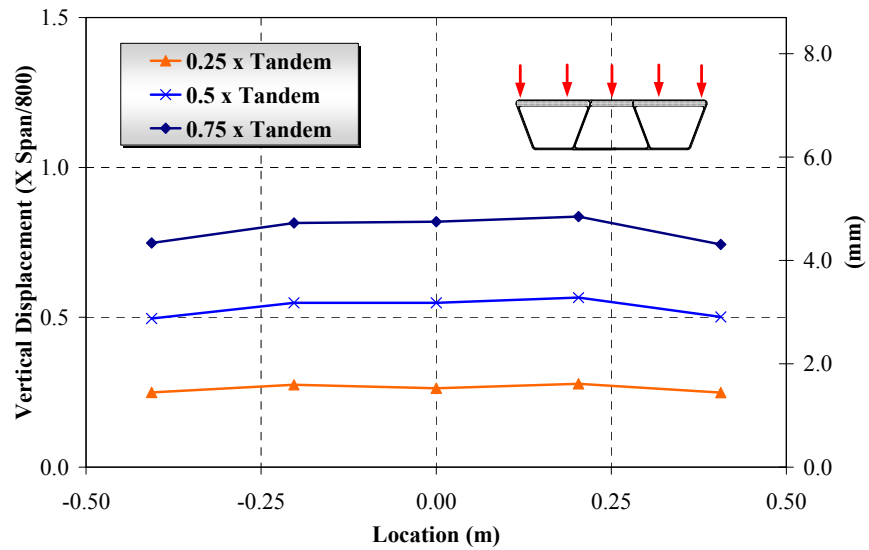


(c) F-BOT-2

Figure 5.24 Forces vs. Displacement at the Top Surface (FRP-Only Specimen in Positive Flexure).

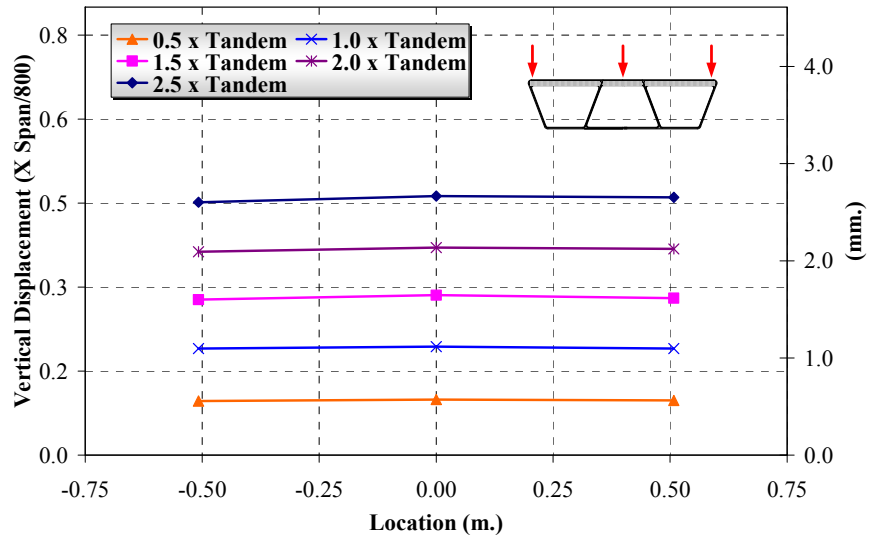


(a) Bottom Surface

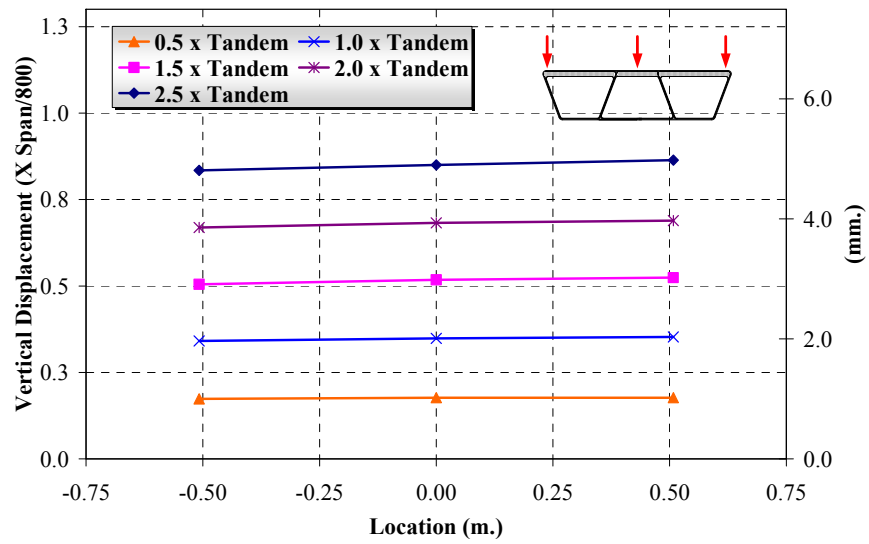


(b) Top Surface

Figure 5.25 Deformed Shapes at Different Load Levels for FRP-only Specimen in Positive Flexure

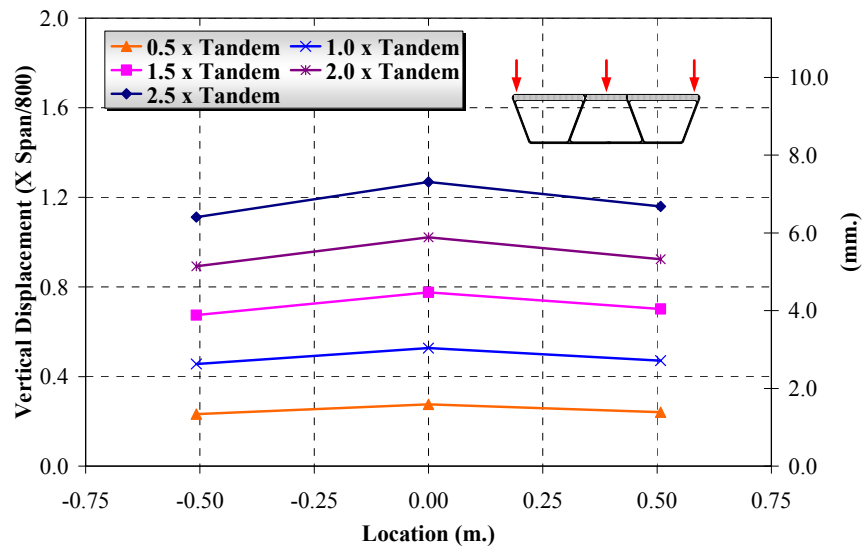


(a) Section I-I

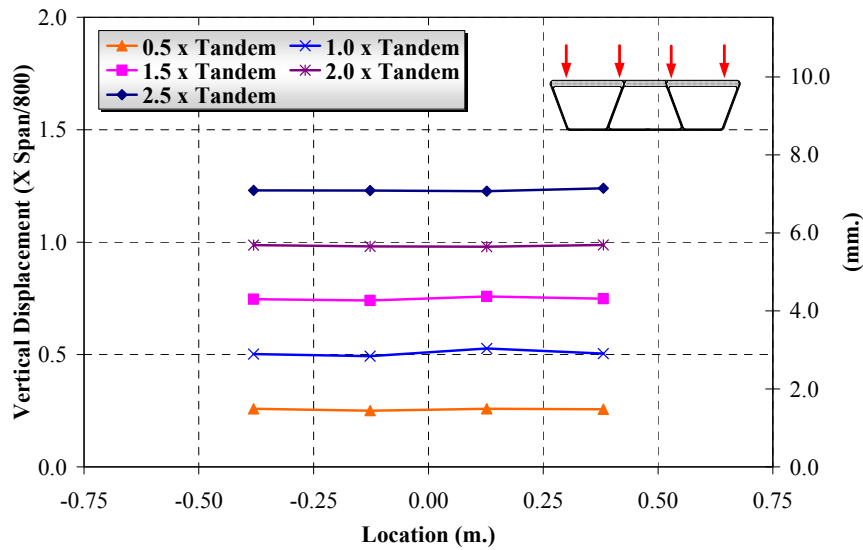


(b) Section H-H

Figure 5.26 Deformed Shapes at Different Load Levels for Hybrid Specimen in Flexure (Top Surface)

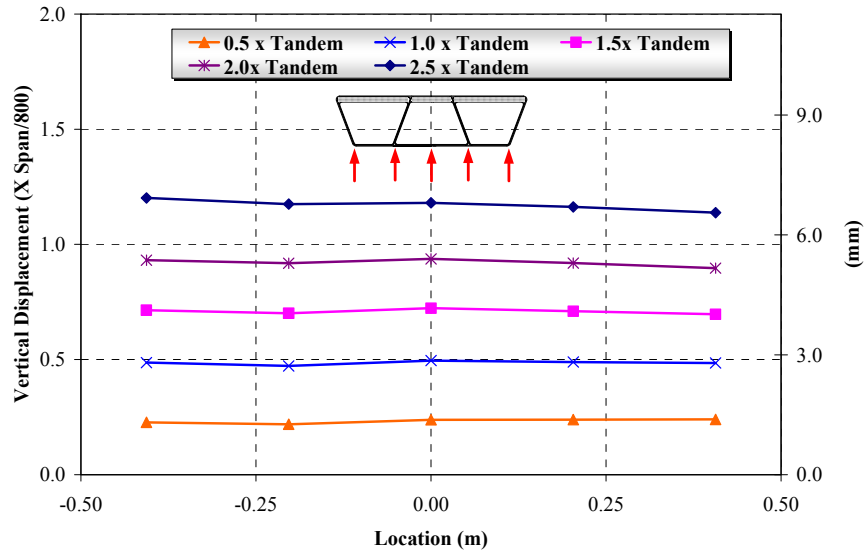


(a) Section G-G

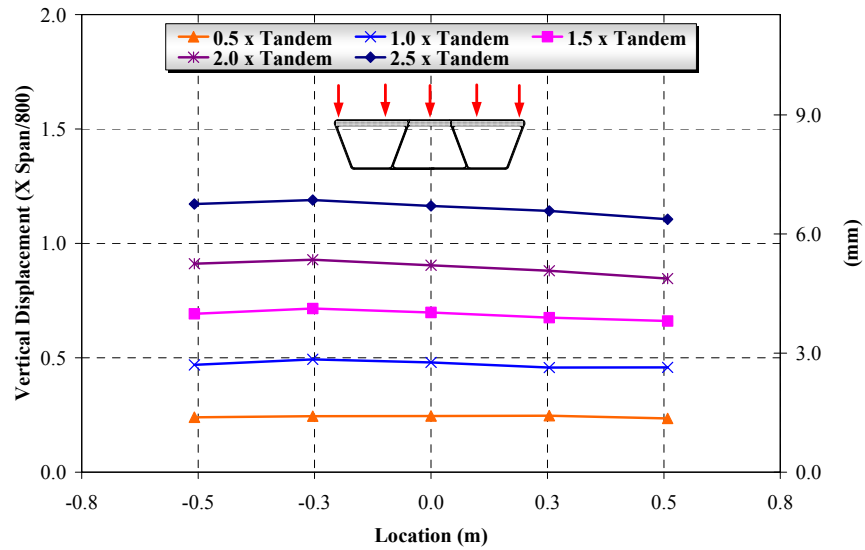


(b) Section F-F

Figure 5.27 Deformed Shapes at Different Load Levels for Hybrid Specimen in Flexure (Top Surface)

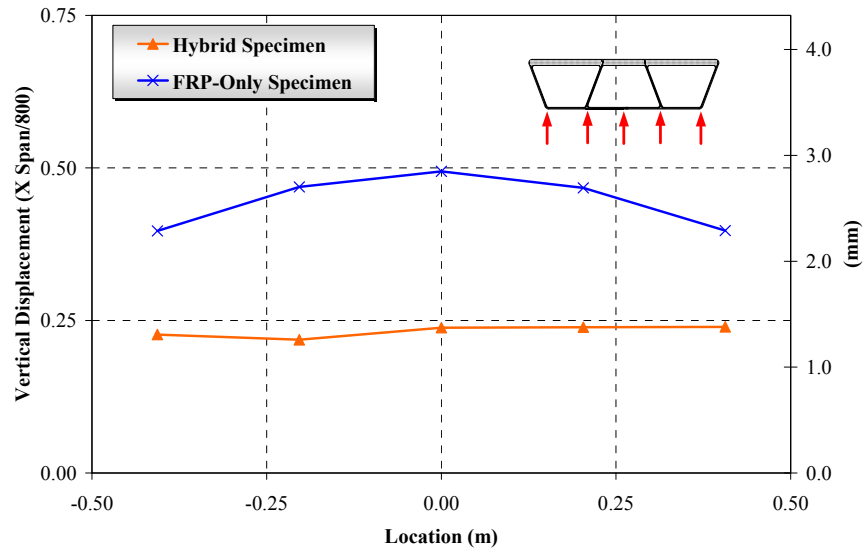


(a) Bottom Surface

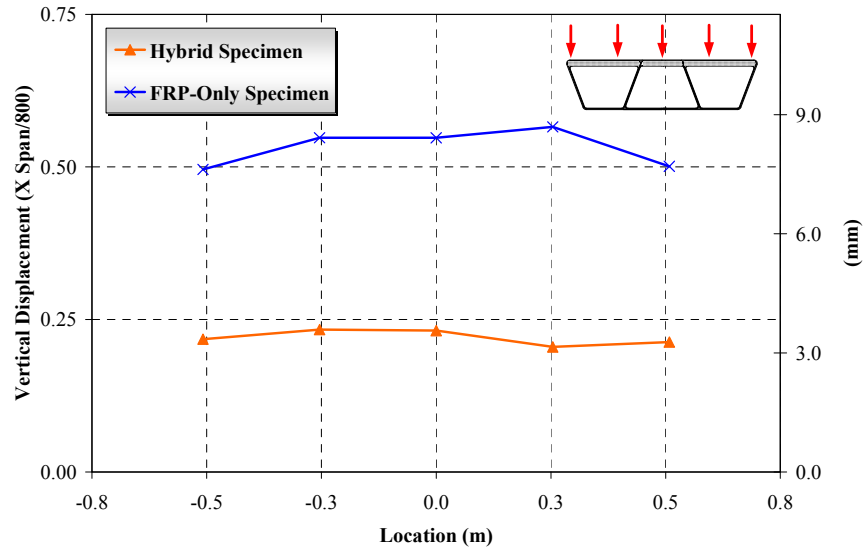


(b) Top Surface

Figure 5.28 Deformed Shapes at Different Load Levels for FRP-only Specimen in Positive Flexure



(a) Bottom Surface



(b) Top Surface

Figure 5.29 Comparison of Deformed Shapes at $0.5 \times$ Tandem Load between FRP-only and Hybrid Specimens in Positive Moment Flexure

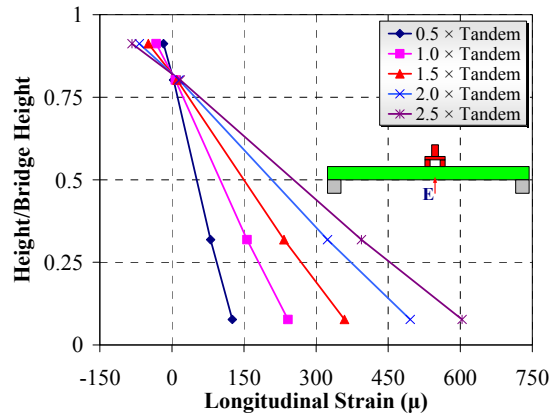


Figure 5.30 Strain Variations on the Exterior Web at Section E (Hybrid Specimen in Positive Flexure).

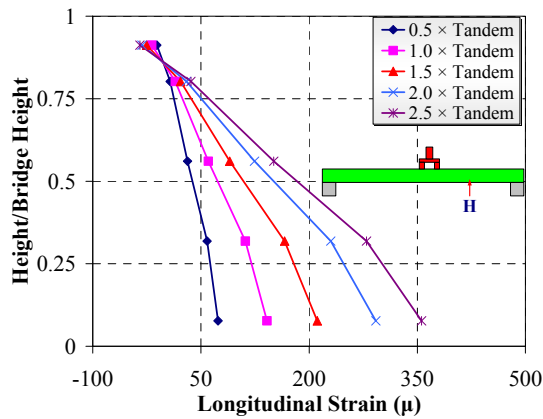


Figure 5.31 Strain Variations on the Exterior Web at Section H (Hybrid Specimen in Positive Flexure)

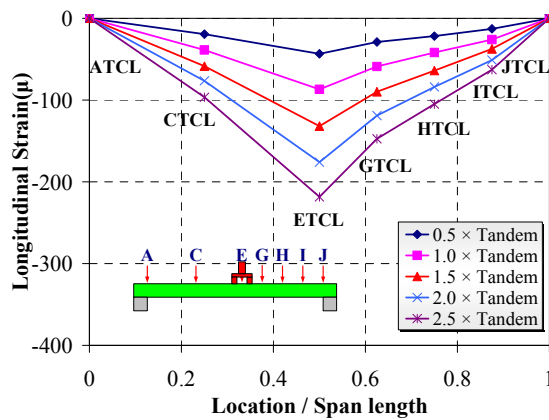


Figure 5.32 Longitudinal Strain Variations along the Centerline at Top Surface (Hybrid Specimen in Positive Flexure)

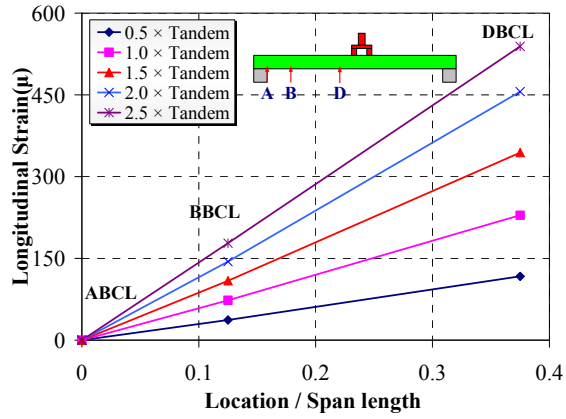


Figure 5.33 Longitudinal Strain Variations along the Centerline at Bottom Surface, Hybrid Specimen in Positive Flexure

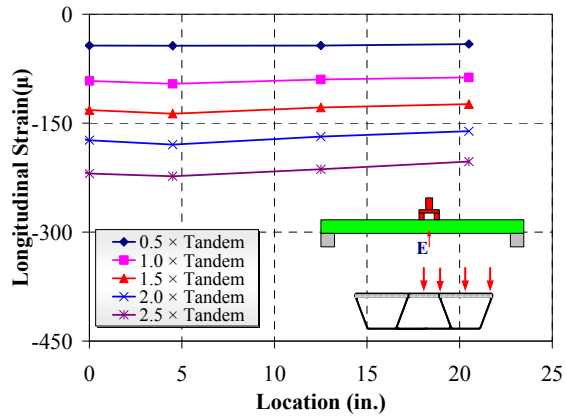


Figure 5.34 Longitudinal Strain Variations along Section E, Hybrid Specimen in Positive Flexure

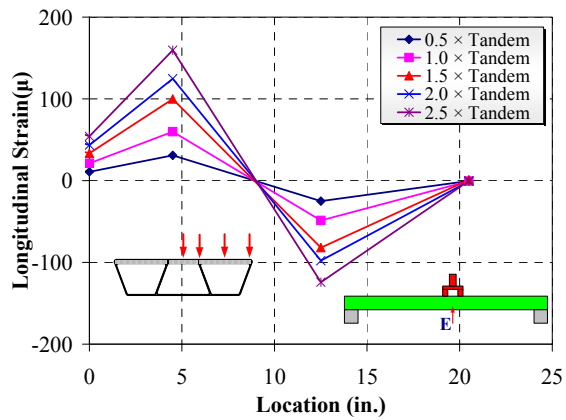
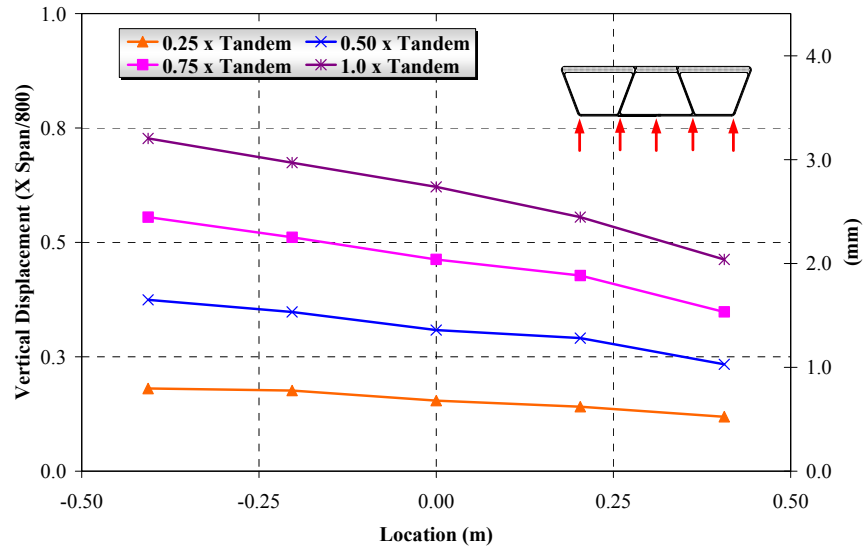
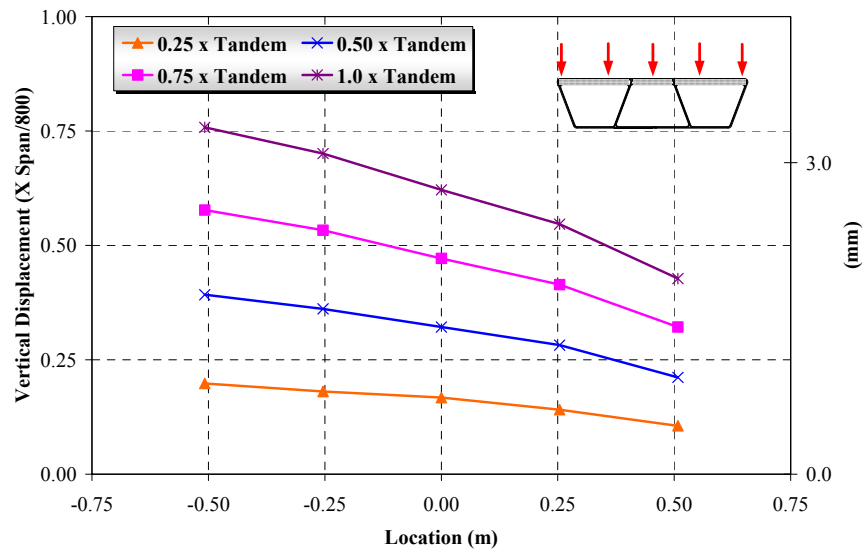


Figure 5.35 Transverse Strain Variations along Section E, Hybrid Specimen in Positive Flexure



(a) Bottom Surface



(b) Top Surface

Figure 5.36 Deformed Shapes at Different Load Levels for the Hybrid Specimen, Off-Axis Flexure

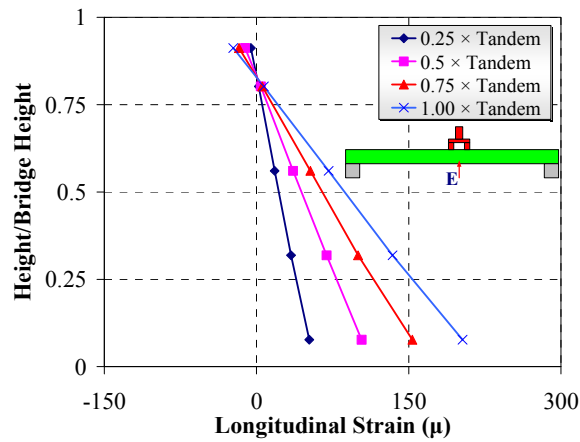


Figure 5.37 Strain Variations on the Exterior Web at Section E, Off-Axis Flexure

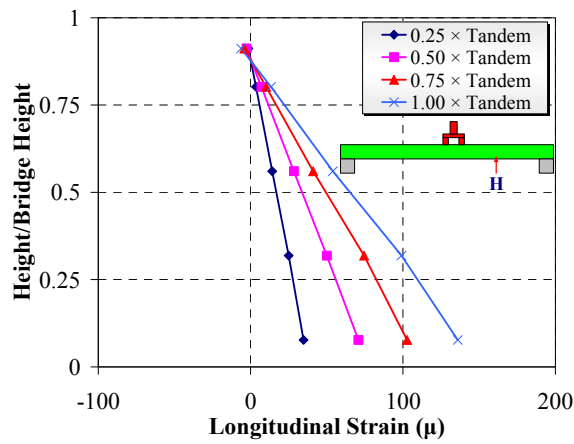


Figure 5.38 Strain Variations on the Exterior Web at Section H, Off-Axis Flexure

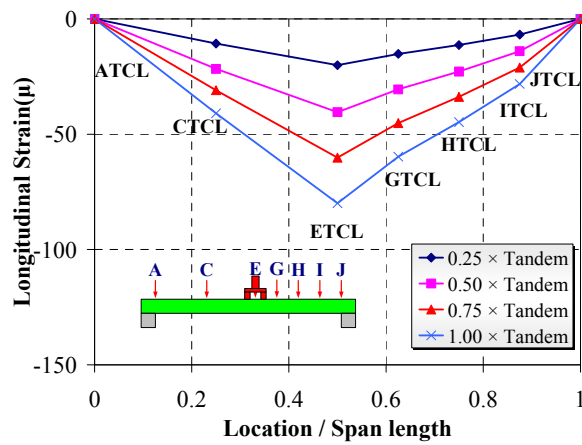


Figure 5.39 Longitudinal Strain Variations along the Centerline at Top Surface, Off-Axis Flexure

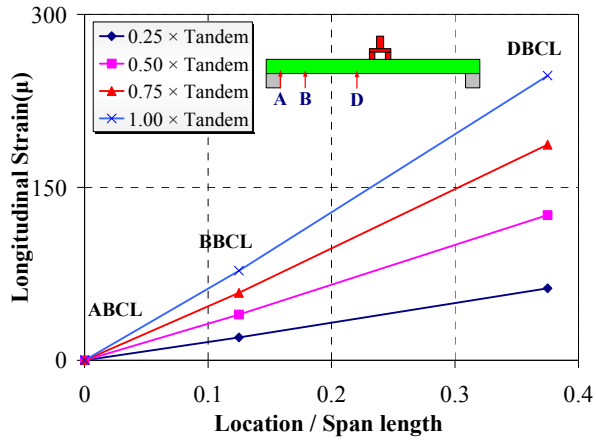


Figure 5.40 Longitudinal Strain Variations along the Centerline at Bottom Surface, Off-Axis Flexure

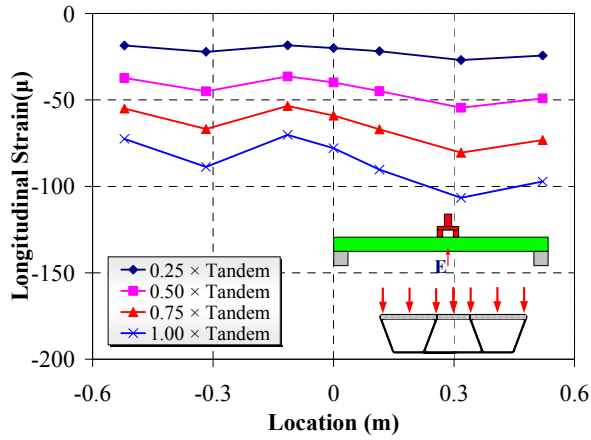


Figure 5.41 Longitudinal Strain Variations along Section E, Off-Axis Flexure

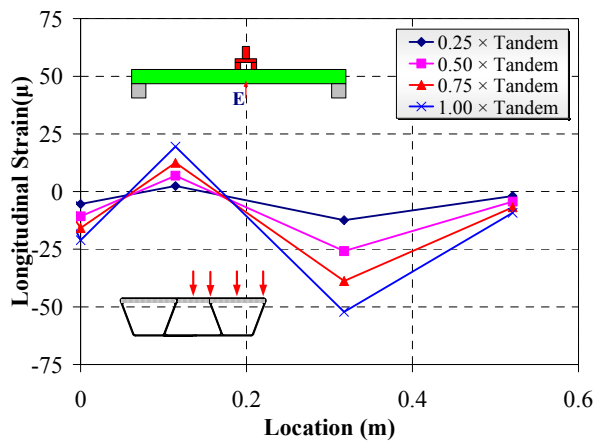
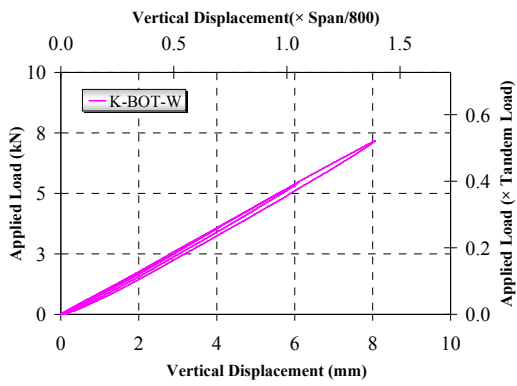
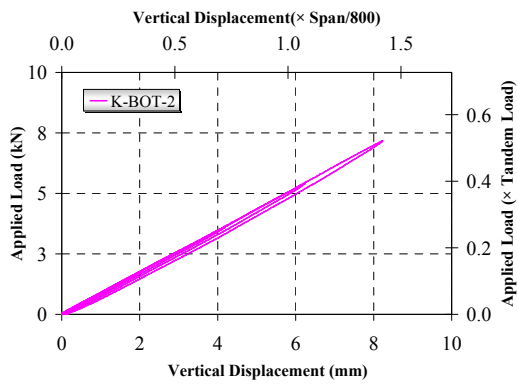


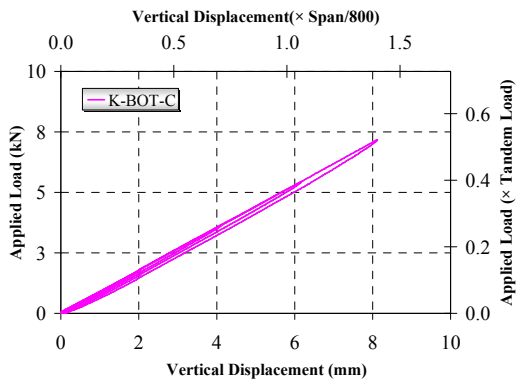
Figure 5.42 Longitudinal Strain Variations along Section E, Off-Axis Flexure



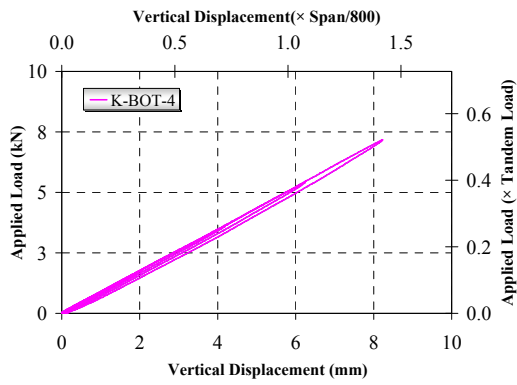
(a) K-BOT-W



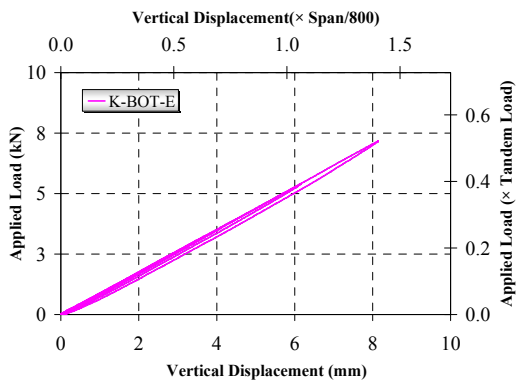
(b) K-BOT-2



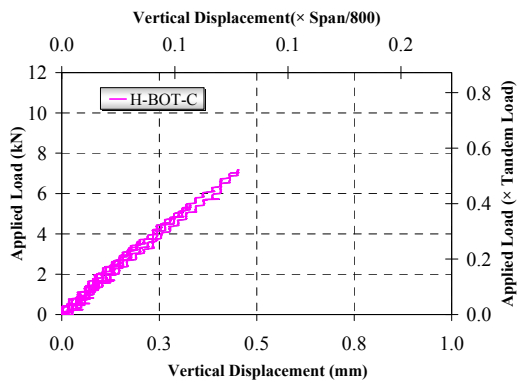
(c) K-BOT-C



(d) K-BOT-4

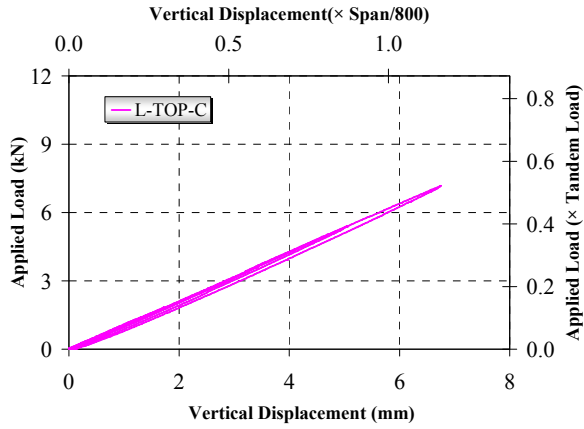


(e) K-BOT-E

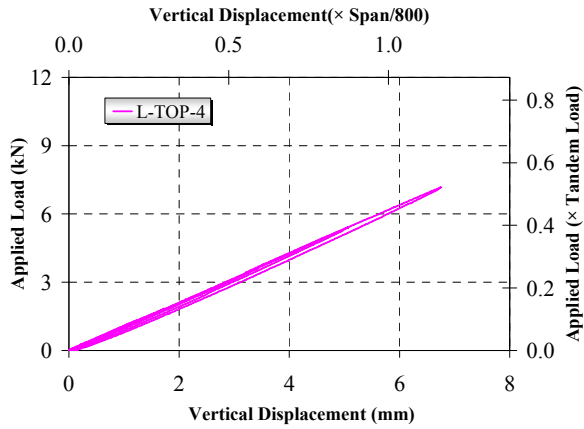


(f) H-BOT-C

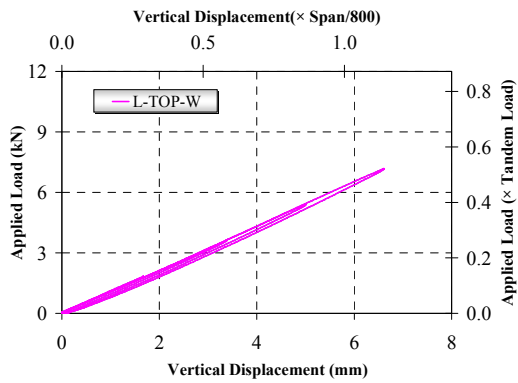
Figure 5.43 Forces vs. Displacement at the Bottom Surface (Negative Flexure)



(a) L-TOP-C

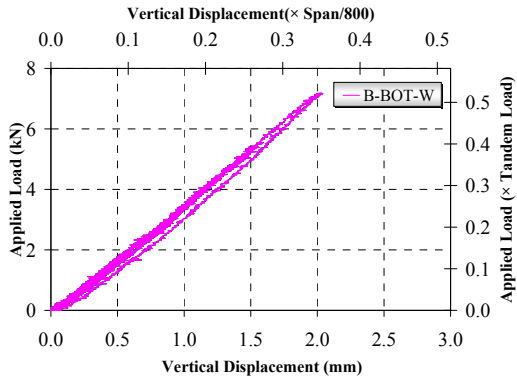


(b) L-TOP-4

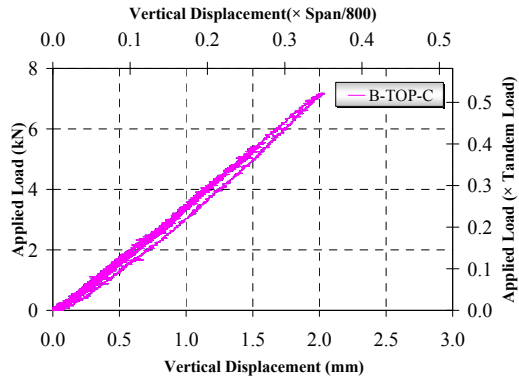


(b) L-TOP-W

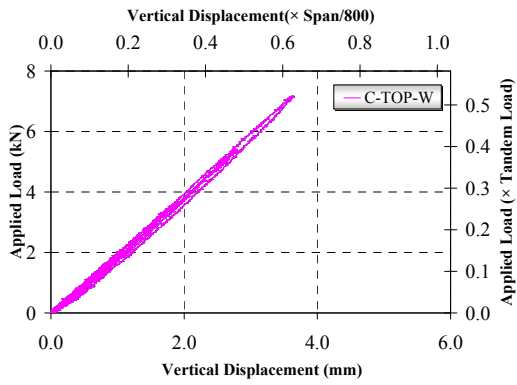
Figure 5.44 Forces vs. Displacement at the Top Surface (Negative Moment Flexure)



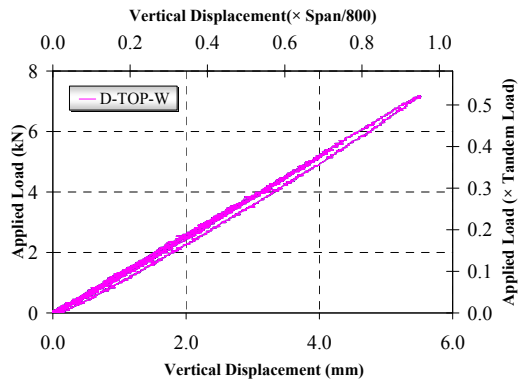
(a) B-BOT-W



(b) B-TOP-C

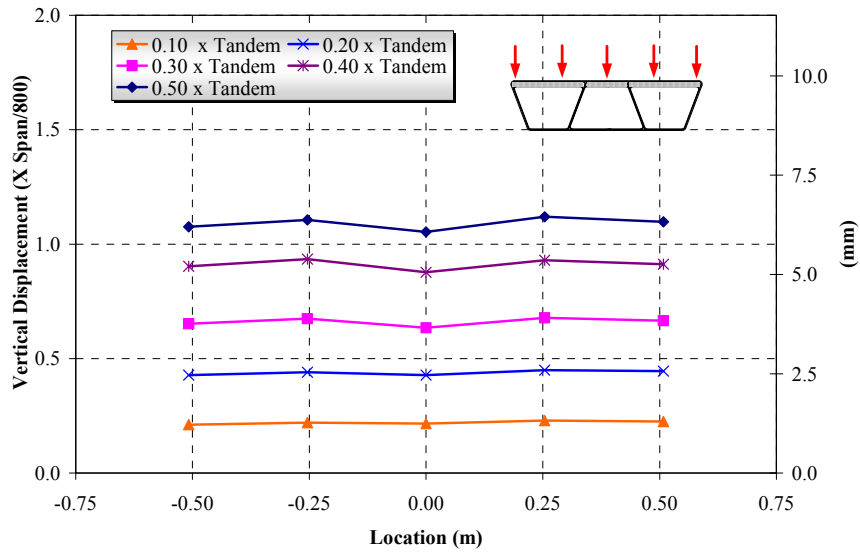


(c) C-TOP-W

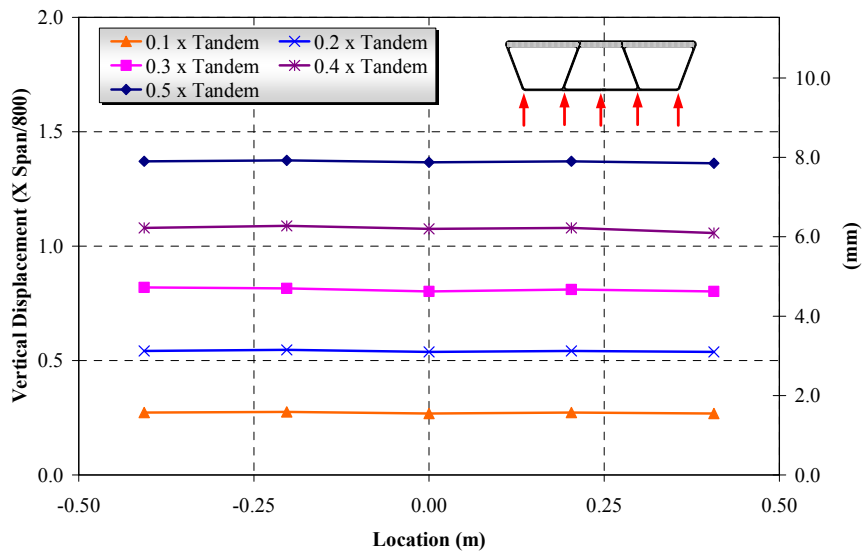


(d) D-TOP-W

Figure 5.45 Forces versus Displacement Relations for the Hybrid Specimen under Negative Flexure Test



(a) Top Surface



(b) Bottom Surface

Figure 5.46 Deformed Shapes at Different Load Levels for Hybrid Specimen in Negative Flexure

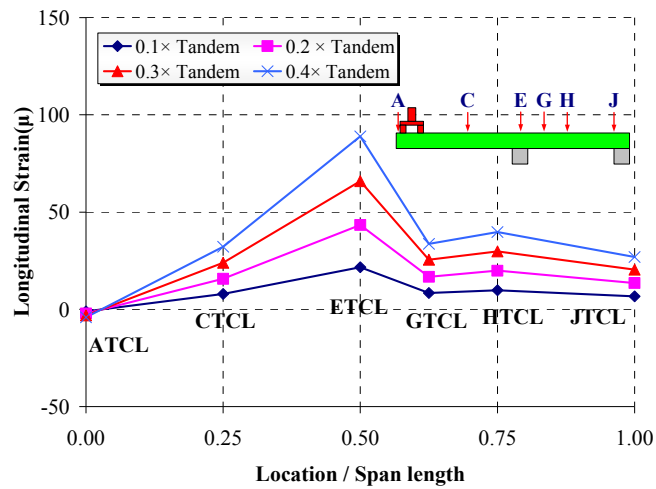


Figure 5.47 Longitudinal Strain Variations along the Centerline at Top Surface (Hybrid Specimen in Negative Flexure)

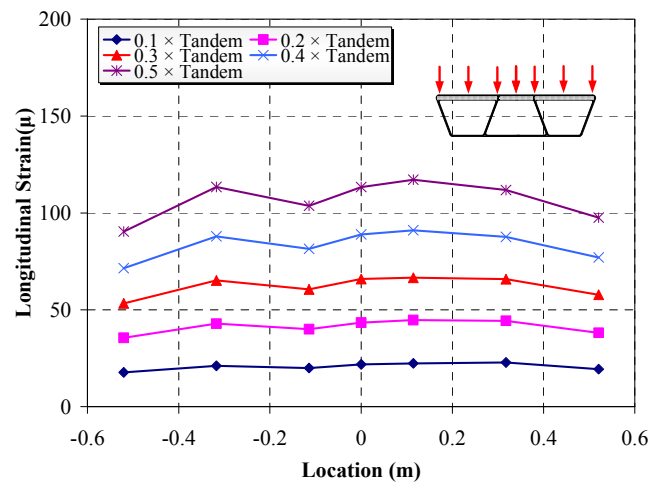
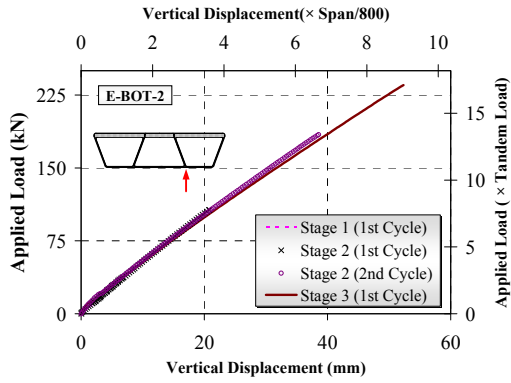
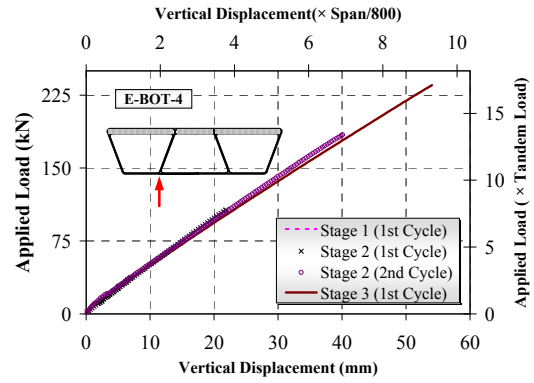


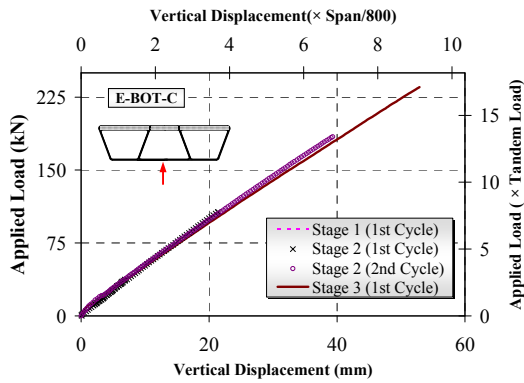
Figure 5.48 Longitudinal Strain Variations along Section E (Hybrid Specimen in Negative Flexure)



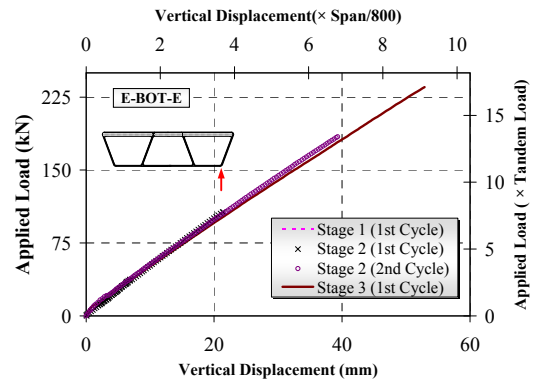
(a) E-BOT-2



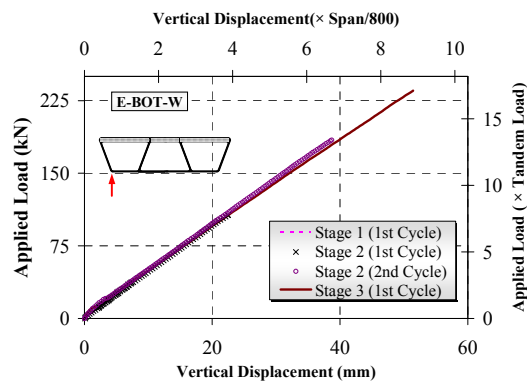
(b) E-BOT-4



(c) E-BOT-C

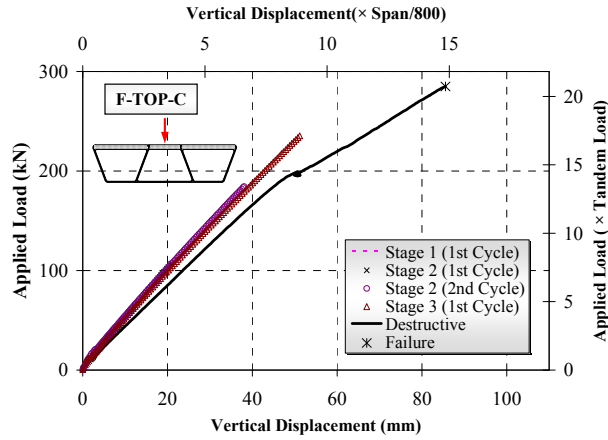


(d) E-BOT-E

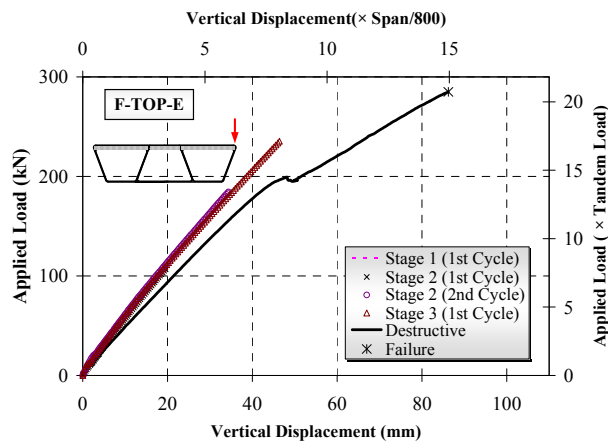


(e) E-BOT-W

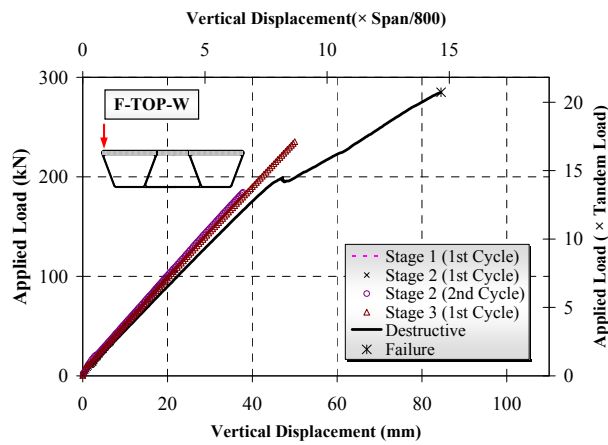
Figure 5.49 Forces vs. Displacement at the Bottom Surface (Destructive Flexure)



(a) F-TOP-C



(b) F-TOP-E



(c) F-TOP-W

Figure 5.50 Forces vs. Displacement at the Top Surface (Destructive Flexure)



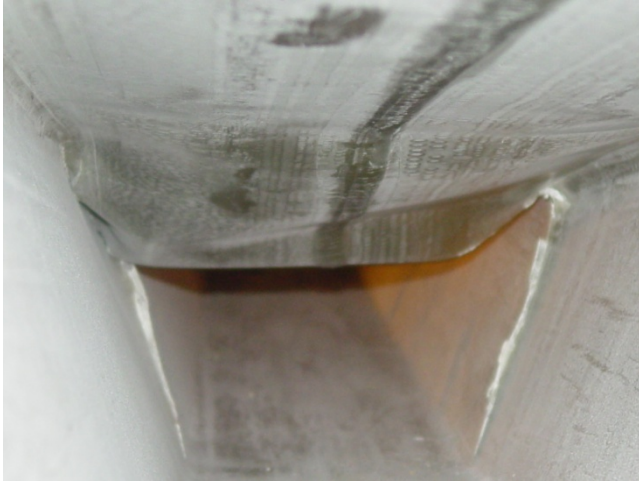
(a) Global Failure Mode



(b) Concrete Slippage

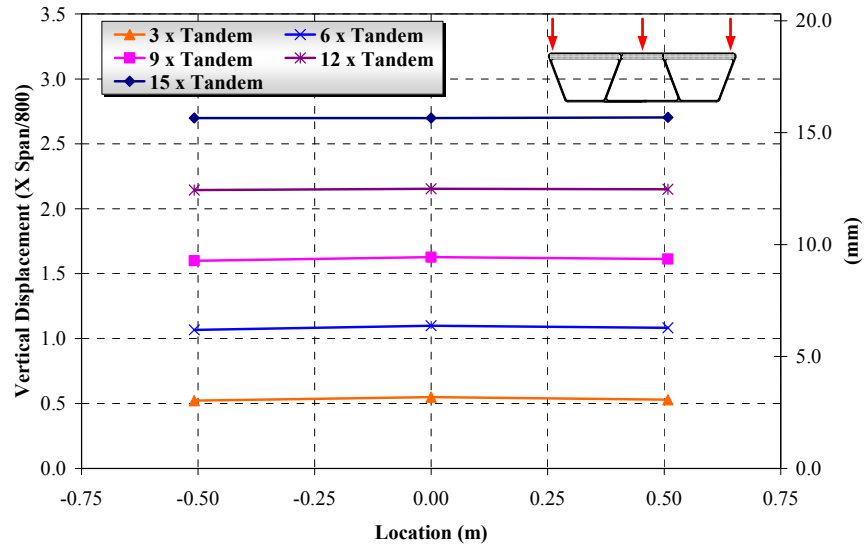


(c) Web Failure Mode

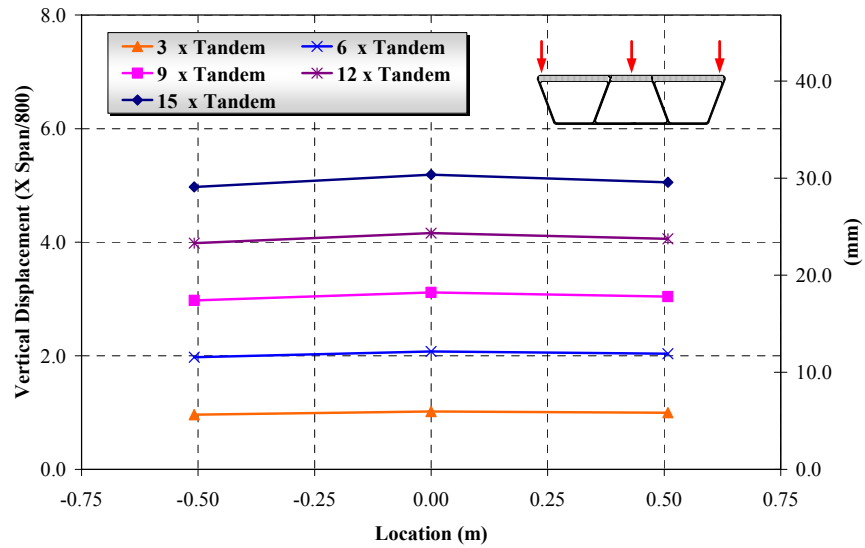


(d) Web Failure Mode

Figure 5.51 Different Failure Modes of Superstructure Specimen at Destructive Test

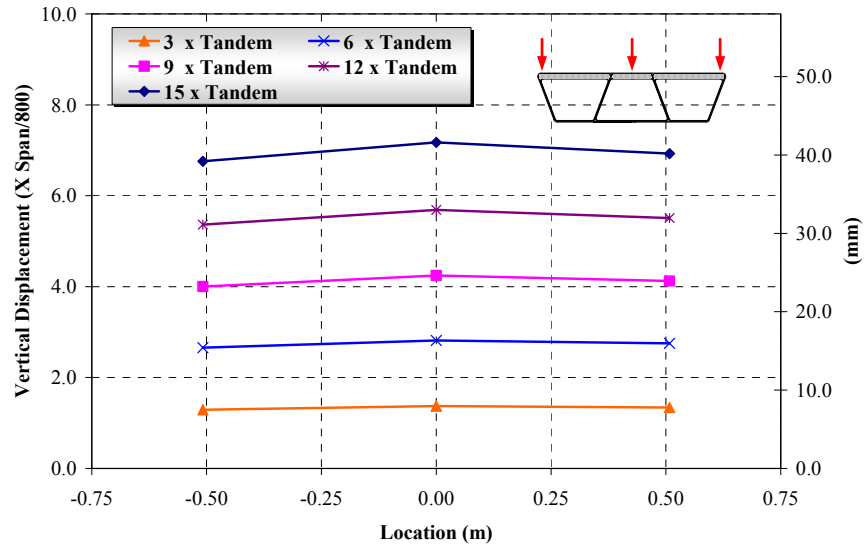


(a) Section I-I

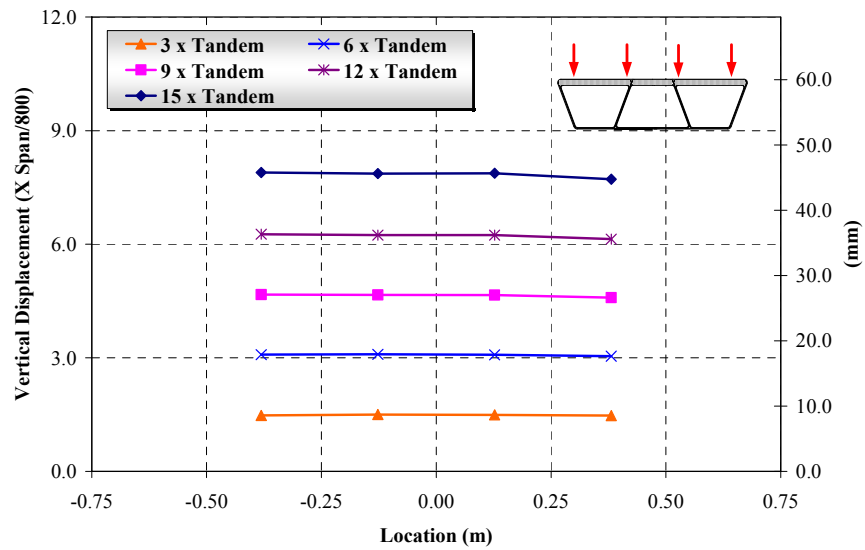


(b) Section H-H

Figure 5.52 Deformed Shapes at Different Load Levels in Destructive Flexure at Top Surface



(c) Section G-G



(d) Section F-F

Figure 5.53 Deformed Shapes at Different Load Levels in Destructive Flexure at Top Surface (cont.)

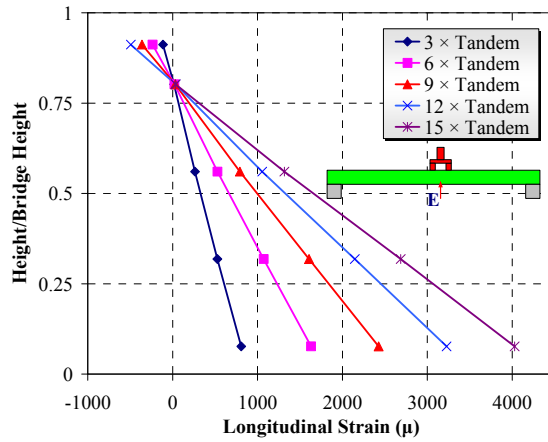


Figure 5.54 Strain Variations on the Exterior Web at Section E (Destructive Flexure)

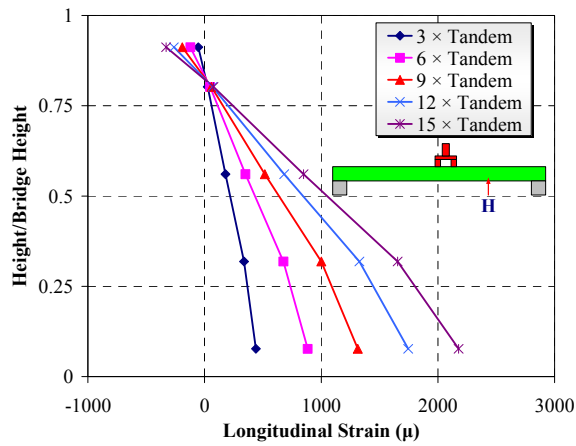


Figure 5.55 Strain Variations on the Exterior Web at Section H (Destructive Flexure)

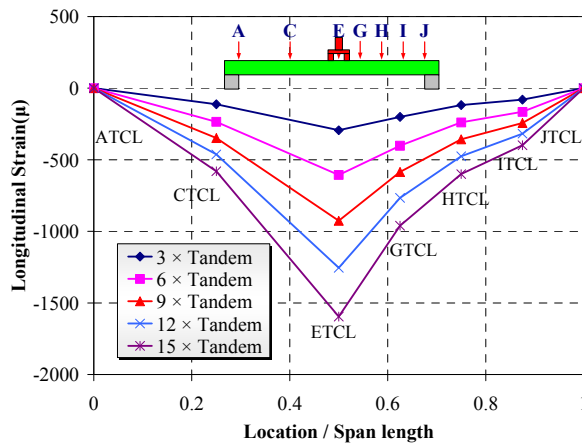


Figure 5.56 Longitudinal Strain Variations along the Centerline at Top Surface (Destructive Flexure)

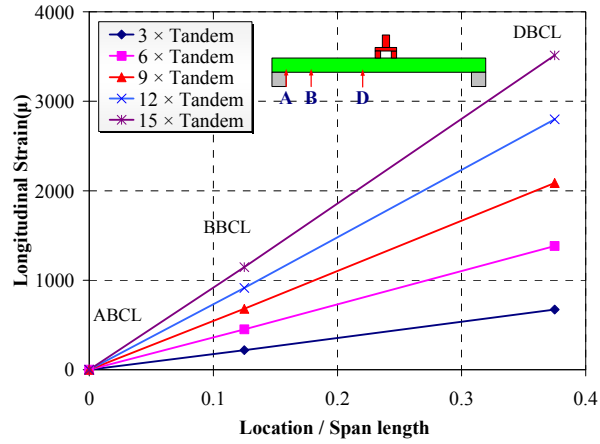


Figure 5.57 Longitudinal Strain Variations along the Centerline at Bottom Surface (Destructive Flexure)

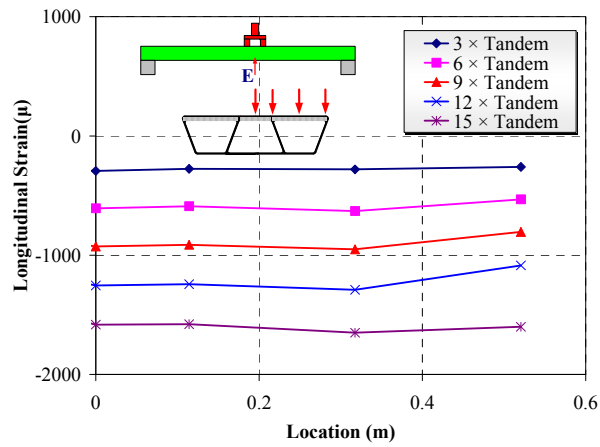
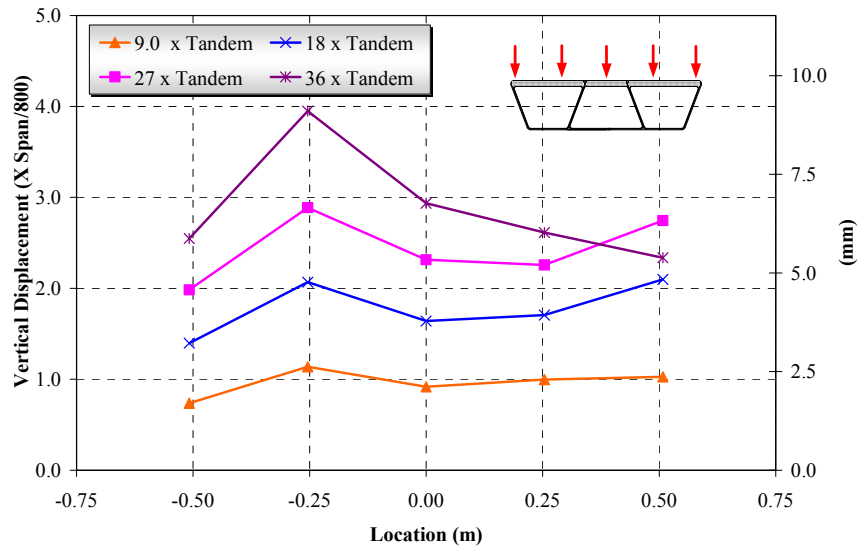
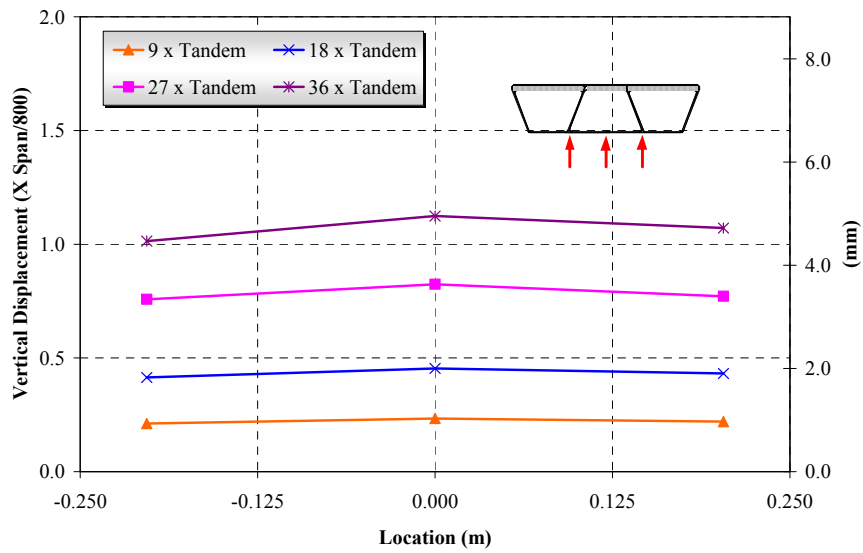


Figure 5.58 Longitudinal Strain Variations along Section E (Destructive Flexure)



(a) Section P-P



(b) Section O-O

Figure 5.59 Deformed Shapes at Different Load Levels for Hybrid Specimen in Shear



(a) Twisting of Spread Beam

(b) Local Deformation at the Top Surface



(c) Global Failure Mode



(d) Punching Shear failure Mode



(e) Shear Failure Mode

Figure 5.60 Failure Modes under the Shear Loading

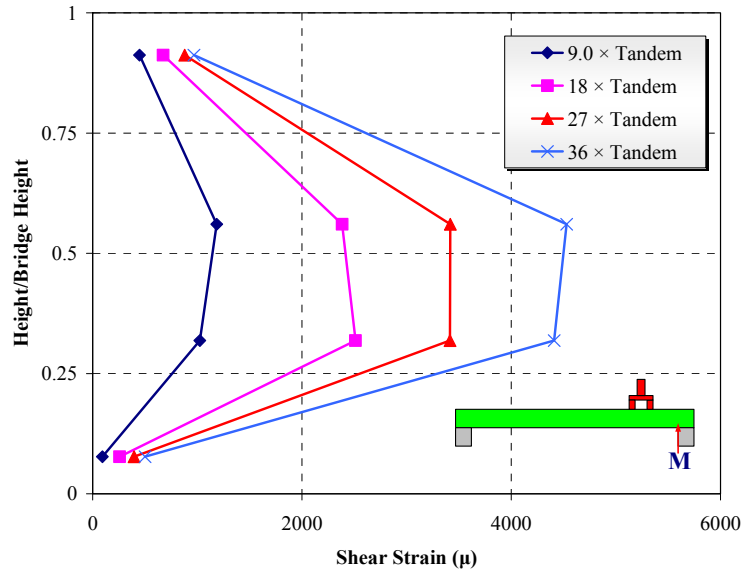


Figure 5.61 Shear Strain Variations on the Exterior Web at Section M (Destructive Shear)

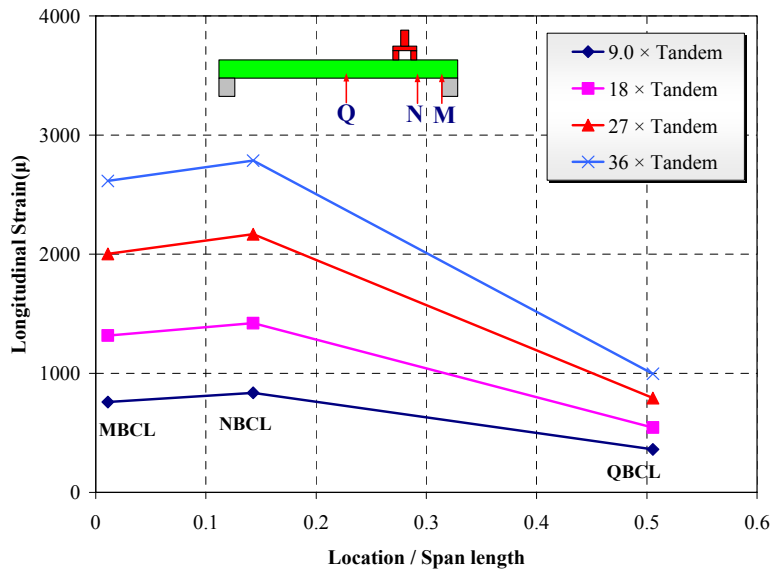


Figure 5.62 Longitudinal Strain Variations along the Centerline at Bottom Surface (Destructive Shear)

EXPERIMENTAL STUDY OF BRIDGE DECK ON STEEL GIRDERS

One of the most likely uses of the proposed hybrid FRP-concrete bridge system in the future is for hybrid bridge decks over steel or concrete girders. In this situation, the proposed system takes the place of traditional steel reinforced concrete decks. In this chapter, the proposed hybrid FRP-concrete structural system is applied to bridge deck systems. The proposed deck offers a number of advantages over the steel reinforced concrete decks. For example, they are resistant to corrosion and they can be placed very rapidly compared to typical cast-in-place reinforced concrete decks. In this chapter, a detailed description of a 3/4 scale steel bridge model with hybrid FRP-concrete deck is presented. In addition, the results of a series of service-level flexural loading tests are presented. The composite action between the hybrid deck and steel girders is analyzed and tested. Details for connecting the hybrid decks to steel girders are investigated. Moreover, the effective flange width (B_{eff}) in the hybrid FRP-concrete deck acting compositely with steel girders is evaluated.

6.1 BRIDGE CONFIGURATIONS

Prototype bridge system was designed as a simply supported steel bridge with a hybrid FRP-concrete deck. The bridge has a length of 6.5 m, and a width of 4.06 m. The height of the hybrid deck was limited to 0.2 m so that the proposed deck can be used for deck renewal projects.

The test specimen was a 3/4 scale model of the 6.5 m prototype steel bridge. The model had a length of 4.88. The deck model supported on steel girders had a length of 3.05 m a width of 3.66 m and a depth of 0.15 m. Similar to the hybrid superstructure which was described in chapter five, the hybrid FRP-concrete deck specimen (FRP part only) was

fabricated at An-Cor Industrial Plastics, Inc. in the N. Tonawanda, NY. Both elevation and side views of the steel bridge with a hybrid FRP-concrete deck are illustrated in Figure 6.1.

The hybrid bridge deck was comprised of three deck panels. Each panel was comprised of seven trapezoidal cross-sections surrounded by an outer shell as shown in Figure 6.2. A thin layer of concrete was placed in the compression zone of each section. Each trapezoidal section consisted of two layers of laminates: the inner tube laminate and the outer tube laminate. The inner tube with fiber orientations of $[0^{\circ}_4]$, was first constructed with a laminate construction, and the outer tube was then constructed over the inner tube laminate with a laminate construction $[0^{\circ}_3]$. The outermost laminate stacking sequence was $[0^{\circ}_5]$. Table 6-1 shows the stacking sequence and thickness of different layers of bridge deck model. As mentioned above, the stacking sequence chosen for all laminates was 0° . This would be because the woven fabric type chosen as reinforcement in this study has almost the same mechanical properties in the two orthogonal directions; also laminates with 0° direction reduce the manufacturing time of the specimen.

Each trapezoidal box section was fabricated individually by the hand lay-up process. The seven trapezoidal sections were then assembled by using vacuum bag process (see Figure 6.3). A layer of glass fiber chopped strand mat wetted with vinyl ester resin was applied between box sections as a bonding material. The seven trapezoidal sections were wrapped with the outer-most laminate.

To achieve good composite action between GFRP laminates and concrete, shear keys, as shown in Figure 6.4 were installed in staggered positions at the interface of the GFRP laminates and concrete. Each shear key had a length of 0.155 m for the side trapezoidal section and 0.076 m for the middle trapezoidal section in the transverse direction. They were installed on the top surface of the inner tube laminate and on the bottom surface of the outer tube laminate with an interval of 0.508 m. These shear keys were also made of GFRP composites.

The concrete layer was poured at the civil engineering laboratory at University at Buffalo. Foam dams were firstly placed in the shear studs holes (see section 6.2.2.5) to avoid leaking of concrete. The FRP-only specimen then was stood up and the concrete

was poured from the top. Wood formwork was placed in the inner cells along the span of the specimen to prevent buckling of the inner flange surface: the inner flange surface of all cells buckle. The cavities were filled completely with concrete.

As seen in Figure 6.1, the hybrid FRP decks were connected to a typical steel bridge. The bridge consisted of three W-beam girders (W300×96). Each of the three girders was spaced at 1.22 m, and the deck overhang was 0.305 m for the exterior girders. Cross-frames were placed within the specimen portion of the bridge at 0.25L, 0.5L, 0.75L (where L is the span length of the bridge specimen) and at the ends as shown in Figure 6.5 for stability. The cross-frames were constructed from L3x3x3/8 stock and welded in place in an 'X' configuration. Cold rolled bars, milled 6.4 mm off the top to ease in welding to the bottom side of the bottom flange, were connected to the girders to act as supports. The end supports, intended to idealize roller supports, were placed on stainless steel plates. The typical support detail is shown in Figure 6.6.

The materials used in this FRP-concrete bridge deck specimen model were the same as that these for the hybrid superstructure specimen described in chapter five.

6.2 JOINING TECHNIQUE FOR THE HYBRID DECK SYSTEM

As FRP-concrete bridge decks are a new structural system, there is no literature available that discusses connection techniques for this type of deck. Three classes of connections involving composites are identified in the Eurocomp Design Code and Handbook (2002): (1) primary joints, which carry major strength and stiffness to an assembly for the whole-life of the structure; (2) secondary structural joints, whose failure would be only local failure without compromising the entire structure; (3) non-structural connections, whose main purpose is to exclude the external environment. Primary and secondary structural joints are most concerned in construction, which include component-component connection, panel-panel connection, and deck-to-support connection. Zhou, and Keller (2005) documented the technical background, development and design guides of FRP bridge deck connections, and design principles concerning the joining of FRP decks. Joining techniques for panel-panel connections and deck-to-support connections for the proposed hybrid deck are discussed in the following sections.

6.2.1 Panel-Panel Connections

Panel level connections are necessary to efficiently transfer bending moment and shear forces between jointed panels, provide resistance to dynamic loads, and ensure deformation compatibility due to thermal and moisture effects.

Panel level connection techniques includes: adhesive bonding and mechanical fixing. Mechanical fixing includes shear keys, splicing tongue–groove connections, and clip-joints. Mechanical fixing has the advantage of easy disassembly. However, load transfer and failure resistant capability of mechanical fixing is not as efficient as bonded joining. Results from constructed projects with shear key connection show that cracks appeared after a period of exposure to highway vehicle loadings (Reising et al., 2004). The cracking at the shear key connection region shows that mechanically fixed connections are not reliable to resist dynamic vehicle loadings. Zetterberg et al. (2001) proposed two different joining techniques for pultruded composite profiles for bridge deck applications. They used both adhesively bonded and bolted joints for panel-to-panel connections, as shown in Figure 6.7. Their analytical results showed that the bonded joint is likely to always be easier to design and will be more amendable for realization.

As mentioned in section 6.1, the hand lay-up method was used to manufacture the proposed hybrid FRP deck panels. Reising et al. (2004) concluded that panels manufactured by hand lay-up method have worse dimension uniformity than those from pultrusion method. Since spliced connections require quality control on the dimensions of deck panels, it is not possible to use spliced connections in this study.

In this study, adhesive bond connections were used to maintain the integrity of the panel-connection-panel system. By using a detailed finite element model that is described in chapter seven, it was found that the maximum transverse shear stress at the interface between two panels of the proposed hybrid deck was 5.44 MPa under service loads (1×Tandem Load) that is smaller than the shear strength of commercially available resin, which ranges from 10.35 to 34.5 MPa (Aref, 1997). However, a disadvantage of bonded connections is the difficulty of their disassembly for repair.

6.2.2 Connection of Hybrid deck on Steel Girders

For system-level connections, shear transfer and connection constructability are the major concerns. One of the challenges with the proposed hybrid deck is the development of a reliable connection between the deck and the girders. So far, there is almost no hybrid FRP-concrete bridge decks are available in service worldwide. Alternatively, a considerable amount of FRP decks were constructed in the last decade. This is of interest since the behavior of the connection for hybrid decks is conceptually similar to that of FRP decks. Consequently, a summary of a literature review of the connection techniques of FRP deck to steel girders is presented the following subsections.

The majority of the current available constructed FRP decks are supported by steel girders. Most of the constructed FRP decks-on-steel girders were designed as non-composite structures: they rely on the steel girders to support longitudinal shear and bending stresses due to dead and live loads, and the deck acts to support vehicular live load and distribute this to the supporting girders. The degree of composite action significantly affects the behavior of the composite section. If there is no composite action and the section is subjected to some arbitrary vertical loading, the bottom surface of the slab is in tension (and elongates) where as the top surface of the beam is in compression (and shortens). Slip occurs between the two surfaces. Where some composite action exists, the slip will be reduced. For full composite action, there is no slip.

Mechanical fixing, adhesive bonding and hybrid joints have been used to connect FRP decks to steel girders. Mechanical fixings include stud-type connections, clamped connections and bolted connections. Depending on the requirements of a specific project, the deck-girder connection could be a permanent joint with composite action or an easily disassembled joint without the need of composite action between the deck and its supports. In connections with composite action, the efficiency of shear transfer and constructability are major factors influencing the design of the connection. The following subsection describes typical connections for FRP decks.

6.2.2.1 Shear Studs Connections

Headed shear studs are routinely used to provide shear continuity across the steel-concrete interface in of steel-concrete composite beams in buildings and bridges. Creative Pultrusions, Inc., Martin Marietta Composites (MMC), and Hardcore Composites (HC) are three manufacturers of FRP bridge decks that have used shear-stud type connections (Market Development Alliance, 2000 and Lesko, 2001). Creative Pultrusions, Inc. manufactures SuperdeckTM, a bridge deck formed by alternating double trapezoidal and hexagonal pultruded sections that are bonded together. The shear connection designed by Creative Pultrusions, Inc. for use with SuperdeckTM involves with a 101.6 mm diameter hole drilled through the deck over a girder (see Figure 6.8). A shear stud is field welded to the girder through the hole. The hole is then blocked off with cardboard and as indicated in the figure filled with non-shrink grout. The hole is then covered with a bonded FRP flat sheet. Duraspan is a similar product to Superdeck. Duraspan manufactured by MMC composed of pultruded trapezoidal sections bonded together. Similar to the SuperdeckTM connection described above, a hole is drilled through the FRP deck above the girder, blocked off with foam inserts, and shear studs are field welded to the top flange of the girder. The Duraspan connections consist of pairs of either 19 mm or 22.2 mm diameter shear studs with a wire spiral. The hole is then filled with non-shrink grout and covered with a FRP overlay. HC manufactures honeycomb sandwich panels using an adaptation of Vacuum Assisted Resin Transfer Molding (VARTM). The HC connection consists of a shear stud fitted in a hole that is drilled through the deck, which is filled with grout to secure the connection.

Moon et al. (2002) investigated three different shear studs connections between steel girders and the MMC Gen4 FRP deck through static and fatigue testing. Figure 6.9 shows the three connections. The shear studs measured 22 mm in diameter, 150 mm in length, and had minimum yield strength of 480 MPa. Static test results suggested that a larger volume of concrete surrounding the shear studs decreased the stress concentration directly behind the shear studs and alleviated local crushing. Moon et al. (2002) concluded that approximately 60–70% of the capacity of a longitudinal connection in a continuous concrete deck was developed with this connection. This decreased capacity

was due to failure modes related to the discrete nature of FRP decks. An expression was proposed to determine the longitudinal capacity for shear stud connections in FRP decks as follows:

$$Q_n = t_{fs} d_{sc} F_{fcp} \leq A_{sc} F_u \quad (6.1)$$

where:

- Q_n : nominal shear capacity of one stud
- t_{fs} : thickness of the bottom face sheet
- d_{sc} : diameter of shear connector
- F_{fcp} : compressive strength of composite material
- A_{sc} : area of shear connector
- F_u : ultimate shear stress of connector

Righman et al. (2004) proposed a clamped shear stud connector for FRP decks to steel stringers. As shown in Figure 6.10, the connection consisted of a threaded shear stud welded to the top flange of the supporting girder and housed inside steel sleeves that were installed within a hole drilled through the FRP deck. The performance of the proposed connector was verified through experimental testing of a reduced scale bridge.

Reising et al. (2004) summarized installation issues for four FRP panel systems installed in a 207 m, five-span, and three-lane bridge. All panels were delivered to the site with pre-drilled stud at 1.2 m intervals; 18 cm studs were welded onto the girders through the stud holes. By monitoring the response of the bridge over a period of two years, it was observed that the thermal characteristics of the FRP panels, which resulted in unexpected uplifts and significant thermal gradient, are mainly responsible of the vertical displacement of the panels related to the girders.

6.2.2.2 Clamped Connections

Kansas Structural Composites, Inc. (KSCI) manufactures a sandwich FRP deck with a sinusoidal honeycomb type FRP core. They have adopted a clamped connection for these panels for bridge applications (Meggers, 2000). The connections are placed at panel-to-panel joints. Each joint contains a FRP tube through which holes are drilled and

bolts installed to secure a clamping device. Figure 6.11 shows details of the KSCI Clamp Connection.

Clamped connection is effectively prevents uplift of the panels at the joints. (although spacing the connections at the ends of the panels only might be too liberal to provide adequate restraint). While in most cases, a composite action between the deck and its support was desirable. Clamped connection is not intended to develop composite action between deck and the supporting girders. As a result, a large portion of impact loads is taken by the FRP deck; therefore, this design is suitable for rehabilitation or repair to reduce the loading impacts on the existing supports. The clamp device is also fairly labor intensive, as the connection needs to be installed from underneath the bridge deck.

6.2.2.3 Bolted Connections

Bolts have been used occasionally to provide a connection between FRP decks and girders (Lesko, 2001), and are installed typically inside of steel sleeves through matched holes drilled through the entire depth of the deck and the top flange of the girder. Bolts are installed from beneath top flange of the girder (see Figure 6.12).

Park et al. (2004) presented a new connection method for deck-to-girder connections of GFRP decks. They proposed a mechanical connection using bolts as shown in Figure 6.13, and concluded that the anchor bolt diameter should be at least 20 mm and recommended an edge distance of between 1.4D and 2.0D times the bolt diameter. Kim et al. (2005) proposed bolted connections for deck to concrete girder connection (see Figure 6.14). The proposed deck-to-concrete girder connection by Kim et al. (2005) is suitable for the deck renewal projects.

6.2.2.4 Adhesive Connections

Adhesive bonding has the advantage of high strength and good corrosion resistance. When the deck supports are wide and flat, it is possible to use an all-adhesive connection. In this case, adhesive bonding is preferable to hybrid connecting mainly because fewer steps are involved in the bonding process and connector forces are evenly distributed along the joint.

Keller and Gurtler (2004) showed that adhesive bonding between FRP bridge deck and steel girders behaved well under quasi-static and fatigue loading. The connection did not

fail and showed no damage after 10 million cycles of loading. Keller and Gurtler (2005) tested two large scale hybrid girders consisting of FRP bridge decks adhesively connected to steel beams. Response of the two girders was studied at the service and failure state. The results showed that the adhesive connection between GFRP bridge decks and steel girders behaved well under creep loading.

6.2.2.5 Summary

The proposed hybrid deck, which was investigated in this study, should serve as transverse load-carrying element as top chord in composite bridge. After studying the performance and installation issues for different connections, which was described in the previous sections, it was decided that a welded shear stud connection is the most efficient for system-level connection. Implementing familiar shear stud technology enables the design to be both easy to install and cost effective. Construction of this connection in this study involved: welding the threaded studs to the girder. Then, a 0.05 m diameter holes were drilled at some desired spacing through the top and inner flange of the hybrid specimen. In addition, rectangular with semi-circle holes were drilled through the bottom face of the specimen (see Figure 6.15). The holes were then blocked off with foam inserts. Subsequently the hybrid deck was placed on the girders. Holes were then filled with non-shrink concrete and covered with the FRP cutouts by using adhesive resin to protect the cutout regions from environmental attacks.

AASHTO LRFD 1998 has design specification for shear studs for only concrete decks. In this study, FEA was used to design the shear studs. The averaged horizontal shear force between the hybrid deck and the steel girders were computed. Then, number of the required shear studs to resist that shear was calculated. Hence, eight (12.7 mm) diameter, (101.6 mm) height stud connectors were used and distributed in certain locations along the entire span (see Figure 6.15). Longitudinal shear studs spacing is specified in Figure 6.16.

The shear studs connectors, which were used in this study, intended to provide composite action between the hybrid deck and steel girders. Composite action offers several advantages for the hybrid deck: (1) the overall stiffness and load resistance capability of the hybrid deck system can be significantly increased compared to its individual girders;

(2) the overall bridge system can have ductile characteristic since the girder is made from ductile material (steel) due to the loads transfer efficiency between the brittle hybrid deck and its ductile support.

6.3 SERVICE LOAD EFFECTIVE FLANGE WIDTH

Under positive bending moment, part of the hybrid deck will act as the compression flange of the hybrid girder. When the spacing between the girders becomes large, beam theory does not apply because the longitudinal compressive stress in the flange will vary with the distance from the girder web. This phenomenon is termed “shear lag.” This phenomenon would be due to the action of in-plane shear strain in the flange plate of a composite girder under flexure where the longitudinal displacements in the parts of the flanges remote from the webs lag behind those near the webs. This phenomenon can result in inaccurate estimation of the deflections and stresses in the flange, based on the simple beam theory as stated by Moffatt and Dowling (1978). For the shear-lag phenomenon in slab-on-girder structures, the concept of an effective flange width was introduced many years ago, for conventional reinforced concrete, to provide a simple procedure to indirectly address shear lag in T-shaped beams. Four factors influence the effective width of concrete flanges for composite beams: (1) span; (2) beam spacing; (3) degree of interaction between slab and beam; and (4) pattern of loading (Elkelish and Robinson, 1986). Codes implement different approaches for specifying effective flange width. For example, the 1998 AASHTO-LRFD Bridge Design Specification contains provisions for the effective flange width of interior and exterior girders. For Interior girders; the effective flange width can be taken as the least of:

- One-quarter of the effective span length;
- Twelve times the average thickness of the slab plus the greater of web thickness or one-half the width of the top flange of the girder; or
- Average spacing of adjacent girders

For Exterior girders, the effective flange width can be taken as one-half the effective flange width of the adjacent interior girder, plus the smallest:

- One-eighth of the effective span length;

- Six times the average thickness of the slab plus the greater of half the web thickness or one-quarter of the width of the top flange of the girder; or
- Width of the overhang.

There is no guidance as for the effective width for composite FRP-steel girders at this time.

Keelor et al. (2004) conducted a field study of a FRP deck-steel girder composite bridge in Pennsylvania. The bridge employed a cellular FRP deck system that was attached to the steel girders by headed shear studs and grouted in place within the FRP cells using a non-shrink grout. The bridge was instrumented and was subjected to a series of service loads. The data were collected and used with standard transformed section calculations to identify appropriate effective widths. Keelor et al. observed that FRP decks and floors acting compositely with underlying steel girders exhibited an effective width, at the service condition, of approximately 75% of the girder spacing for interior girders and 90% of the total distance, made up of the girder spacing added to the deck overhang, for the case of exterior girders.

Guidelines for hybrid FRP effective widths useful in the design of fully composite hybrid deck-steel girder installations in the service load condition were provided in this study. The service load level is important for the case of hybrid deck-steel girder composite construction since the ultimate strength performance of such systems is currently not known and hence frequently not considered in design. However, the service load composite response of these systems is frequently assumed to hold and hence the composite cross section is considered when computing live load deflections. To support this design approach, effective compression flange widths are required for the service load condition. The data were collected from experimental results as will be discussed in section 6.7, and used with standard transformed section calculations to identify appropriate effective widths. Effective width ratio can be defined as the ratio between the effective flange width to the girder spacing for interior girder installations, and to the total distance, made up of half of the girder spacing added to the deck overhang, for the case of exterior girders.

6.3.1 Transformed Section Calculations

Based on the upward shift in the measured steel girder neutral axis location, it is possible to compute the level of assistance the hybrid deck provided in resisting the internal moments needed to equilibrate the tandem loadings. The strain gages data of the steel girders obtained from test results under service loads as will be discussed in section 6.4, had been used to determine the neutral axis location of steel girder. Using this approach it is then possible to back-calculate the hybrid deck effective compression flange width using standard transformed section properties related to the modular ratio of steel to both FRP and concrete.

Figure 6.17 presents the idealized cross-sectional used for calculating effective width for service loading computations. The first approximation is that only a portion of the hybrid FRP-concrete deck cross section is effective in resisting the compressive stress that develops during the formation of the internal equilibrating moment of the composite cross section: the three “FRP face sheets” in combined with the concrete layer of the hybrid deck are the only portion of the hybrid system that is continuous over the entire span of the steel girder. This last point may be understood when considering that the hybrid deck may be thought of as being made of hollow square tubes bonded together and oriented such that the tubes are perpendicular with the steel beam longitudinal axis. As a result of this, it can be assumed that, due to voids inside the tubes, it is only the top, inner flange, and bottom tube walls in combined with the concrete layer that are in continuous contact across tube interfaces and thus represent the only contiguous elements within the hybrid system considered. A detailed discussion of the transformed section calculations that incorporate the experimental results may be found in the Appendix B.

6.4 INSTRUMENTATION

Various instruments (strain gages, potentiometers, KRY, etc) were used to capture the specimen behavior during testing. Slightly altered arrangements of instrumentation were used according to service loading conditions

Only a quarter of the test specimen was instrumented due to symmetry. To acquire a good resolution of the deck shear lag in the positive moment regions for service loadings, strain gages were located at several cross-sections along the span of the specimen. The

layout of the strain gages on the top surface of the hybrid deck is presented in Figure 6.18. A significant number of gages were placed at the midspan of the specimen since one objective of this experiment was to investigate the behavior of cross sections that would achieve maximum strain during loading. A significant number of gages were placed along girder 1 and 2 to provide information on composite action. Another transverse line of strain gages was placed at 0.77L from bridge support to provide data at locations removed from local effects due to loading. Other gages were placed to provide data to plot the strain profile through the thickness of the deck.

Other gages were placed on the bottom surface of the hybrid deck to provide information on the strain variation in plan across the width of the deck. The layout of strain gages on the bottom surface of the hybrid deck is presented in Figure 6.19.

Potentiometers were placed under the girders as shown in Figure 6.20 so that the deflected shape could be measured directly. LEDs were installed on the top of the hybrid deck to measure vertical displacements at several locations along the specimen. Figure 6.21 shows the location of LEDs for service test cases 1 to 5; Figure 6.22 shows plan of LEDs for service test cases 6 and 7.

To measure the slip between the hybrid deck and girder and between the concrete box holding the shear studs and the deck, during the service tests, slip gages were installed along the central girder and one of the two edge girders at midspan. The readings from these gages represent the relative displacement between the deck and the girder. To achieve a direct comparison between FEM and experimental results, applied force values are required. This project was not focused on distribution of load to girders; therefore load cells were installed above the spread beam to capture the force being applied to the specimen.

6.5 EXPERIMENTAL SET-UP

Figure 6.23 shows service load test fixture. The three steel girders were simply supported on W 760×284 beams. Loads were applied to the top surface of the test specimen by the compression stack beam from actuators attached to the strong floor. In the transverse direction, the actuators were stabilized by a steel box. The load configuration simulates the tandem load specified in the 1998 AASHTO LRFD Bridge

Design Specifications. The design tandem load is defined as a live load that has two axles of 110 kN. One axle is 1.2 m away from the other. Each axle has two tires that are 1.8 m apart center-to-center. Each tire area is 0.510 m wide and 0.385 m long. For the 3/4 scale model, this design tandem load becomes two axles of 61.875 kN 1.35 m apart. The two tires of each axle are 0.9 m apart and each tire area is 0.383 m wide and 0.289 m long. To simulate the tire areas, four steel plates covered by rubber with the same area as the scaled tire area were attached to the bottom face of the spreader beams. Figure 6.24 presents photographs of steps in the specimen setup.

6.6 EXPERIMENTAL PROTOCOL

The objectives of the experimental investigation was to 1) capture the global response of the specimen subjected to a series of service flexural loading tests under different loading conditions, 2) to investigate the shear connection developed in section 6.2.2.5 and 3) to provide guidelines for computation of effective flange widths to be employed in the design of FRP deck system. The maximum applied load to the specimen was 123.75 kN which represents ($1 \times$ Tandem Load).

Figure 6.25 shows the seven service load cases. The locations at which the load was applied are identified by the four boxes in each figure. Case 1 was designed to simulate the tandem load specified in the 1998 AASHTO LRFD Bridge Design Specifications. Cases 2 and 3 were designed to determine the governing case for the interior girder. Case 4 was intended to maximize the shear lag over the girders. Case 5 sought to identify the governing case for an exterior girder. Cases 6 and 7 are identical to cases 2 and 5 with the design tandem shifted to $0.62L$ to examine the panel-to-panel joints. The maximum applied load for each case was applied three times during each test.

6.7 TEST RESULTS

Selected results for all seven different service loading cases are presented in this section. No sound of cracking GFRP laminates was heard during the service loading of the specimen. Visual inspection after each loading case revealed no cracking in the exterior GFRP laminates. No signs of damage were observed in the shear connection.

There was no slip between either the hybrid deck and the girders or the concrete box (holding the shear studs) and the deck during the service load tab.

6.7.1 Service Load Case 1

Figure 6.26 shows the test set up for service load case 1. The deformed shapes of the top surface of the specimen are shown in the panels of Figure 6.27. In these figures, the vertical axis represents the vertical displacement. From Figure 6.27(a) it can be seen that the displacement was greatest at the point closest to the loading point. All three panels show near linear relationships between force and displacement which indicates that the hybrid deck can be modeled as a linear material for service loads. From Figure 6.27(b) it can be seen that the displacement along the cross section was nearly the same since it is far from the loading points

Figure 6.28 shows deformed shapes of the bottom surface at different load levels (refer to Figure 6.20 for measurement locations). According to AASHTO (1998), the maximum deflection under (1+IM)×truck load is $L/800 = 6.10$ mm, where L is the span length. However, the (1+IM)×tandem load was used here for comparison since the loading configuration in the test simulates the tandem load. One can see from Figure 6.28(c) that the deformation in the hybrid deck measured at B-BOT-C due to (1+IM)×tandem load was 2.79 mm ($0.46 \times L/800$). This hybrid deck easily satisfied the AASHTO live load deflection limit. Displacements of the exterior steel girder are shown in Figure 6.28(b). The maximum deformation at the midspan of the exterior steel girders measured at A-BOT-5 due to (1+IM)×tandem load was 1.96 mm ($0.32 \times L/800$).

Figure 6.29 shows the variation in strain along the interior and exterior steel girders at sections C and H. This figure shows that the plane section before deformation remains plane after deformation. The linearity of strain means that beam theory can be used to design of the deck under service load. The location of the neutral axis obtained from the test was shifted upward due to the composite bending action between the hybrid deck and the underlying steel girder, but did not move as the load was increased from 0.25×Tandem to 1.00×Tandem. The strain variation through the steel girders was used to calculate the location of the neutral axis for each of the two instrumented cross sections in the interior and exterior girders. From strain variation in Figure 6.29(d), it can be said

that the hybrid deck and the exterior steel girder are interacting in a fully composite way at section H under service loads as evinced by the continuity in strain at the hybrid deck-to-steel interface, no slip between the FRP deck and the steel girder at that cross section.

Based on the upward shift in neutral axis location from the centroid of the steel beam alone, it is a simple exercise to compute the contribution of the hybrid deck to the internal moment and the effective compression flange width. The results are summarized in Table 6-2 for both interior and exterior girders; Appendix B provides the detailed calculations. Based on the current results it was observed that the hybrid decks, acting fully compositely with the steel girders, exhibit an effective width, at service condition, of approximately 54% of the girder spacing for the interior girder installations and 61% of the half of the girder spacing and the deck overhang for the exterior girders.

Figure 6.30 shows the measured longitudinal and transverse strains at different cross sections of the specimen. Figure 6.30(a) and (b) show the transverse and longitudinal strain variations along the centerline of the top surface of the hybrid deck, respectively. Figure 6.30(b) shows that the longitudinal strain varies substantially in the section because Section D is very close to the loading points.

The longitudinal strain along section K is not uniform as a result of shear lag. Figure 6.30(d) presents the measured transverse strain profile along section G. Figure 6.30(e) presents the measured longitudinal strains at bottom surface of the deck at midspan. Figure 6.30(e) indicates that the longitudinal strain does not vary in the cross section. Figure 6.30(f) presents the longitudinal strains measured along the centerline of bottom surface. At the load level of $1 \times$ Tandem Load, the strain measured at location DBCL was 254μ , which is a very small value when compared to the averaged ultimate strain obtained from the material tests.

6.7.2 Service Load Case 2

Service load case 2 is similar to service load case 1 except the tandem load was shifted and the axle tires were placed at the centerlines between the girders as shown in Figure 6.25.

The deformed shapes of the top surface of the specimen are shown in Figure 6.31(a), (b) and (c). The measured displacements correlate well with those of service load case 1.

This confirms that the measurement system was consistent. Figure 6.32 shows deformed shapes of the bottom surface of the specimen at different load levels; the measured displacements also correlated well with those of service load case 1.

Figure 6.33 shows strain variation along the interior and exterior steel girders at section C and H.

Figure 6.34 shows the measured longitudinal and transverse strains along different cross sections of the specimen. Figure 6.34(a) and (b) show the transverse and longitudinal strain variations along the centerline of the top surface of the hybrid deck, respectively. The longitudinal strain along section K (See Figure 6.34) of the deck is not uniform. As a result of shear lag. Figure 6.30(d) presents the measured transverse strain profile along section G. Figure 6.34(e) shows the longitudinal strains measured along the centerline. Figure 6.34(f) shows the measured strains on the interior web at Sections F-East (refer to Figure 6.19 for location). This figure shows that the plane section before deformation remains plane after deformation. The location of the neutral axis of the hybrid deck obtained from the test was shifted upward due to concrete layer in the compression zone.

6.7.3 Service Load Case 3

Service load case 3 was designed to determine the governing case for the interior girder. The tandem load was shifted, and one axle of tires was placed exactly on centerline between girders, and the other one was placed on the interior girder, as shown in Figure 6.35.

The deformed shapes of the top surface of the specimen are shown in the panels of Figure 6.36. Figure 6.37 presents the deformed shapes of the bottom surface of the specimen at the different load levels. Deformation of the exterior steel girder is shown in Figure 6.37(b). The maximum deformation at the midspan of the interior steel girders measured at A-BOT-5 due to $(1+IM) \times$ tandem load was 1.9 mm ($0.31 \times L/800$).

Figure 6.38 presents the variation in strain along the interior and exterior steel girders at sections C and H. Figure 6.39 presents the longitudinal and transverse strains along different cross sections of the specimen. Figure 6.39(a) and (b) show the transverse and longitudinal variation in strain along the centerline of the top surface of the hybrid deck, respectively. The longitudinal strain along section K of the deck is not uniform. This is a

result of the shear lag. Figure 6.30(d) presents the transverse strain profile along section G. Figure 6.34(e) shows the longitudinal strains measured along the centerline. Figure 6.34(f) shows the measured strains on the interior web at Sections F-East.

6.7.4 Service Load Case 4

Service load case 4 intended to maximize shear lag over the girders. The tandem load was shifted over the interior and the exterior girders, as shown in Figure 6.40.

The deformed shapes of the top surface of the specimen are shown in the panels of Figure 6.41. Figure 6.42 presents deformed shapes of the bottom surface at the different load levels. Results showed that the entire bridge specimen acted together under such a loading condition; the hybrid deck bended as one unit. The deformation of the exterior steel girder is shown in Figure 6.42 (b). The maximum deformation at the midspan of the interior steel girders measured at A-BOT-5 due to $(1+IM)\times$ tandem load was 2.46 mm ($0.40\times L/800$).

Figure 6.43 presents the variation in strain along the interior and exterior steel girders at sections C and H. Figure 6.44 shows the measured the longitudinal and the transverse strains along different cross sections of the specimen. Figure 6.44(a) and (b) show the transverse and longitudinal the variation in the strain along the centerline of the top surface of the hybrid deck, respectively. Figure 6.44(c) presents the measured transverse strain profile along section K. Figure 6.44(d) presents the longitudinal strains measured along the centerline. The longitudinal strain along section K of the hybrid deck is not uniform. This is a result of the shear lag. Figure 6.44(e) shows the longitudinal strain along section G.

6.7.5 Service Load Case 5

Service load case 5 sought to identify the governing case for an exterior girder, and the overhang of the hybrid deck. The tandem load was shifted over the interior and the exterior girders, as shown in Figure 6.45.

The deformed shapes of the top surface are shown in the panels of Figure 6.46. Figure 6.47 presents the deformed shapes of the bottom surface at the different load. The deformation in overhang of the hybrid deck due to $(1+IM)\times$ tandem load was 4.66 mm ($0.76\times L/800$). The overhang of the hybrid deck easily satisfied the AASHTO live

load limit. Displacement of the exterior steel girder is shown in Figure 6.28(b). The maximum deformation at the midspan of the exterior steel girders measured at A-BOT-5 due to $(1+IM)\times$ tandem load was 4.60 mm ($0.75\times L/800$).

Figure 6.48 presents the strain variation along the interior and exterior steel girders at sections C and H. From strain variation along section H-west, it can be said that the hybrid deck and the exterior steel girder are interacting in a partially composite way at service loads as evinced by the discontinuity in strain at the hybrid deck-to-steel interface. This result means that there was slip between hybrid deck and steel girder. Figure 6.49 presents the measured longitudinal and transverse strains along different cross sections of the specimen. Figure 6.49(a) and (b) present the transverse and longitudinal strain variations along the centerline of the top surface of the hybrid deck, respectively. Figure 6.49(c) shows the measured transverse strain profile along section K. Figure 6.49(d) presents the longitudinal strains measured along the centerline. The longitudinal strain along section K of the hybrid deck is not uniform particularly above the exterior beam. Again, this is a result of the shear lag. Figure 6.49(e) shows the transverse strain along section G. Figure 6.49(f) shows the measured strains on the interior web at Sections F-East.

6.7.6 Service Load Case 6

Service load case 6 is identical to the service load case 2 with the exception that the load was applied at $0.62\times L$ (where L is the bridge span length), as shown in Figure 6.50.

The deformed shapes of the top surface of the specimen are shown in Figure 6.51(a), (b) and (c). Figure 6.52 presents deformed shapes of the bottom surface of the specimen at the different load levels. The maximum deformation at midspan of the exterior girder is much less than that when the specimen was subjected to load case 2. Figure 6.53 presents measured strain variation along the interior and exterior steel girders at sections C and H. From strain variation along section C-Exterior, it can be said that the hybrid deck and the exterior steel girder are interacting in a partially composite way at $(1\times$ tandem load) as evidence by the discontinuity in strain at the hybrid deck-to-steel interface. Figure 6.54 presents the measured longitudinal and transverse strains along

different cross sections of the specimen. Figure 6.54(a) and (b) show the transverse strain variations along sections D and K of the top surface of the hybrid deck, respectively. Figure 6.54(c) presents the measured longitudinal strain profile along section K. Figure 6.54(d) presents the transverse strains measured along the section G. The longitudinal strains measured along the centerline of the hybrid deck are unbroken, indicating that adjacent deck panels were acting together rather than as separate pieces. This suggests that the adhesive connection between panels is providing adequate transfer of load between the two adjacent panels. Figure 6.54(f) presents the measured strains on the exterior web at Sections O-East. This variation in strain was not expected and was likely a result of calibration problems of strain gages at this location.

6.7.7 Service Load Case 7

Service load case 7 was simulated to service load case 5 with the exception that the load was applied at $0.62 \times L$, as shown in Figure 6.25.

The deformed shapes of the top surface of the specimen are shown in Figure 6.56(a), (b) and (c) (see Figure 6.22 for the location). Figure 6.57 presents the deformed shapes of the bottom surface of the specimen at the different load levels. Figure 6.58 presents the strain variation along the interior and exterior steel girders at sections C and H. The longitudinal and transverse strains at different cross sections of the specimen as shown in Figure 6.59. Figure 6.59(a) and (b) show the transverse and longitudinal strain variations along sections D and K on the top surface of the hybrid deck, respectively. Figure 6.59(c) presents the measured transverse strain profile along section G, while Figure 6.59(d) presents the longitudinal strain measured along the centerline of the bottom surface. The longitudinal strains measured along the centerline of the bottom surface of the deck are unbroken, indicating that adjacent deck panels were acting together rather than as separate pieces. Figure 6.59(e) shows the measured strains on the exterior web at Sections O-West. This variation in strain was not expected and was likely a result of calibration problems of strain gages at this location.

6.8 SUMMARY

To be efficiently used in modern bridge decking application, the proposed hybrid deck must be made to act compositely with underlying steel girders. To behave compositely, a sufficiently robust shear transfer interface at the hybrid deck to steel transition zone is required. Welded shear studs were used to connect the hybrid deck to steel girders. The hybrid FRP-concrete deck on steel girders specimen was subjected to a series of service flexural loading tests under seven different loading conditions to capture the global response of the specimen, and to investigate the shear composite action of the bridge. The tests results demonstrated the excellent performance of the hybrid FRP-concrete bridge deck. No signs of damage were observed in the shear connection during the entire test. The shear connections at girder-deck interface demonstrated an excellent performance under service load.

All results showed linear deformation load relationship, which indicates that, the hybrid deck can be modeled as a linear material for the deck deformation serviceability design context. Also, the plane section before deformation remains plane after deformation. The linearity of strain means that the principle of elastic beam theory can be used in design of the deck under service load. In addition, it was observed that the hybrid deck and the underlying steel girders are interacting in a partially composite way at large load; as evinced by the discontinuity in strain at the hybrid deck-to-steel interface. Effective width calculations of the hybrid deck showed that they are less than AASHTO prescribed effective width for concrete decks. This is expected since that FRP decks are not as axially stiff as concrete decks.

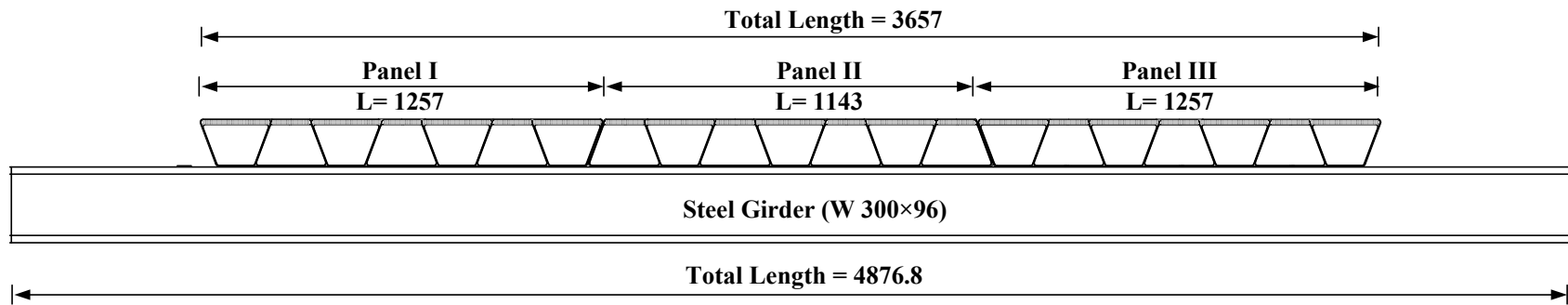
Table 6-1 Thickness and Stacking Sequence of the Hybrid Deck Model

| | Stacking Sequence | Thickness (mm) |
|---------------------------|-------------------|----------------|
| Inner Tube Laminate | $[0^{\circ}_4]$ | 1.524 |
| Outer Tube Laminate | $[0^{\circ}_3]$ | 1.143 |
| Outer- Most Tube Laminate | $[0^{\circ}_5]$ | 1.905 |

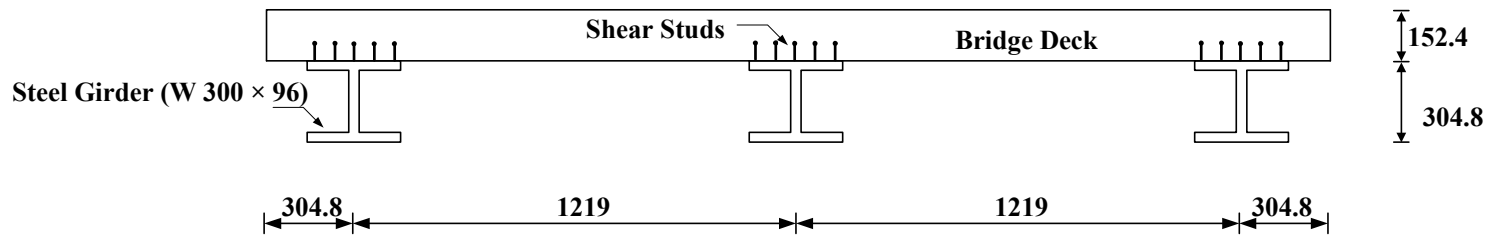
Table 6-2 Effective Flange Width (b_{eff}), and Effective Flange Width Ratio (b_{eff}/b) for Interior and Exterior Girders

| Service Load Case | Interior Girder b_{eff} (m) | Exterior Girder b_{eff} (m) | Exterior Girder b_{eff}/b | Exterior Girder b_{eff}/b |
|-------------------|-------------------------------|-------------------------------|-----------------------------|-----------------------------|
| Case 1 | 0.558 | 0.46 | 0.559 | 0.61 |

| | | | | |
|----------------|-------|------|------|------|
| Case 2 | 0.532 | 0.44 | 0.53 | 0.58 |
| Case 3 | 0.637 | 0.52 | 0.53 | 0.58 |
| Case 4 | 0.595 | 0.49 | 0.43 | 0.48 |
| Case 5 | 0.584 | 0.48 | 0.37 | 0.4 |
| Case 6 | 0.506 | 0.42 | 0.45 | 0.49 |
| Case 7 | 0.506 | 0.42 | 0.34 | 0.37 |
| Average | 0.559 | 0.46 | 0.46 | 0.50 |



(a) Elevation



(b) Side View

Figure 6.1 3/4 Scale Model of Steel Bridge with a Hybrid FRP-Concrete Bridge Deck (units in mm)

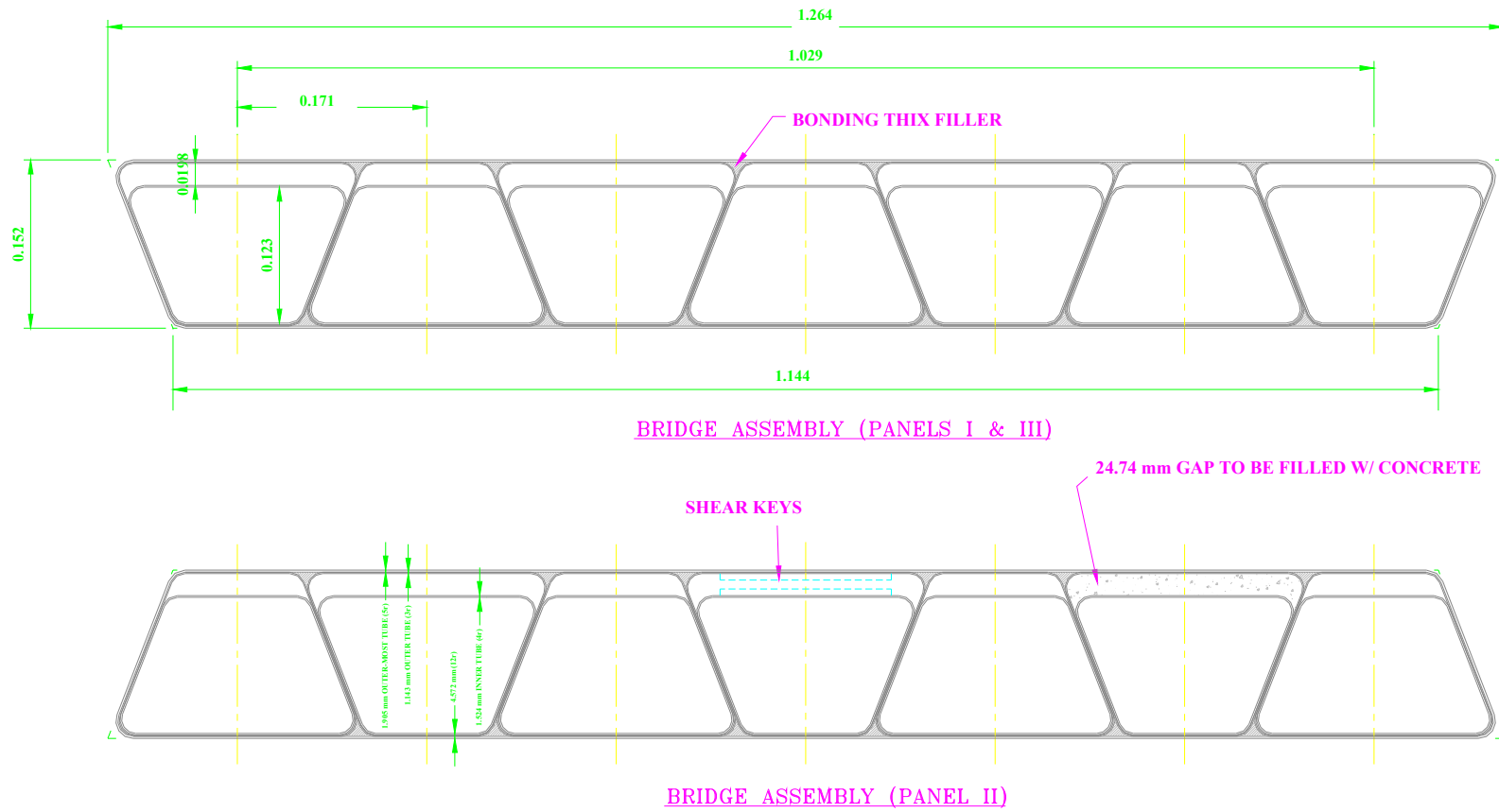


Figure 6.2 Cross Section of the 3/4 Scale Model of a Hybrid FRP-Concrete Bridge Deck Panels (units in mm)



(a) Assembly of the Seven Trapezoidal Box Sections



(b) Assembly of Trapezoidal Box Sections by Vacuum Bag Process

Figure 6.3 Manufacturing Steps for the Hybrid Deck

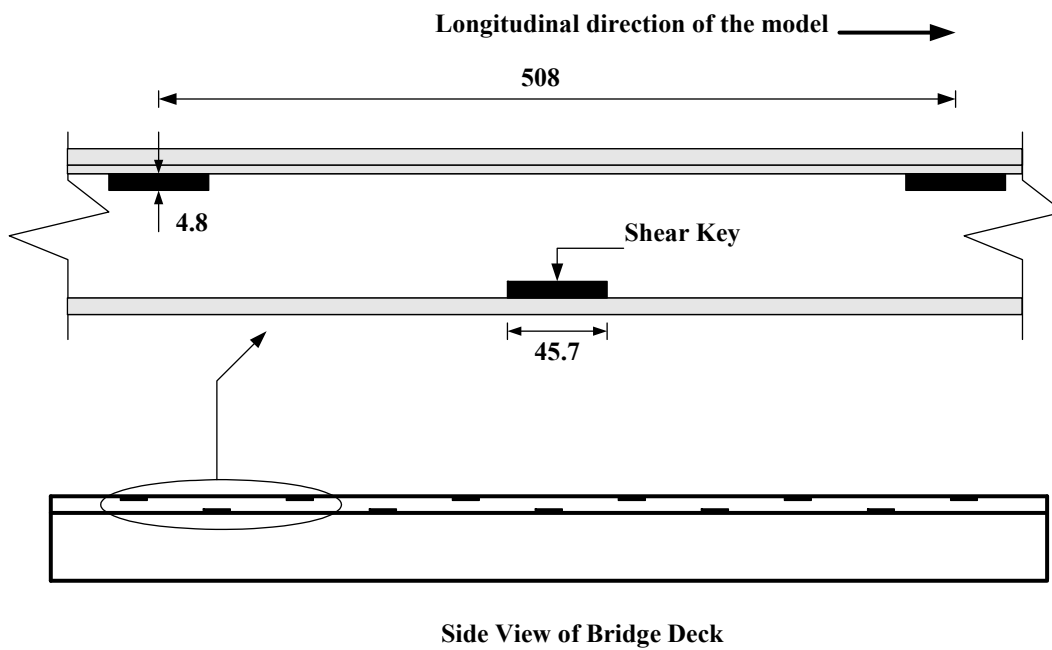


Figure 6.4 Shear Keys (units in mm)

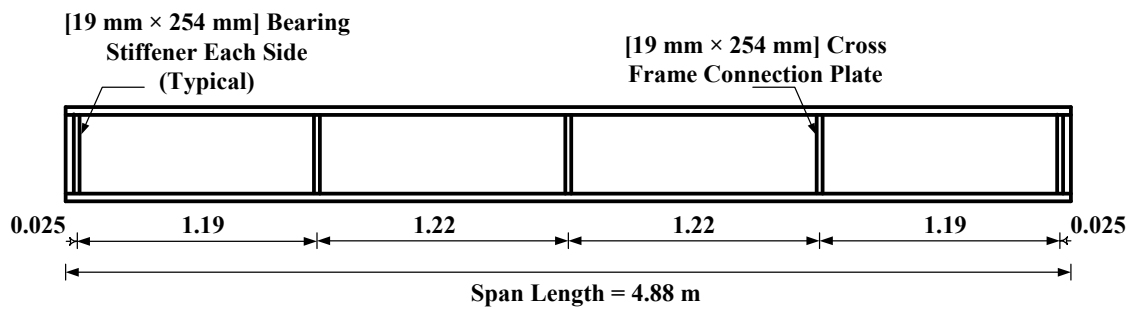


Figure 6.5 Elevation of the Three Steel Girders Model (units in m)



(a) Girders Supports



(b) Bracing Connection

Figure 6.6 Details of Girders Supports

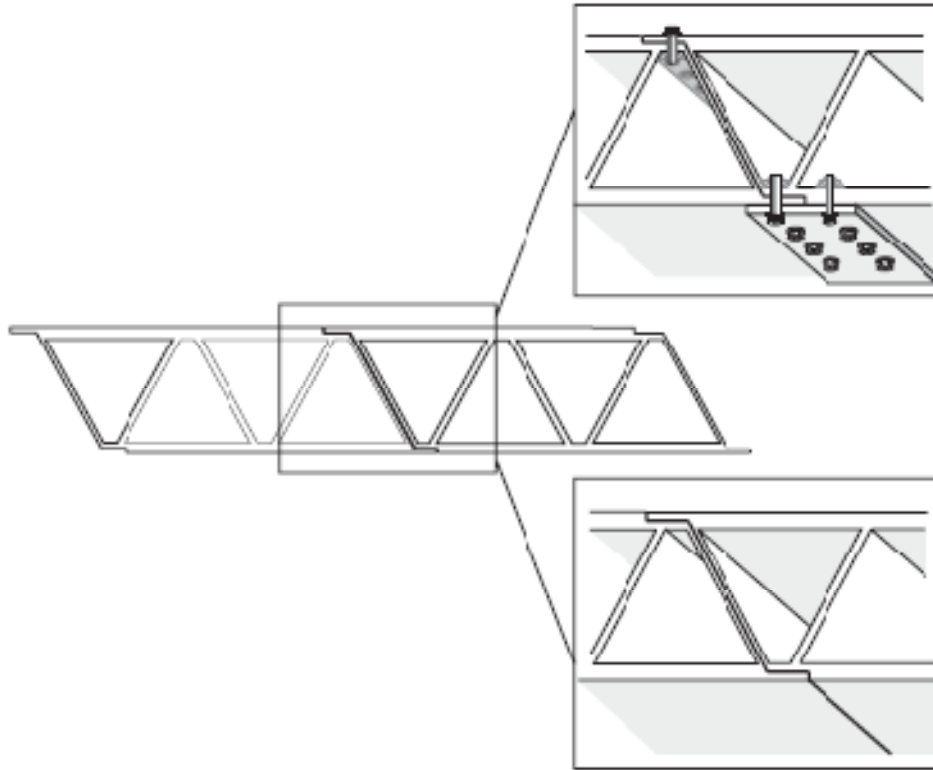


Figure 6.7 Adhesively Bonded and Bolted Joints (Zetterberg, 2001)

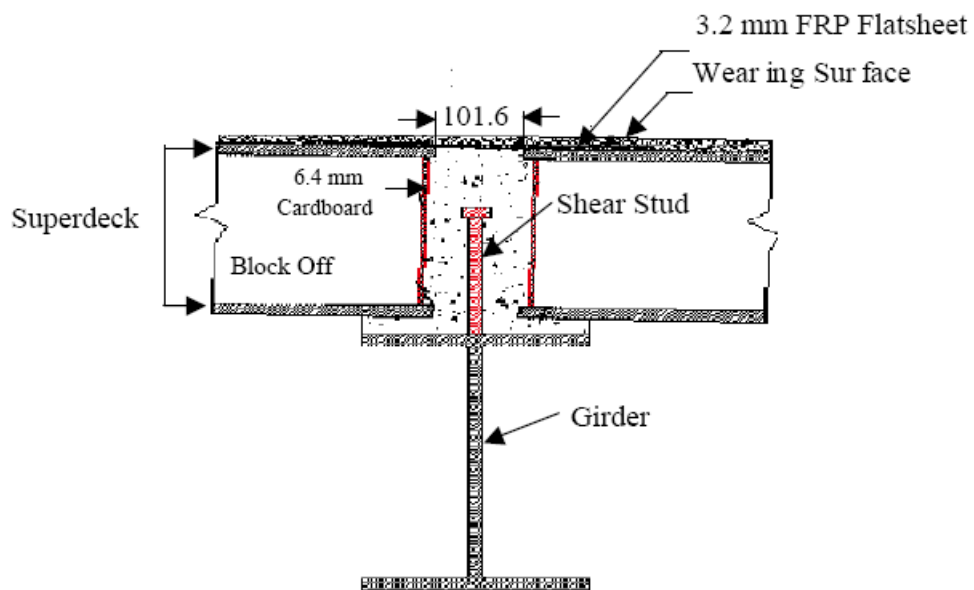
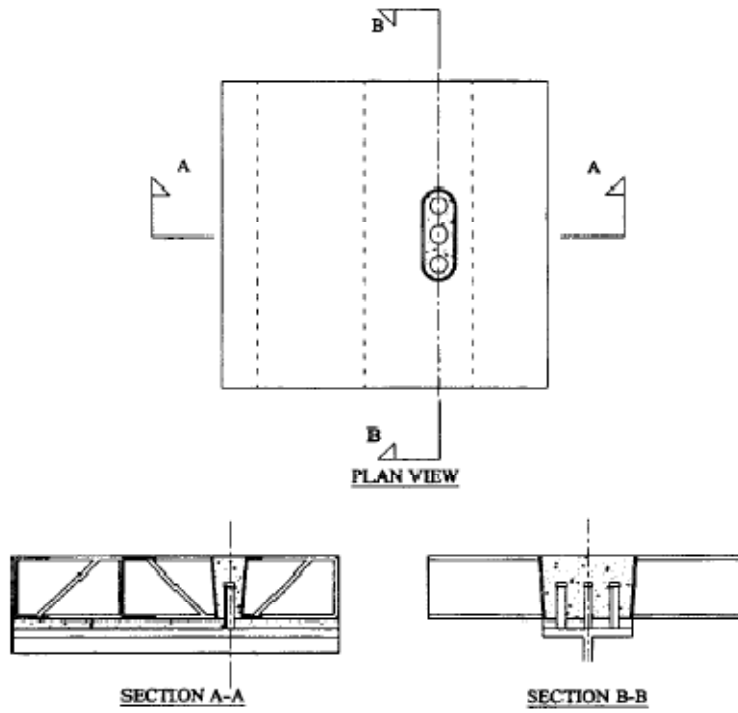
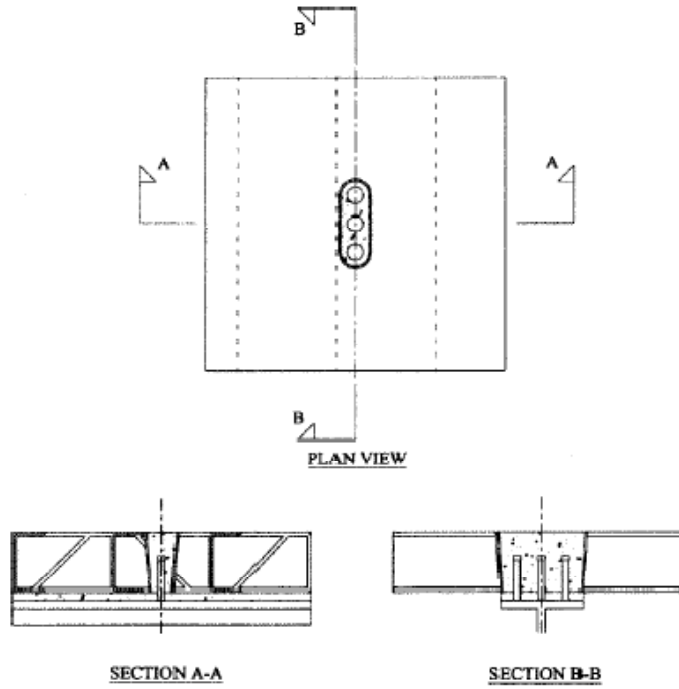


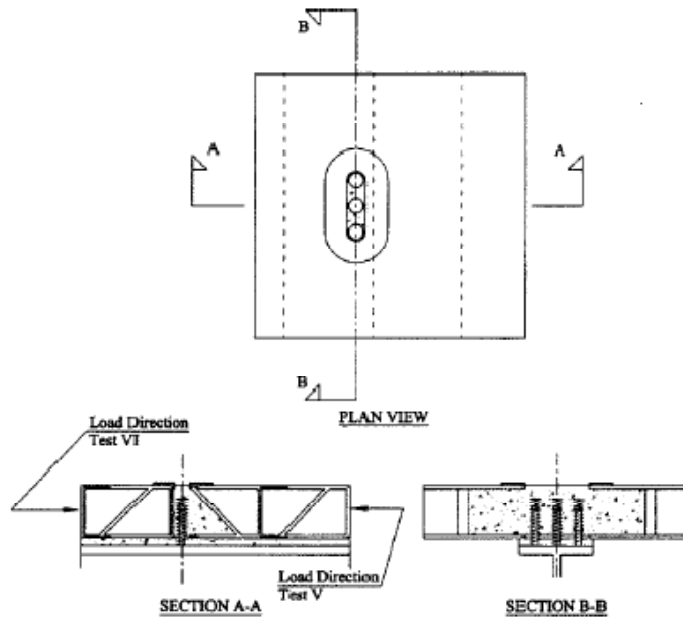
Figure 6.8 SuperdeckTM Shear Stud Connection



(a) Connection 1



(b) Connection 2



(c) Connection 3

Figure 6.9 Schematic of Three Different Connections (Moon et al., 2002)

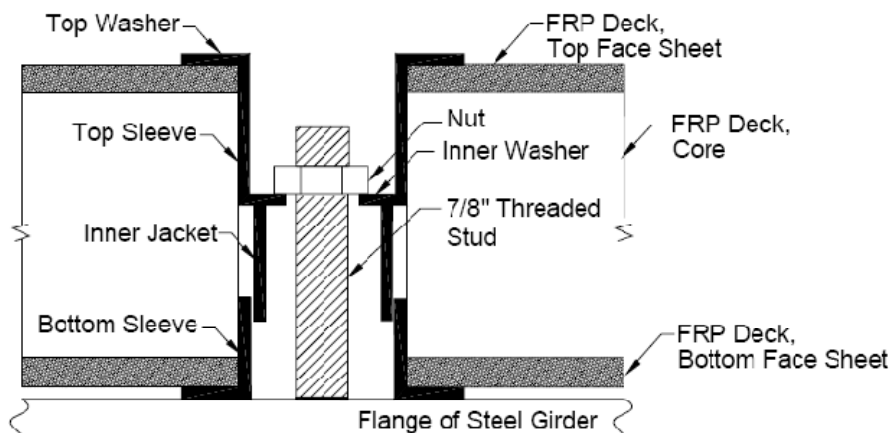


Figure 6.10 Proposed Connection for FRP Decks to Steel Girders (Righman et al., 2004)

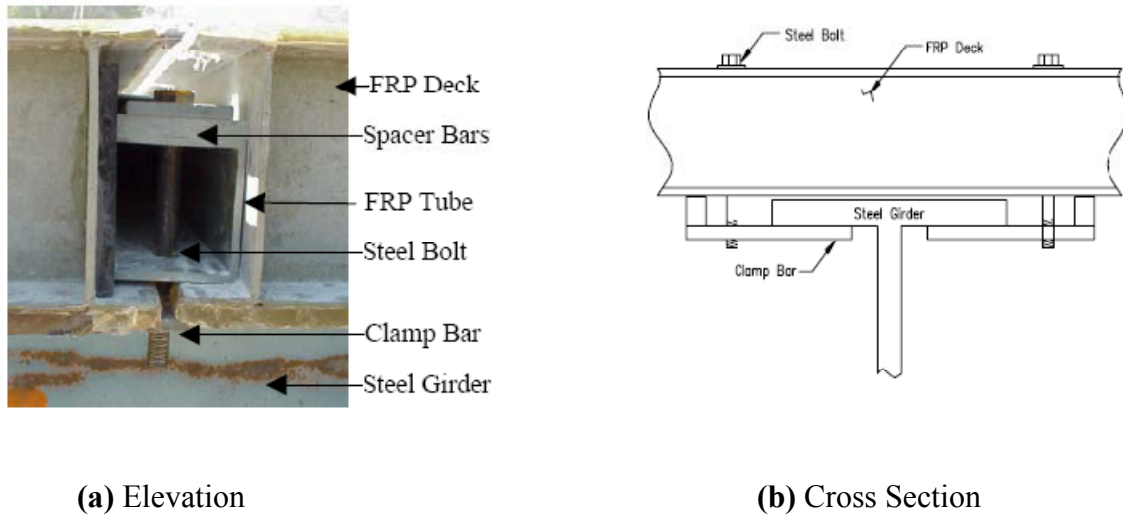


Figure 6.11 KSCI Clamp Connection

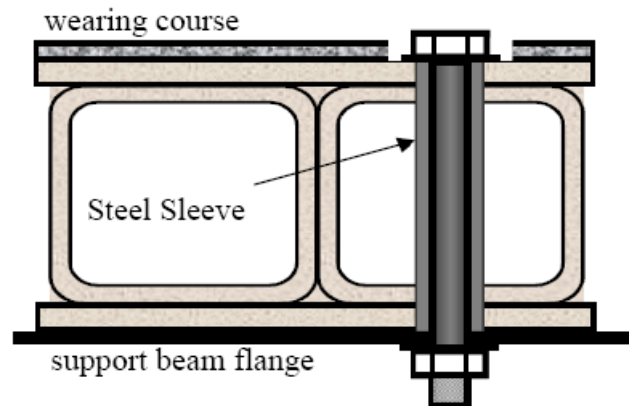


Figure 6.12 Details of Bolted Connection

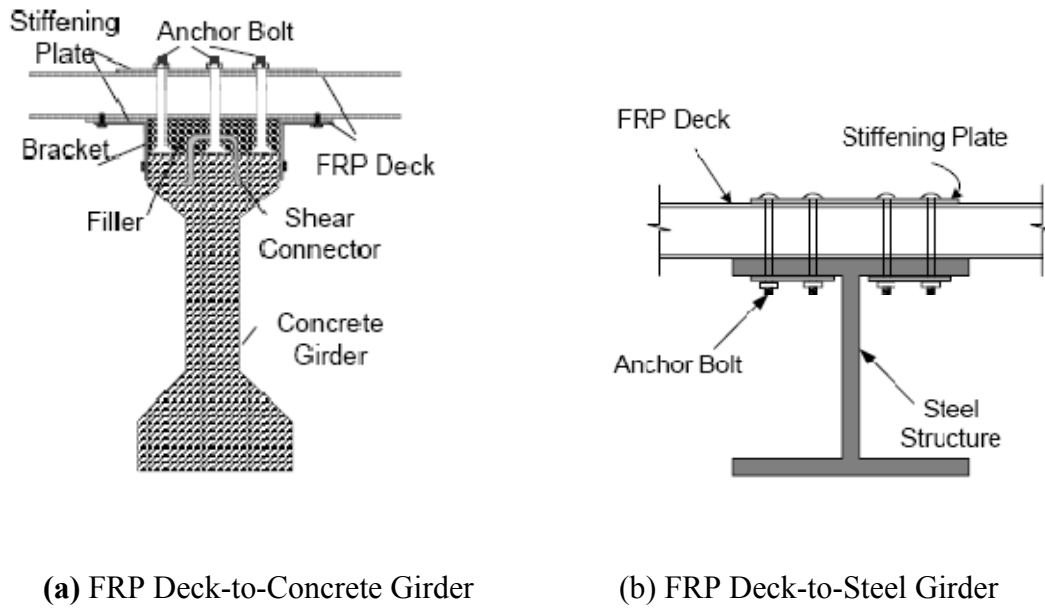


Figure 6.13 Schematic of Proposed Deck-to-Girder Connection (Park et al., 2004)

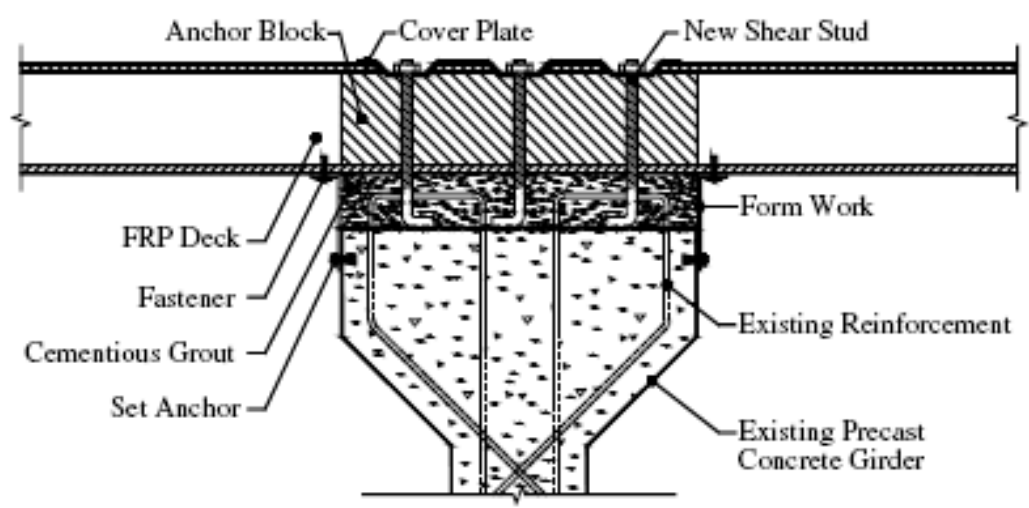


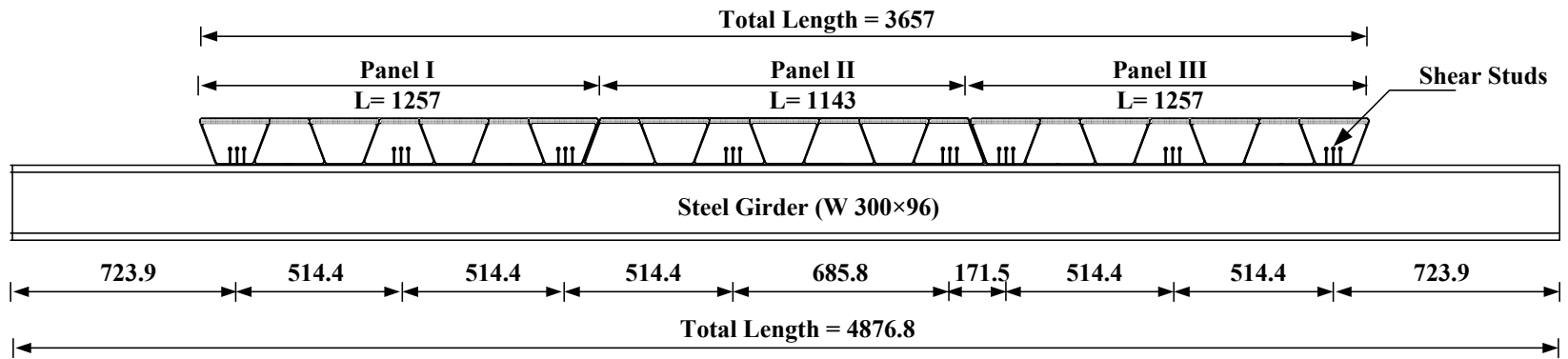
Figure 6.14 Schematic of Proposed Deck-to-Girder Connection (Kim et al., 2005)



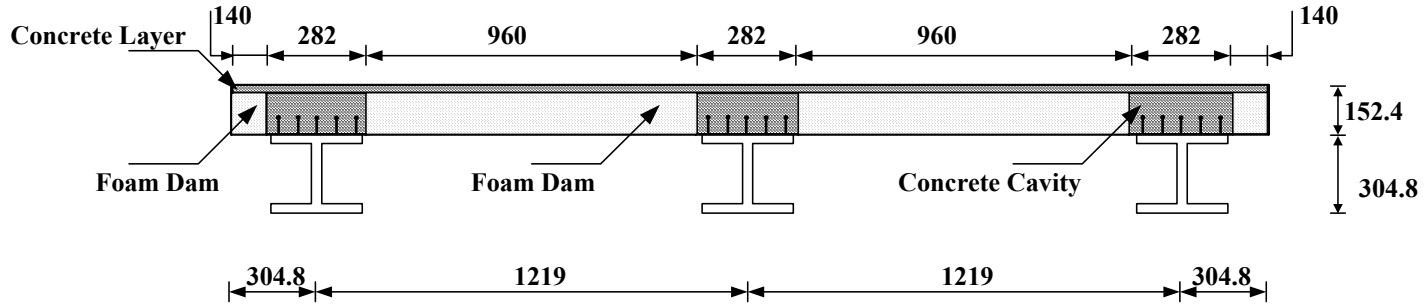
(a) Shear Studs

(b) Close Look

Figure 6.15 Shear Studs Details for the Proposed Hybrid Deck



(a) Elevation



(b) Cross Section

Figure 6.16 Shear Stud Configuration (units in mm)

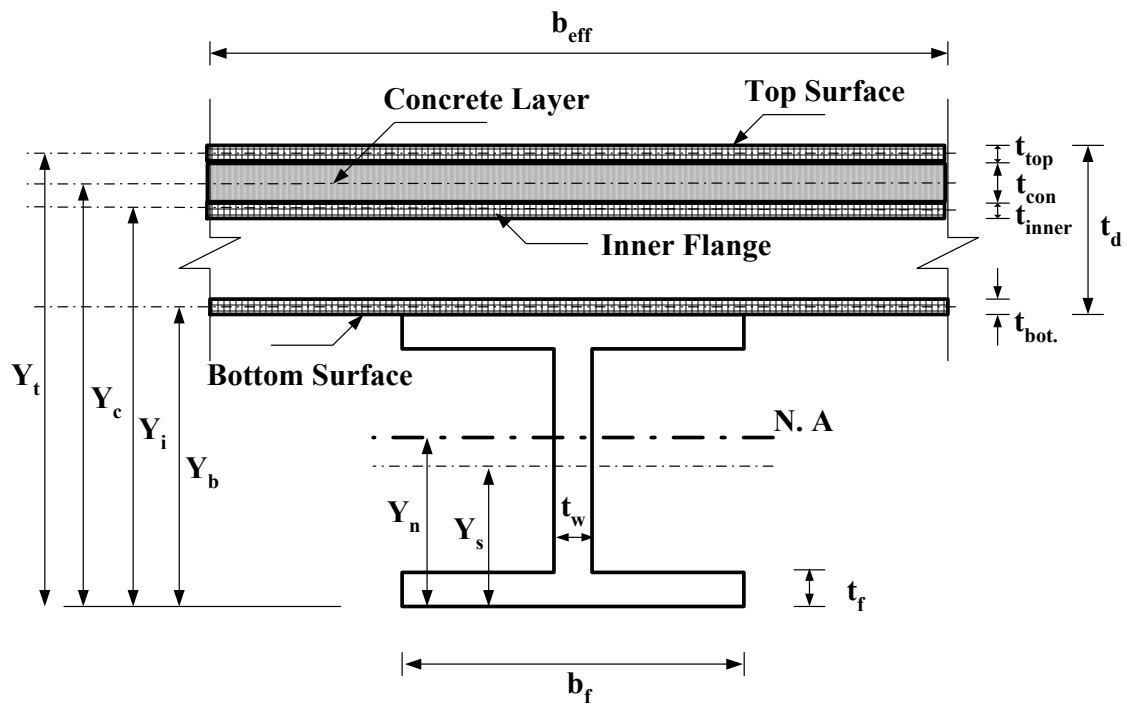


Figure 6.17 Idealized Cross Section of the Transformed Section of the Bridge

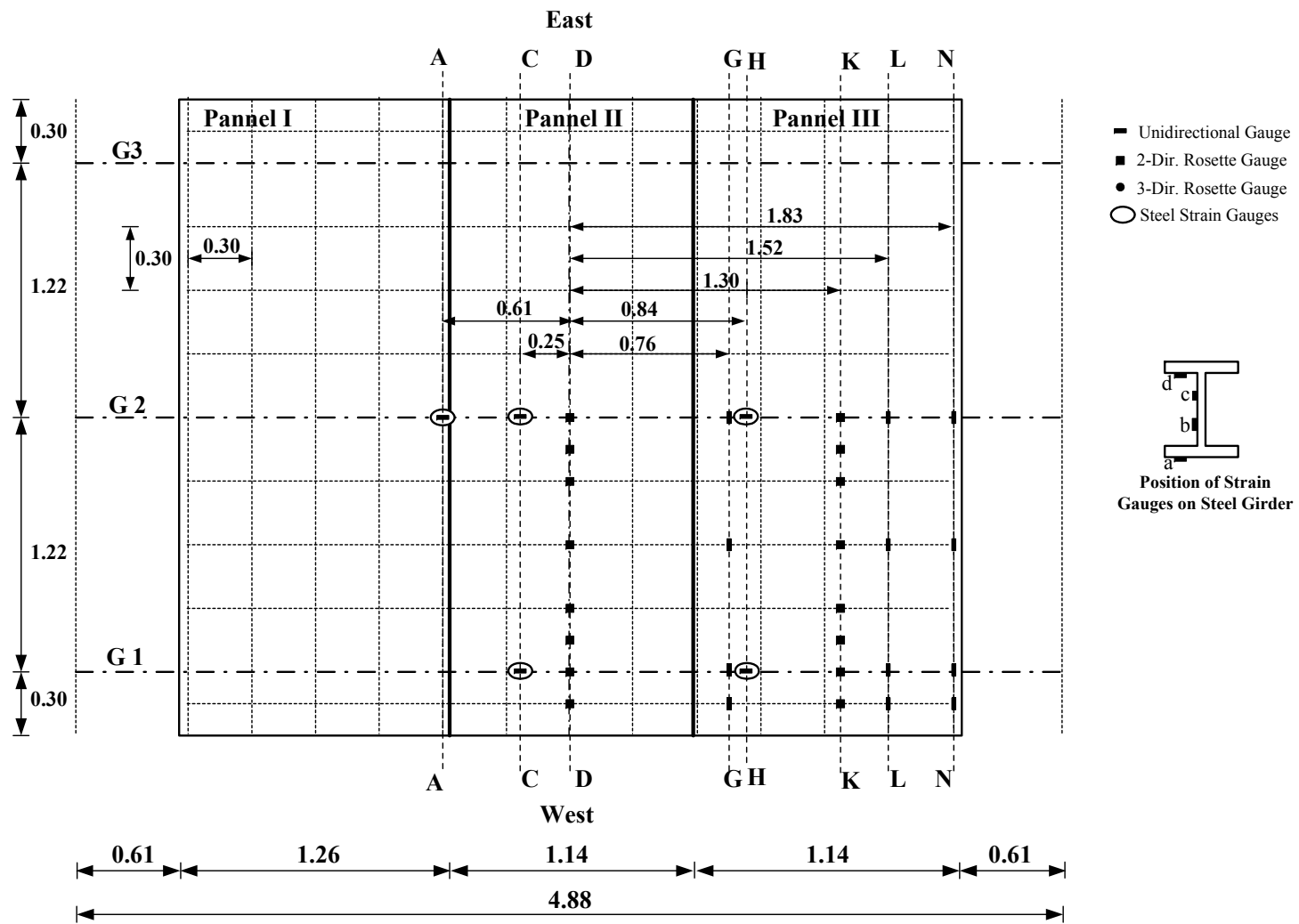


Figure 6.18 Strain Gages Locations for Deck Top Surface and Steel Girders (dimensions in m)

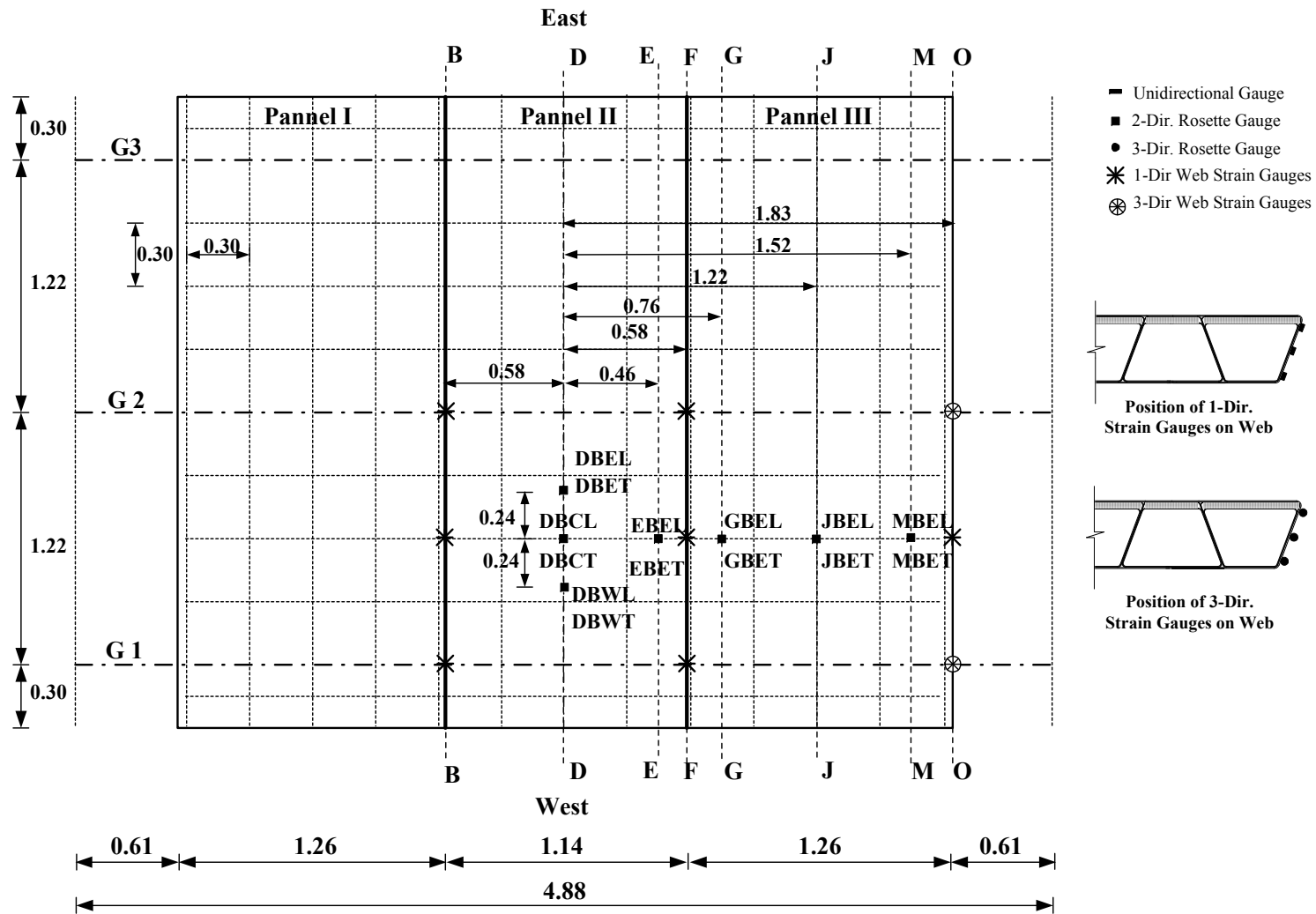


Figure 6.19 Strain Gages Locations for Bottom Surface and Webs of the Hybrid Deck (dimensions in m)

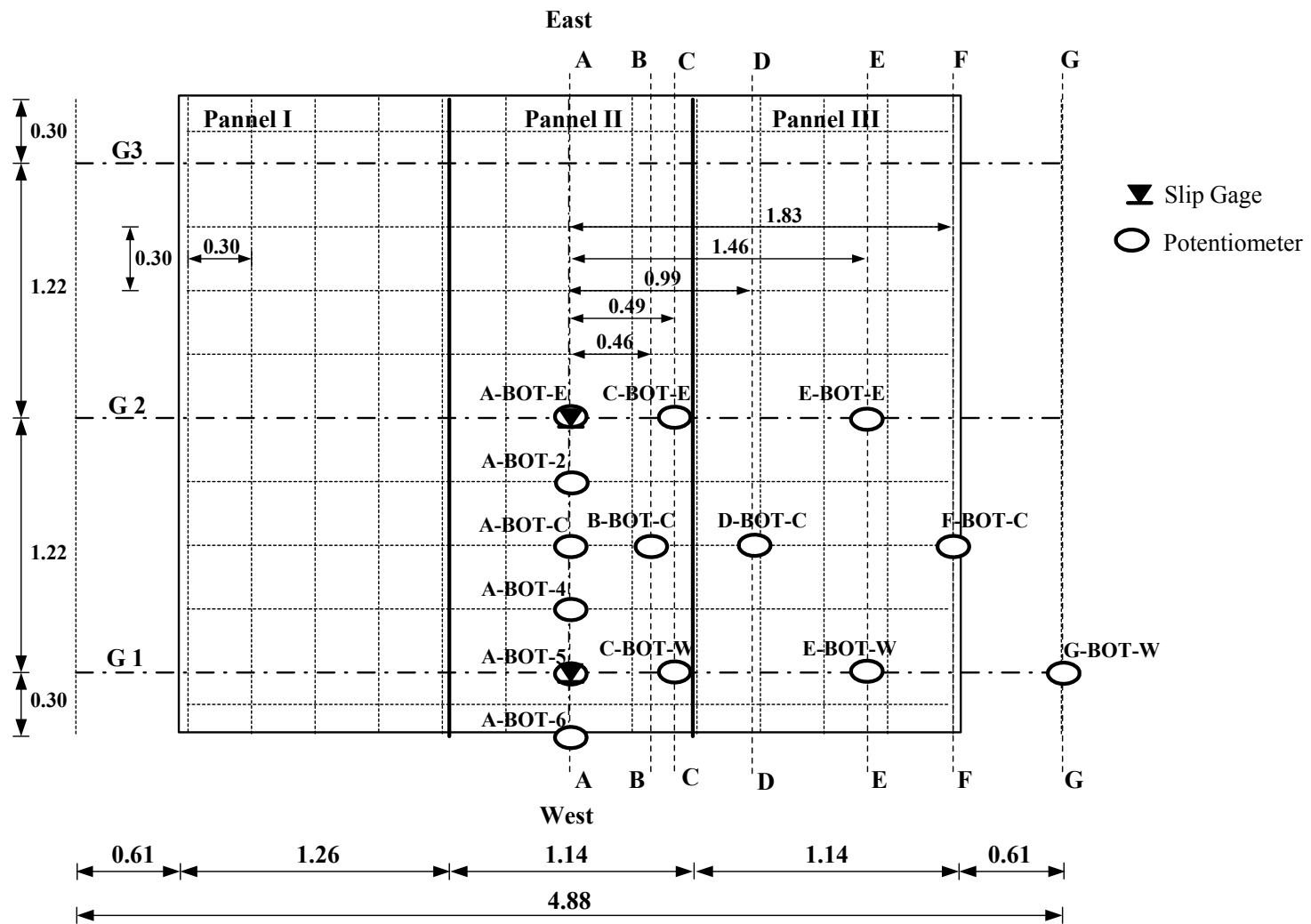


Figure 6.20 Potentiometer Locations for Bottom Surface and Webs of the Hybrid Deck (dimensions in m)

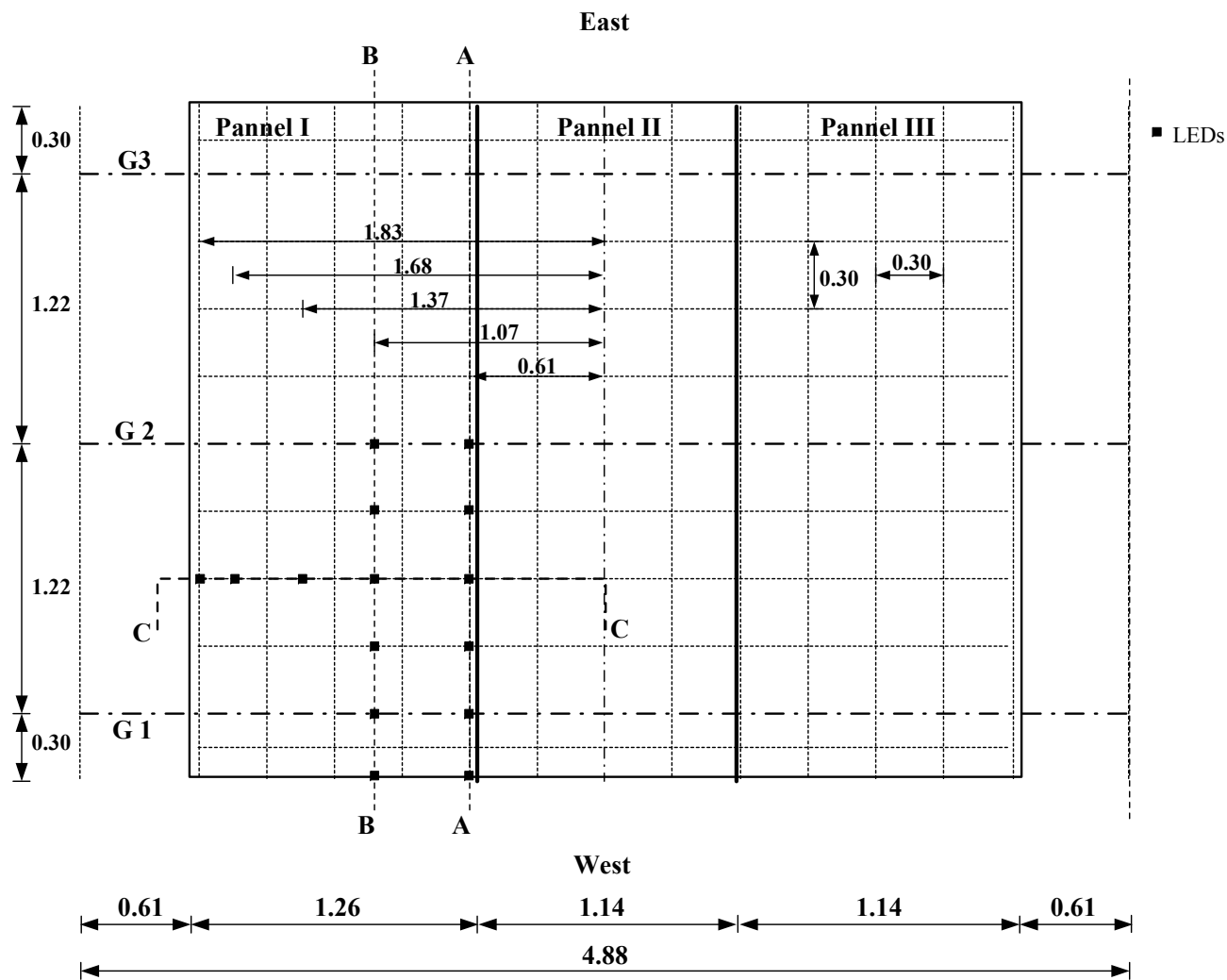


Figure 6.21 Layout of LEDs Locations for the Service Test Cases 1 to 5 (dimensions in m)

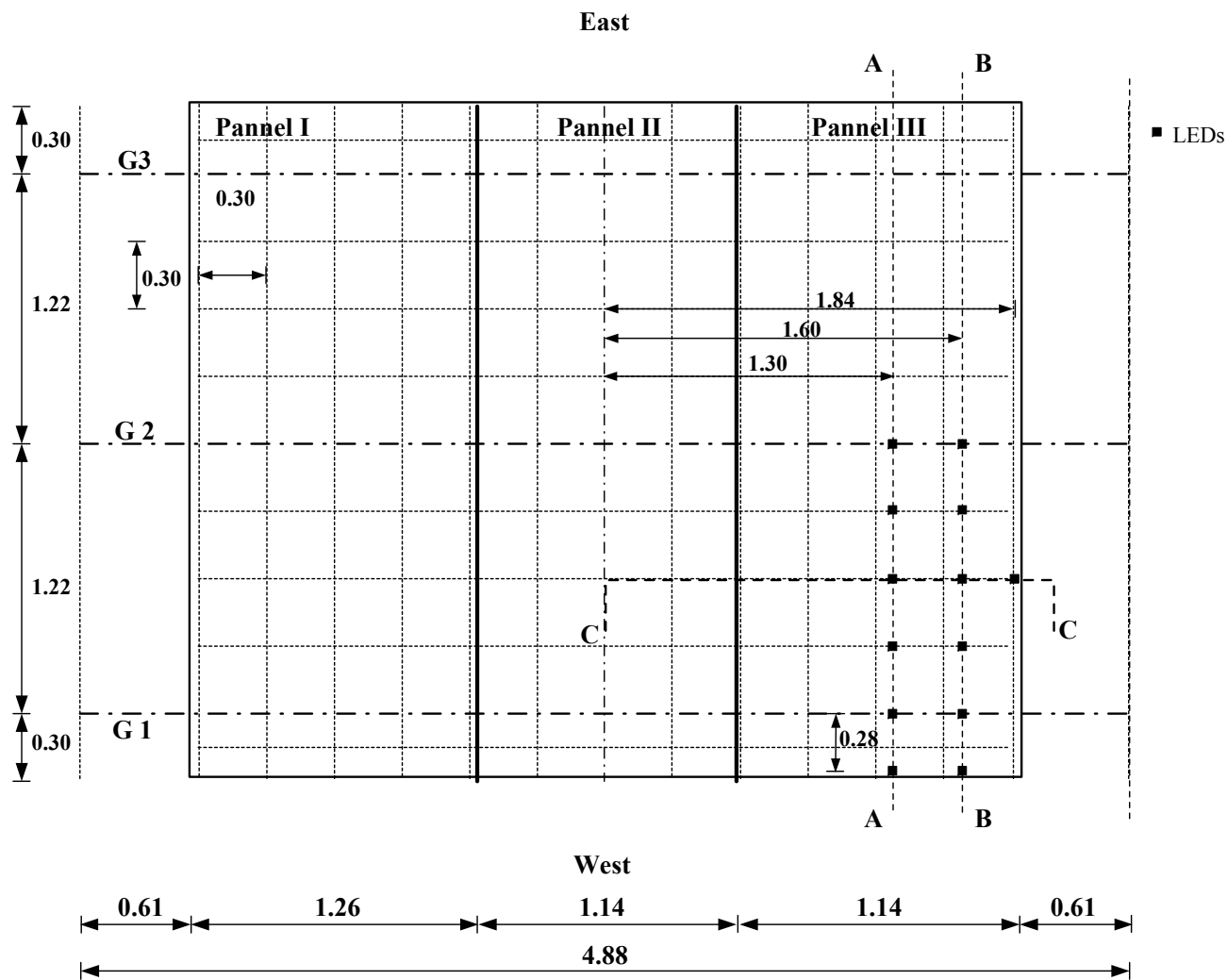
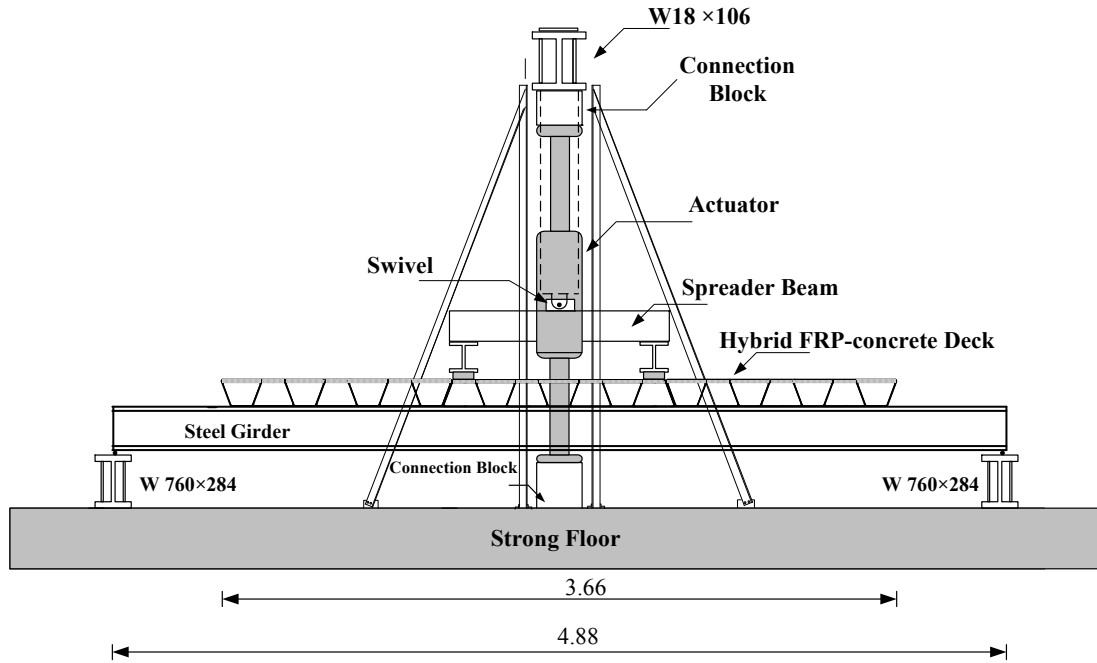
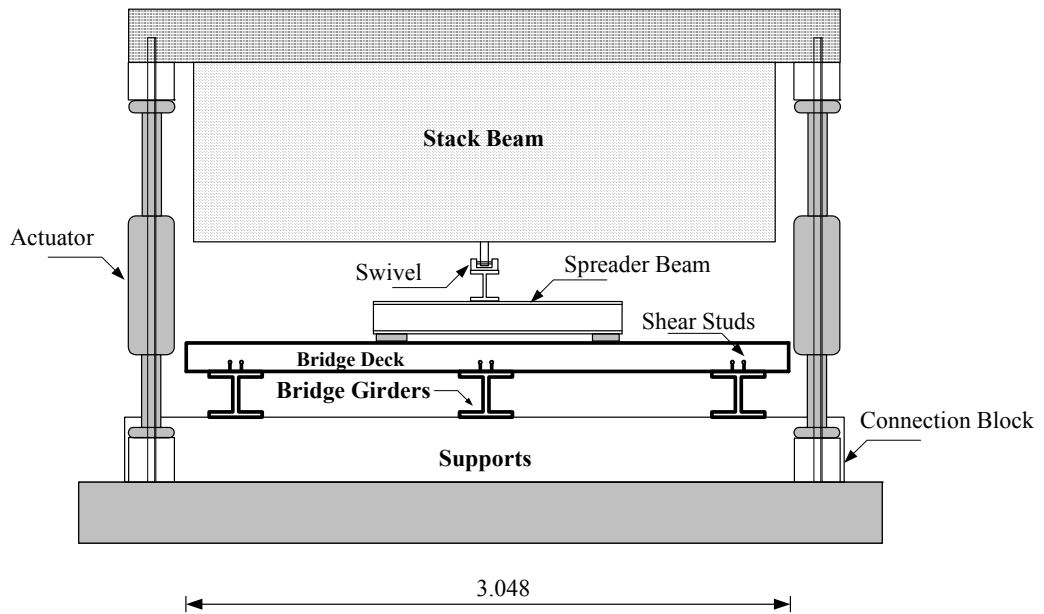


Figure 6.22 Layout of LEDs Locations for the Service Test Cases 6 and 7 (dimensions in m)



(a) Longitudinal Elevation



(b) Transverse Elevation

Figure 6.23 Test Configuration for Service Test (dimensions in m)



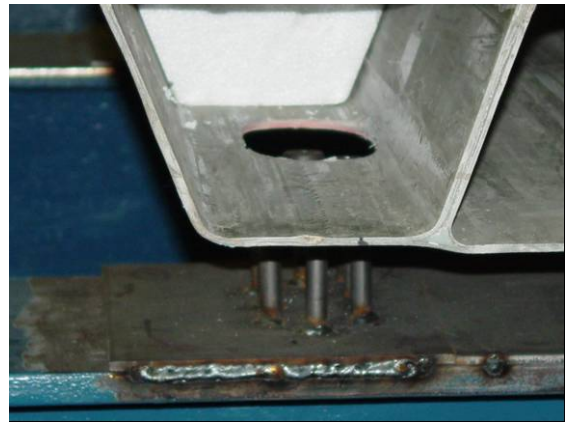
(a) Holes for Shear Studs



(b) Hybrid Deck



(c) Deck- Steel Girders Installation



(d) Shear Studs

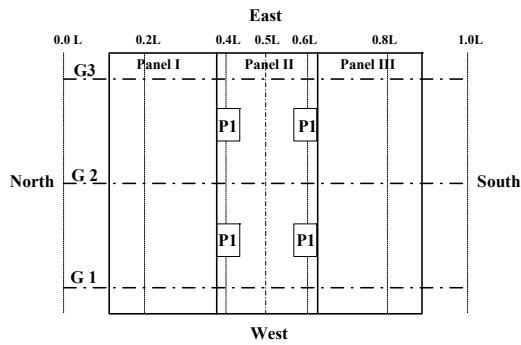


(e) Holes after

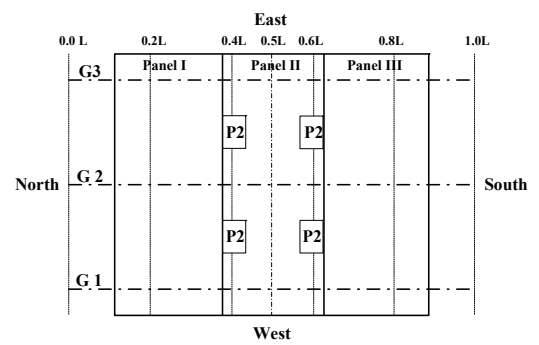
Pouring of Concrete

(f) Test Specimen

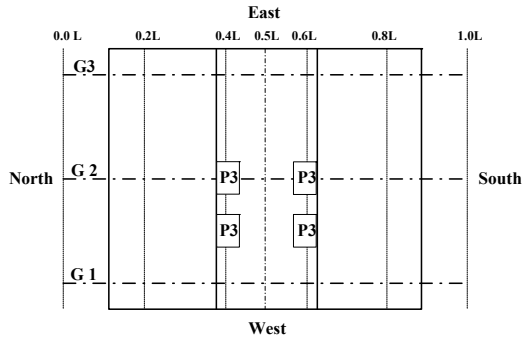
Figure 6.24 Photographs of Steps in Specimen Setup



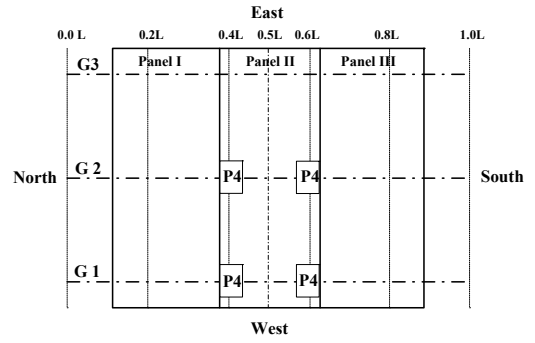
(a) Case 1



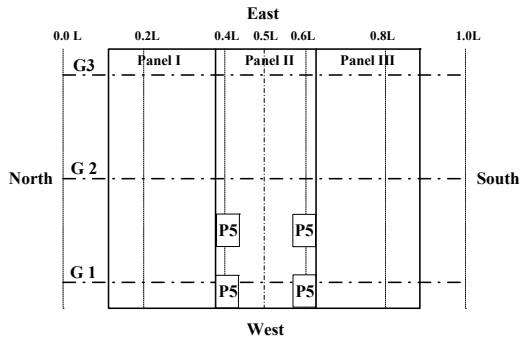
(b) Case 2



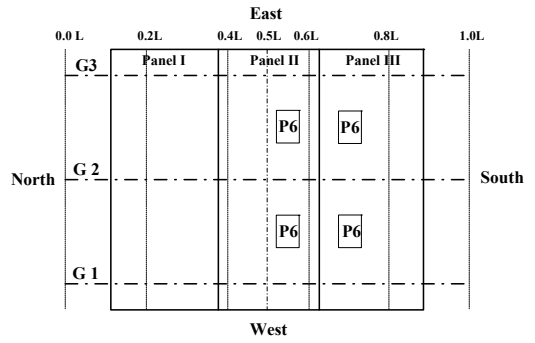
(c) Case 3



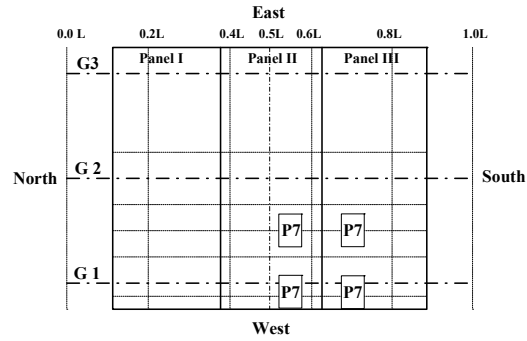
(d) Case 4



(e) Case 5



(f) Case 6



(g) Case 7

Figure 6.25 Seven Service Load Cases.

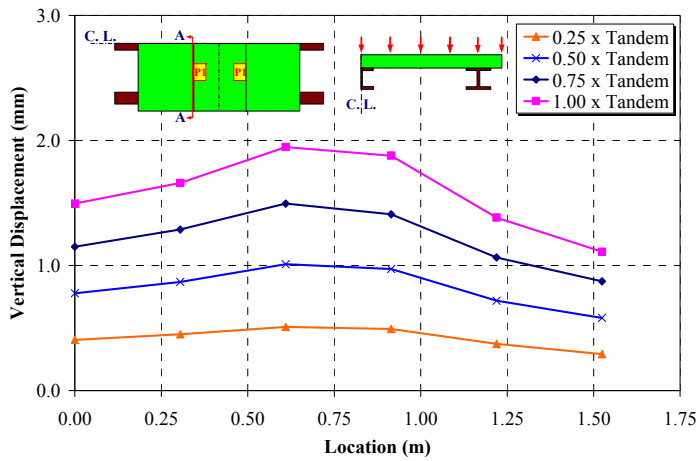


(a) Elevation

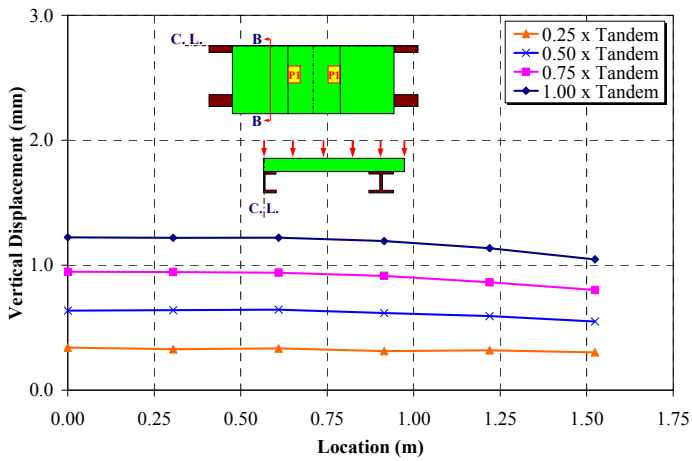


(b) Side View

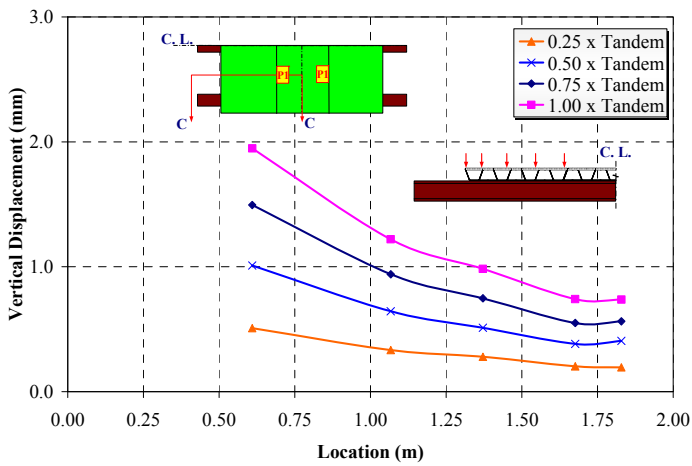
Figure 6.26 Test Set-Up for Service Load-Case 1



(a) Section A-Top Surface

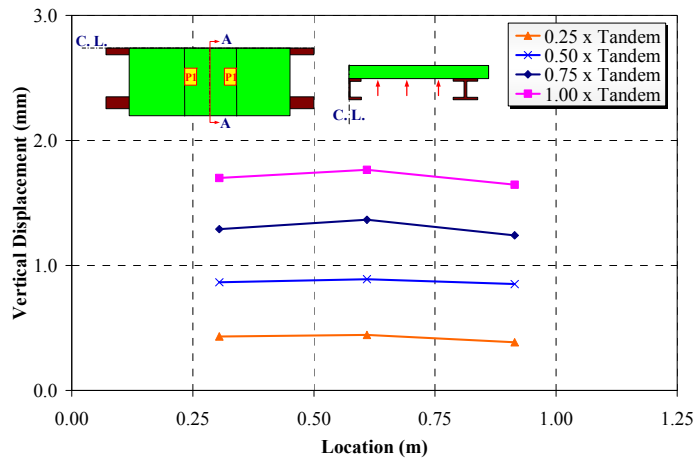


(b) Section B-Top Surface

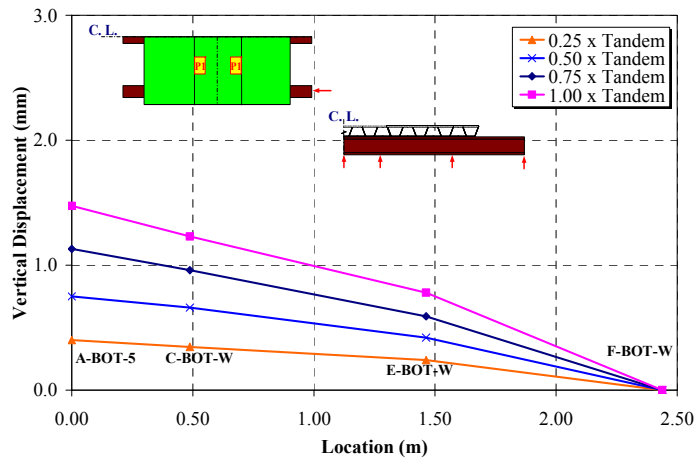


(c) Section C-Top Surface

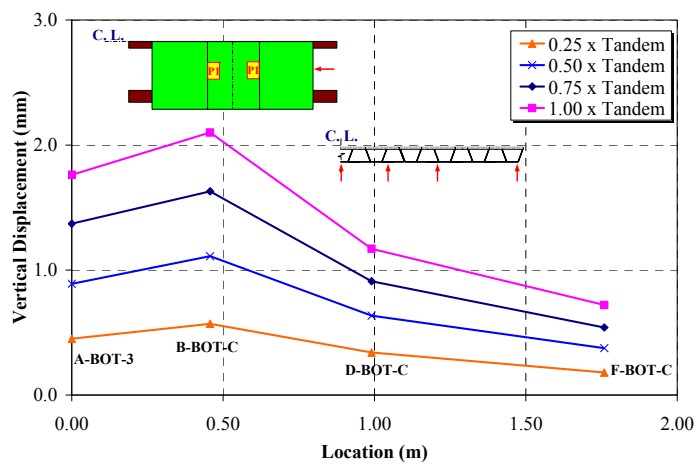
Figure 6.27 Deformed Shapes of the Deck at Different Load Levels under Load Case No.1



(a) Bottom Surface-Transverse Direction

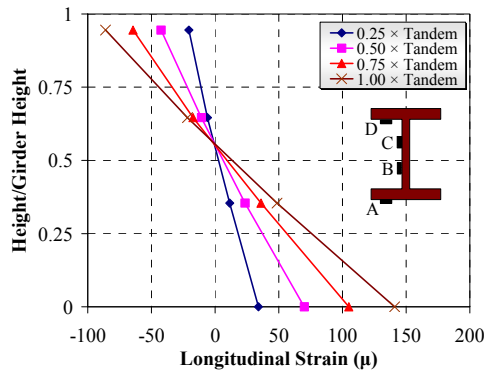


(b) Exterior Girder-Bottom Surface

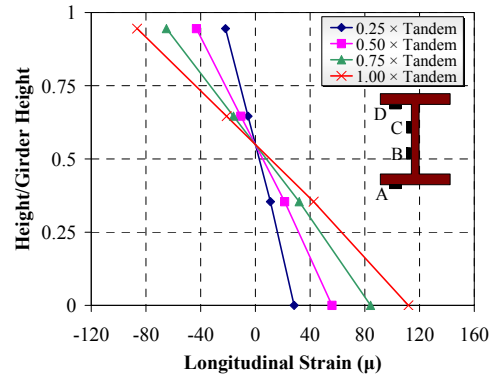


(c) Bottom Surface-Longitudinal Direction

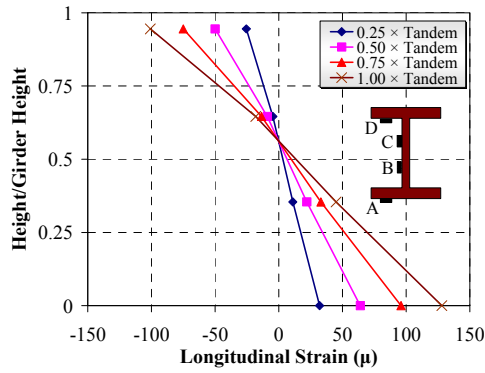
Figure 6.28 Deformed Shapes at Different Load Levels under Load Case No. 1



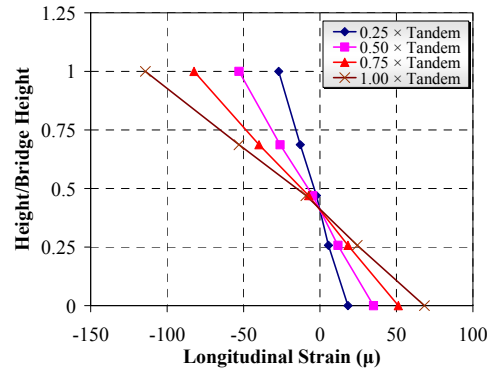
(a) Section C-Interior



(b) Section C-Exterior

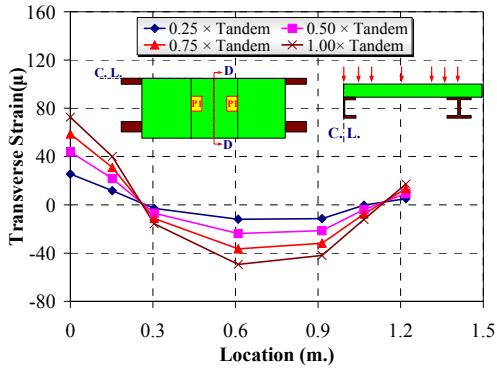


(c) Section H-Interior

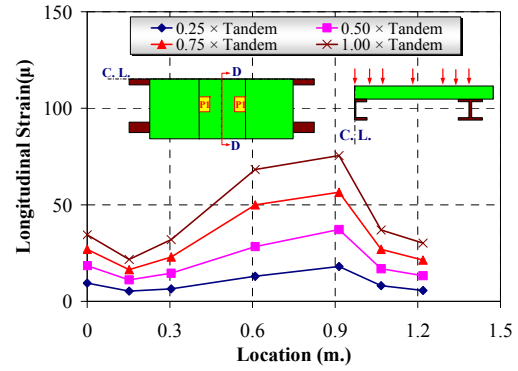


(d) Section H-Exterior

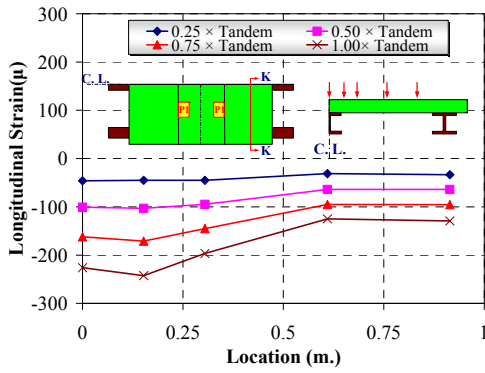
Figure 6.29 Strain Profile at Different Sections under Load Case No. 1



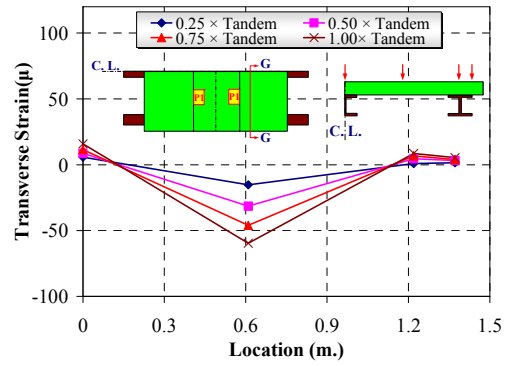
(a) Section D-Transverse



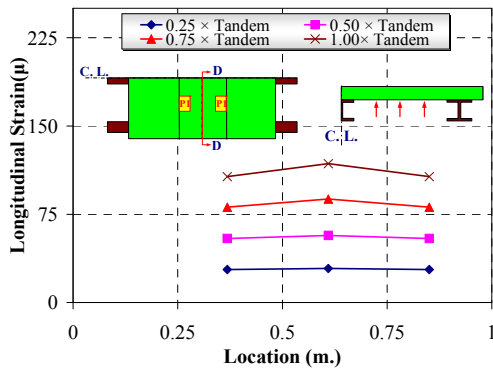
(b) Section D-Longitudinal



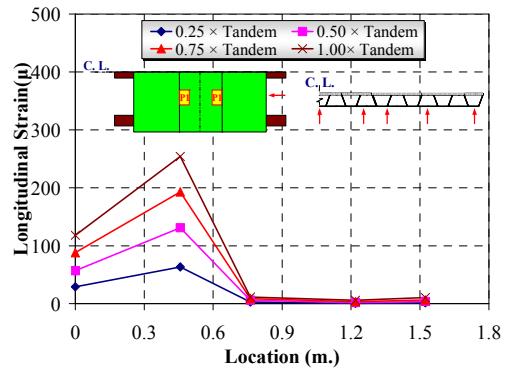
(c) Section K-Longitudinal



(d) Section G-Transverse

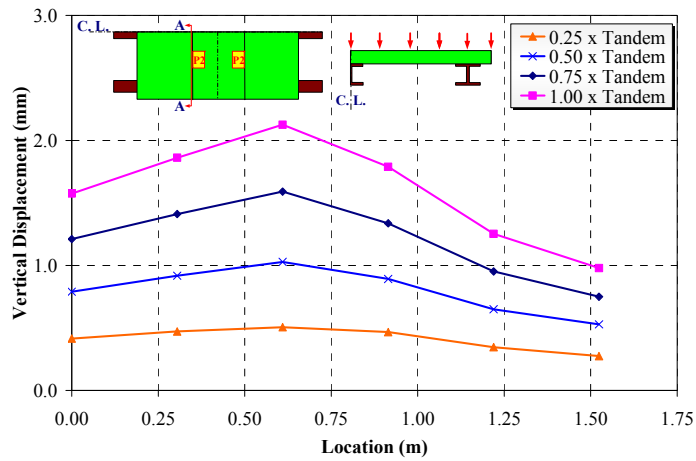


(e) Section D-Longitudinal

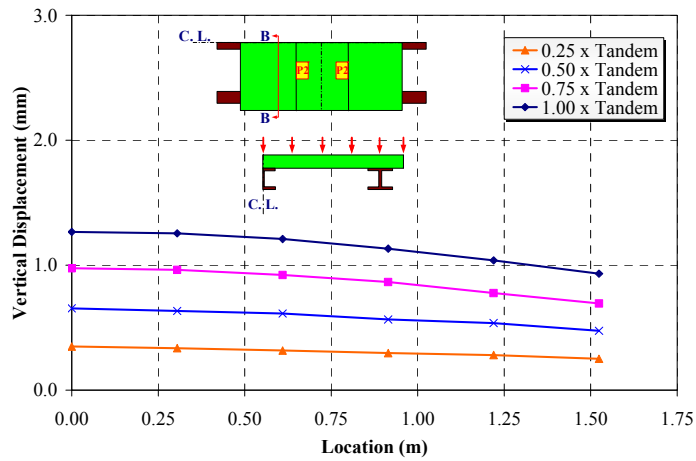


(f) Longitudinal Strain

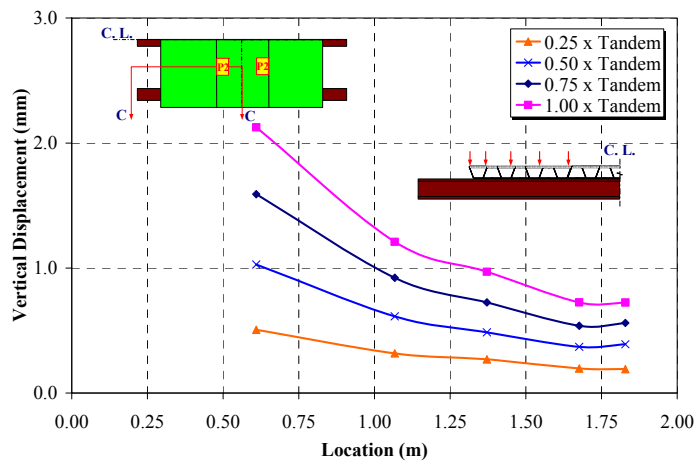
Figure 6.30 Strain Profile at Different Sections of the Deck under Load Case No. 1



(a) Section A-Top Surface

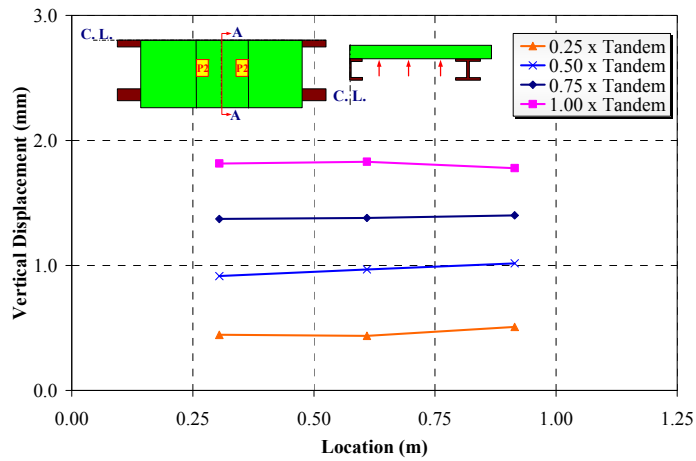


(b) Section B-Top Surface

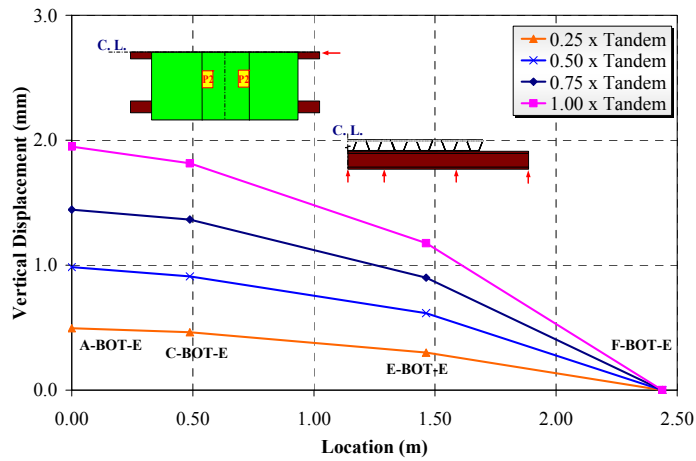


(c) Section C-Top Surface

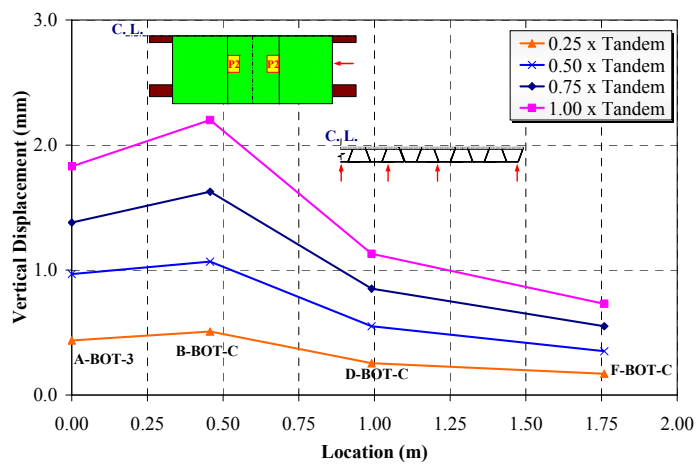
Figure 6.31 Deformed Shapes of the Deck at Different Load Levels under Load Case No. 2



(a) Bottom Surface-Transverse Direction

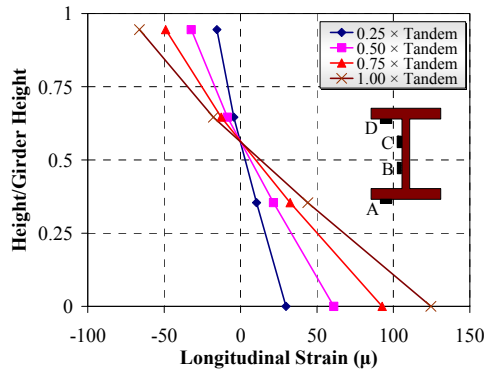


(b) Interior Girder -Bottom Surface

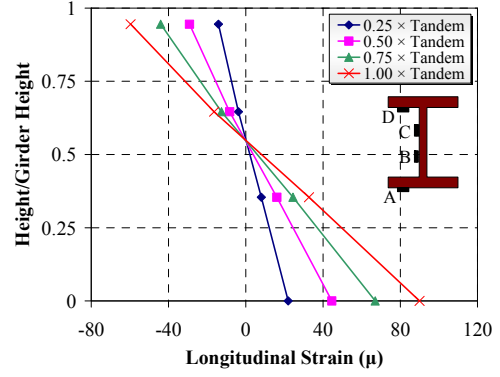


(c) Bottom Surface-Longitudinal Direction

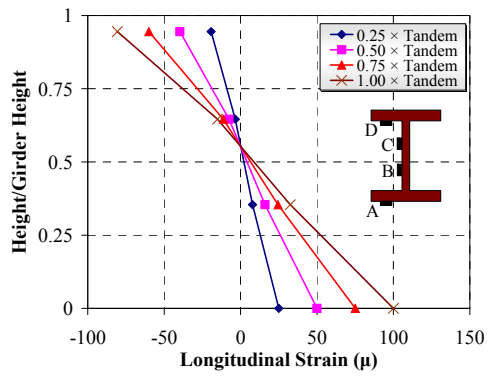
Figure 6.32 Deformed Shapes at Different Load Levels under Load Case No. 2



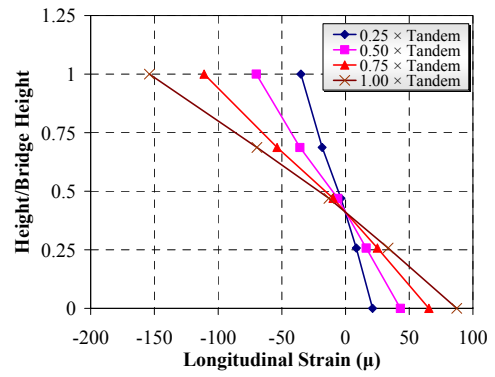
(a) Section C-Interior



(b) Section C-Exterior

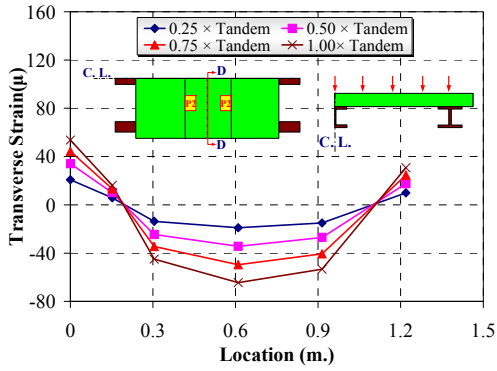


(c) Section H-Interior

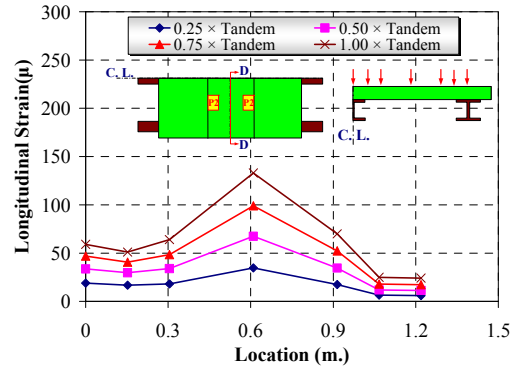


(d) Section H-Exterior

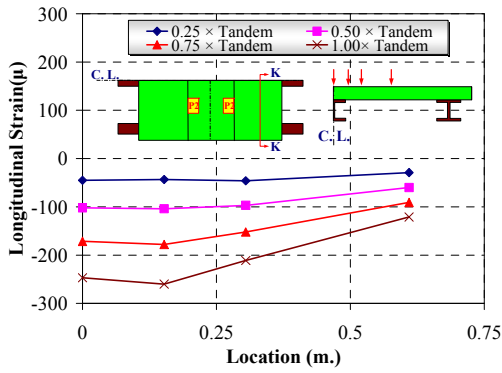
Figure 6.33 Strain Profile through Different Sections under Load Case No. 2



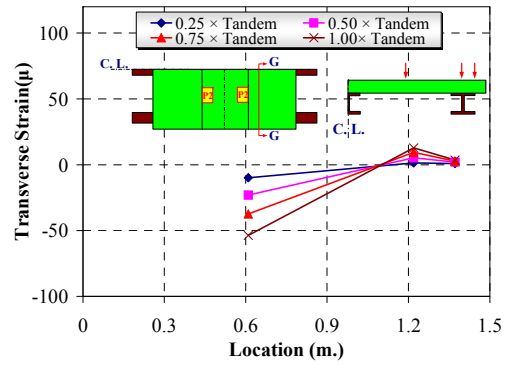
(a) Section D-Transverse



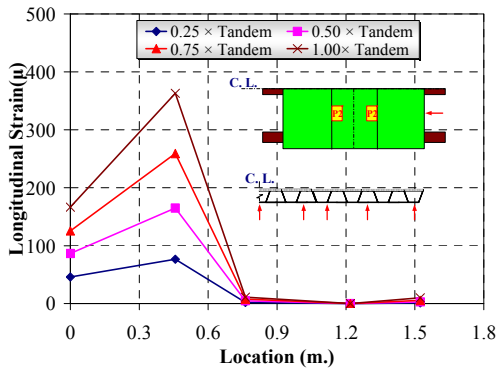
(b) Section D-Longitudinal



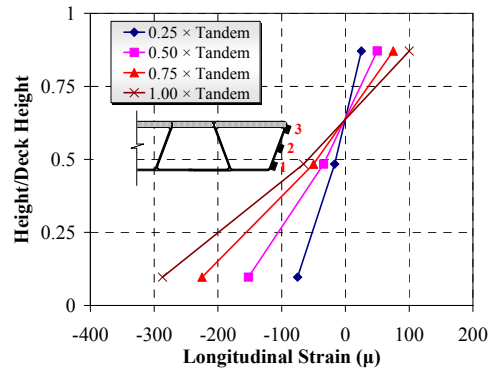
(c) Section K-Longitudinal



(d) Section G-Transverse



(e) Longitudinal Strain



(f) Section F-East

Figure 6.34 Strain Profile through Different Sections of the Deck under Load Case No. 2

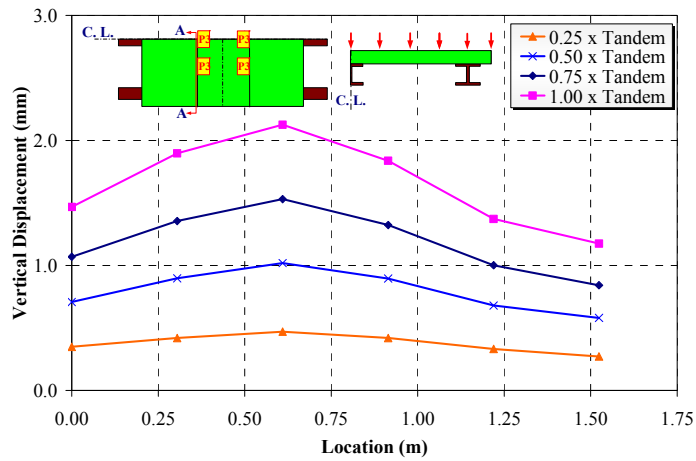


(a) Elevation

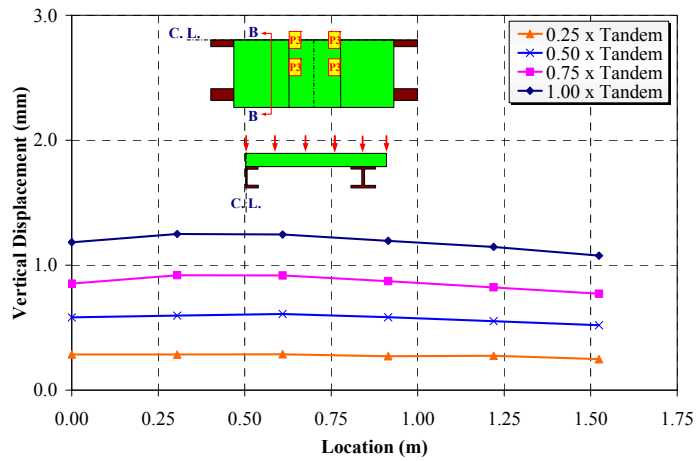


(b) Side View

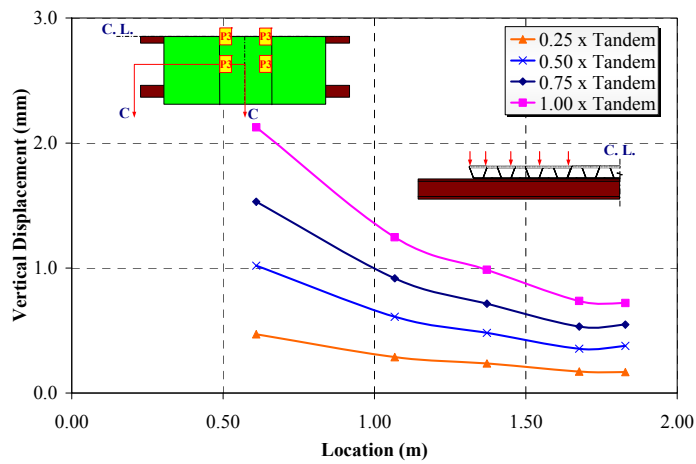
Figure 6.35 Test Set-Up for Service Load-Case 3



(a) Section A-Top Surface

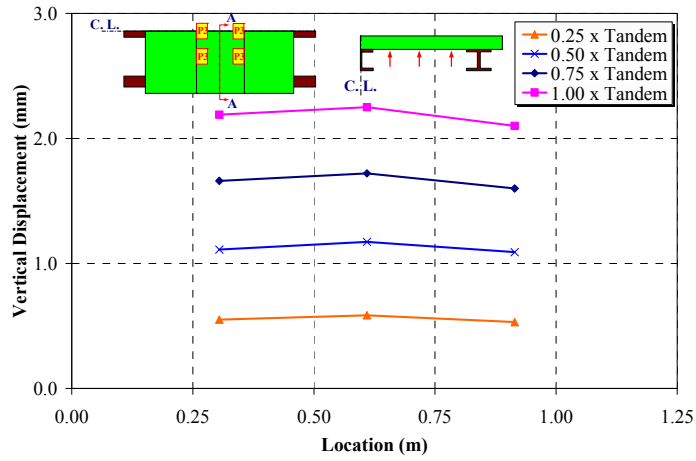


(b) Section B-Top Surface

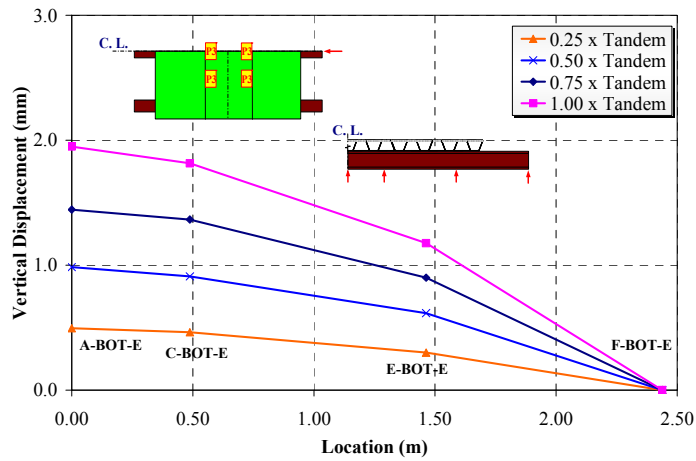


(c) Section C-Top Surface

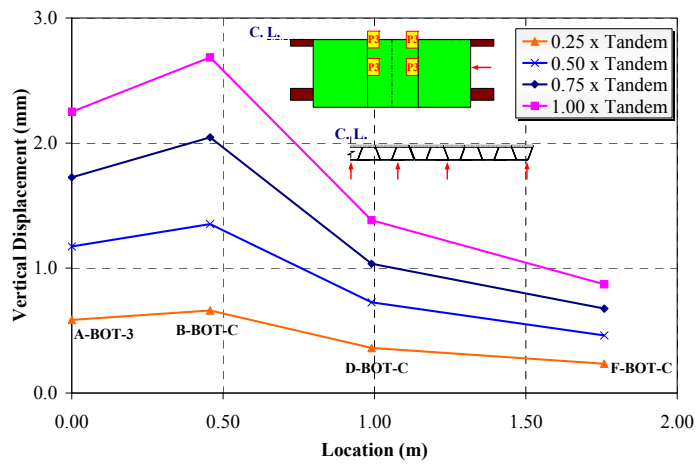
Figure 6.36 Deformed Shapes of the Deck at Different Load Levels under Load Case No. 3



(a) Bottom Surface-Transverse Direction

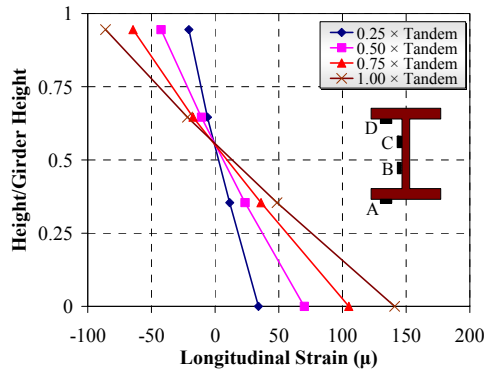


(b) Interior Girder -Bottom Surface

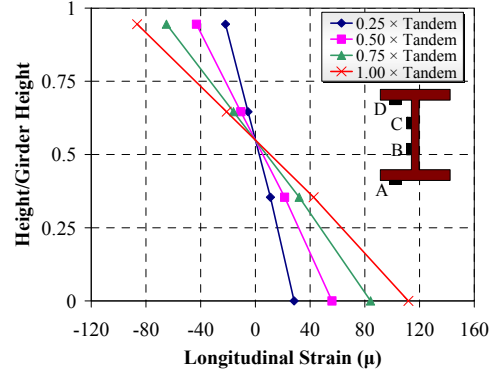


(c) Bottom Surface-Longitudinal Direction

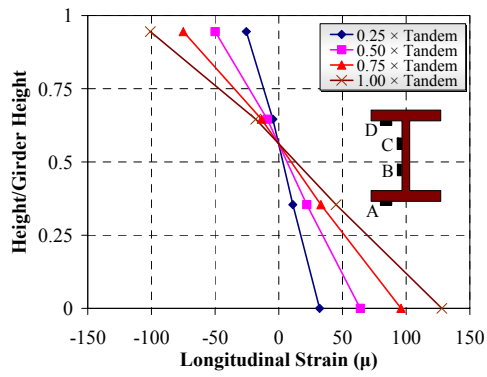
Figure 6.37 Deformed Shapes at Different Load Levels under Load Case No. 3



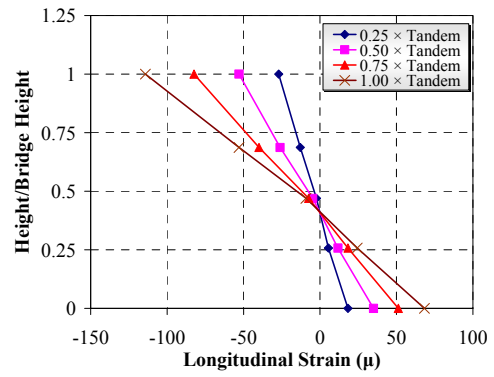
(a) Section C-Interior



(b) Section C-Exterior

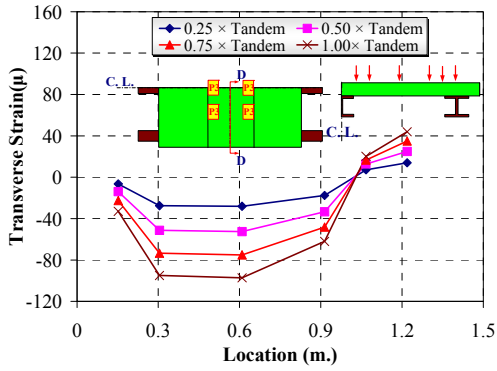


(c) Section H-Interior

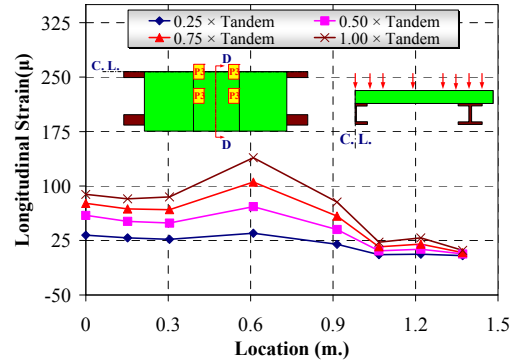


(d) Section H-Exterior

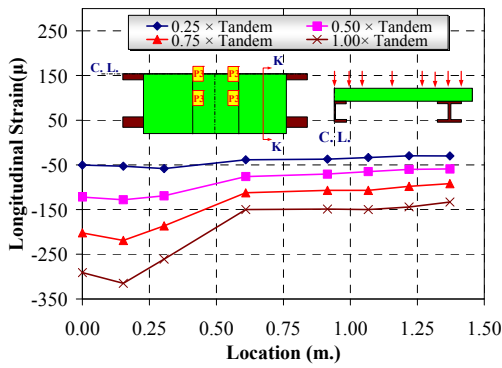
Figure 6.38 Strain Profile through Different Sections under Load Case No. 3



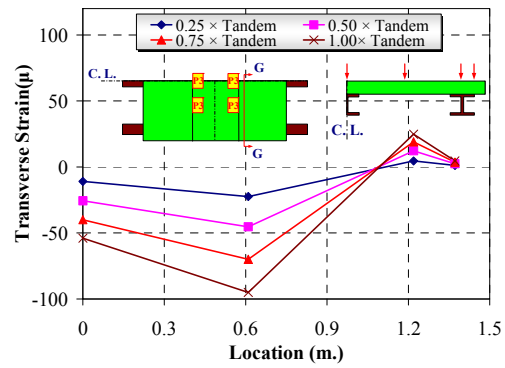
(a) Section D-Transverse



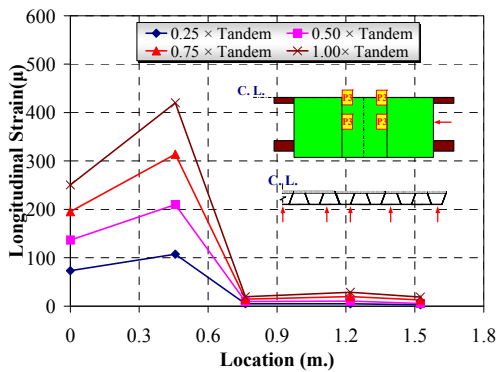
(b) Section D-Longitudinal



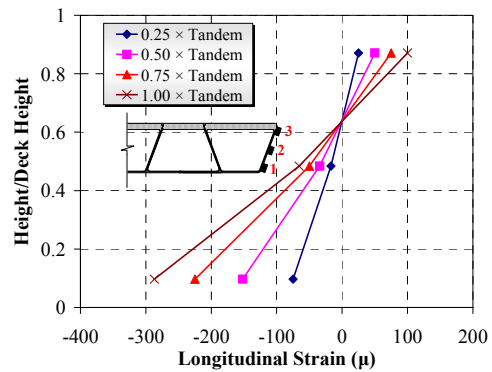
(c) Section K-Longitudinal



(d) Section G-Transverse



(e) Longitudinal Strain



(f) Section F-East

Figure 6.39 Strain Profile through Different Sections of the Deck under Load Case No. 3

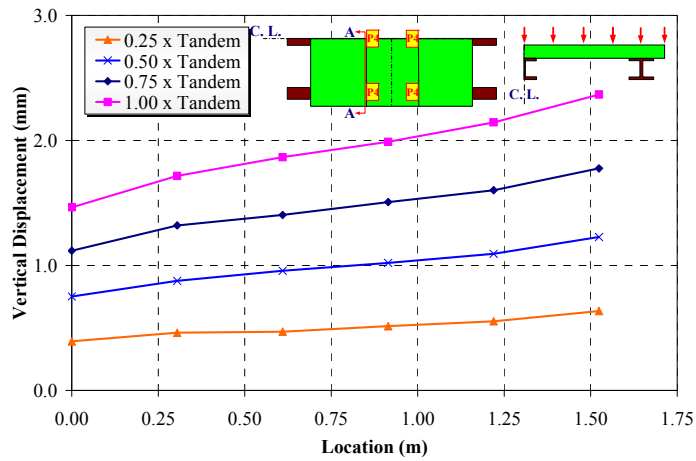


(a) Elevation

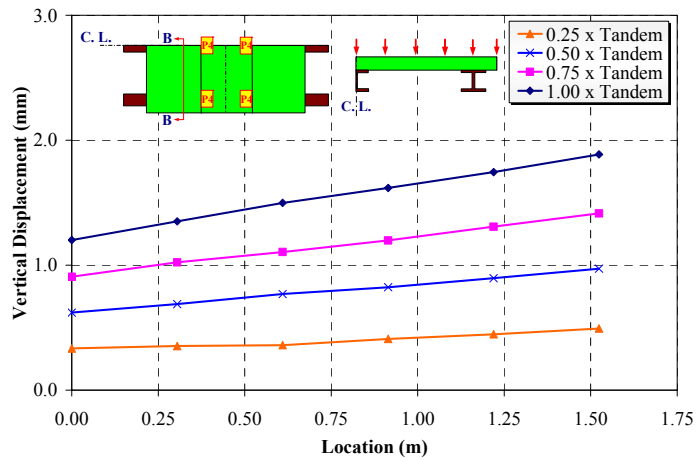


(b) Side View

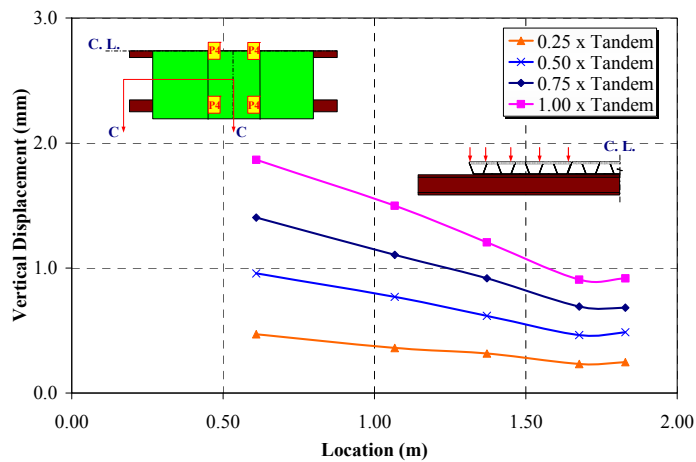
Figure 6.40 Test Set-Up for Service Load-Case 4



(a) Section A-Top Surface

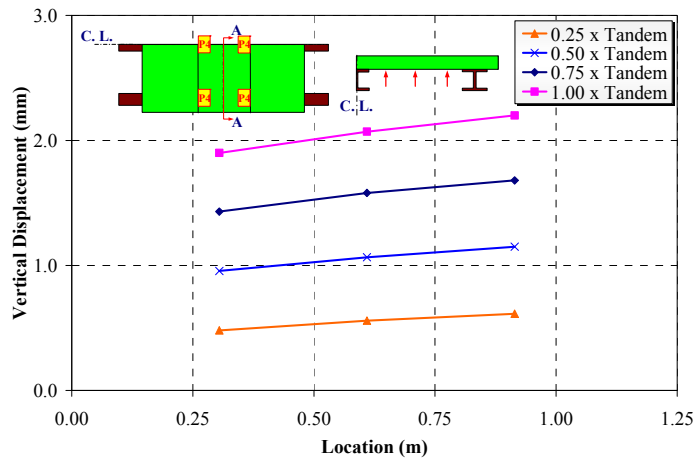


(b) Section B-Top Surface

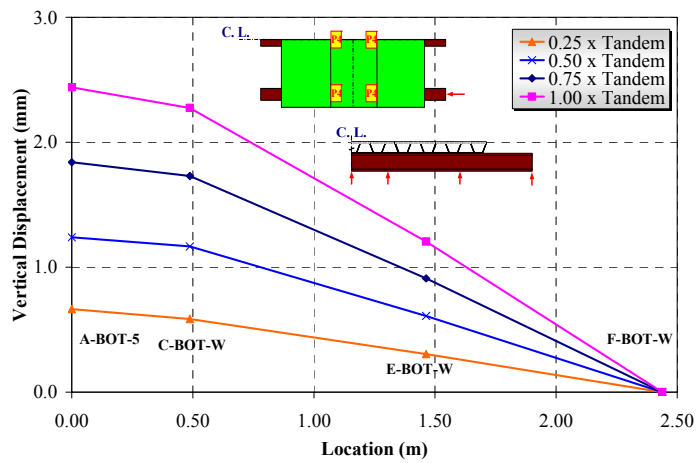


(c) Section C-Top Surface

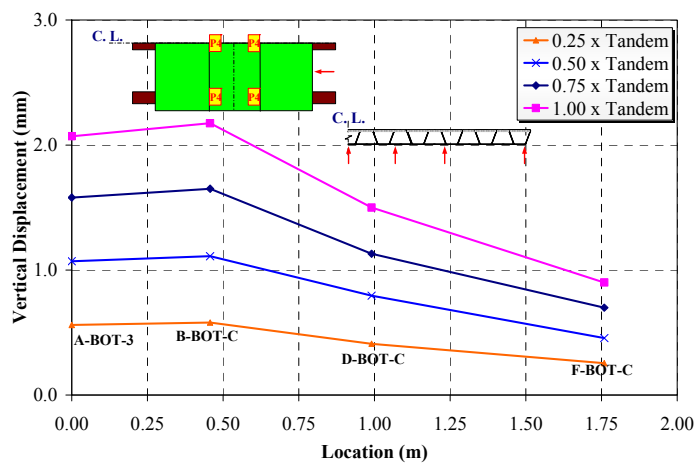
Figure 6.41 Deformed Shapes of the Deck at Different Load Levels under Load Case No. 4



(a) Bottom Surface-Transverse Direction

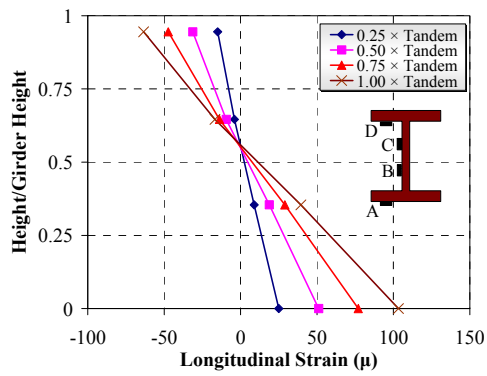


(b) Exterior Girder -Bottom Surface

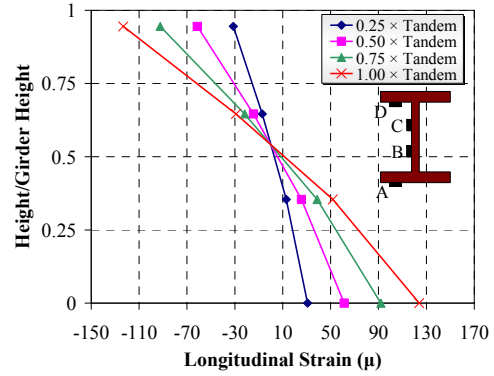


(c) Bottom Surface-Longitudinal Direction

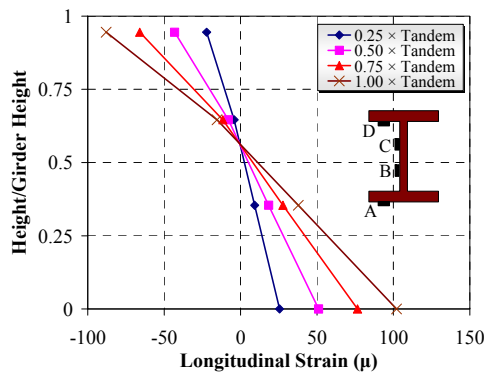
Figure 6.42 Deformed Shapes at Different Load Levels under Load Case No. 4



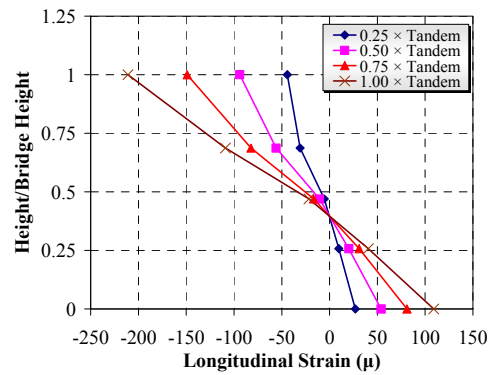
(a) Section C-Interior



(b) Section C-Exterior

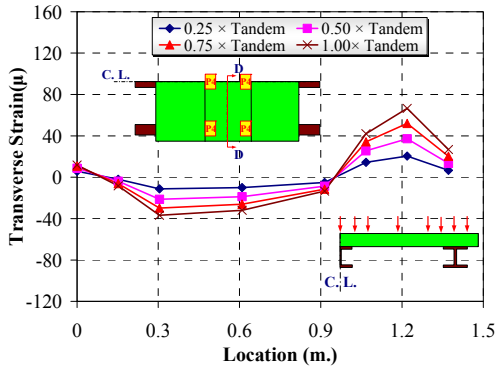


(c) Section H-Interior

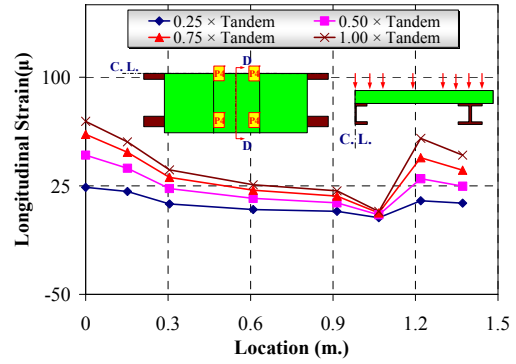


(d) Section H-Exterior

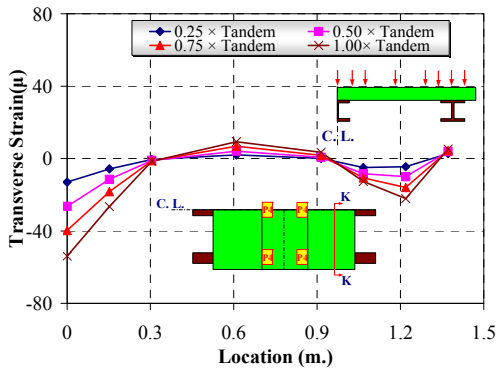
Figure 6.43 Strain Profile through Different Sections under Load Case No. 4



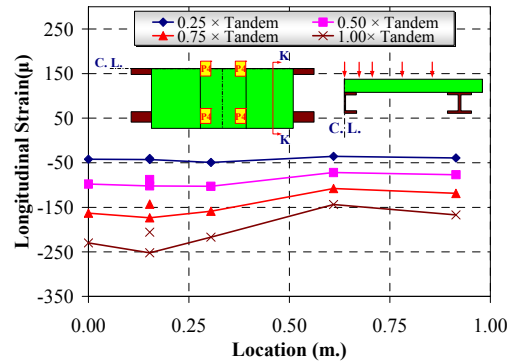
(a) Section D-Transverse



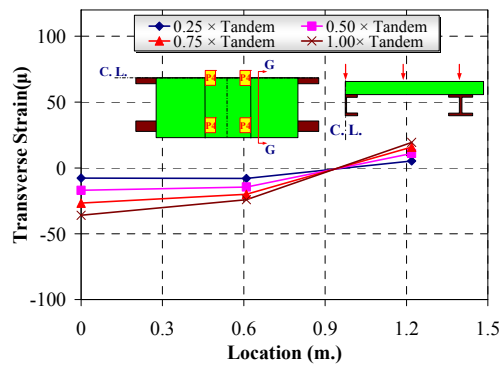
(b) Section D-Longitudinal



(c) Section K-Transverse



(d) Section K-Longitudinal



(e) Section G-Transverse

Figure 6.44 Strain Profile through Different Sections of the Deck under Load Case No. 4

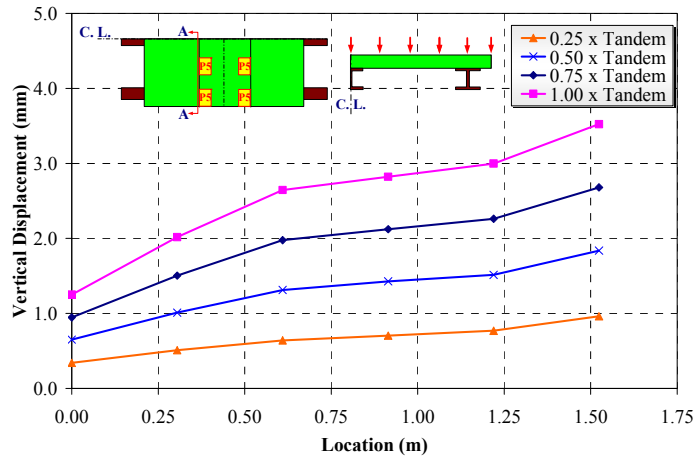


(a) Elevation

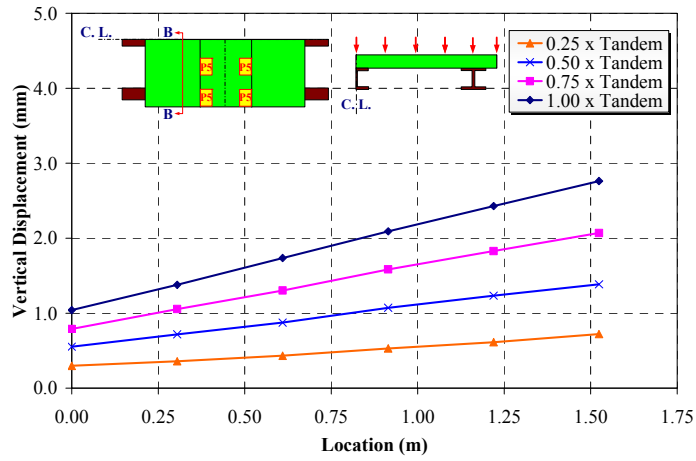


(b) Side View

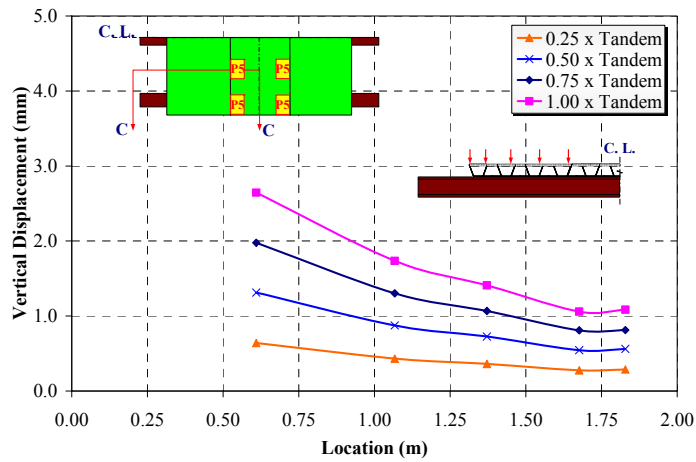
Figure 6.45 Test Set-Up for Service Load-Case 5



(a) Section A-Top Surface

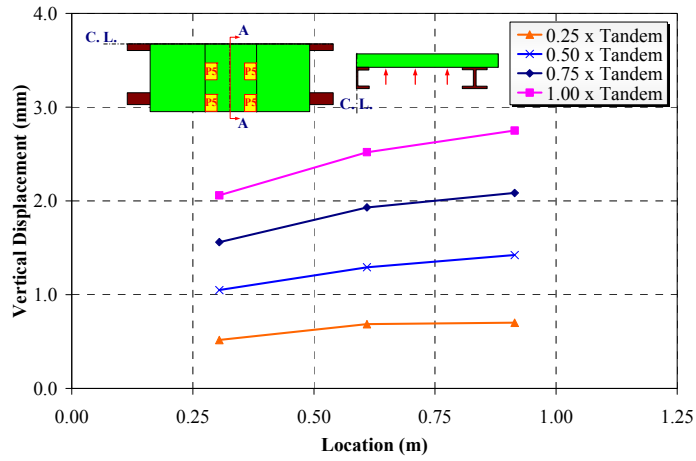


(b) Section B-Top Surface

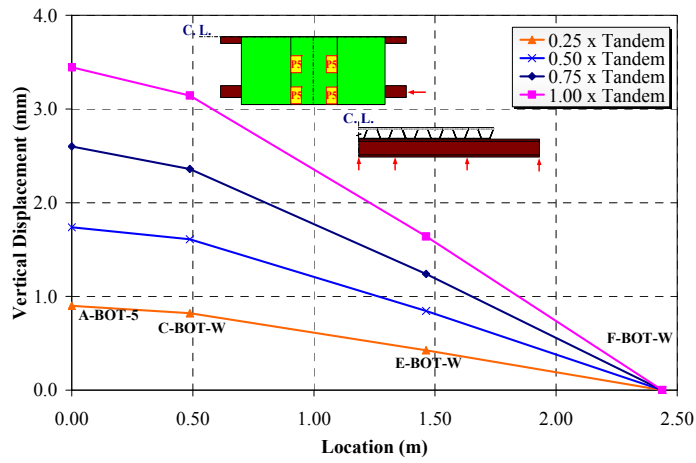


(c) Section C-Top Surface

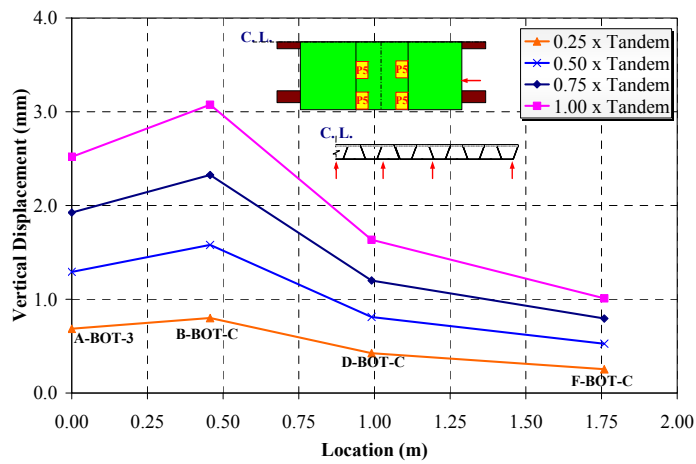
Figure 6.46 Deformed Shapes of the Deck at Different Load Levels under Load Case No. 5



(a) Bottom Surface-Transverse Direction

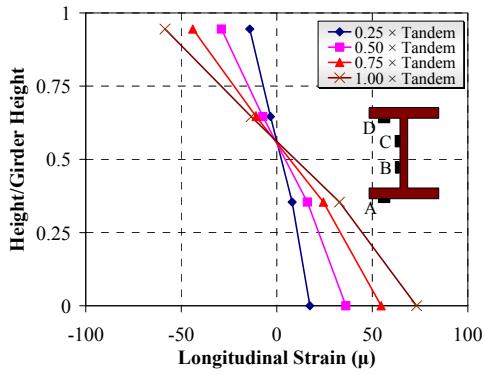


(b) Exterior Girder-Bottom Surface

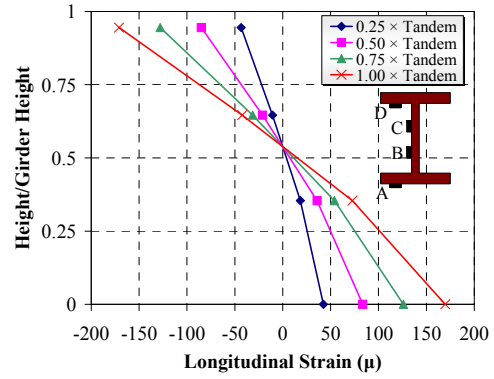


(c) Bottom Surface-Longitudinal Direction

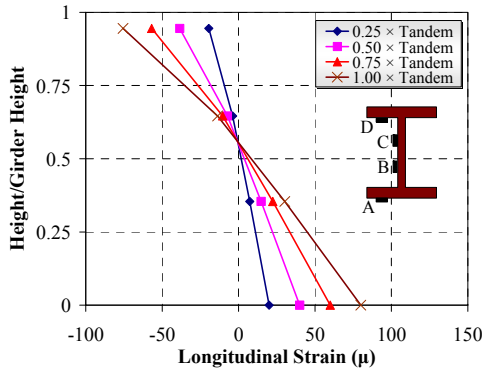
Figure 6.47 Deformed Shapes at Different Load Levels under Load Case No. 5



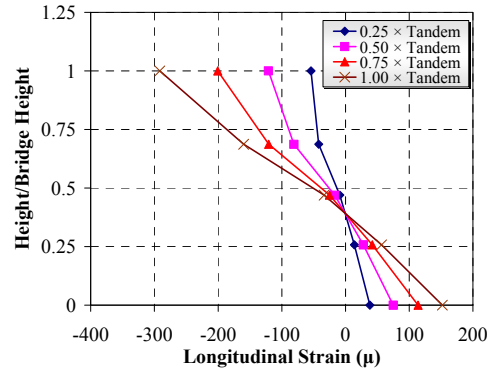
(a) Section C-Interior



(b) Section C-Exterior

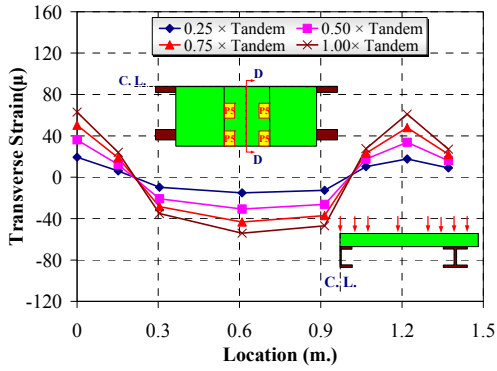


(c) Section H-Interior

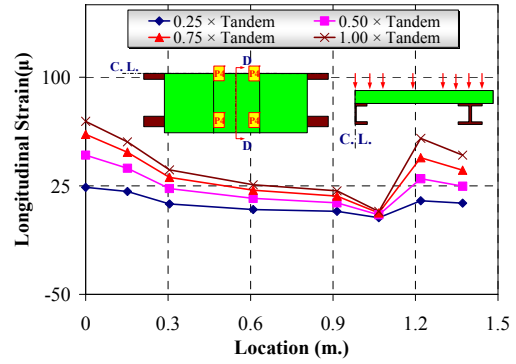


(d) Section H-Exterior

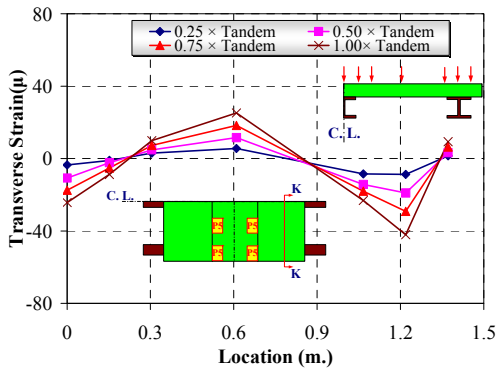
Figure 6.48 Strain Profile through Different Sections under Load Case No. 5



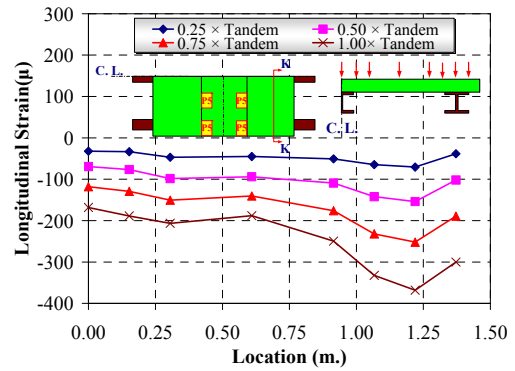
(a) Section D-Transverse



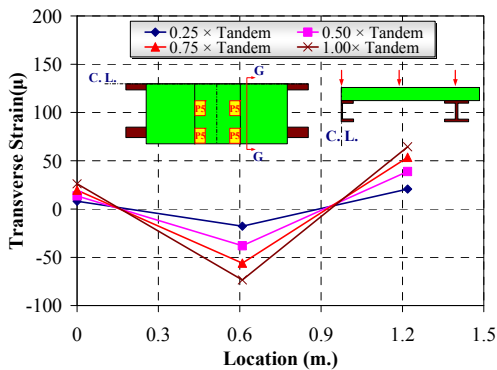
(b) Section D-Longitudinal



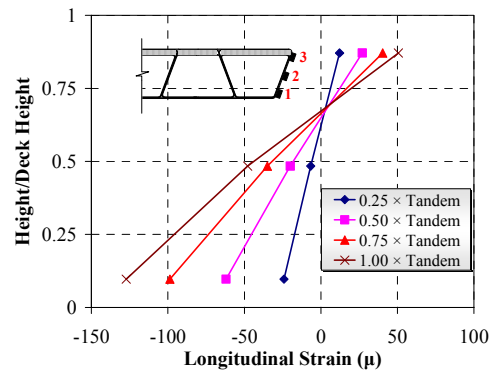
(c) Section K-Transverse



(d) Section K-Longitudinal



(e) Section G-Transverse



(f) Section B-East

Figure 6.49 Strain Profile through Different Sections of the Deck under Load Case No. 5

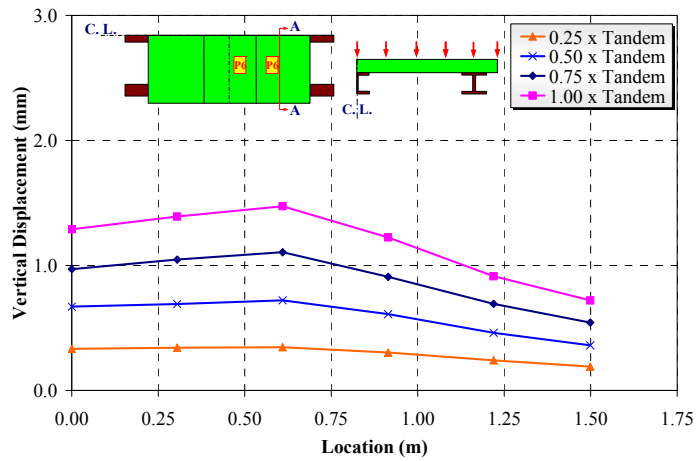


(a) Elevation

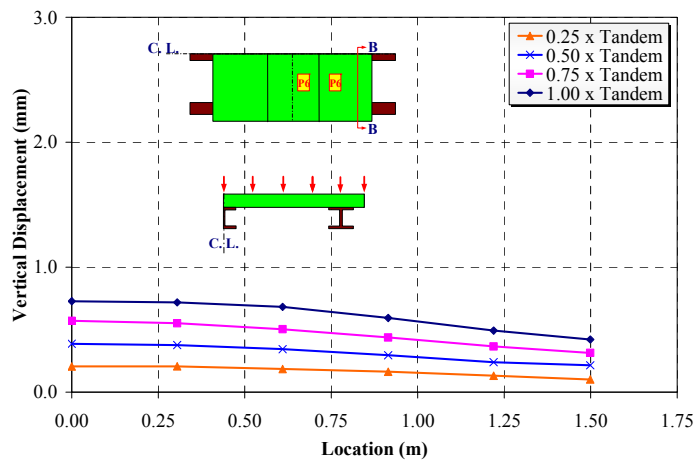


(b) Side View

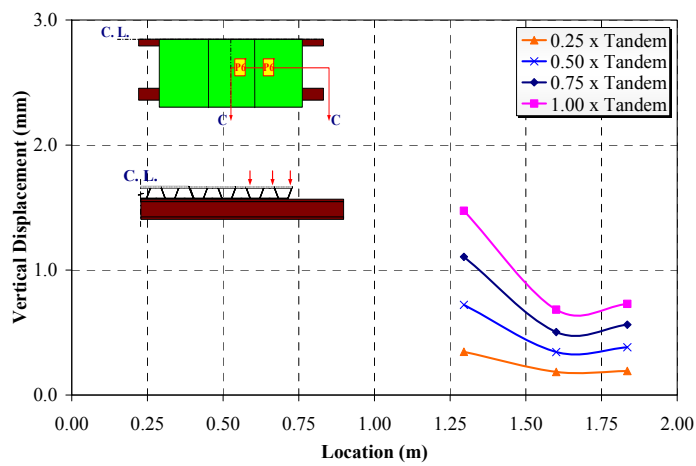
Figure 6.50 Test Set-Up for Service Load-Case 6



(a) Section A-Top Surface

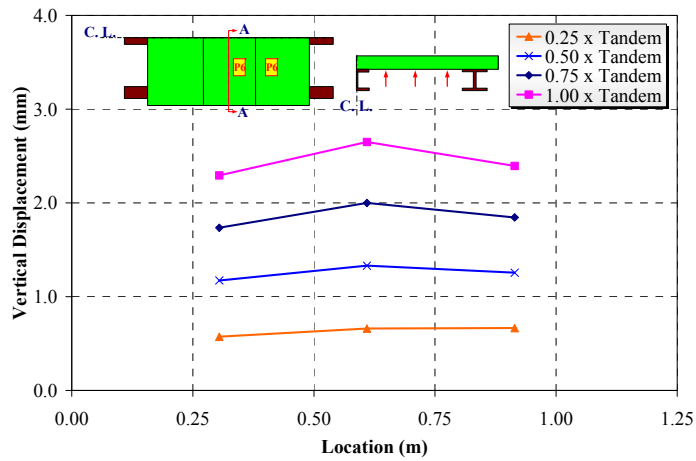


(b) Section B-Top Surface

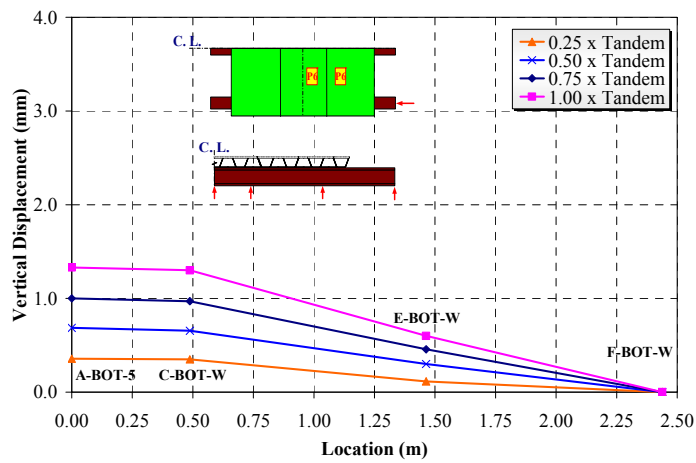


(c) Section C-Top Surface

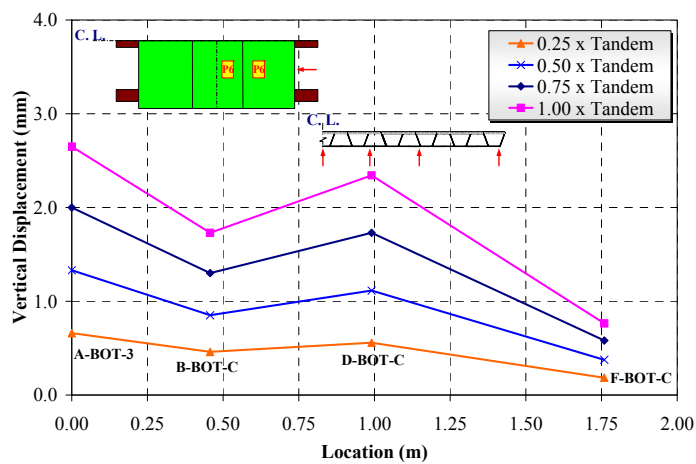
Figure 6.51 Deformed Shapes of the Deck at Different Load Levels under Load Case No. 6



(a) Bottom Surface-Transverse Direction

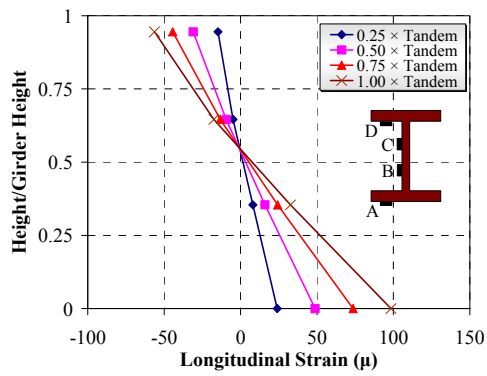


(b) Exterior Girder -Bottom Surface

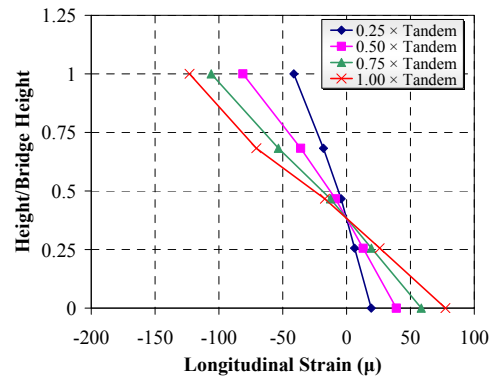


(c) Bottom Surface-Longitudinal Direction

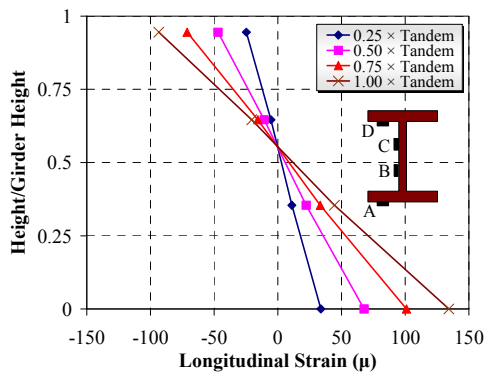
Figure 6.52 Deformed Shapes at Different Load Levels under Load Case No. 6



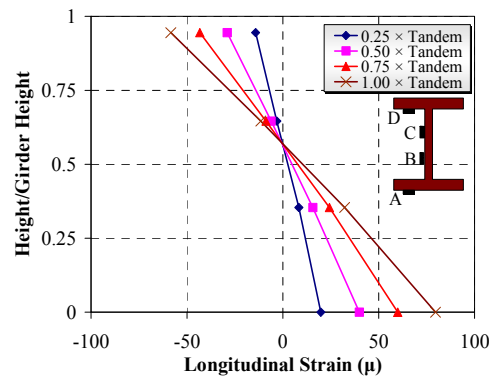
(a) Section C-Interior



(b) Section C-Exterior

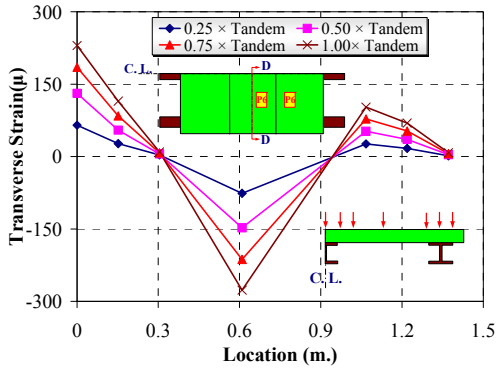


(c) Section H-Interior

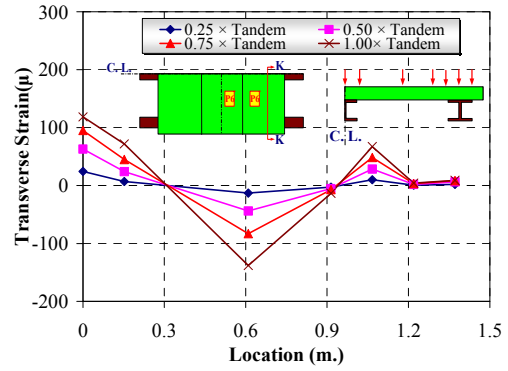


(d) Section H-Exterior

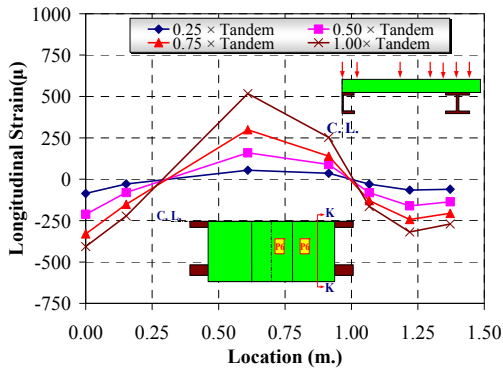
Figure 6.53 Strain Profile through Different Sections under Load Case No. 6



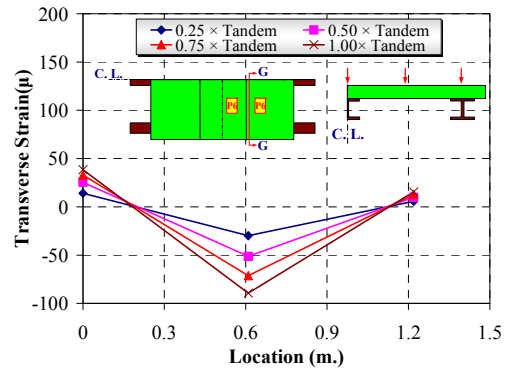
(a) Section D-Transverse



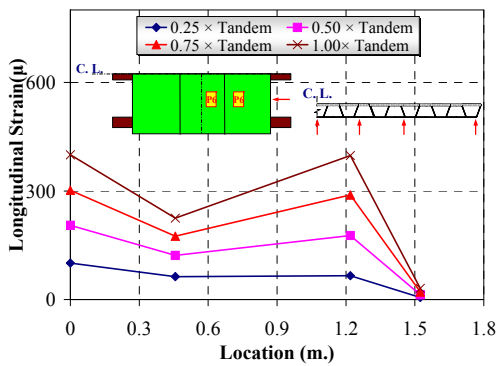
(b) Section K-Transverse



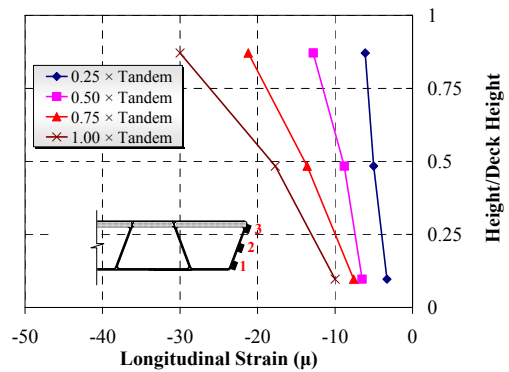
(c) Section K-Longitudinal



(d) Section G-Transverse



(e) Longitudinal Strain



(f) Section O-East

Figure 6.54 Strain Profile through Different Sections of the Deck under Load Case No. 6

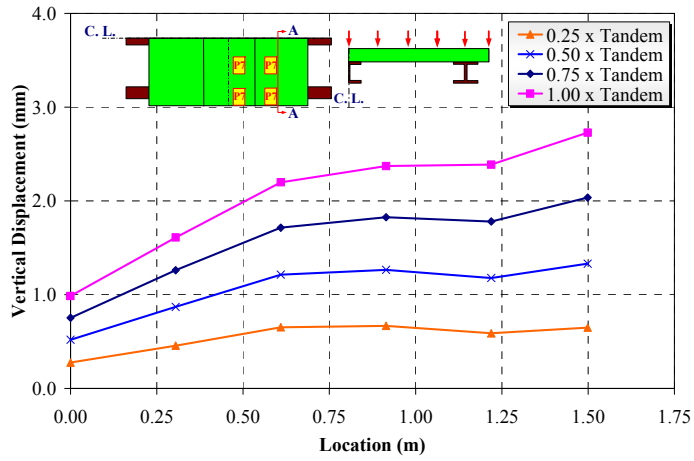


(a) Elevation

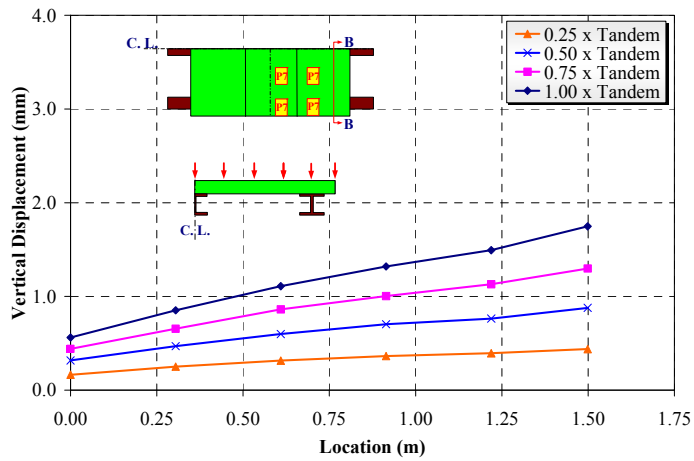


(b) Side View

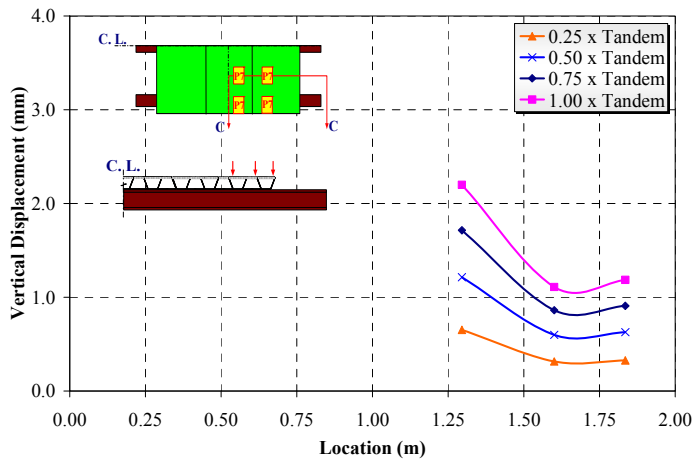
Figure 6.55 Test Set-Up for Service Load-Case 7



(a) Section A-Top Surface

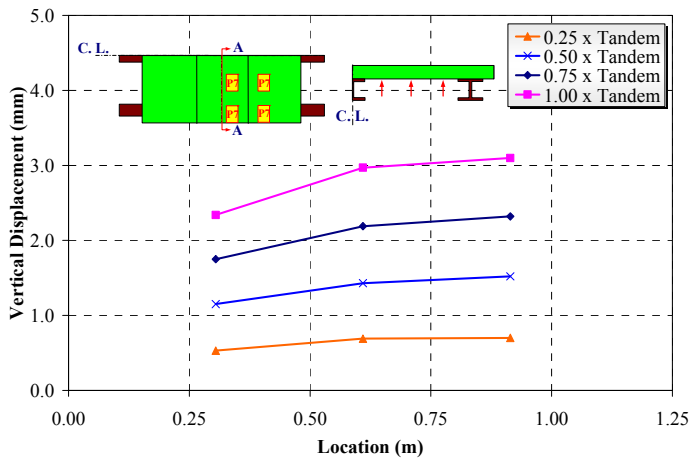


(b) Section B-Top Surface

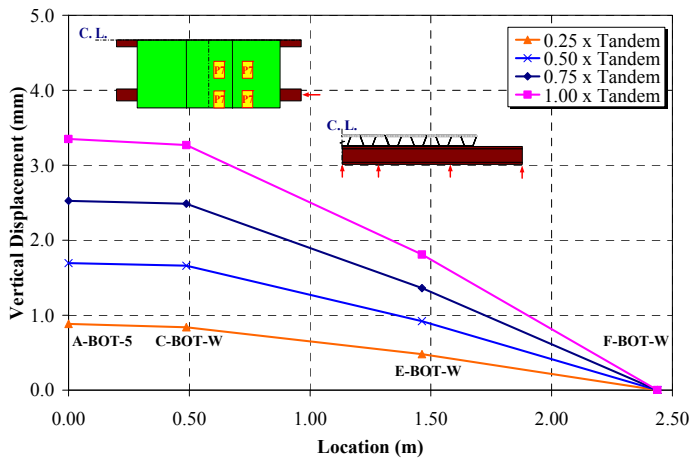


(c) Section C-Top Surface

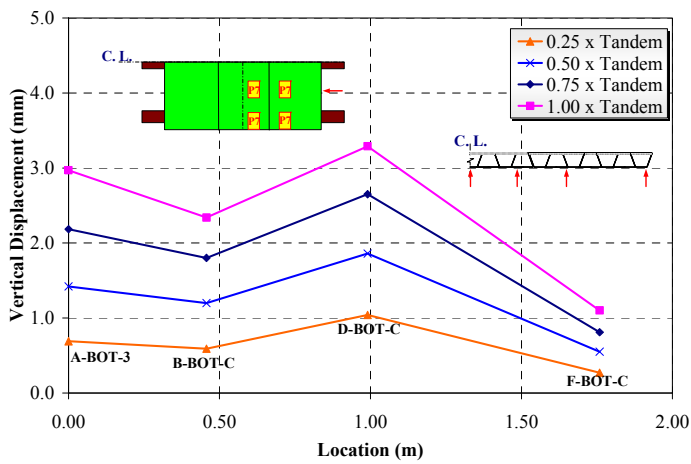
Figure 6.56 Deformed Shapes of the Deck at Different Load Levels under Load Case No. 7



(a) Bottom Surface-Transverse Direction

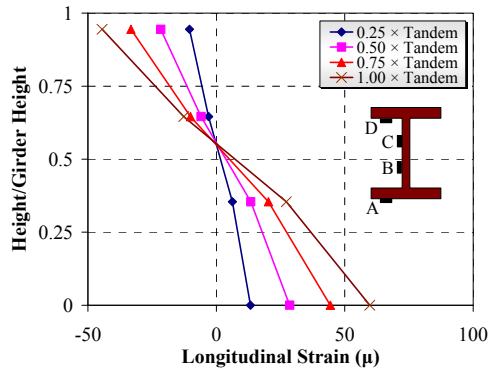


(b) Exterior Girder-Bottom Surface

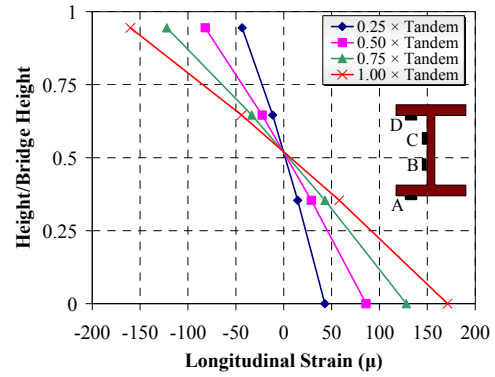


(c) Bottom Surface-Longitudinal Direction

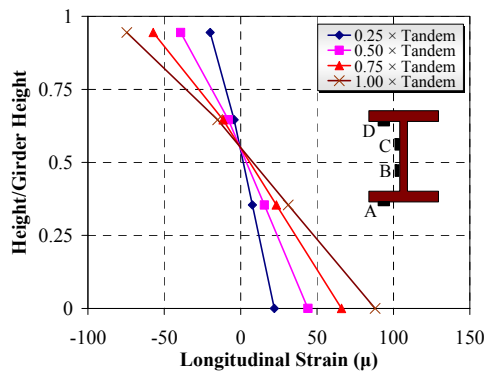
Figure 6.57 Deformed Shapes at Different Load Levels under Load Case No. 7



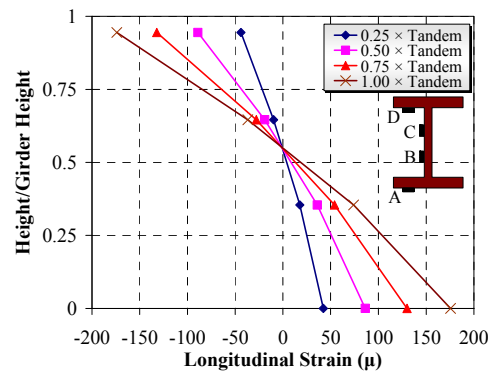
(a) Section C-Interior



(b) Section C-Exterior

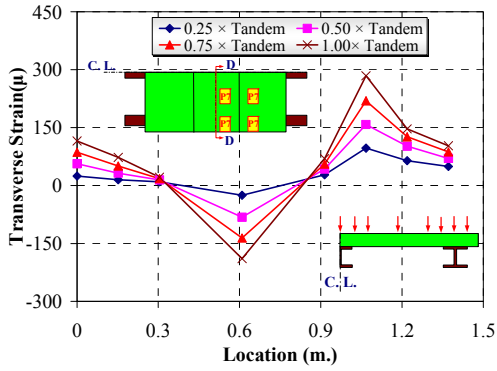


(c) Section H-Interior

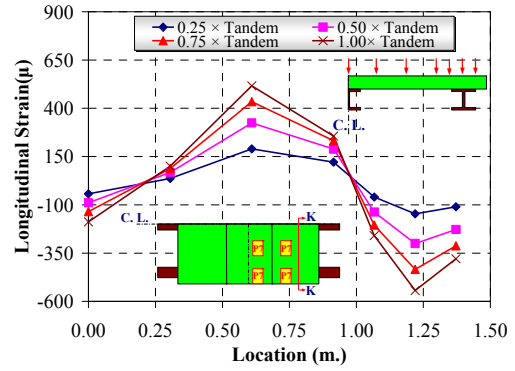


(d) Section H-Exterior

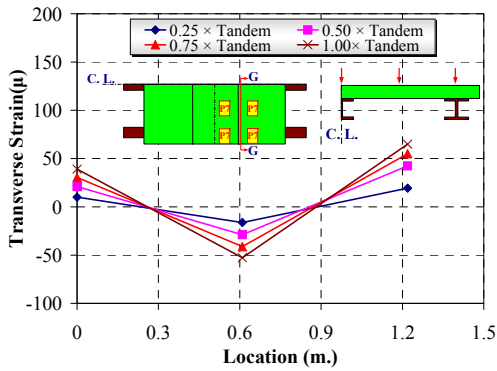
Figure 6.58 Strain Profile through Different Sections under Load Case No. 7



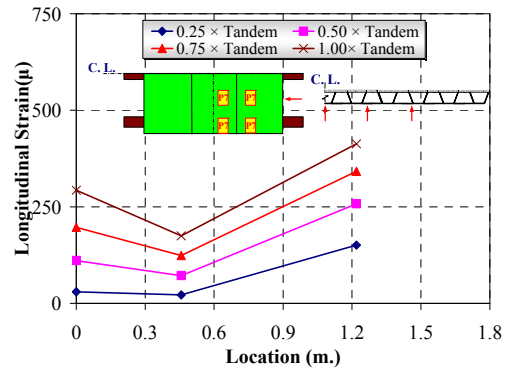
(a) Section D-Transverse



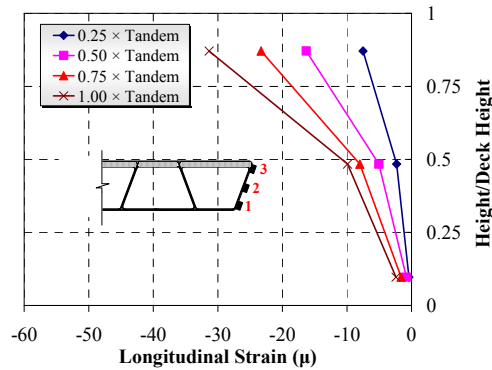
(b) Section D- Longitudinal



(a) Section G-Transverse



(b) Longitudinal Strain



(e) Section O-West

Figure 6.59 Strain Profile through Different Sections of the Deck under Load Case No. 7

FINITE ELEMENT ANALYSIS

An analytical study of the scale-model bridges presented in Chapter 5 and 6 was performed. The goal of the analytical study was to develop finite element models of the bridges that accurately predict structural parameters such as deflections and strains that can be compared with the experimental results. The modeling techniques, if validated, could be used to design hybrid bridges. The general purpose finite element analysis software, ABAQUS (Hibbit, Karlsson & Sorensen, Inc., 2002), was used for the finite element analysis.

7.1 BRIDGE SUPERSTRUCTURE

7.1.1 Geometric and Boundary Condition Modeling

This model was created using the material properties obtained from the material tests (see Chapter 5). Shell elements were the principal element type used since the superstructure was made of GFRP laminates. The reduced integration S4R5 element (4-node doubly curved thin shell element; each node with five degree of freedom) was used to model the thin GFRP laminate. Reduced integration was performed on 5 gauss points. The continuum or solid element C3D8R (8-node linear brick, reduced integration) was used to model the concrete. The advantages of employing the reduced integration continuum elements are: (1) a significant reduction in computation time, and (2) prevention of shear locking effect from full integration (especially in first-order integrated elements). However, appropriate hourglass control parameters must be introduced into the reduced integration continuum elements because this type of element can be highly distorted due to having only a single integration point that could result in zero strain values. The FEM model of the prototype hybrid FRP-concrete bridge superstructure model is shown in Figure 7.1. The total number of elements was 46,720

(27,040 S4R5; 19,680 C3D8); the total number of nodes was 38,640. The elastomeric bearing pads were not modeled. Perfect bond between concrete and GFRP laminates was assumed.

Boundary conditions were imposed at the structural supports on two lines of nodes on the bottom surface. These supports rested on elastomeric bearing pads. Appropriate displacement boundary conditions were required as follows: nodes at $y=0$ and $z=0$ were restrained in the y and z directions (pinned condition) and nodes at $y=L$ and $z=0$ were restrained in the z direction (roller condition). The nodes at $x=0$, $z=0$, and $y=0$ and $y=L$ were restrained in the x direction.

7.1.2 Material Modeling

A linear finite element model can predict the behavior of a hybrid bridge with sufficient accuracy if the strain induced in the materials is within the strain ranges where the elastic moduli of the materials were obtained. Both concrete and GFRP were shown to behave nonlinearly in the higher strain range. However, material nonlinearity was not considered for the initial phase of the analysis (see Chapter 8).

7.1.3 Static Stress Analysis

7.1.3.1 Prototype Bridge Superstructure

As noted in Chapter 3, both stiffness and strength criteria were considered in the design of the hybrid FRP-concrete superstructure bridge. A detailed finite element analysis was performed on the optimized prototype bridge superstructure to check AASHTO stiffness and strength criteria.

To check whether the maximum deflection under $(1+IM) \times$ truck load is smaller than $L/800$ (22.9 mm), the load equivalent to $(1+IM) \times$ truck load was applied to the prototype superstructure FE model. The maximum vertical displacement was 21.8 mm ($0.95 \times L/800$), which satisfied the AASHTO limit. Figure 7.2 shows the vertical displacement contours of the prototype superstructure. For the strength I limit analysis (see section 3.3.2), the maximum Tsai-Hill failure index for GFRP laminates was well below 1.0 (see Figure 7.3). The maximum value for the GFRP laminates was 0.364, which was reached at stress concentration at the corners of the superstructure. The

maximum transverse shear stress at the interface between two trapezoidal box sections was 5.58 MPa, which is smaller than the shear strength of commercially available resins which range from 10.4 to 34.5 MPa (Aref, 1997). The compressive stress in the concrete elements was smaller than the compressive strength limit ($0.8 \times f'_c$). The maximum compressive stress in the concrete elements was 8.2 MPa ($0.28 \times f'_c$), located at the top of the concrete layer immediately below the tire of the second axle.

7.1.4 Verification with Experimental Results

The verification of the finite element modeling scheme described in previous sections can be accomplished by comparing the results generated by analysis to those obtained from scaled model laboratory tests.

Deflections and strain data recorded at key locations on the panel were compared to the analytical prediction. Results from the finite element model (see Figure 5.12 and Figure 5.14 for locations) and the experiments are presented in Table 7-1. Also reported in the table is the percent difference between the results, where the percent difference is calculated as the difference between the two values divided by the minimum value. The percent difference for the deformations varies between 0 to 4 %. The average error between the deformation obtained from the experiment and the analysis at the tandem load is 2%; the difference at a load equal to twice the tandem load is 4%.

Figure 7.4 to Figure 7.6 show the deformed shapes obtained from the experiment and the linear analysis. Figure 7.4 presents deformation of the top surface at different load levels for sections I and H; Figure 7.5 presented deformed shapes at different load levels for sections G and F (refer to Figure 5.12 for measurement locations). In general, the analysis predicted the experimental results extremely well. The difference between results is insignificant, which can be explained by the use of the reduced-integration formulation in the solid elements. Figure 7.6 presents deformed shapes of the bottom and top surfaces at different load levels for sections E and F (refer to Figure 5.12 for measurement locations). The finite element analysis results show good correlations with the experimental results. Figure 7.7 presents the force-displacement response predicted by the linear finite element analysis and experimental results at F-TOP-W, and E-BOT-2, respectively. The finite element and experimental results are well correlated in the elastic

range. In the inelastic range, the experimental curve showed loss of strength while the finite element analysis results did not. This deviation is as a result of material nonlinearity of both concrete and GFRP composites. As the strain in the GFRP increases, the tangent modulus of GFRP decreases.

Figure 7.8 and Figure 7.9 present strains predicted by the FEA and those from the experiments. Figure 7.8 presents the strain variation on the exterior web at section E. Longitudinal strains on the tension side were predicted better than those on the compression side. Figure 7.9 illustrates the longitudinal strain variation in section G. The FEA predicted the strain distributions in the test specimen relatively well, although there are small discrepancies. The discrepancies may be caused because Section E is very close to the loading points, which cause a partial damage of gauges close to the loading points.

7.2 BRIDGE DECK ON STEEL GIRDERS

7.2.1 Geometric and Boundary Condition Modeling

The hybrid FRP-concrete deck model was created using the material properties, and element types which were used in modeling of the hybrid FRP-concrete superstructure (see section 7.1). Steel girders were modeled in a similar manner as the concrete layer, using a continuum element with reduced-integration formulation (C3D8R in *ABAQUS*).

The area between the girders and deck was modeled using contact elements. The girder top surface was assumed to be the master surface, while the deck bottom surface was assumed as the slave. The connection between the girders and deck was assumed as fully composite at the locations where these connections existed in the physical model. By using a composite bond in the connection modeling, bond-slip effects cannot be detected. However, only a static monotonic loading was considered in this research, and overall global behavior is considered more significant than local effects such as bond-slip in this investigation. Perfect bond between the deck panels was assumed in all analyses carried out in this study. The FEM model of the prototype hybrid FRP-concrete bridge deck model is shown in Figure 7.10.

7.2.2 Material Modeling

The concrete, the steel and GFRP were assumed to be linear.

7.2.3 Verifications with Experimental Results

Figure 7.11 and Figure 7.12 and Figure 7.13 present the deformed shapes predicted by the linear FEA and those obtained from the flexural loading on the hybrid deck test specimen. As well, the FEA predicted the behavior of the hybrid specimen very well. Figure 7.11 shows the deformed shapes of the top surface obtained from the experiments and the linear FEA under load case no. 1, while Figure 7.12 shows the deformed shapes of the top surface under load case no. 2 (refer to Figure 6.21 for measurement locations). The FEA predicted the deformed shape in the test specimen relatively well, although there are small discrepancies at locations close to the loading points because of local deformations. Figure 7.13 presents the deformed shapes of the bottom surface of the inner girder and the hybrid deck, respectively. Finite element analysis results exhibit a larger global flexibility when compared with the experimental results. The difference between results is not significant. Overall, the finite element results correlate well with the test results.

Figure 7.14 and Figure 7.15 present the strain predicted by the FEA and those from the experiments. Figure 7.14 presents strain profile through steel girder under load case no. 2 at section C, while Figure 7.15 presents strain profile through steel girder under load case no. 2 at section H, respectively. A negative value indicates compressive strain, while a positive value indicates tensile strain. The correlation between the result of finite element analysis and experimentation are very good results, especially at the bottom flange of the girder. This is because the boundary conditions which were assumed in the FEA at top flange of steel girders were different from those in the experiment.

7.3 SUMMARY

Linear FEA was found to be very accurate in predicting the flexural behavior of the proposed hybrid bridge systems in the elastic range. Linear FEA can be a good tool to be used in design of the proposed hybrid bridge systems.

Table 7-1 Analytical and Experimental Results

| Location | At the tandem load | | | At twice tandem load | | |
|-----------------|--------------------|-------------|---------------|----------------------|-------------|---------------|
| | Linear FEA(mm) | Exper. (mm) | Different (%) | Linear FEA(mm) | Exper. (mm) | Different (%) |
| F-TOP-E | 2.77 | 2.70 | 2.53 | 5.54 | 5.25 | 5.23 |
| F-TOP-2 | 2.82 | 2.84 | 0.71 | 5.65 | 5.35 | 5.31 |
| F-TOP-C | 2.84 | 2.77 | 2.46 | 5.67 | 5.21 | 8.11 |
| E-BOT-E | 2.79 | 2.81 | 0.72 | 5.59 | 5.37 | 3.94 |
| E-BOT-W | 2.79 | 2.79 | 0.00 | 5.59 | 5.17 | 7.51 |
| H-TOP-E | 1.91 | 1.97 | 3.14 | 3.81 | 3.86 | 1.31 |
| H-TOP-C | 1.95 | 2.01 | 3.08 | 3.91 | 3.93 | 0.51 |
| G-TOP-E | 2.54 | 2.63 | 3.54 | 5.07 | 5.14 | 1.38 |
| F-TOP-II | 2.82 | 2.84 | 0.71 | 5.60 | 5.69 | 1.61 |
| Average | | | 1.88 | | | 3.88 |

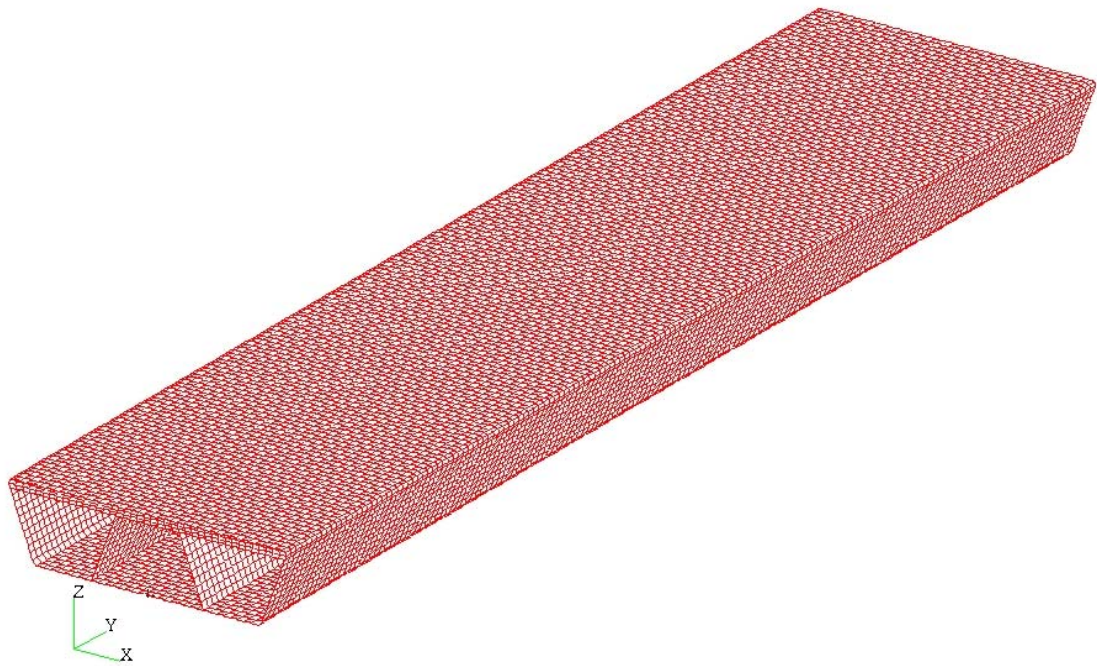


Figure 7.1 Finite Element Model of the Prototype Bridge Superstructure

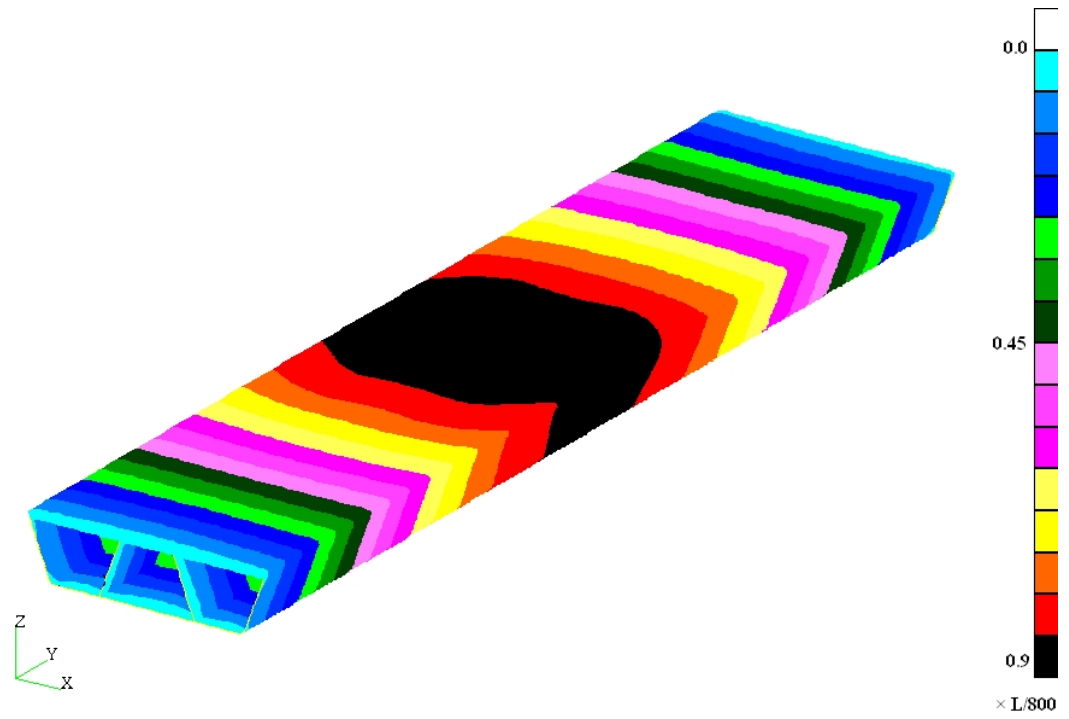


Figure 7.2 Vertical Displacement Contour for the Deflection Check

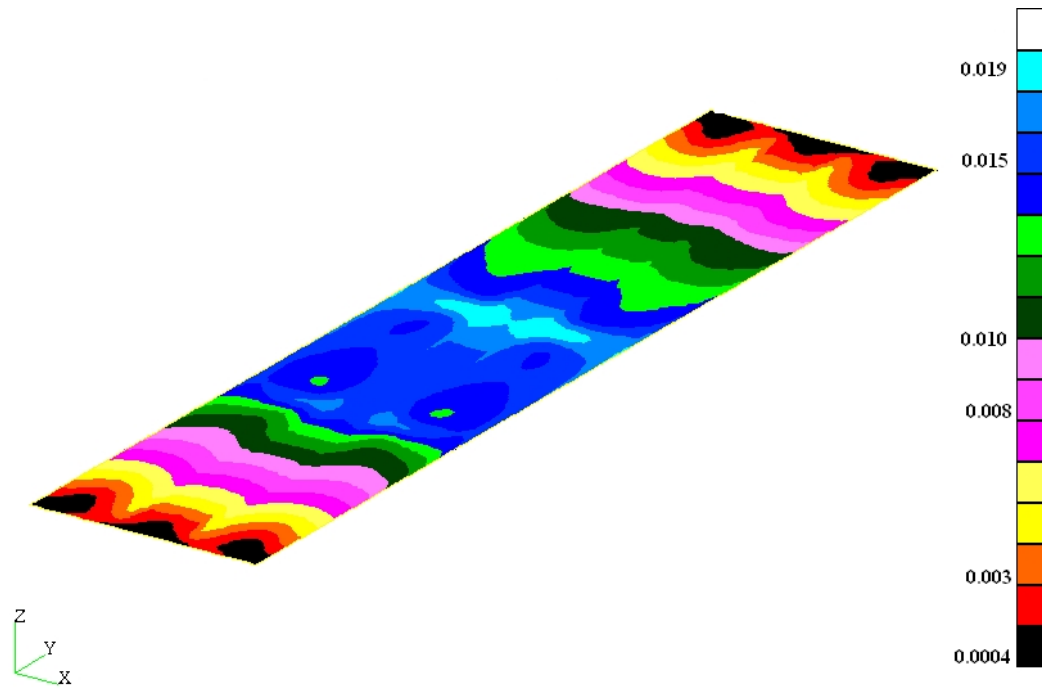
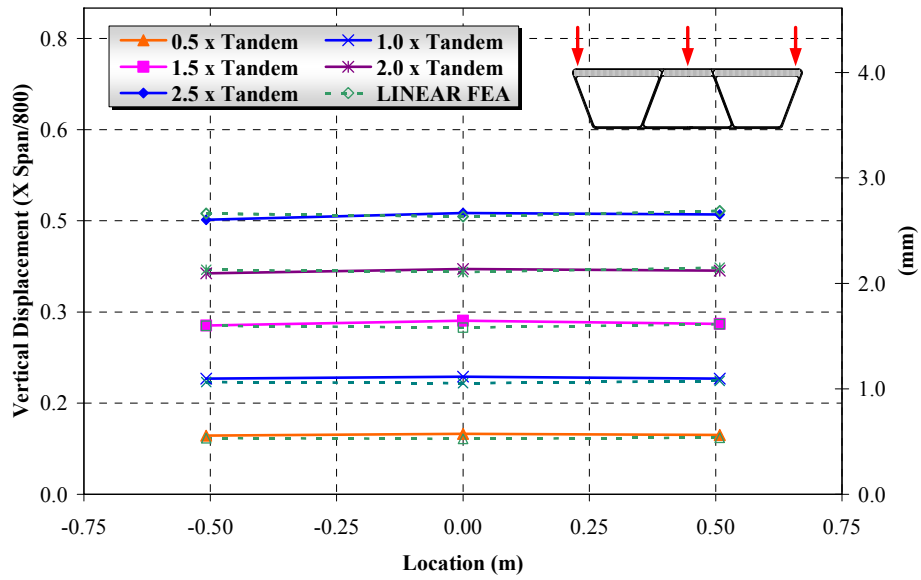
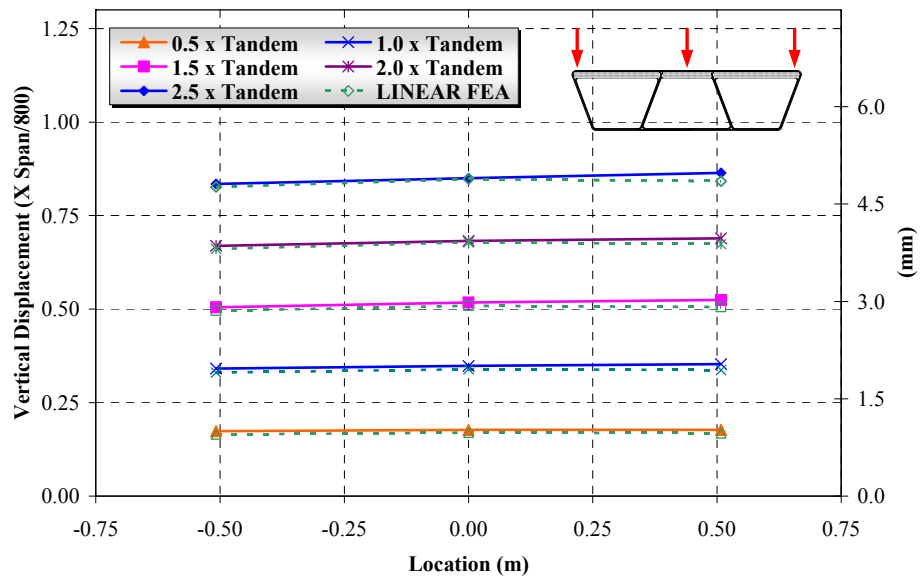


Figure 7.3 Tsai-Hill Failure Index for the Strength I Limit at the Top Surface

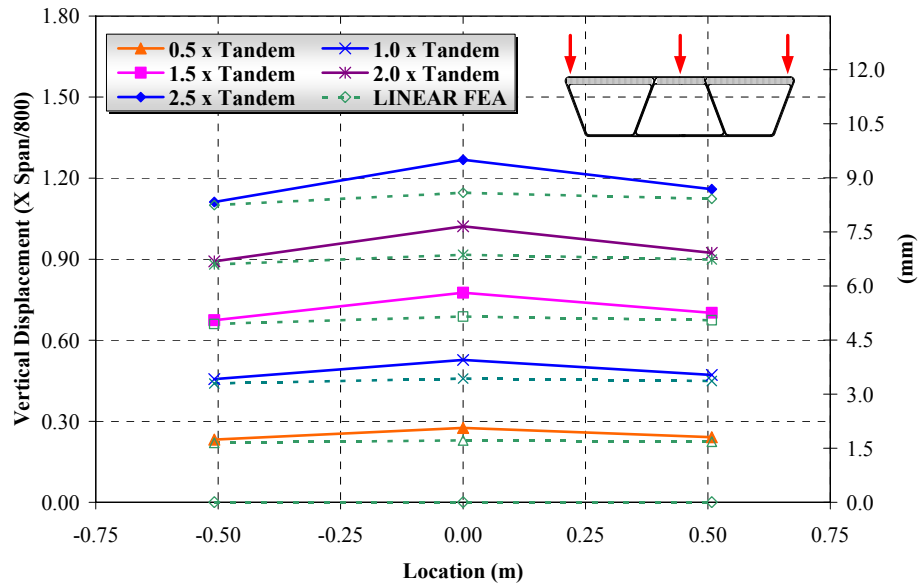


(a) Section I

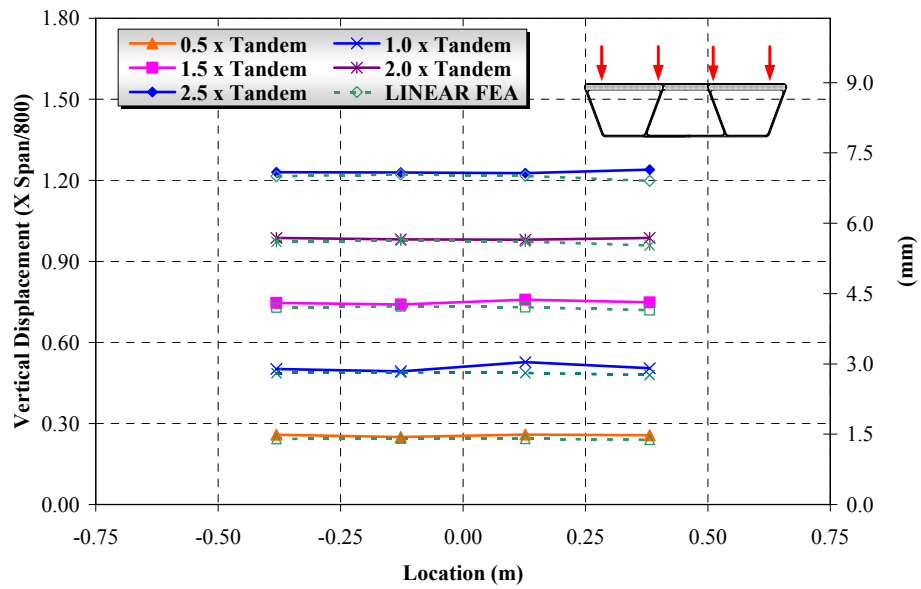


(b) Section H

Figure 7.4 Deformed Shapes at Sections I and H

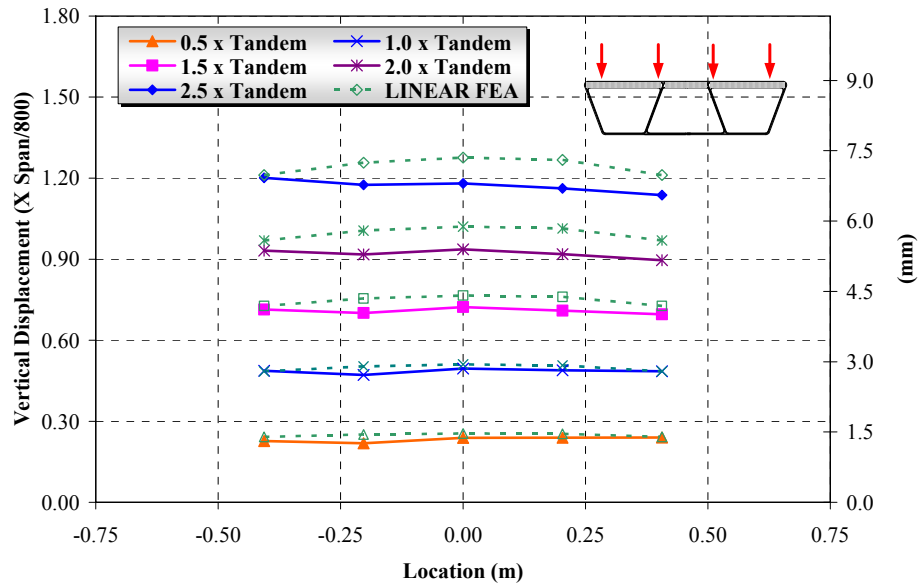


(a) Section G

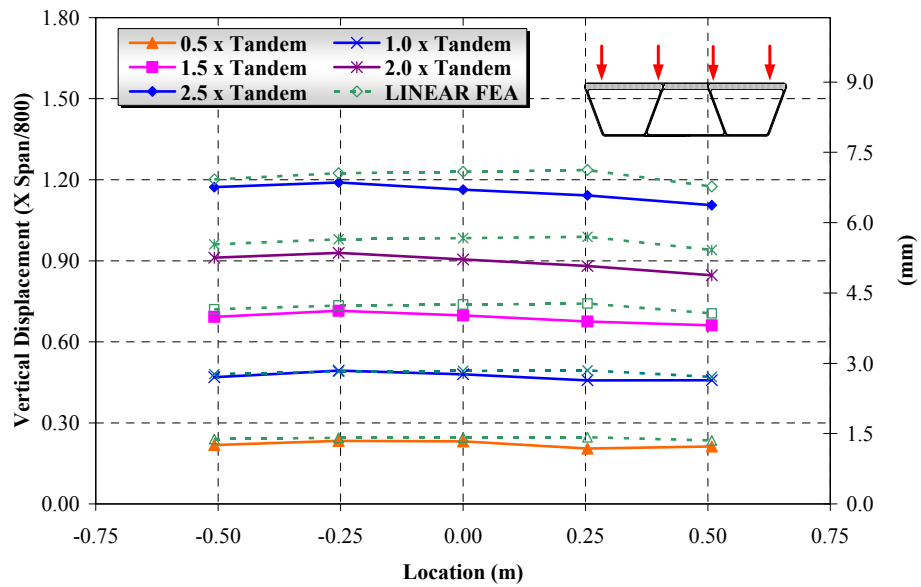


(b) Section F

Figure 7.5 Deformed Shapes at Sections G and F

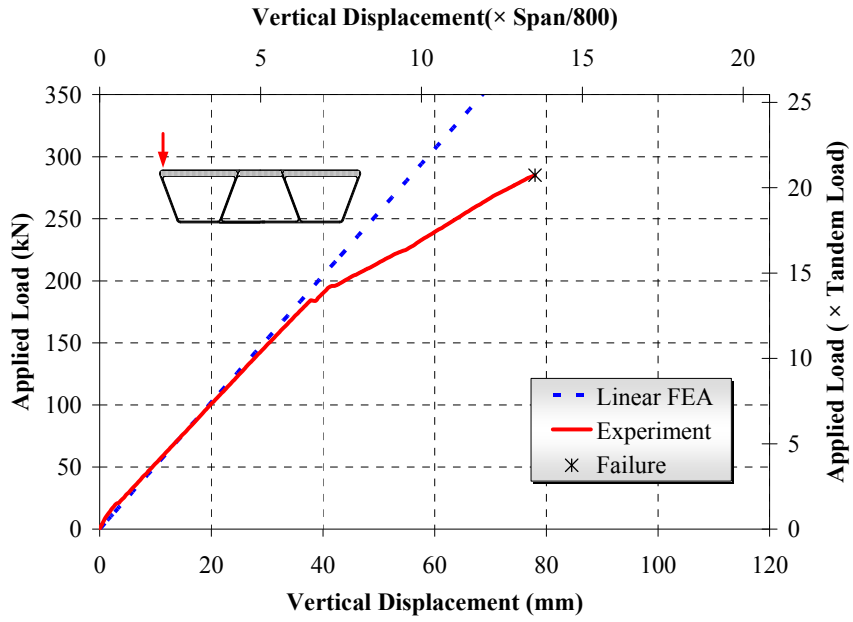


(a) Bottom Surface (Section E)

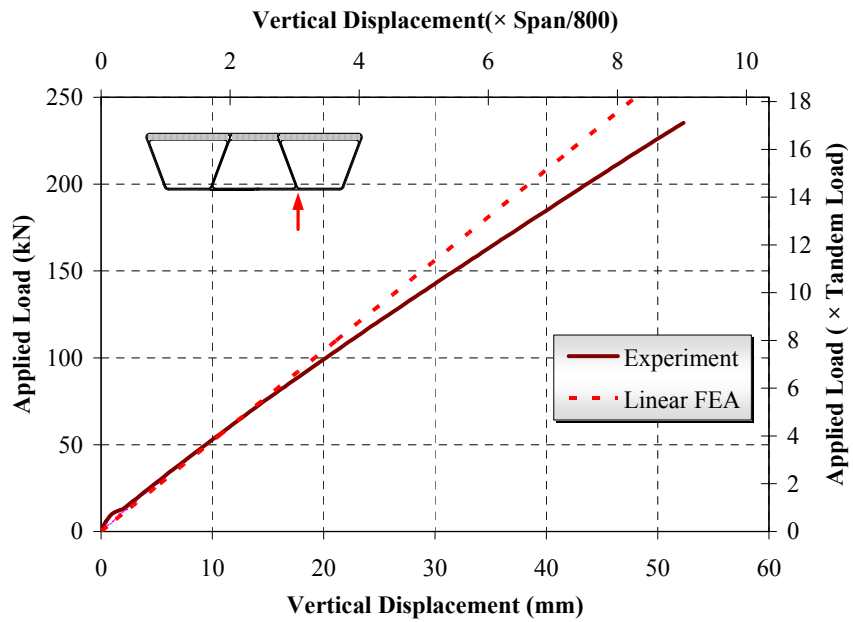


(b) Top Surface (Section F)

Figure 7.6 Deformed Shapes at the Bottom and Top Surfaces



(a) F-TOP-W



(b) E-BOT-2

Figure 7.7 Force-Displacement Response

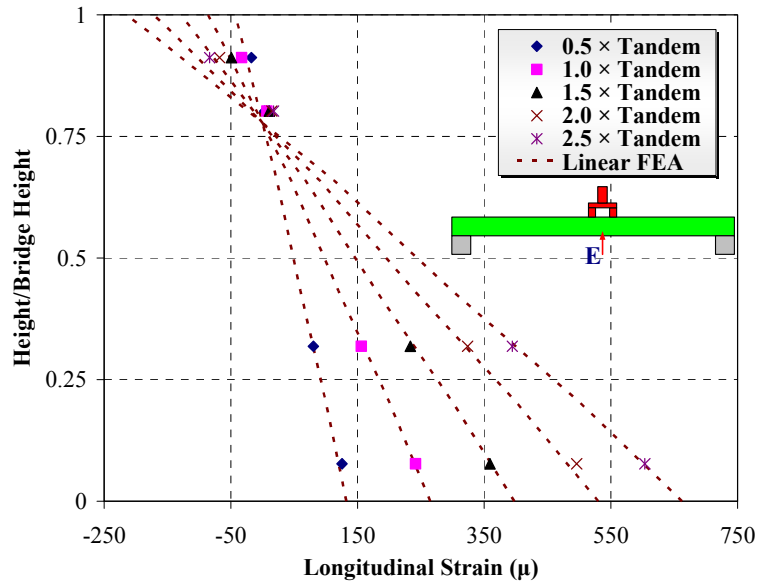


Figure 7.8 Strain Variation on the Exterior Web at Section E

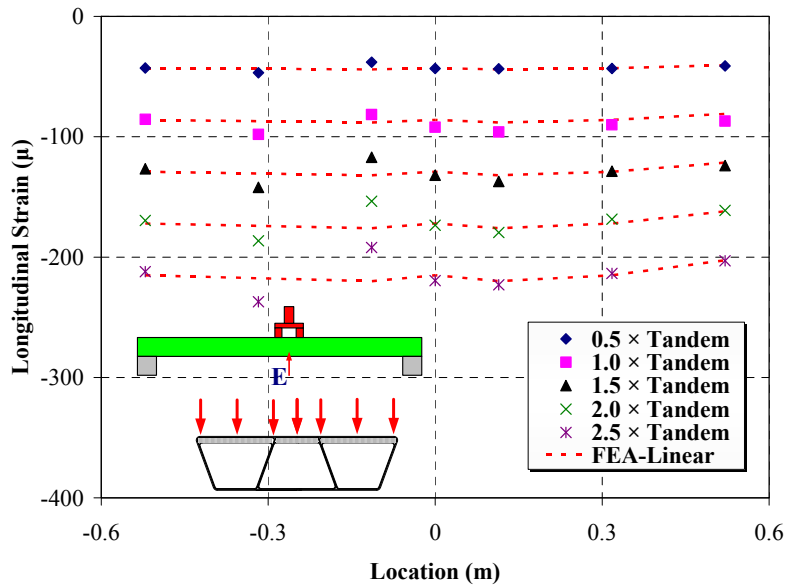


Figure 7.9 Longitudinal Strain Variation in Section E

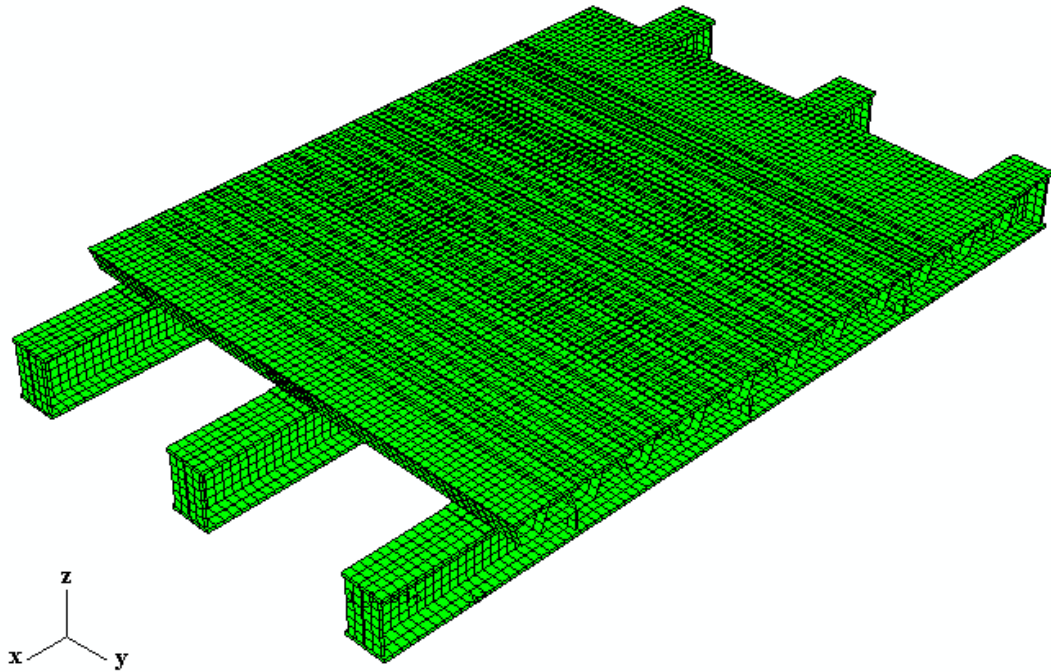
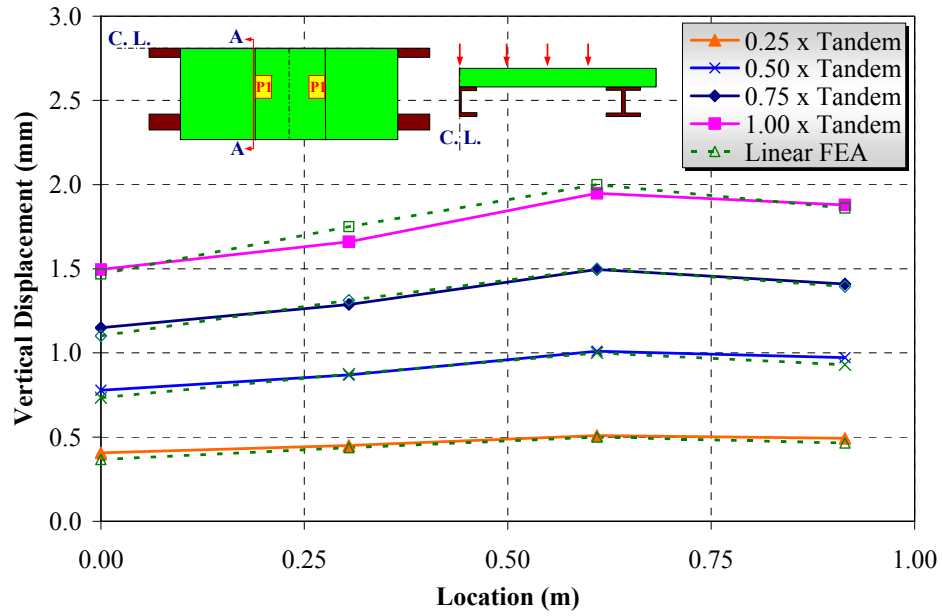
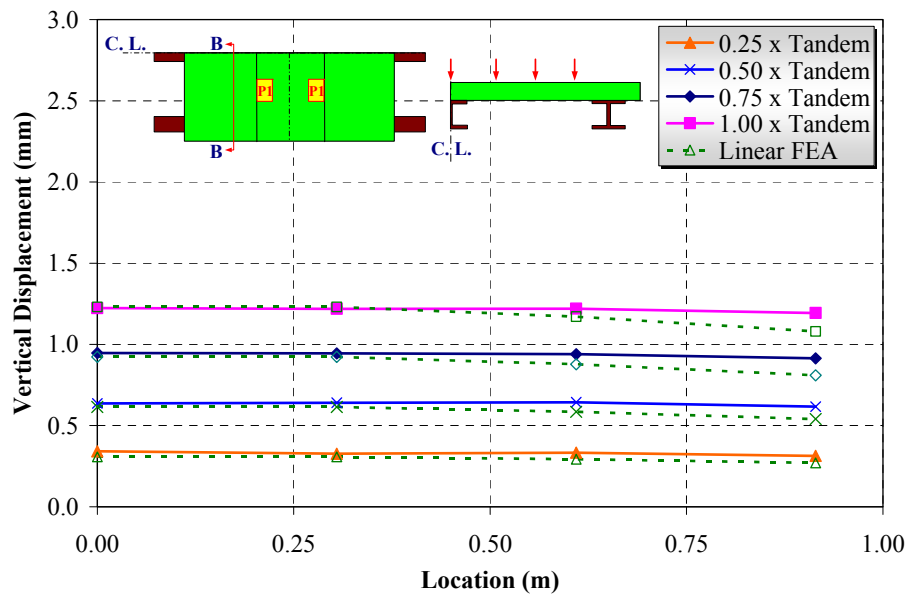


Figure 7.10 Finite Element Model of the Prototype Bridge Deck

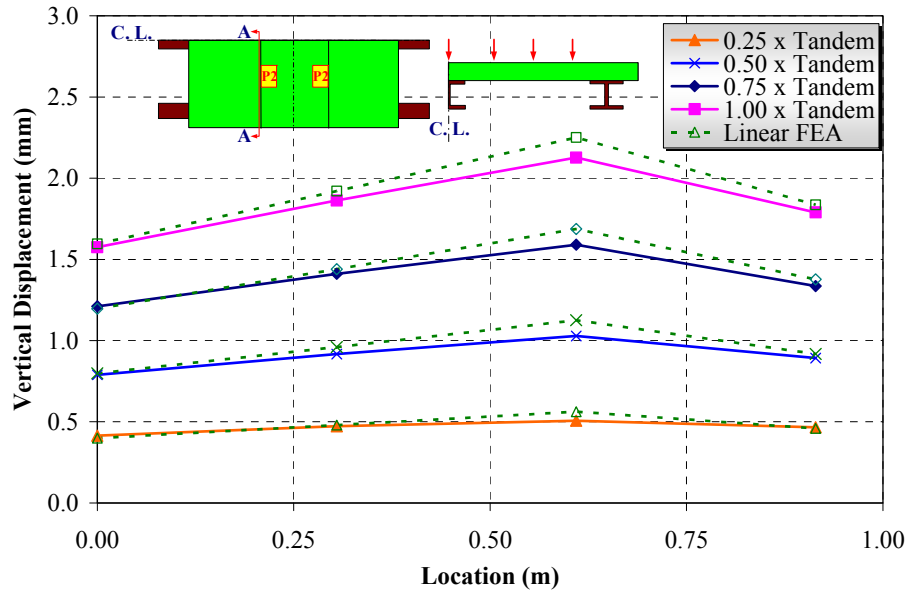


(a) Section A-Top Surface

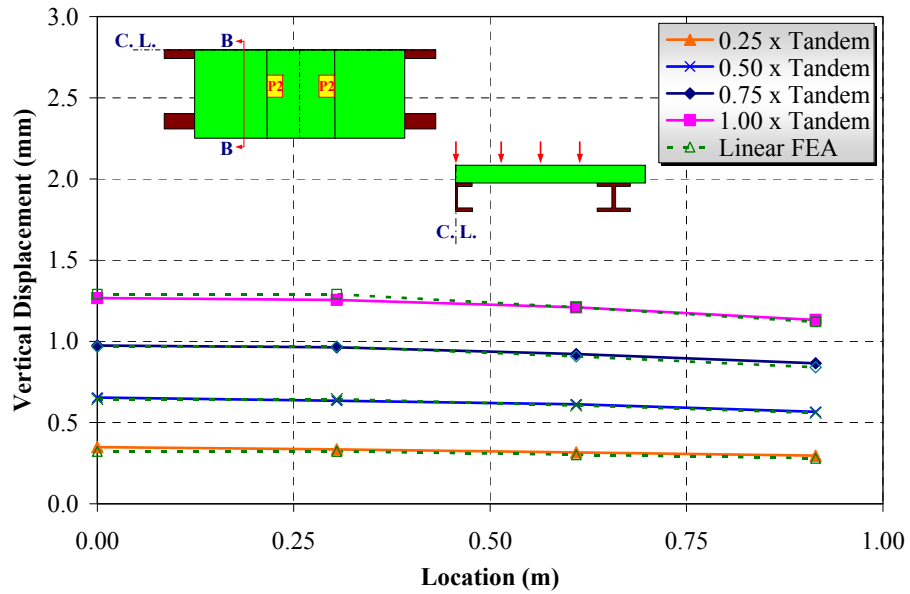


(a) Section B-Top Surface

Figure 7.11 Deformed Shapes under Load Case No. 1

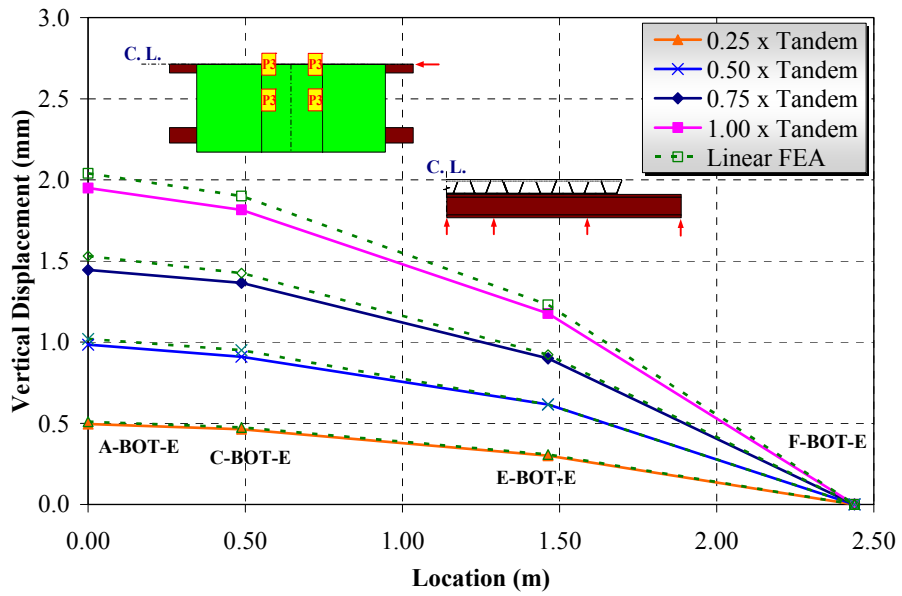


(a) Section A-Top Surface

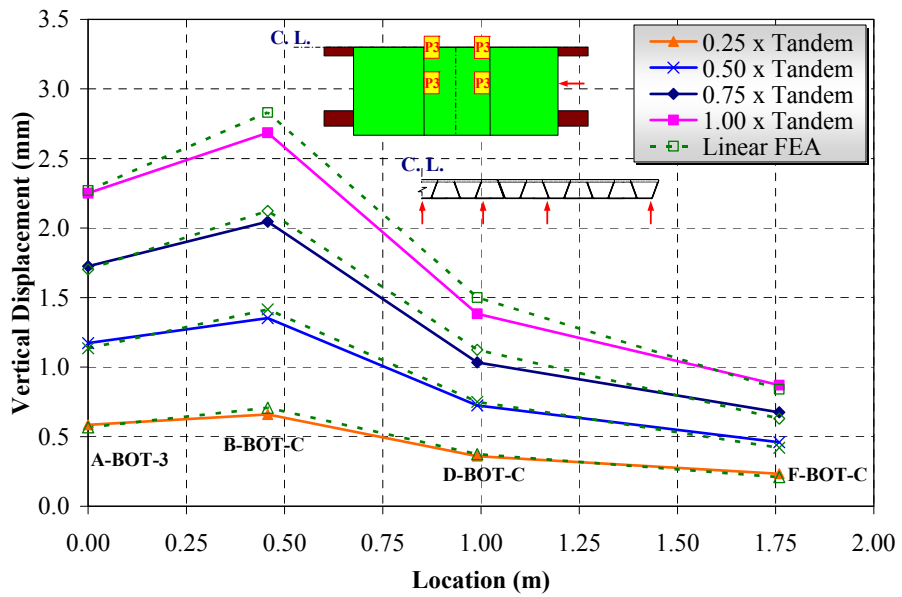


(b) Section B-Top Surface

Figure 7.12 Deformed Shapes under Load Case No. 2

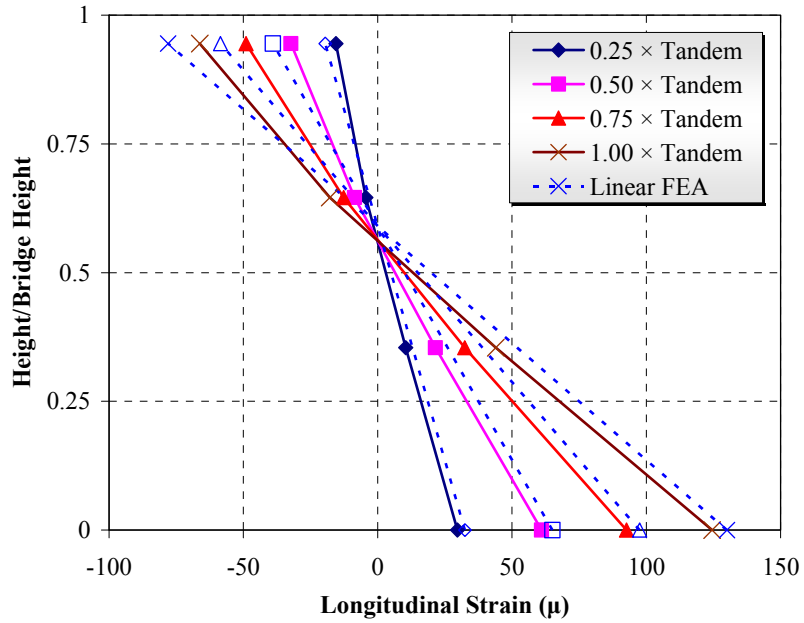


(a) Interior Girder-Bottom Surface

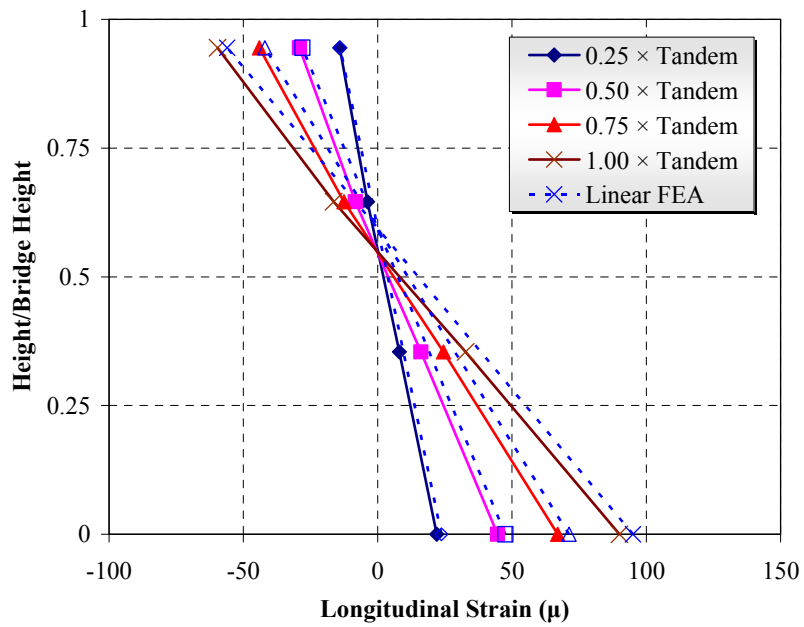


(b) Interior Girder-Bottom Surface

Figure 7.13 Deformed Shapes under Load Case No. 3

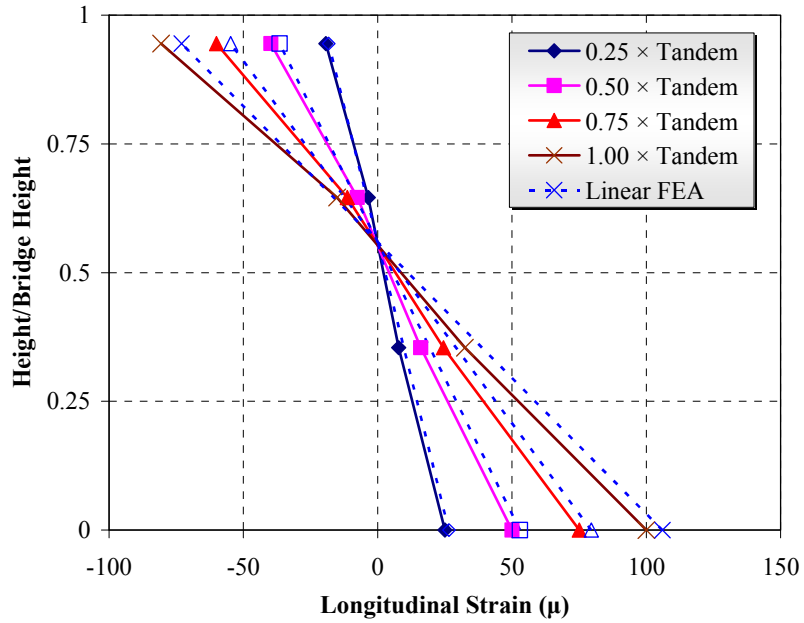


(a) Section C-Interior

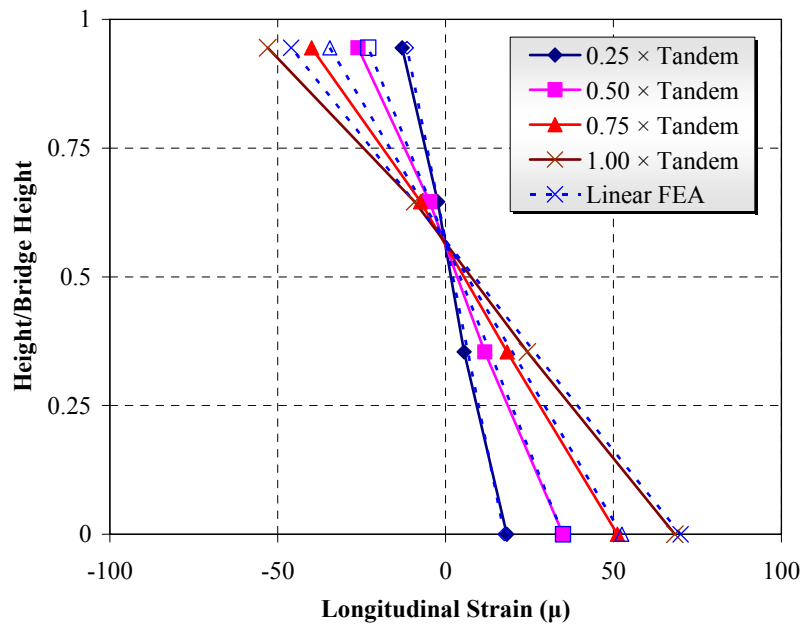


(b) Section C-Exterior

Figure 7.14 Strain Profiles through Section C under Load Case No. 2



(a) Section H-Interior



(b) Section H-Exterior

Figure 7.15 Strain Profiles through the Steel Girder at Section H under Load Case No. 2.

CHAPTER 8

SUMMARY, CONCLUSIONS AND RECOMMENDATIONS

8.1 SUMMARY

This report presented an experimental and analytical study of hybrid FRP-concrete structural systems. Hybrid FRP-concrete structural systems were applied to bridge superstructure and bridge deck. The scope of work of this study can be summarized as follows:

1. Investigate an appropriate hybrid structural system for bridge system that combines FRP and concrete.
2. Optimize the hybrid FRP-concrete bridge system for bridge superstructure and bridge deck systems.
3. Develop a design procedure for a hybrid bridge superstructure and a hybrid bridge deck on steel girders.
4. Perform experimental studies of the proposed hybrid bridge superstructure and bridge deck to verify system performance.
5. Evaluate composite action between the hybrid deck and the steel girders.
6. Develop and analyze finite element model for both the hybrid bridge superstructure and the hybrid deck on steel girders to verify the experimental results.

The following remarks summarize the work done in this study.

8.2 THE PROPOSED HYBRID BRIDGE

In this study, two hybrid FRP-concrete bridge systems were investigated. The first system consists of trapezoidal cell units forming either a bridge superstructure or a bridge deck unit. The second system is formed by arch cells. The two systems rely on using cellular components to form the core of the deck system, and an outer shell to wrap around the cells to form the integral unit of the bridge. Both systems were investigated

analytically by using finite element analysis. From the FE studies, it was concluded that first system is more efficient than the second. Therefore, the first hybrid FRP-concrete system was used to investigate the feasibility of the FRP-concrete structural systems in the remainder of the study. The concrete thickness was chosen to be less than 10% of the bridge depth since concrete will not be used efficiently to increase the bending rigidity when the thickness becomes larger than 10%. The stiffness of the hybrid specimen became much higher than that of the FRP-only specimen. The stiffness of the hybrid specimen is 35% higher than that of the FRP-only specimen, which shows the effectiveness of concrete in enhancing stiffness. In addition, the local deformation under the loading point was dramatically reduced. This is an additional advantage of this hybrid bridge design. Although the proposed hybrid bridge system consists of concrete and FRP composites, the weight is much less than that of a conventional deck and is comparable to that of all-composite decks.

8.2.1 Design Optimization

One of the most important reasons for optimizing a hybrid bridge system is to reduce the structural weight. In the absence of reliable information about manufacturing costs, we assumed that the cost is directly related to the weight of the bridge and used weight as the objective function with a modification to account for the difference in cost between concrete and GFRP. An optimization scheme based on the optimality criteria and a simplified analysis method using the transformed plate formulation to represent the structural system was implemented. Since the design of hybrid bridge systems is stiffness-driven in this study, the maximum allowable deflection was used as a constraint in the optimization design procedure. Based on classical laminate theory (see Appendix A), simplified analysis was used to calculate the maximum deflection of the bridge. In this study, we limited the design variables to the thickness of the plies in the inner, outer, and most outer tube laminates of the proposed bridge system. The optimization scheme reduced the weight of the hybrid superstructure by 35 % from the initial design. The number of cells in the hybrid deck was not optimized; instead, the effects of number of cell on various structural properties of the deck were examined by finite element analysis. Results showed that as number of cells increased, both stiffness and strength increased.

8.2.2 Experimental Studies

8.2.2.1 Bridge Superstructure

The hybrid bridge superstructure was subjected to a series of non-destructive and destructive quasi-static loading tests. The tests results demonstrated the excellent performance of the hybrid FRP-concrete bridge superstructure based on AASHTO specifications. The measured force-displacement responses were near linear under service loads. The maximum deflection of the specimen due to $(1+IM) \times \text{tandem}$ load was $0.67 \times L/800$ (where IM is the dynamic load allowance; $L/800$ is the AASHTO live load deflection limit). The specimen satisfied the AASHTO live load deflection limit. The destructive load tests revealed the failure modes of the bridge superstructure. Local failure mode was occurred before the global failure mode. This local failure mode was within the concrete under the tire patches. The failure load for this local mode was $14.2 \times \text{tandem}$ load, which is 6.3 times the AASHTO requirement of $1.75(1+IM) \times \text{tandem}$ load for live loads in the strength limit I state. A global failure mode was obtained at $20.8 \times \text{tandem}$ load, which is 9.0 times the $1.75(1+IM) \times \text{tandem}$ load. A two-fold failure mechanism was observed; the concrete failed first in compression, leading to the GFRP flanges resisting the compressive force that was originally carried by concrete; the GFRP compression flanges then failed in compression after the applied load was increased.

8.2.2.2 Hybrid FRP-Concrete Deck

A similar hybrid FRP-concrete system to that used in the superstructure study was optimized and then tested as a bridge deck. Welded shear studs were used to connect the hybrid deck to steel girders. The specimen was subjected to a series of service-level flexural loading tests under seven different loading conditions to capture the global response of the specimen and to investigate the composite action of the bridge. The experimental results showed that the hybrid FRP-concrete bridge deck under service loads exhibited excellent performance. No signs of damage were observed in the shear stud connections during the entire test. Similarly, the shear connections at girder-deck interface demonstrated excellent performance under service loads.

The specimen showed linear deformation-load relationship for service loads, which indicates that, the hybrid deck can be modeled as a linear material for the deck

deformation serviceability check. The maximum deformation in the hybrid deck due to $(1+IM)\times$ tandem load was $0.46\times L/800$. This hybrid deck specimen satisfied the AASHTO live load deflection limit.

For the test specimen under service loads, plane sections remained plane and beam theory can be used to design the hybrid decks for service loads. The hybrid deck and the steel girders were interacting in a partially composite way at service-load condition; as evinced by the discontinuity in strain at the hybrid deck-to-steel interface. Based on the upward shift in the neutral axis location from the centroid of the steel girder alone, it was possible to compute the contribution of the hybrid deck to the internal moments needed. It was observed that the hybrid deck acting compositely with steel girders exhibit an effective width, at service-load condition, of approximately 54% of the girder spacing for the interior girder installations and 61% of the half of the girder spacing and the deck overhang for the exterior girder. Effective width calculations for the hybrid deck showed that the effective flange width for hybrid decks are less than AASHTO prescribed effective width for concrete decks. This is expected since that FRP decks are not as axially stiff as concrete decks.

8.2.3 Finite Element Analysis

Finite element analyses of the bridge superstructure and the bridge deck were performed using a general purpose finite element analysis package ABAQUS (2002). The linear FEA and the experimental results are well correlated under service loads. However, under destructive loads, the experimental results showed a loss of strength whereas the linear FEA results did not. This deviation is a direct result of the nonlinearity in both concrete and the GFRP composites. Material nonlinearity models for concrete, GFRP, and steel were implemented in the FE Models to predict the behavior under destructive loads (see Appendix C). Based on the progressive failure analysis (see Appendix C), the predicted failure load of the hybrid bridge deck specimen was $6.2\times$ tandem load, which is 2.7 times the AASHTO requirement for live loads in the strength limit I state.

8.3 CONCLUSIONS

The key conclusions of the study reported in this report are as follow:

1. A combination of FRP composites and concrete provide a promising advancement in civil infrastructure applications. In this study, the stiffness of the hybrid bridge is 35% higher than that of the FRP-only bridge, which shows the effectiveness of concrete that was selected by optimization procedure.
2. As is often the case with GFRP composite bridges, the design of the proposed hybrid bridge superstructure and deck systems are stiffness-driven.
3. The optimality criteria method considered in this study can be used efficiently for the design of stiffness controlled hybrid FRP-concrete bridge systems. The results obtained for the hybrid bridge superstructure and deck systems showed excellent computational efficiency of the method.
4. The experimental study showed the feasibility of the proposed hybrid FR-concrete bridge superstructure and deck systems. It was validated experimentally that the proposed hybrid bridge superstructure and deck systems satisfied the AASHTO stiffness and strength limits.
5. The proposed hybrid deck acting compositely with steel girders exhibited an effective width, at service-load condition, of approximately 54% of the girder spacing for the interior girder installations and 61% of the half of the girder spacing and the deck overhang for the exterior girder.
6. Linear FEA was found to predict accurately the flexural behavior of hybrid bridge systems in the elastic range. Linear FEA can be a good tool in the design of the hybrid bridge systems.

8.4 RECOMMENDATIONS FOR FUTURE INVESTIGATIONS/ IMPLEMENTATION

The following recommendations are provided based on the observations, results and finding of this study:

1. The hybrid bridge specimens were fabricated by a hand lay-up process. Reising et al. (2004) concluded that panels manufactured by hand lay-up method have worse dimension uniformity than those from pultrusion method. To have quality control

on material properties and the bridge dimensions, specimen section should be fabricated by an automated process and be standardized. The trapezoidal section in the hybrid bridge studied here can be made as a standard section. As to the automated fabrication process, filament winding as an open molding technology and resin transfer molding or vacuum assisted resin transfer molding as a closed molding technology are candidates for a fabrication process suitable for the trapezoidal section. In any fabrication process, an efficient way to create the cavity for concrete has to be invented.

2. The hybrid bridge satisfied the AASHTO live load deflection criteria. It was also shown that the proposed design has much higher strength than it is required to have. In fact, based on the current work, it is suggested that the existing AASHTO deflection requirements may not be appropriate for use in FRP installations. A parametric study should be conducted in order to propose a new deflection criterion for FRP bridge systems.
3. The optimization procedure developed in this study is a single-objective problem (i.e., to optimize the bridge weight). One promising direction for future research is the use of multi-objective approaches by minimizing the weight and maximizing the structural stiffness simultaneously.
4. Effective width calculations for the hybrid deck showed that the effective flange width for hybrid decks are less than AASHTO prescribed effective width for concrete decks. However, this result is only applicable to the hybrid bridge studied herein. A parametric study should be conducted with different span lengths, different cross sectional heights, girder spacing, and skew angle, to generalize the result.
5. A one lane simply-supported bridge system was investigated in this study. However, multilane continuous bridge system needs to be addressed. This will raise many questions regarding methods to expand traffic lanes and the effective ways of providing reliable connections to ensure the continuity of the hybrid deck system.
6. Fatigue and Creep characteristics of the hybrid bridge have to be investigated. Also, stiffness degradation due to the fatigue cyclic loading should be

characterized. This can be done by testing the bridge under cycling loading for various stress levels.

7. As cavities that concrete was poured into in the experimental bridge models were small, it is prudent to include a retardant admixture so that adequate time is available for concrete placement.
8. Methods of connecting and anchorage of steel and concrete traffic barriers with the hybrid deck systems should be investigated analytically and experimentally.
9. We have not included any thermal or moisture effects in this study. The moisture and thermal affects should be investigated to assess the performance under extreme environmental conditions.
10. Extended monitoring an FRP bridge deck installation from when it is constructed through multiple years of seasonal temperature and climate variations would yield very useful and important durability information.

REFERENCES

- Adali, S., Walker, M. and Verijenko, V. E. (1996), "Multi-Objective Optimization of Laminated Plates for Maximum Pre-Buckling, Buckling and Post-Buckling Strengths Using Continuous and Discrete Ply Angles", *Composite Structures*, Vol. 35, Iss. 1, pp. 117-130.
- American Association of State Highway and Transportation Officials, (1998), *AASHTO LRFD Bridge Design Specifications*, Second Edition, AASHTO, Washington, D.C.
- Aref, A. J. (1997), A Novel Fiber Reinforced Composite Bridge Structural system, Ph.D. Dissertation, the University of Illinois at Urbana-Champaign.
- Aref, A. J., and Parsons, I. D. (1999), "Design Optimization Procedures for Fiber Reinforced Plastic Bridges", *Journal of Engineering Mechanics*, Vol. 125, No. 9, pp. 1040-1047.
- Ashby, M. F. (1991), "Overview No.92 – Materials and Shape", *Acta Metallurgica et Materialia*, Vol. 39, No. 6, pp. 1025-1039.
- Bakeri, P. A., and Sunder, S. S. (1990), "Concepts for Hybrid FRP Bridge Deck Systems," *Serviceability and Durability of Construction Materials*, Proceedings of the First Materials Engineering Congress, Denver, Colorado, August 13-15, 1990, ASCE, Vol. 2, pp. 1006-1015.
- Bakis, C. E., Bank, L. C., Brown, V. L., Consenza, E., Davalos, J. F., Lesko, J. J., Machida, A., Rizkalla, S. H., and Triantafillou, T. C. (2002), "Fiber Reinforced Polymer Composites for Construction – State-of-the-Art Review", *Journal of Composites for Construction*, Vol. 6, No. 2, pp. 73-87.
- Brailsford, B., Mikovich, S. M., and Hopwood, T. (1995), *Definition of Infrastructure Specific Markets for Composite Materials*, Technical Report, Project P93-121/A573, BIRL, Northwestern University, Evanston, IL.

Busel, J. P., Editor (2000), *Product Selection Guide: FRP Composite Products for Bridge Applications*, First Edition, The Market Development Alliance of the FRP Composites Industry, Harrison, NY.

Camanho, P. P., and Davila, C. G. (2002), “Mixed-Mode Decohesion Finite Elements for the Simulation of Delamination in Composite Materials,” NASA/TM-2002–211737, pp. 1–37.

Cheung, M.S., and Chan, M.Y.T. (1978), “Finite strip evaluation of effective flange width of bridge girders”, *Canadian Journal of Civil Engineering*, Vol. 5, pp.174-185.

Construction Engineering and Management (2000a), “Modular FRP Composite Bridge Deck”, *Emerging Construction Technologies – Civil Technologies –*, Construction Engineering and Management, Purdue University, West Lafayette, IN, <http://www.new-technologies.org/ECT/Civil/superdeck.htm> [Dec.03.02].

Cook, R.D., Malkus, D.S., and Plesha, M.E. (1989), *Concepts and Applications of Finite Element Analysis*, 3rd Edition, John Wiley & Sons, Inc.

Dow Plastics (1999), *DERAKANE Epoxy Vinyl Ester Resins – Chemical Resistance and Engineering Guide*, The Dow Chemical Company.

Davol, A., Burgueno, R., and Seible, F. (2001), “Flexural Behavior of Circular Concrete Filled FRP Shells”, *Journal of Structural Engineering*, Vol. 127, No. 7, pp. 810-816.

Deskovic, N., Meier, U., and Triantafillou, T. C. (1995b), “Innovative Design of FRP Combined with Concrete: Long-Term Behavior”, *Journal of Structural Engineering*, Vol. 121, No. 7, pp. 1079-1089.

Deskovic, N., Triantafillou, T. C., and Meier, U. (1995a), “Innovative Design of FRP Combined with Concrete: Short-Term Behavior”, *Journal of Structural Engineering*, Vol. 121, No. 7, pp. 1069-1078.

Fam, A. Z. and Rizkalla, S. H. (2002), “Flexural Behavior of Concrete-Filled Fiber-Reinforced Polymer Circular Tubes”, *Journal of Composites for Construction*, Vol. 6, No. 2, pp. 123-132.

Federal Highway Administration (2002), “Current Practices in FRP Composites Technologies,” *Bridge Technology*, FHWA, [http://www.fhwa.dot.gov/bridge/frp/frppract .htm](http://www.fhwa.dot.gov/bridge/frp/frppract.htm) [Dec.03.02].

Federal Highway Administration, and Federal Transit Administration (2003), 2003 Status of the Nation’s Highways, Bridges and Transit: Conditions and Performance-Report to Congress, [http://www.fhwa.dot.gov/policy/2002cpr/report .htm](http://www.fhwa.dot.gov/policy/2002cpr/report.htm) [Oct.0 3. 03].

Fukunaga, H., and Vanderplaats, G. N. (1991), “Strength Optimization of Laminated Composites with Respect to layer Thickness and/or Layer Orientation Angle”, *Computer and Structure*, V. 40, pp. 1429-1439.

Fukunaga, H., and Vanderplaats, G. N. (1991) “Minimum Weight Design of Laminated Composite Panels under Strength and Displacement Constraints,” *JSME International Journal, Series I, Solid Mechanics Strength of Materials*, Vol. 34, PP. 171-177.

Elkelish, S. and Robinson, H. (1986), “Effective Widths of Composite Beams With Ribbed Metal Deck”, *Canadian Journal of Civil Engineering*, Vol. 13, No. 5, pp. 575-582.

Grace Construction Products (2002a), *Product Information: ADVA Flow – Superplasticizer ASTM C 494, Type F*, http://www.na.graceconstruction.com/concrete/download/DC-30E_6.pdf [Dec.03.02].

Grace Construction Products (2002b), *Engineering Bulletin 1: Eclipse – Shrinkage Reducing Admixture*, [http://www.na.graceconstruction.com/concrete /download/EC-2E_1.pdf](http://www.na.graceconstruction.com/concrete/download/EC-2E_1.pdf) [Dec.03.02].

Haftka, R. T., Gurdal, Z., and Kamat, M. P. (1990), “Elements of Structural Optimization,” kluwer Academic Publishers.

Hall, J. E. and Mottram, J. T. (1998), “Combined FRP Reinforcement and Permanent Formwork for Concrete Members”, *Journal of Composites for Construction*, Vol. 2, No. 2, pp. 78-88.

Hayes, M. D. (1998), *Characterization and Modeling of a Fiber-Reinforced Polymer Composite Structural Beam and Bridge Structure for Use in the Tom's Creek Bridge Rehabilitation Project*, Master Thesis, Virginia Polytechnic Institute and State University, Blacksburg, Virginia.

Hayes, M. D., Ohanehi, D., Lesko, J. J., Cousins, T. E., and Witcher, D. (2000), "Performance of Tube and Plate Fiberglass Composite Bridge Deck," *Journal of Composites for Construction*, Vol. 4, No. 2, pp. 48-55.

He, Y., and Aref, A. J. (2003) "An Optimization Design Procedure for Fiber Reinforced Polymer Web-Core Sandwich Bridge Deck Systems," *Composite Structures*, Vol. 60, pp. 183-195.

Hibbit, Karlsson & Sorensen, Inc. (2002), *ABAQUS/Standard User's Manual*, Version 6.3, Hibbit, Karlsson & Sorensen, Inc.

Hillman, J. R. and Murray, T. M. (1990), "Innovative Floor Systems for Steel Framed Buildings," *Mixed Structures, Including New Materials*, Proceedings of IABSE Symposium, Brussels, Belgium, Vol. 60, IABSE, Zurich, pp. 672-675.

Hullat, J., Hollaway, L., and Thorne, A. (2003), "The Use of Advanced Polymer Composites to Form An Economic Structure Unit", *Construction and Building Materials*, Vol.17, pp. 55-68.

Jones, R. M. (1999), *Mechanics of Composite Materials*, 2nd Edition, Taylor & Francis Inc., Philadelphia, PA.

Karbhari, V. M. and Zhao, L. (2000), "Use of Composites for 21st Century Civil Infrastructure," *Computer Methods in Applied Mechanics and Engineering*, Vol. 185, pp. 433-454.

Keelor, D.C., Luo V., Earls, C.J., Yulismana, W. (2004), "Service Load Effective Compression Flange Width in FRP Deck Systems Acting Compositely with Steel Stringers", *Journal of Composites for Construction, American Society of Civil Engineers*, Vol. 8 No. 4, pp. 289-297.

- Keller, T. and Gurtler, H. (2005a), “Quasi-static and fatigue performance of a cellular FRP bridge deck adhesively bonded to steel girders”, *Composite Structures*, Vol. 70, No. 4, pp. 484-496.
- Keller, T. and Gurtler, H. (2005b), “Composite Action and Adhesive Bond Between Fiber-Reinforced Polymer Bridge Decks and Main Girders”, *Journal of Composites for Construction*, Vol. 9, No. 4, pp. 360-368.
- Khot, N. S. (1981), “Algorithms Based on Optimality Criteria to Design Minimum Weight Structures”, *Engineering Optimization*, V.5, pp. 73-90, 1981.
- Kim, H., Hwang, Y., Park, K., Lee, Y. and Kim, S. (2005), “Fiber reinforced plastic deck profile for I-girder bridges”, *Composite Structures*, Vol. 67, No. 4, pp. 411-416.
- Kitane, Y. and Aref, A. (2004), “Static and fatigue testing of hybrid fiber-reinforced polymer-concrete bridge superstructure”, *Journal of Composites for Construction*, Vol. 8, No. 2, pp. 182-190.
- Lesko, J. J., Hayes, M. D., Schniepp, T. J. and Case, S. W. (2001), “Characterization and durability of FRP structural shapes and materials”, *Composites in Construction: A reality*, pp. 110-120.
- Market Development Alliance of the FRP Composites Industry (2002), *Industry Overview: Overview of the FRP Composites Industry – A Historical Perspective*, Market Development Alliance of the FRP Composites Industry, http://www.mada.composites.org/Industry_Overview.htm [Dec.03.02].
- Martin Marieta Composites, “*DuraSpan Fiber Reinforced Polymer (FRP) Bridge Deck*”, 2001.
- Maxwell, C. (1890), *Scientific Paper II*, Cambridge University Press.
- Meggers, D. Kansas Department of Transportation. 2000. "Fiber reinforced polymer bridge decks—The Kansas experience." *Rep. Prepared for the Kansas Department of Transportation* (CD-ROM), Topeka, Kan.
- Michell, A. G. M. (1904), “The Limits of Economy of Material in Frame-Structures”, *Philosophical Magazine*, Series 6, Vol. 8, No. 47.

- Mirmiran, A. (1999a), "Acoustic Emission Monitoring of Hybrid FRP-Concrete Columns", *Journal of Engineering Mechanics*, Vol. 125, No. 8, pp. 899-905.
- Mirmiran, A. (1999b), "Strength and Durability of Hybrid FRP-Concrete Beam-Columns," *Journal of Structural Engineering*, Vol. 125, No. 10, pp. 1085-1093.
- Mirmiran, A., Shahawy, M., and Beitleman, T. (2001), "Slenderness limit for hybrid FRP-concrete columns," *Journal of Composites for Construction*, Vol. 5, No. 1, pp. 26-34.
- Moon, FL., Eckel, DA., Gillespie, JW. (2002), "Shear Stud Connection for the Development of Composite Action between Steel Girders and Fiber Reinforced Polymer Bridge Decks", *Journal of Structural Engineering*, Vol. 128, No. 6, pp. 762-770
- MSC Software Corporation (1999): *MSC/Patran Version 9 - User's Guide*.
- Mufti, A. A., Labossière, P., and Neale, K. W. (2002), "Recent Bridge Applications of FRPs in Canada", *Structural Engineering International*, Vol. 12, No. 2, pp. 96-98.
- Nystrom, H. E., Watkins, S. E., Nanni, A., and Murray, S. (2003), "Financial Viability of Fiber-Reinforced Polymer (FRP) Bridges", *Journal of Management in Engineering*, Vol. 19, No. 1, pp. 2-8.
- Park, K. T., Hwang, H. Y., Kim, H. Y., Lee, Y. H. and Kim, S. M. (2004), "Deck-to-Girder Connections for GFRP Bridge Decks", In Proceedings, 4th International Conference on the Advanced Composite Materials in Bridges and Structures, Calgary, Alberta, July 20-23, 2004. Montreal: Canadian Society for Civil Engineering, 9 p.
- Reising, R., Shahrooz, B., Hunt, V., Neumann, A., Helmicki, A. and Hastak, M. (2004), "Close Look at Construction Issues And Performance of Four Fiber-Reinforced Polymer Composite Bridge Decks", *Journal of Composites for Construction*, Vol. 8, No. 1, pp. 33-42.
- Ribeiro, M. C. S., Tavares, C. M. L., Ferreira, A. J. M., and Marques, A. T. (2001), "Static Flexural Performance of GFRP-Polymer Concrete Hybrid Beams",

Proceedings of the International Conference on FRP Composites in Civil Engineering, Vol. II, December 12-15, 2001, Hong Kong, China, J. G. Teng, Editor, Elsevier Science Ltd., New York, pp. 1355-1362.

Righman, J., Barth, K. and Davalos, J. (2004), "Development of an efficient connector system for fiber reinforced polymer bridge decks to steel girders", *Journal of Composites for Construction*, Vol. 8, No. 4, pp. 279-288.

Saiidi, M., Gordaninejad, F., and Wehbe, N. (1994), "Behavior of Graphite/Epoxy Concrete Composite Beams", *Journal of Structural Engineering*, Vol. 120, No. 10, pp. 2958-2976.

Samaan, M. and Mirmiran, A. (1998), "Model of Concrete Confined by Fiber Composites", *Journal of Structural Engineering*, Vol. 124, No. 9, pp. 1025-1031.

Schmit, L. A. Jr. (1960), "Structural Design by Systematic Synthesis", Second Conference of Electronic Computation, Pittsburg, PA.

Spallino, R., and Rizzo, S. (2002), "Multi-objective Discrete Optimization of Laminated Structures", *Mechanics Research Communications*, Vol. 29, pp. 17-25.

Tang, B., and Podolny, W. (1998), "A Successful Beginning for Fiber Reinforced Polymer (FRP) Composite Materials in Bridge Applications", Proceedings of the International Conference on Corrosion and Rehabilitation of Reinforced Concrete Structures, December 7-11, 1998, Orlando, FL, Federal Highway Administration.

Uddin, N., Fouad, F., Khotpal, A., Vaidya, U. and Serrano-Perez, J. (2006), "Structural characterization of hybrid fiber reinforced polymer (FRP) - Autoclave Aerated Concrete (AAC) panels", *International SAMPE Technical Conference, SAMPE 2004*, pp. 2761-2775.

U.S. Department of Transportation, Bureau of Transportation Statistics (2001), *National Transportation Statistics 2000*, BTS0101, U.S. Government Printing Office. U.S. Department of Transportation.

Van Erp, G. (2002a), "Road Bridge Benefits from Hybrid Beams", *Reinforced Plastics*, Vol. 46, No. 6, Elsevier Science Ltd., Oxford, UK.

Van Erp, G., Heldt, T., McCormick, L., Carter, D., and Tranberg, C. (2002b), *An Australian Approach to Fibre Composite Bridges*, Fibre Composites Design and Development, University of Southern Queensland, Toowoomba, Australia, <http://www.fcdd.com.au> [Dec.01.02].

Venkayya, V. S. (1989), “Optimality Criteria: A basis for Multidisciplinary Design Optimization”, *Computational Mechanics*, V.5, pp. 1-21.

Yang, Q., Qin, Q., and Zheng, D. (2002), “Analytical and Numerical Investigation of Interfacial Stresses of FRP-Concrete Hybrid Structure”, *Composite Structures*, Vol. 57, pp. 221-226.

Zetterberg, T., Astrom, B. T., Backund, J. and Burman, M. (2001), “On Design of Joints between Composite Profiles for Bridge Deck Applications”, *Composite Structures*, Vol. 51, pp. 83-91.

Zhou, A. and Keller, T. (2005), “Joining techniques for fiber reinforced polymer composite bridge deck systems”, *Composite Structures*, Vol. 69, No. 3, pp. 336-345.